Cubic Silicon Carbide For Direct Photoelectrochemical Water Splitting

by Dipl.-Phys Sven Tengeler, born in Hamburg

UNIVERSITÉ
Grenoble
Alpes

IDS-FunMat

Graduate School of
Energy Science
and Engineering

TECHNISCHE
UNIVERSITÄT
DARMSTADT

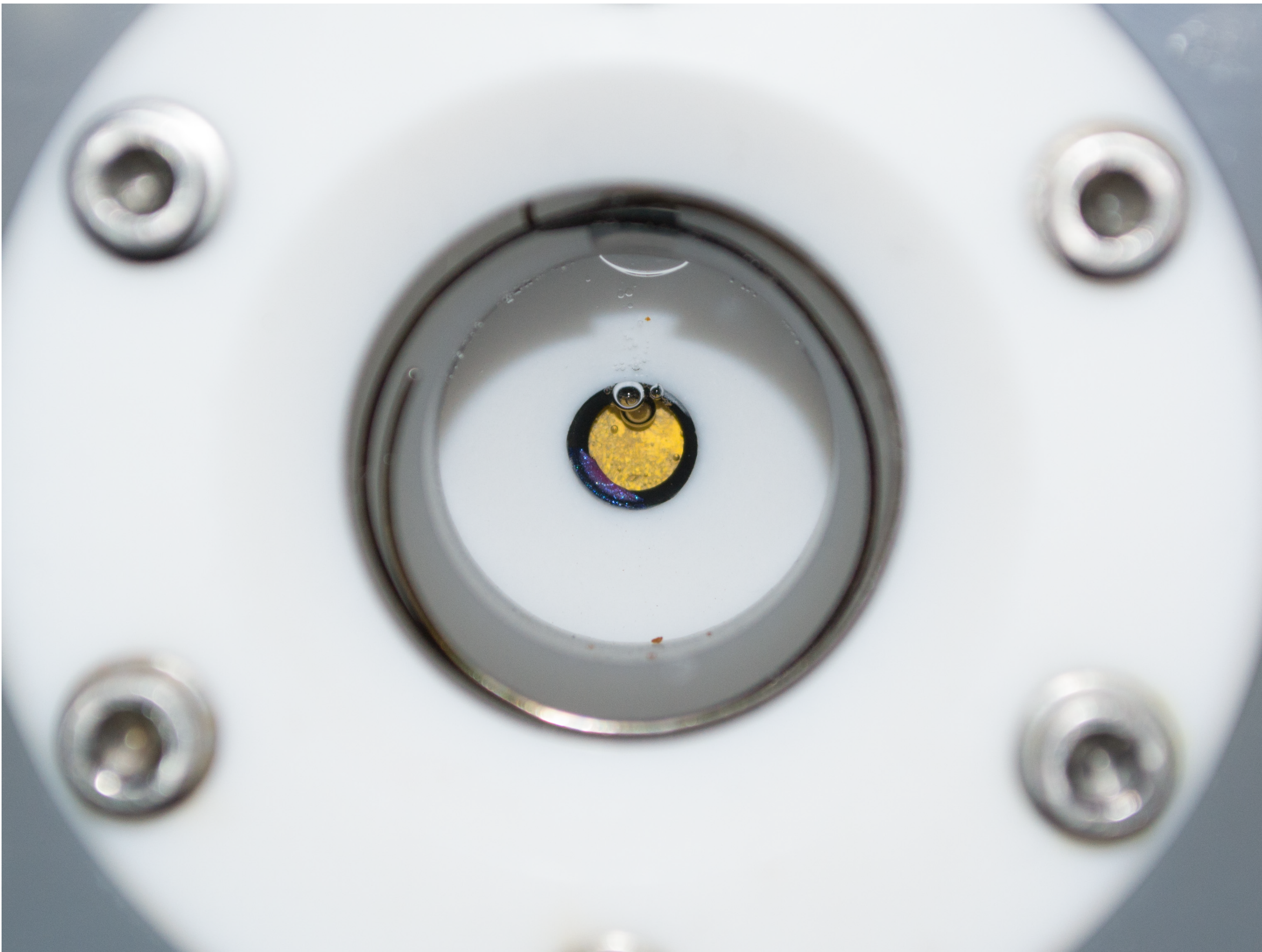

Cubic silicon carbide for direct photoelectrochemical water splitting

Carbure de silicium cubique pour la dissociation photo-électrochimique direct de l’eau

Thèse pour obtenir le grade de
Docteur de la Communauté Université Grenoble Alpes

Spécialité : Matériaux, Mécanique, Génie Civile, Electrochimie
au sein de l’Ecole Doctorale I-MEP2

Présentée par

Sven Tengeler

Directeur de thèse: Prof. Dr. Wolfram Jaegermann
Directeur de thèse: Prof. Dr. Didier Chaussende

Cubic silicon carbide for direct photoelectrochemical water splitting

Kubibisches Siliziumkarbid für die direkte photoelektrochemische Wasserspaltung

Vom Fachbereich Material- und Geowissenschaften
der Technischen Universität Darmstadt

zur Erlangung des akademischen Grades eines

Doktor-Ingenieurs (Dr.-Ing)

genehmigte
Dissertation

vorgelegt von

Dipl.-Phys Sven Tengeler
aus Hamburg

Referent: Prof. Dr. Wolfram Jaegermann
Referent: Prof. Dr. Didier Chaussende

Tag der Einreichung: 13/09/2017
Tag der mündlichen Prüfung: 09/11/2017

D17 - Darmstadt 2017

Statement regarding the thesis

I hereby confirm that I have written the present thesis independently and without illicit aid from third parties, using solely the aids mentioned. All passages from other sources are marked as such. This work has not been presented to an examination office before in this or a similar form.

Déclaration sur la dissertation

Je déclare par la présente que la thèse a été rédigée sans l’aide d’un tiers et que toutes les aides et supports ont été mentionnés. Toutes les sources ont été indiquées. Ce travail n’a pas été présenté antérieurement devant un comité d’examen, que ce soit en totalité ou en partie,

Erklärung zur Dissertation

Hiermit versichere ich, die vorliegende Dissertation ohne Hilfe Dritter nur mit den angegebenen Quellen und Hilfsmitteln angefertigt zu haben. Alle Stellen, die aus Quellen entnommen wurden, sind als solche kenntlich gemacht. Diese Arbeit hat in gleicher oder ähnlicher Form noch keiner Prüfungsbehörde vorgelegen.

Darmstadt, den 28/11/2017

(Sven Tengeler)

Abstract

English:

The goal of this work was to investigate cubic silicon carbide as anode material for direct photoelectrochemical water splitting. From the performed measurements (mostly photoelectron spectroscopy, electrochemical measurements, Raman and UV-Vis spectroscopy) n-type cubic silicon carbide's low oxygen evolution efficiency could be related to some fundamental problems. Primarily, the attainable photocurrent is limited by the flux of photo generated holes to the semiconductor surface. As cubic silicon carbide is an indirect semiconductor, the low absorption coefficient in combination with a high doping concentration and low hole diffusion length were determined as limiting factors. Deposition of an additional epitaxial n^- cubic silicon carbide layer resulted in a significant improvement of the observed photocurrent.

The obtainable photovoltage and recombination losses are mostly dependent on the surface properties. While a buried junction between the silicon carbide and a thin catalyst layer has proven to be promising for improving both properties, it still needs optimization, as Fermi level pinning from interface defect states drastically reduces the obtained photovoltage.

Français:

Le but de ce travail était d'évaluer la capacité du carbure de silicium cubique comme matériau d'anode pour le fractionnement photo-électrochimique direct de l'eau. Les données obtenues (principalement par spectroscopie de photoélectrons, électrochimie, spectrométrie Raman et spectrométrie UV-Vis) ont permis d'identifier les problèmes fondamentaux à l'origine de la faible efficacité du carbure de silicium cubique dopé n pour la production d'oxygène. Le courant photoélectrique atteignable est principalement limité par le flux de trous vers la surface du semi-conducteur, et générés par l'absorption de photon. Comme le carbure de silicium cubique possède une bande interdite de nature indirecte, le faible coefficient d'absorption combiné à un dopage élevé et à une faible longueur de diffusion des trous ont été déterminés comme des facteurs limitant. La mise en œuvre d'un film épitaxial additionnel de carbure de silicium cubique ayant un faible dopage n^-, a conduit à une augmentation significative du courant photoélectrique.

La tension photoélectrique obtenue et les pertes dues aux recombinaisons dépendent principalement des propriétés de surface. Même si l'utilisation de jonctions enterrées entre le carbure de silicium et des films minces de catalyseurs s'est révélée prometteuse pour l'amélioration des deux propriétés, une optimisation soigneuse est nécessaire car la forte densité d'états d'interface liés à des défauts limitent considérablement la tension photoélectrique.

Deutsch:

Ziel dieser Arbeit war es die Tauglichkeit von kubischem Siliziumkarbid als Anoden-Material für die direkte photoelektrochemische Wasserspaltung zu untersuchen. Dabei konnte die geringe Effizienz von n-dotiertem, kubischen Siliziumkarbid für die Sauerstoffentwicklung aufgrund der erhobenen Daten

(überwiegend Photoelektronenspektroskopie, Elektrochemie, Raman und UV-Vis Spektroskopie) auf grundlegende Probleme zurückgeführt werden. In erster Linie wird der erreichbare Photostrom durch den Fluss fotogenerierter Löcher zur Oberfläche begrenzt. Dabei sorgen der geringe Absorptionskoeffizient in Kombination mit der hohen Dotierung und der geringen Loch-Diffusionslänge dafür, dass nur wenige Löcher die Oberfläche erreichen um dort zur Redox Reaktion beizutragen. Die Abscheidung einer dünnen epitaktischen Siliziumkarbid Schicht mit niedrigerer Dotierkonzentration hat sich als probates Mittel erwiesen, den Photostrom signifikant zu verbessern.

Die erreichbare Photospannung sowie auftretende Rekombinationsverluste an der Oberfläche hängen überwiegend von der Oberflächenbeschaffenheit ab. Hier hat sich die Verwendung von dünnen Katalysatorschichten als vielversprechender Ansatz bewiesen, welcher allerdings noch der Optimierung bedarf, da Defektzustände an der Grenzfläche das Fermi-Level pinnen und so die Photospannung limitieren.

Contents

1 Introduction

This chapter gives a short introductory motivation on the topic of renewable energies and water splitting for energy storage. The basic idea behind direct photoelectrochemical water splitting will be discussed, and different design approaches briefly highlighted. Along with requirements on suitable materials for interface junctions, and why 3C SiC might be a promising candidate.

1.1 Why Renewable Energies?

Over the last centuries, mankind has managed to transfer his workload from man (or animal) powered labour to more efficient means. While the early transitions used renewable energy (wind and water), later transitions required fossil fuels (from steam to oil and now electricity). The resulting efficiency increase, has enabled our society to shift an ever increasing percentage of our workforce from providing for our basic needs (like keeping us warm and feed), to further improving our lifestyle based on a rapid technological progress over the last century. However, this progress is tightly linked to an ever growing demand for energy, as increasingly sophisticated machinery takes over more and more of our workload - a trade-off between increased productivity and energy dependence.

Our modern lifestyle is deeply coupled with all kinds of energy demanding machinery. Either for transportation (public, cars, planes), to power the production facilities supplying us with a high variety of cheap food and articles of daily use, to heat and illuminate our buildings, and to power large scale chemical reactions (providing modern fertilizers, medicine etc.), our vast information infrastructure (Google alone needed 2.3 TWh in 2011 [1]), or the smart phone in our very pocket. The above list could be extended at will. But one conclusion can be drawn with certainty, our current way of living makes us totally dependant on a constant and secure energy supply. And while power consumption may stay constant in richer countries,

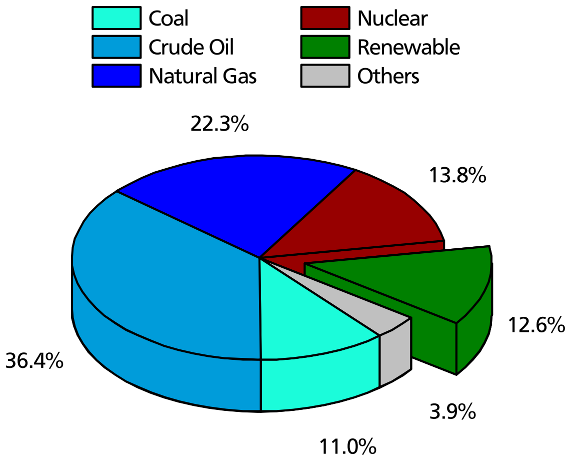

Figure 1.1.: *Gross inland consumption (B_100900 in [2]) of the main energy sources. The total energy consumption (not just electricity) of all EU-28 states in 2015, was 1603.1 megatons of oil equivalent (Mtoe) or* 18 512 TWh. *Above diagram is based on data from Eurostat [3–7].*

a result of more efficient equipment, it is definitely bound to increase, as more second or third world countries will adapt a 'Western lifestyle'.

The current (2015) energy mix for Europe is displayed in figures 1.1 and 1.2. Despite extensive promotion of renewable energies over the last decade, close to 90 % of our energy mix is still based on non-renewable sources. Predictions, on how long the available fossil fuels will last, vary tremendously, depending on the assumed consumption and the ongoing discovery of new resources. However, at some point, about a century from now, all fossil fuel reserves will be exhausted [8–10].

In addition to the supply limitation, our fossil fuel consumption gives rise to a number of related drawbacks. Global warming, as a result of an ever increasing CO_2 emission, could severely impact the available drinking water supply, and crop production, not to mention the sea level rise, and increasingly hazardous weather conditions [11]. Mining accidents, like Deepwater Horizon, can wreak havoc on entire ecosystems, and cause substantial cost for necessary restoration projects. The same is true for nuclear power plants, where the incidents of Tschernobyl and Fukushima serve as examples for the risks and potential costs of malfunctioning reactors, not even considering the problem of radioactive waste longterm storage.

On the other hand, modern power plants are steadily improving in terms of efficiency, pollution output, and safety. Therefore, there is no reason for overt haste in turning our backs on fossil fuels. Which we could not do anyway, as it will take a long time to build up the necessary renewable energy production capacity, and rebuild our whole energy infrastructure to match.

For electrical power, modern power grids were designed around a small number of huge power plants, with ever thinner power cables further down the supply chain. This design is not meant to handle a huge number of small renewable power plants all over the place. Another thing to consider is the maintenance of a steady frequency for the power network. Switching from gas or oil powered heating machinery to electric ovens of heat storage setups is uncomplicated. However, mobility from renewable energy sources will require major investments as a network of refuelling stations for the increasing numbers of electrical or hydrogen vehicles has to be set up and maintained.

All of the problems mentioned above can be solved with the technologies currently at hand. However, the renewable harvesting technologies, with the greatest potential for growth, are wind- and solar power, see figure 1.2. Both have the disadvantage of being highly volatile. This is critical, especially where electrical power is concerned, as unfavourable weather conditions (clouds, no wind) could result in blackouts, if the percentage of wind- and solar power would be high enough. It is illusory to assume the power consumption could be reduced accordingly, therefore a continuous power supply has to be ensured with other means. In the end, the only reasonable approach are backup

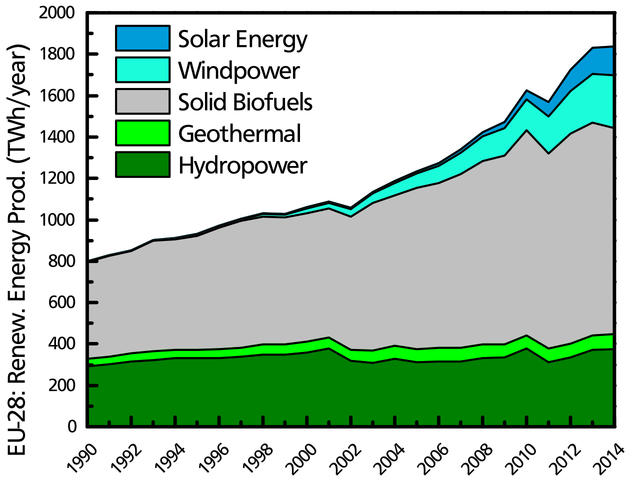

Figure 1.2.: *Development of renewable energy (not just electricity) production in Europe since 1990. The main increase stems from windpower, solar energy (photovoltaic and thermal) and solid biofuels (all 'organic, non fossil material of biological origin'). Based on data from Eurostat [2, 7].*

power plants, which have to be able to perform rapid run up / shut down cycles. Gas power plants would be well suited for the task, the same is true for large scale fuel cells. This also means, that almost twice the actually needed capacity needs to be installed and paid for.

A good example, of the disruptions renewable energies can cause, is Germany, due to the massive increase in installed renewable energy capacity. A result of the extensive funding in form of the 'Erneuerbare Energie Gesetz' from 2000 [12]. In 2013, the total installed capacity of wind and solar power has reached up to 70.1 GW [13]. The total energy consumption for Germany in 2013 was 596 TWh [14]. Neglecting the power consumption dependency on daytime, this yields an average energy demand of 68 GW. Apparently, there will be times when the installed renewable capacity is already sufficient to meet the total demand in electrical power. Which requires that conventional power plants, who were designed to run continuously, have to shut down or reduce their output, momentarily, as renewable power is preferred.

1.2 Chemical Energy Storage

Proceeding from there, a total replacement of fossil fuels and nuclear power with renewable energies, will have to be accompanied by a storage solution for large amounts of renewable energy, in order to bridge any power shortage arising from this volatility. A storage capacity of about two weeks energy demand is assumed most often. While batteries are used for peak shaving and short term storage, their maximum capacity limits their use for long term storage on a national scale.

Battery Storage Example

Two weeks out of 18512 TWh means a **required storage capacity** of approximately **712 TWh**. A standard car battery (60 to 100 Ah at 12 V) has a capacity around 1 kWh. Therefore, at least **712,000,000,000 car batteries** would be needed for storage, **1400 for each** of Europe's 508 million citizens.

Therefore, large scale energy storage could best be implemented via the creation of suitable chemical compounds, like hydrogen or various hydrocarbons. This approach is known as chemical energy storage. The basic idea is to transform some kind of chemical reactant into an energetically uphill product, requiring a certain amount of energy. Once needed, a reverse reaction can be initiated, returning part of the originally invested energy. The most fundamental reaction of this kind would be the electrolysis of water into hydrogen and oxygen, according to

$$\begin{aligned}
&\text{Cathode (HER):} && 4\,H_2O + 4\,e^- \longrightarrow 2\,H_2 + 4\,OH^- \\
&\text{Anode (OER):} && 4\,OH^- \longrightarrow 2\,H_2O + O_2 + 4\,e^- \\
&\text{Redox Reaction:} && 2\,H_2O \longrightarrow O_2 + 2\,H_2
\end{aligned}$$

for an alkaline solution [15]. From there, the hydrogen itself can be stored, much like fossil gas, thus the necessary storage capacities are already installed. Alternatively, the H_2 can be used as reactant in the Fischer-Tropsch reaction

$$n\mathrm{CO} + (2n+1)\mathrm{H}_2 \longrightarrow \mathrm{C}_n\mathrm{H}_{2n+2} + n\mathrm{H}_2\mathrm{O} \quad ,$$

in order to produce hydrocarbons, which possess a higher energy density [16]. Both products have their respective (dis)advantages. In the end, it comes down to a trade-off between energy density and efficiency, as each additional reaction step increases energetic losses.

Where energy density is non-critical, hydrogen has some advantages. It has the lowest transformation losses. A direct (and highly efficient) conversion to electrical power is possible via fuel cells. Finally, burning hydrogen, either for energy, mobility, or heat, does produce neither fine dust nor hazardous compounds, only water.

Water splitting via electrolysis, in general, is rather straight forward. All that is needed are two electrodes, some water, and electrical power, supplied at a sufficiently high potential. Problems arise for keeping the reaction running for extended durations, and reaching a high efficiency. A potential difference of at least 1.23 V is needed in order to split water. This is also the maximum potential to be gained from the back reaction. In reality, significantly higher potentials are needed for the electrolysis, in order to achieve meaningful current densities, while the usable potential will often be lower. These additional potentials are called overpotentials, they depend on the catalyst used and increase with the current density [15].

Above considerations give rise to two different design approaches. First, a stand alone electrolyser can be used to convert surplus electrical energy, from any surrounding power source, into hydrogen. High current densities will result in higher overpotentials. Second, so called photoelectrochemical water splitting can be performed. It can be imagined, as a combination of a solar cell with an electrolyser, directly producing hydrogen, instead of electrical power. The much smaller current densities should allow a higher efficiency.

A direct photoelectrochemical cell requires some specific design characteristics. The solar cell component has to provide a sufficiently high photovoltage to cover the 1.23 V plus any overpotentials and ohmic loses in the device, while also supplying a sufficiently high current density at the same time. Considering, the HER overpotential for platinum (0.07 V), and the OER overpotential for ruthenium(IV)oxide (0.36 V), which are among the best known catalysts, the supplied photovoltage must exceed 1.66 V [17]. Conventional semiconductors, like silicon or gallium arsenide, can not provide this with a single junction, because of their small band gap (E_{BG}), e.g. 1.1 eV for silicon. However, wide band gap semiconductors, with E_{BG} slightly above 2 eV might be well suited to the task [18, 19]. It has to be kept in mind though, that a large E_{BG} will limit the fraction of the solar spectrum the cell will be able to absorb. Multi junction solar cells would also be able to supply the desired photovoltage.

At the same time, the cell has to be chemical inert, as it will be in direct contact to the electrolyte (normally a weak acid or base in order to reduce ohmic resistance loses). Normal solar cells are sealed in order to prevent this kind of exposure, as it will cause degradation of the semiconductor materials, and ultimately destroy the cell. Therefore, a suitable semiconductor material will either have to be inert under operating conditions, or some kind of additional protection layer has to prevent degradation.

1.3 3C SiC for Water Splitting?

Silicon carbide (SiC) is a cutting-edge material, with a wide range of potential applications. Equal parts of silicon (Si) and carbon (C) are bound in a way that each carbon atom forms four covalent

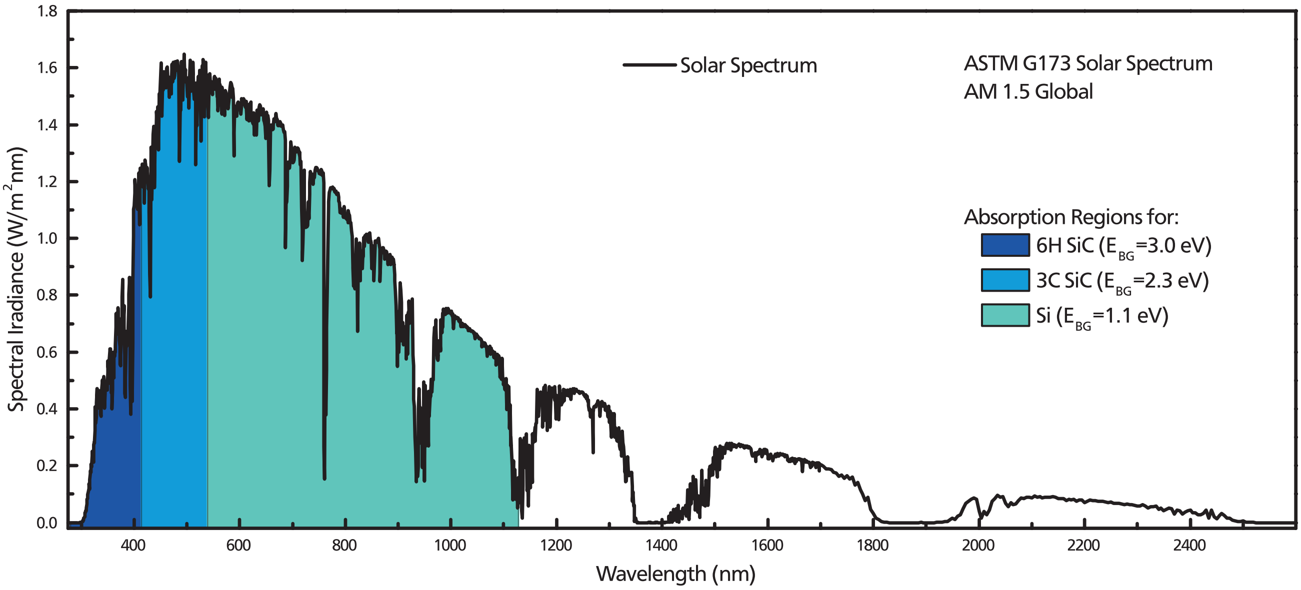

Figure 1.3.: *The ASTM G173 AM 1.5 Global spectrum gives the incident power from solar irradiation on earth's surface, with an integrated total power of* $1000\,\mathrm{W/m^2}$ *[20]. Because semiconductors only can absorb light of energy equal to or greater than their band gap, the three discussed materials (6H and 3C SiC, Si) can harvest different portions of the solar spectrum. The relation between band gap* E_{BG} *and wavelength* λ *is* $\lambda(\mathrm{nm}) = \frac{1240\,\mathrm{nm\,eV}}{E_{BG}(\mathrm{eV})}$.

bonds to the surrounding silicon atoms and vice versa. This results in silicon-carbon bilayers, which can be arranged in various stacking sequences. As a result, SiC is available in over a hundred polytypes, with 3C (cubic), 4H and 6H (hexagonal) or 15R (rombohedral) being the most common [21].

All polytypes share some impressive material properties, such as a high thermal conductivity (4.9 to 7.0 W/cm K), electrical breakdown fields (3×10^6 to 2.4×10^7 V/cm), and a high saturation electron drift velocity (2.0×10^7 to 2.5×10^7 cm/s) [22, 23]. The properties mentioned above, make SiC well-suited for high power electronics (breakdown voltage is one order of magnitude above silicon) or hazardous environments. But it is their high durability under mechanical and chemical strain, in combination with their large band gaps, that make them interesting for water splitting applications. E_{BG} differs with the polytype, it ranges from 3.3 eV for 4H to 2.3 eV for 3C. The band gap is indirect for all polytypes [24].

A first examination of SiC for direct water splitting applications was performed by Gleria and Memming (two pioneers of electrochemistry) in 1975 [25]. This was followed by Morisaki et al. in 1984, Lauermann et al. in 1997, Van de Lagemaat in 1998 and others [26–28]. All of them conducted their experiments on the 6H SiC polytype. Because of its large band gap of 3 eV, 6H SiC can supply the necessary photovoltage for direct photoelectrochemical water splitting. At the same time, its absorption range is limited to a very small fraction of the solar spectrum, see figure 1.3.

The cubic polytype, 3C SiC, with its band gap of 2.3 eV would allow higher current densities. It was first investigated by Lauermann et al. in 1997 [27]. As their 3C SiC samples were n-type, with doping concentrations of $10 \times 10^{17}\,\mathrm{cm^{-3}}$ and above, they were investigated in regard to the (anodic) oxygen evolution reaction (OER).

In recent years, research activity in hydrogen production via direct photoelectrochemical water splitting has risen yet again. This extends to the performance of 3C SiC. Yasuda et al. reported on n-type 3C SiC in 2012 [29]. While Ma et al. (2012) and Kato et al. (2014) investigated p-type material for the (cathodic) hydrogen evolution reaction (HER) [30, 31]. Achieved efficiencies were never very high, and most publications were mainly aimed at presenting the obtained current densities. Thus, this work is focused on further investigating the 3C SiC performance, for direct photoelectrochemical water splitting, by identifying the limiting factors responsible for the low efficiencies, and figuring out if and how those can be overcome.

One further remark: the low amount of research on 3C SiC for water splitting is, at least partially, a result of the technical difficulties in the synthesis. While the physical vapour method (PVT) works well for the growth of hexagonal SiC crystals (which have been commercially available for quite some time), the operation temperatures are often exceeding 2000 °C, which prevents a controllable stabilization of the 3C SiC polytype [32, 33]. While thin hetero-epitaxial 3C SiC layers of good quality can be grown on large silicon substrates, thicker layers remain problematic [34]. In conclusion, so far nobody has been able to really grow larger 3C SiC bulk single crystals of good quality [33].

2

Theoretical Background Information

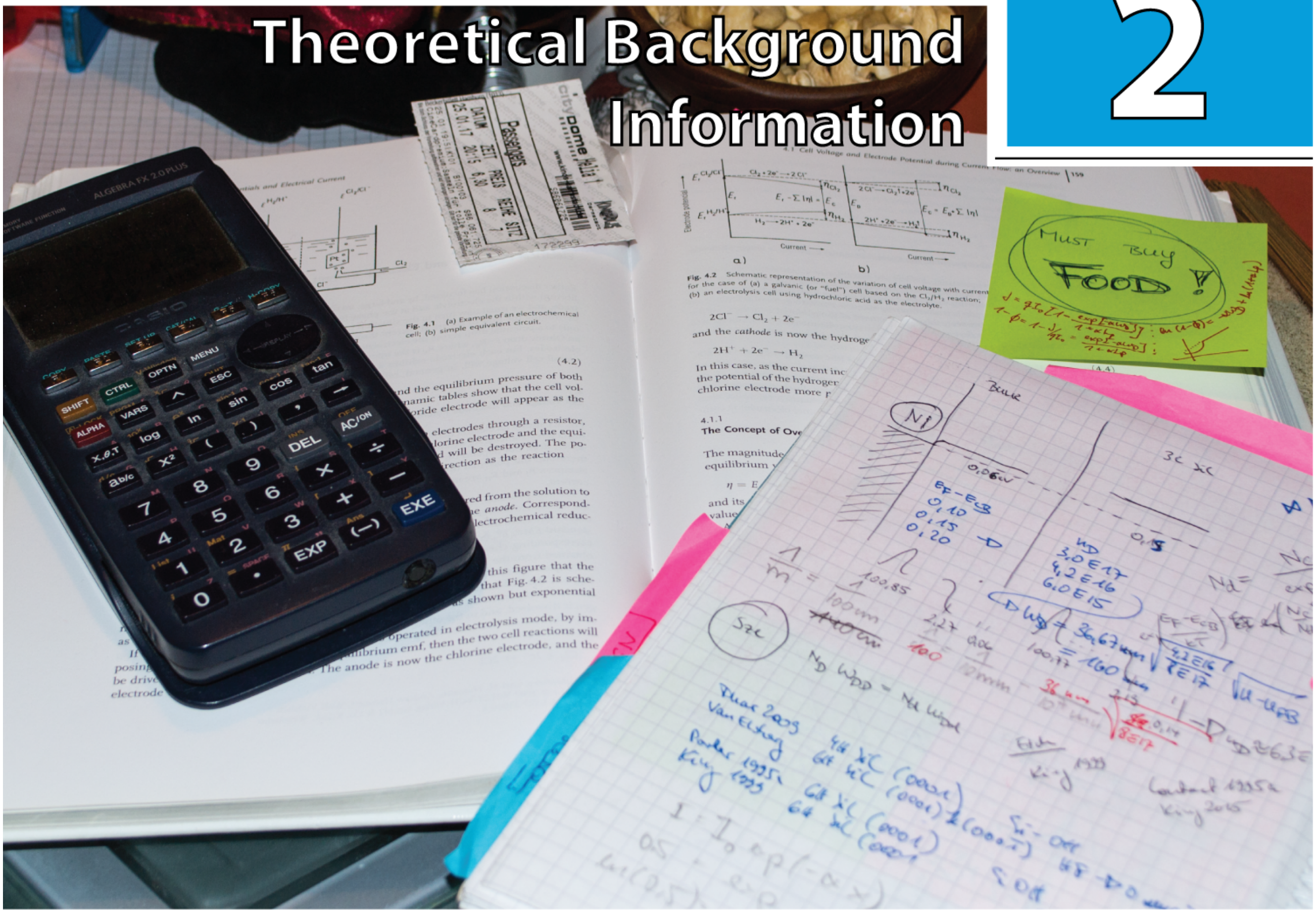

Most chapters of this work were written with the aim of supplying all information necessary to follow the discussion of the observed effects and their interpretation. Some basic knowledge will be required, though. Within this chapter, the most important basic concepts will be presented, summarized and briefly explained. For the reader interested in a more complete, in-depth explanation some literature recommendations are included, as such explanations would exceed the scope of this work.

2.1 Solid State Physics

This works main focus is on the interactions of the semiconductor cubic silicon carbide (3C SiC) with other solids and liquids in the context of self driven, direct photoelectrochemical water splitting. The interactions are governed by the material properties, which in turn are determined by the bonds formed between the composing atoms, and the resulting restrictions on the valence electrons. One useful model, frequently used in semiconductor physics, is that of 'band diagrams', which display the allowed energy ranges of the outer electrons in relation to the samples cross section.

Metal / Semiconductor / Isolator

In isolated atoms, the electrons are restricted to a set of discrete energy levels. For crystals, the well ordered atomic structure, and the resulting periodic potential, give rise to allowed energy ranges instead. Those are displayed as, so called, dispersion curves, a graphical representation of the allowed energy states as function of the momentum in the reciprocal space (given by the wave vector k), see left hand curves in figure 2.1 (A) and (B). As this kind of atomic scale is less important for most applications, the dispersion curves are frequently simplified to rectangular bands. Those include the whole allowed energy range, and discard the spa-

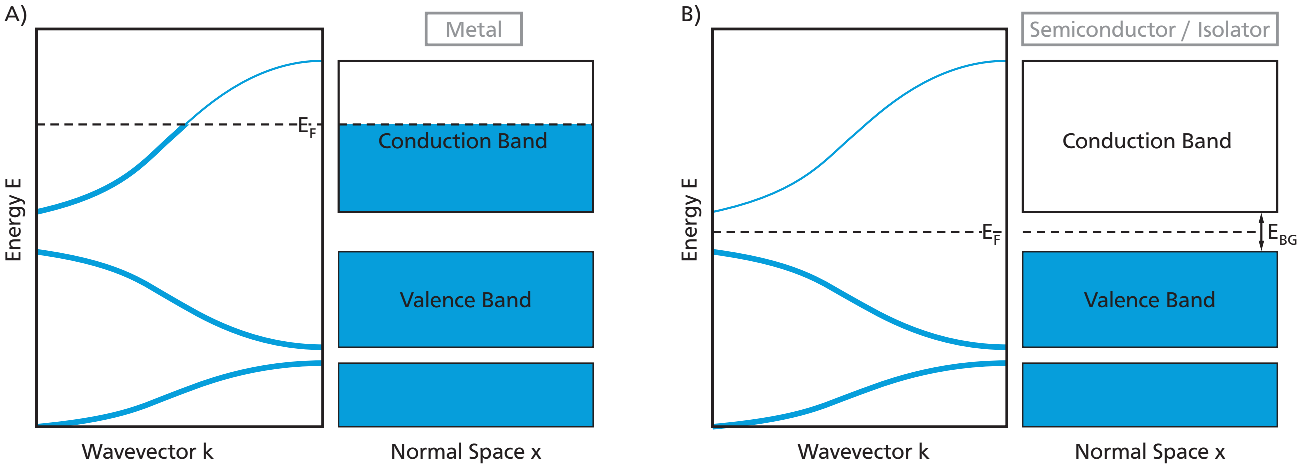

Figure 2.1.: *Exemplary dispersion curves and energy band diagrams for a crystal with one atomic base. The resulting symmetry of the potential causes certain energy ranges to be 'forbidden'. Allowed energy states are filled up to the 'Fermi-level'* E_F. *(A) The Fermi level is located within a band, the material is classified as a metal. (B) Should the Femi level be located between two bands, the material is either a semiconductor (small band gap* E_{BG}*) or an isolator (large* E_{BG}*) [35,36].*

tial information, see right hand diagrams in figure 2.1 (A) and (B).

Depending on the constituent atoms, only a certain amount of the allowed energy levels are occupied. The energy, at which the probability of it being occupied by an electron is exactly 0.5 is called the Fermi energy, or Fermi level E_F. E_F is a convenient way of describing, which electronic states are filled, which greatly influences a material's electronic properties. There are two general cases to be considered.

In the first, the uppermost occupied energy band is only partially filled. This band is called the conduction band (CB), while the band below is the valence band (VB). See figure 2.1 (A). Electrons in this band are de-localised. They will be able to move relatively freely, as those electrons near E_F will only need a small amount of energy to move to a free energy state above E_F. Application of an electric potential will result in a current flow, mainly from the electrons close to E_F, making these materials good conductors. A material with E_F within a band is classified as a 'metal'.

In the second case, the uppermost occupied energy band is completely filled, see figure 2.1 (B). This will cause E_F to be located between CB and VB. As there are no accessible free energy states, an applied electric potential will not be able to generate a current, making it an 'insulator'. However, if some electrons from the VB are enabled to ascend into the CB (for example via thermal excitation), those unbound electrons, and the resulting free energy states in the VB (holes), can contribute to a (weak) current flow. Thermal excitation of electrons from VB to CB is strongly dependent on the energy band gap (E_{BG}) between the bands. Materials with a large band gap ($E_{BG} > 3\,\mathrm{eV}$) are classified as 'insulators', and those with a small band gap ($E_{BG} < 3\,\mathrm{eV}$) as 'semiconductors'. Nevertheless, this distinction is not strict, and non-metals with $E_{BG} \approx 3\,\mathrm{eV}$ are often called 'wide band gap semiconductors'.

Semiconductor Doping

Intrinsic (meaning totally pure) semiconductors are of limited use. It is the possibility of changing their electronic properties via the deliberate addition of different atoms, called doping, which enables most of their modern applications, like diodes, solar cells and so on. There are two kinds of doping to be considered:

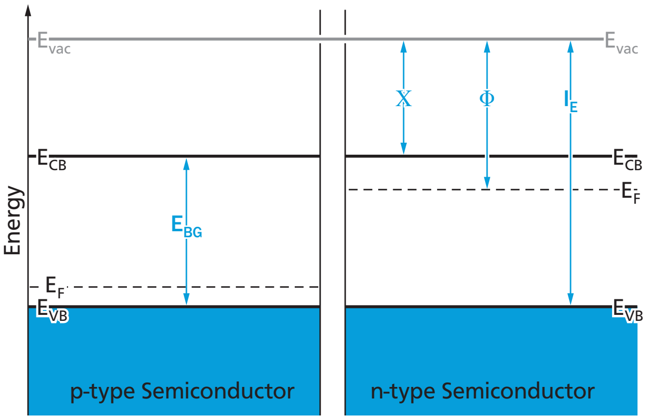

Figure 2.2.: *Graphical display of a p- and an n-type semiconductor, not in contact, as described by the band model. The doping concentration for the p-type is higher, therefore* E_F *is located closer to the valence band edge. Energy values are given in regard to the vacuum energy* E_{vac}*.* X *is the electron affinity,* Φ *the material's work function,* I_E *its ionisation energy, and* E_{BG} *the band gap [35–37].*

N-type, where the foreign atoms have more valence electrons (donator) than the semiconductor atoms. Those additional atoms are localised around the dopant at first, but if their energy level is close enough to the CB, they can be excited into the CB and move freely. The increased number of electrons in the CB also causes E_F to rise, the donator doping concentration is abbreviated with n_D.

P-type, vice versa to n-type, the foreign atom has less (acceptor) electrons, than the semiconductor atom. If the free energy states from the acceptor are close enough to the VB, electrons from the VB can be excited to occupy the free acceptor states, thus creating free states in the VB (holes), which can participate in charge transfer. The decreased number of electrons in the VB causes E_F to descent, the acceptor doping concentration is abbreviated with n_A.

Both types of doped semiconductors are displayed in figure 2.2, along with the common terminology for energies in the vacuum energy scale. It should be noted that they are not in contact with each other. The electron affinity X describes the energy difference between the lower CB edge and the vacuum energy level E_{vac}. A material's work function Φ, is the minimal energy needed for an electron to actually leave the material ($E_{vac} - E_F$). It can be measured via XPS/UPS, but the surface properties can influence the obtained values (via surface dipoles, adsorbates, and surface morphology), making the determination of a hypothetical bulk value Φ rather difficult. Last, the ionisation energy I_E is the energy needed for the uppermost electrons (weakest binding energy) to leave the sample.

The E_F position within the band gap can be estimated from the doping concentration. Assuming the semiconductor is non-degenerate, all dopant atoms are ionized, and the doping concentration is significantly smaller than the density of states at the band edges, the Fermi level position can be determined from

$$E_F - E_{VB} = k\mathrm{T} \cdot \ln\left(\frac{N_{VB}}{n_A}\right) \tag{2.1}$$

for p-type, and

$$E_{CB} - E_F = k\mathrm{T} \cdot \ln\left(\frac{N_{CB}}{n_D}\right) \tag{2.2}$$

for n-type [37]. Here, k is the Boltzmann constant, and T the temperature in Kelvin, while N_{VB} and N_{CB} are the effective densities of states in the valence, respectively, the conduction band.

For SiC they are defined as

$$N_{VB} = 2\left(\frac{2\pi m_{dh} k\mathrm{T}}{h^2}\right)^{3/2} \tag{2.3}$$

and

$$N_{CB} = 2\left(\frac{2\pi m_{de} k\mathrm{T}}{h^2}\right)^{3/2} M_C \tag{2.4}$$

respectively [37].

As all 3C-SiC samples, within the context of this work, are n-type, only N_{CB} will be needed. Using the longitudinal and transverse effective electron

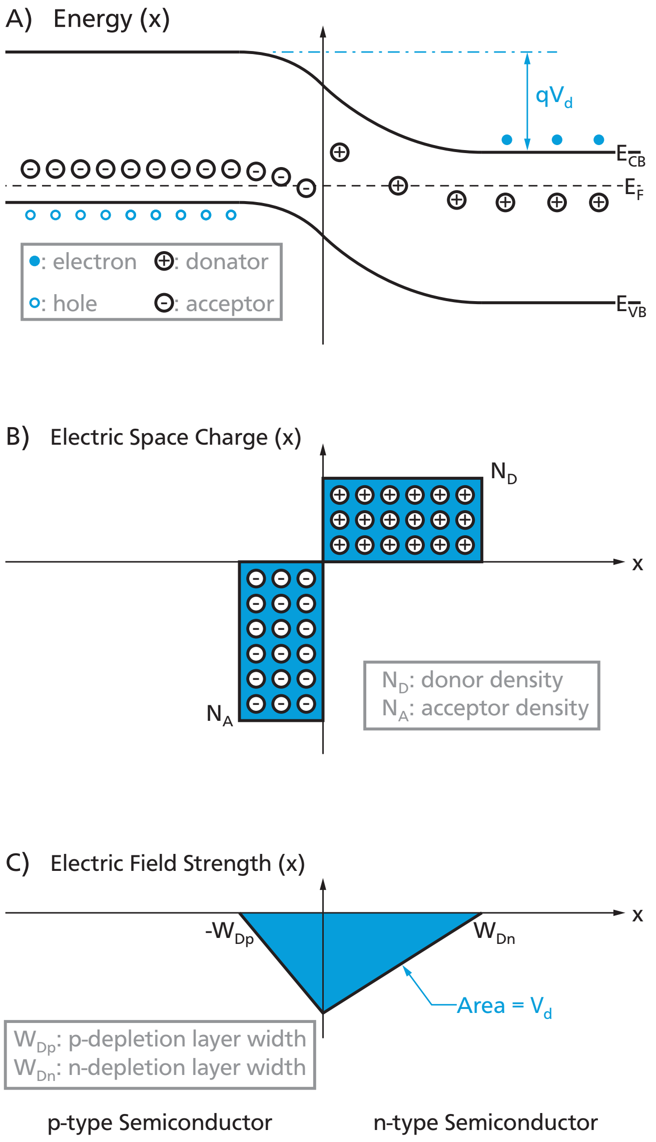

Figure 2.3.: *Graphical representation of an ideal pn-junction. Both p- and n-type are the same elementary semiconductor, forming a homo-junction. (A) Displays the energy levels in the band diagram depiction. The Fermi level alignment results in a, so called, band bending. (B) Shows the distribution of charge from the ionised dopants. Because of its higher doping concentration, the space charge region is smaller in the p-type region. (C) In case of the ideal space charge distribution displayed above, the electric field strength will increase linearly through the depletion layer [35, 36].*

masses $m_l^* = 0.68m_0$ and $m_t^* = 0.25m_0$ [38, 39], the electron effective mass $m_{de} = (m_l^* m_t^{*2})^{1/3} = 0.35m_0$ [37], the electron mass m_0, the absolute temperature T (in Kelvin), the Boltzmann constant k, Planck's constant h and the number of equivalent minima in the conduction band $M_C = 3$, results in

$$N_{CB} = 1.496 \times 10^{19}\,\mathrm{cm}^{-3}$$

for the effective density of states in the CB.

Typical doping concentrations range between 10^{13} and $10^{18}\,\mathrm{cm}^{-3}$, where the first would be lowly doped, and the later highly doped. Semiconductors with a doping concentration near to, or exceeding the effective density of states (N_{CB} and N_{VB}), are called 'degenerate'. They require some adjustments to the formula, as the Boltzmann statistics approximation has to be replaced by a Fermi-Dirac integral.

Semiconductor/Semiconductor Interface

Should a p- and an n-type semiconductor be brought into contact with each other, their Fermi levels will align, a result of the different carrier concentrations. This interface is called a 'pn-junction' . The varying hole (p-type) and electron (n-type) concentrations produce a diffusion potential for the free charge carriers. They diffuse across the interface and recombine with their counterparts, see figure 2.3 (A) for the equilibrium situation. The ionised dopant atoms remain, as they are immobile, and generate two regions of opposing charge (B). Those, in turn, produce an electric field (C), which opposes the charge carrier diffusion across the interface. At some point an equilibrium is reached, the diffusion current and the field current will precisely cancel each other. The resulting regions without mobile charge carriers are called depletion layers. An integration of the electric field across the depletion layers yields the diffusion potential V_d of the junction.

Their spatial dimensions, the depletion layer widths

$$W_{Dp} = \sqrt{\frac{2\varepsilon_0\varepsilon_S V_d}{q}\frac{n_D}{n_A(n_A+n_D)}} \tag{2.5}$$

$$W_{Dn} = \sqrt{\frac{2\varepsilon_0\varepsilon_S V_d}{q}\frac{n_A}{n_D(n_A+n_D)}} \tag{2.6}$$

depend on the respective doping concentrations and the (built in) diffusion potential V_d [37]. With the relative permittivity ε_S of 9.72 for 3C SiC [40], and ε_0, the vacuum permittivity.

Applying an external potential U to a pn-junction will change the current flow in dependence of the potentials direction. Most of the potential drop will occur across the depletion layer, which has a high resistance, due to the limited number of mobile carriers. Here, the applied potential disturbs the afore mentioned equilibrium between electric field and diffusion potential. The applied potential's sign is defined contrary to V_d, thus replacing the pure diffusion potential with $V_d - U$. As the barrier height varies with U, so does the diffusion current, thus diffusion and field current will no longer cancel out.

The current voltage behaviour of an ideal pn-junction under an external potential is described by

$$J(U) = J_p + J_n = J_0\left[\exp\left(\frac{qU}{kT}\right) - 1\right] \tag{2.7}$$

the Shockley equation, and is displayed in figure 2.4 [35, 37]. Most semiconductor devices, like solar cells, transistors, or LEDs, are based on pn-junctions.

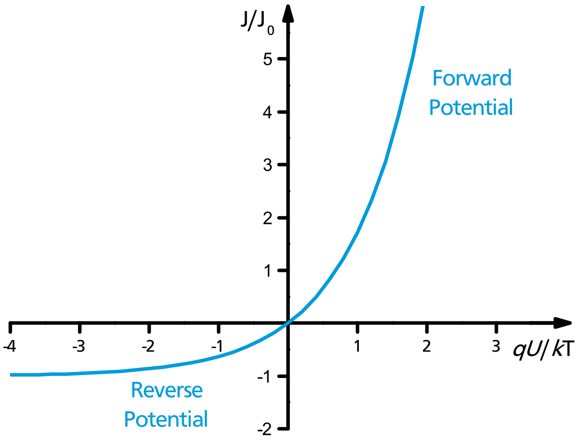

Figure 2.4.: *Ideal current-voltage behaviour of a pn-junction under reverse and forward bias potential. The slope of the forward potential current is mainly determined by the semiconductor's E_{BG} [37].*

Semiconductor/Metal Interface

The contact between a semiconductor and a metal works similar to that between two semiconductors. But as the metal has a much higher density of states, the diffusion potential drop occurs almost completely in the semiconductor. Therefore, the depletion layer is located completely in the semiconductor as well, and its width

$$W_D = \sqrt{\frac{2\varepsilon_0\varepsilon_S(V_d - U)}{qn_D}} \tag{2.8}$$

changes accordingly. Ideally, the junction properties would be mostly dependant on the difference in work function between the two materials, see figure 2.5 (A) to (C).

Should Φ_{sc} exceed the metal work function Φ_m, electrons from the metal will flow into the semiconductor, until the Fermi levels align, see (B). The resulting field will not hinder electron transfer across the interface and the contact shows ohmic behaviour. For an ohmic contact, the current increases linearly with the applied potential. The potential's direction does not influence the current.

In the contrary case ($\Phi_{sc} < \Phi_m$) the resulting field is opposed to the carrier transfer across the interface, a Schottky contact is formed, see (C). The total potential difference an electron has to over-

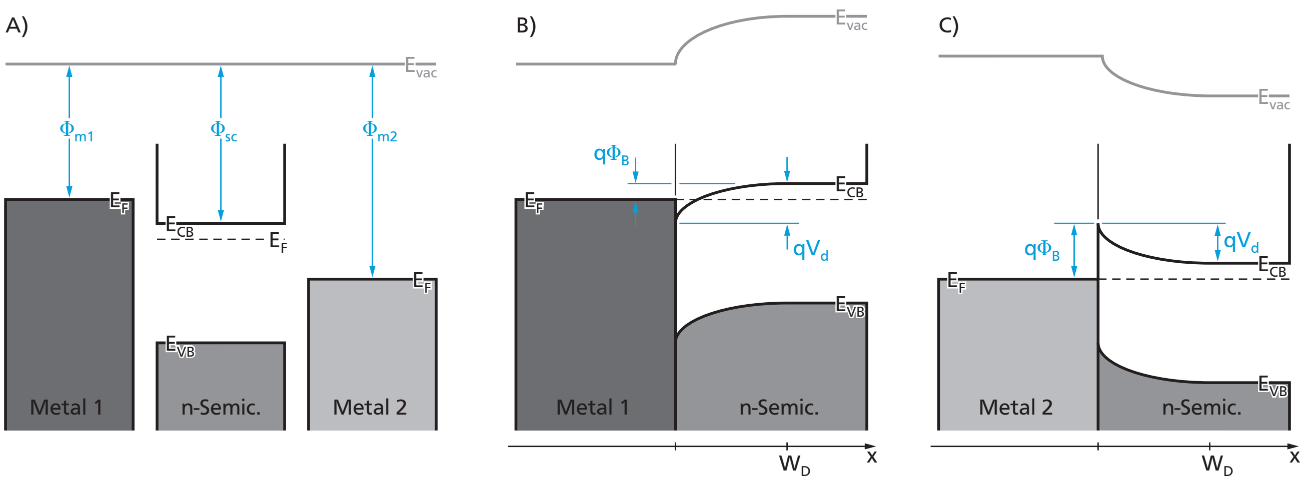

Figure 2.5.: *Band diagrams of metal/n-type semiconductor junctions. (A) displays the three materials, a low work function metal 1, the n-type semiconductor, and the high work function metal 2, separately. (B) a contact between the metal 1 and the n-semiconductor results in downward band bending in the semiconductor. The resulting barrier height* $q\Phi_B$ *is low, the junctions shows ohmic behaviour. (C) the contact between n-semiconductor and metal 2 produces upward band bending in the semiconductor, creating a barrier electrons have to overcome in order to cross the junction. This is a rectifying or Schottky contact [35,37].*

come in order to move from the metal into the SC, is called the Schottky barrier Φ_B. The current voltage behaviour is similar to that of a pn-junction, and dependent on the potential's direction.

Φ_B should be defined by the work functions Φ_{sc} and Φ_m and the Fermi level position within the band gap. Surprisingly, experimental data contradicts. While measured barrier heights depend on the semiconductor, the selected metal frequently has little to no influence on the measured Φ_B. The reason for this is the formation of, so called, surface states at the semiconductor/metal interface. Their position is fixed with regard to the band edges in the semiconductor. Once the Fermi level reaches the surface states energy levels, they are ionised, and the Fermi level stops moving. The remaining work function alignment occurs in form of an potential drop at the interface, thus the Fermi level is pinned [35,37].

Electron Excitation via Photon Absorption

Besides thermal excitation, the absorption of light can also raise electrons to a higher state of energy. This happens via the quantum photoelectric effect, where the absorption of a photon supplies an electron with enough energy to ascend to a free state of higher energy. If the resulting electron hole pair remain bound to each other it is called an exciton.

As displayed in figure 2.6, the photon can only be absorbed if $E_\lambda \geq E_{BG}$, for an excitation from the VB to the CB. Here,

$$E_\lambda(\lambda) = \frac{hc}{\lambda} = \frac{1240\text{ eV}}{\lambda\text{ (nm)}} \tag{2.9}$$

is the photon energy, depending on its wavelength λ. Provided E_λ is high enough, the electron can be excited to positions within the CB, where it will promptly drop to the lowest possible energy state, normally the lower CB edge, emitting the excess energy as heat. Thus only E_{BG} can be used, no matter the photon's original energy. Even higher E_λ allow the excitation into energy bands above the CB or enable the electron to leave the semiconductor altogether, as in the case in X-ray photoelectron spectroscopy, see chapter 3.1 [37].

Without an electric field, the newly created electron and hole will move at random. If the possibility arises, electrons from the CB will recombine

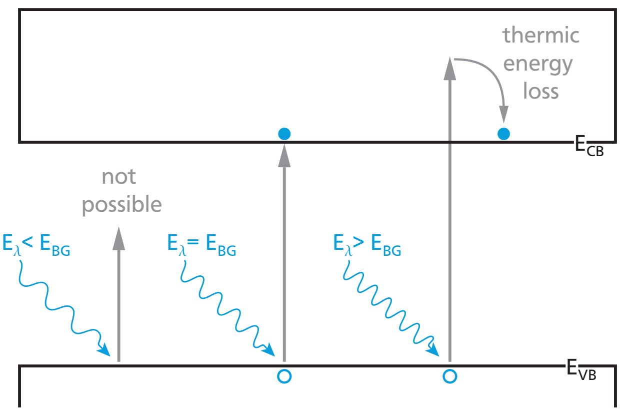

Figure 2.6.: *Graphical presentation of the photoelectric effect. Only photons with an energy E_λ equal or greater E_{BG} can excite an electron from the VB to the CB [37].*

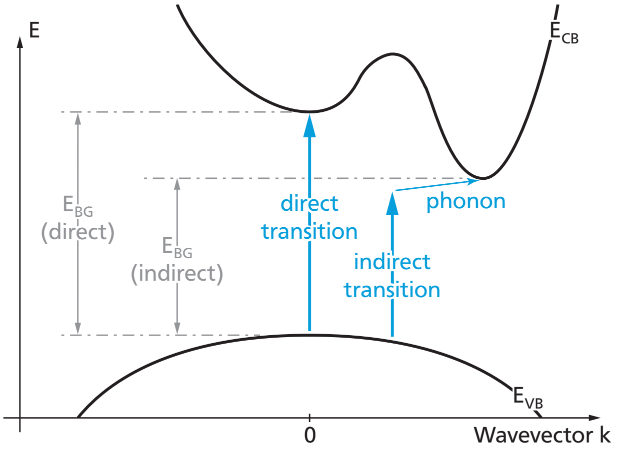

Figure 2.7.: *Direct and indirect electron transitions as result of the asymmetric dispersion curve shape [37]. Participation of a phonon allows changes in k (momentum), between the initial and final state.*

with holes in the VB. Thus, the respective lifetime τ of such carriers depends strongly on the available charge carriers of opposite polarity. For an n-type semiconductor the number of electrons in the CB is high, they are named 'majority charge carriers'. Any photo-excited holes will be less numerous, and thus named 'minority charge carriers'. They will recombine in a very short time frame, as electrons from the CB want to occupy any available lower energy state. Obviously, this works the other way around for p-semiconductors.

However, E_{BG} is not the only factor determining whether photons of energy E_λ, can be absorbed or not, see figure 2.7. Direct transitions between VB and CB, are those without a change in momentum (k), thus initial and final state have to be located at the same k value. Indirect transitions, allow a change in k, but the momentum has to be conserved. As photons only have a very small momentum, the participation of a phonon (lattice vibration) is required.

While this allows lower energy transitions, across the indirect E_{BG} instead of the direct one, it also lowers the transition probability. As the probability of a simultaneous absorption of photon and phonon is small, a photon is significantly less likely to be absorbed in an indirect semiconductor than in a comparable direct one. This result in rather low absorption coefficients α for indirect semiconductors.

Silicon Carbide Dispersion Curves

There were numerous publications, on the dispersion curves of 3C SiC, over the last decades [41–46]. All of them report 3C SiC (and the other SiC polytypes) as indirect semiconductor.

2.2 Electrochemistry

Electrochemistry refers to a linking between chemical reaction and electric current. Whether the electrical potential is the cause (f.e. electrolysis) or the result (f.e. voltaic cell) of the chemical reaction is irrelevant. The transfer of a single electron,

$$\mathrm{Ox} + ne^- \rightleftharpoons \mathrm{Red} \qquad (2.10)$$

without the creation or breaking of any chemical bonds, would be the simplest case. As electrochemical reactions are reversible, they can be separated in two half reactions, the cathodic forward reduction reaction

$$\text{reduction: } \mathrm{Ox} + ne^- \longrightarrow \mathrm{Red} \qquad (2.11)$$

and the anodic reverse process

$$\text{oxidation: } \mathrm{Ox} + ne^- \longleftarrow \mathrm{Red} \qquad (2.12)$$

for the redox couple (Red/Ox). Most of the time, only one of the half reactions is investigated. This is achieved via a three electrode setup, see chapter 3.5 for more information on half cells.

Redox Potentials

In an electrochemical cell, the oxidation takes place at the anode, and the reduction at the cathode. A redox couple (Red/Ox), has a characteristic potential for its thermodynamic state of equilibrium, the redox potential E_{redox}, at which forward and backward reaction take place at the same rate. As these rates are, normally, not zero, the resulting equilibrium is dynamic. Common redox couples and their equilibrium potentials are supplied in tabulated form, the standard electrode potentials [47].

Deviation from standard conditions will cause a corresponding change in the redox potential. A common example would be that of unequal reactant concentrations. The resulting change of the redox potential can be calculated via

$$E_{redox} = E^0_{redox} + \frac{RT}{nF} \ln\left(\frac{a_{ox}}{a_{red}}\right) \quad , \qquad (2.13)$$

the Nernst equation for simple reactions [15]. Where E^0_{redox} is the redox potential under standard conditions, n the number of electrons transferred in the reaction, F the Faraday Constant $F = q \cdot N_A$, T the temperature in Kelvin, and R the gas constant $R = k \cdot N_A$. The activities, a_{red} and a_{ox}, are those of the reduced and oxidized species, respectively. In most cases, activities are equal to concentration.

In real systems, more than one redox couple can be present. In case of the water splitting reaction, there are two redox couples to be considered.

Standard Electrode Potentials

Literature standard electrode potentials are supplied relative to the **standard hydrogen electrode (SHE)**. Traditionally, they are written in form of the **reduction reaction**. The provided values are valid for the following conditions:

- **temperature** T=298.15 K (25 °C)
- **pressure** p=1.013 25 bar (1 atm) for each gaseous species
- **effective concentration** of 1 mol/L for each aqueous species

HER, HOR, OER, And ORR

The **four possible redox half reactions** for water splitting are typically abbreviated:

- **HER** - hydrogen evolution reaction ($\longrightarrow$ in eq. 2.14)
- **HOR** - hydrogen oxidation reaction ($\longleftarrow$ in eq. 2.14)
- **ORR** - oxygen reduction reaction ($\longrightarrow$ in eq. 2.15)
- **OER** - oxygen evolution reaction ($\longleftarrow$ in eq. 2.15)

For acidic aqueous solutions they are (H_2/H^+) and (H_2O/O_2). The resulting redox reactions are

$$\text{Red:}\quad 2\,H^+(aq) + 2\,e^- \rightleftharpoons H_2(g) \tag{2.14}$$

$$\text{Ox:}\quad O_2(g) + 4\,H^+(aq) + 4\,e^- \rightleftharpoons 2\,H_2O(l)\quad . \tag{2.15}$$

In alkaline aqueous solutions they are

$$\text{Red:}\quad 2\,H_2O(l) + 2\,e^- \rightleftharpoons H_2(g) + 2\,OH^-(aq) \tag{2.16}$$

$$\text{Ox:}\quad O_2(g) + 2\,H_2O(l) + 4\,e^- \rightleftharpoons 4\,OH^-(aq) \tag{2.17}$$

respectively. The redox potential of (H_2/H^+), also known as the standard hydrogen electrode (SHE), is used as reference potential. Accordingly, the redox potentials for equations 2.14 to 2.17 are

$$\begin{aligned} E^0_{redox}(H^+/H_2) &\equiv 0.0\,V \\ E^0_{redox}(H_2O/O_2) &= 1.23\,V \\ E^0_{redox}(H_2O/H_2) &= -0.83\,V \\ E^0_{redox}(OH^-/O_2) &= 0.40\,V\quad . \end{aligned}$$

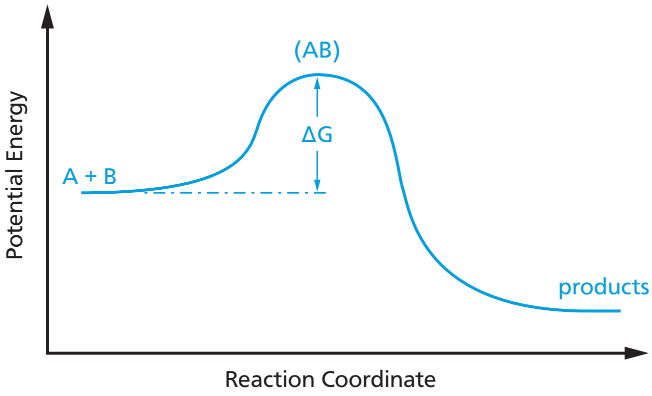

Figure 2.8.: *Potential energy diagram of the exothermic reaction $A + B \longrightarrow$ products. The energy barrier between the reactants $A + B$ and the products is ΔG, the activation energy [48].*

The potential difference of the two occurring half reactions

$$\begin{aligned} \Delta E_{redox} &= E^0_{redox}(H_2O/O_2) - E^0_{redox}(H_2/H^+) \\ &= 1.23\,V \end{aligned} \tag{2.18}$$

provides the minimum bias potential necessary for the water splitting reaction to take place (under standard conditions).

Electron Transfer Theory

Chemical reactions are often considered in terms of activated complexes. For a simple reaction like

$$A + B \xrightarrow{(AB)} \text{products}$$

this means that the energy difference (or activation energy) ΔG between $A + B$ and the activated complex (AB), has to be overcome, see figure 2.8 [15]. The activation energy is directly related to the rate constant

$$k_r = k_r^0 \exp\left(\frac{-\Delta G}{RT}\right) \tag{2.19}$$

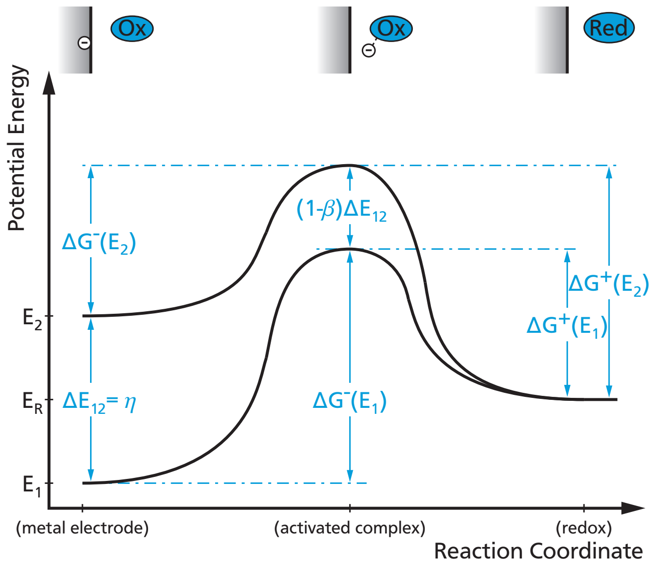

Figure 2.9.: *Potential energy diagram of the electrochemical reaction* $Ox + e^- \longrightarrow Red$*. The electron has to be transferred from the inert metal electrode, to an activated intermediate state (complex), before the redox reaction can be completed. An applied external potential* ΔE_{12} *at the electrode can influence the electrons starting potential energy. The electrode potential* E_1 *is more negative than* E_2 *[15].*

via the Arrhenius equation [48]. The total reaction rate

$$\nu = c_A c_B k_r = k_r^0 c_A c_B \exp\left(\frac{-\Delta G}{RT}\right) \tag{2.20}$$

would then depend on k_r and the reactants concentrations c_A and c_B. Obviously, a small ΔG will result in a large ν, and vice versa.

A similar case can be considered for an electrochemical reaction, like the transfer of an electron from an inert metal electrode to a suitable redox couple in solution, see eq. 2.10. Assuming, neither of the redox species becomes adsorbed on the electrode surface, their potential energy will not be affected by an applied external potential. The opposite is true for electrons in the electrode, their potential energy can be shifted between energy level E_1 and E_2 by applying the potential $\Delta E_{12} = E_1 - E_2$. This is demonstrated in figure 2.9.

Similar to the previous case, the electron has to bring up the activation energy, and form the activated complex, before the reaction can proceed. While the external potential can enhance the reaction, by raising the reactants potential energy, the activation energy is only lowered by the fraction $(1-\beta)\Delta E_{12}$. The factor β is called the 'asymmetry parameter', and governs how the applied potential influences the dynamic equilibrium between the redox reactions. It can adopt values between 0 and 1. Keeping in mind that $\Delta E_{12} < 0$, and moving from a single electron to larger quantities, a large $\beta > 0.5$ will enhance the cathodic (red) reaction

$$\Delta G^-(E_2) = \Delta G^-(E_1) + \beta nF \cdot \Delta E_{12} \tag{2.21}$$

more than

$$\Delta G^+(E_2) = \Delta G^+(E_1) - (1-\beta)nF \cdot \Delta E_{12} \tag{2.22}$$

the anodic (ox) reaction [15].

Above considerations can be used to determine the reaction rate from equation 2.20. Which in turn can be identified with the current density, providing the cathodic

$$j^-(E) = -nFc_{Ox}k^- \cdot \exp\left(\frac{\Delta G^-(E)}{RT}\right) \tag{2.23}$$

and anodic

$$j^+(E) = -nFc_{Red}k^+ \cdot \exp\left(\frac{\Delta G^+(E)}{RT}\right) \tag{2.24}$$

current densities.

The exponential terms without ΔE_{12} can be treated as constants, and the potential E is then expressed as

$$E = E_r + \eta \tag{2.25}$$

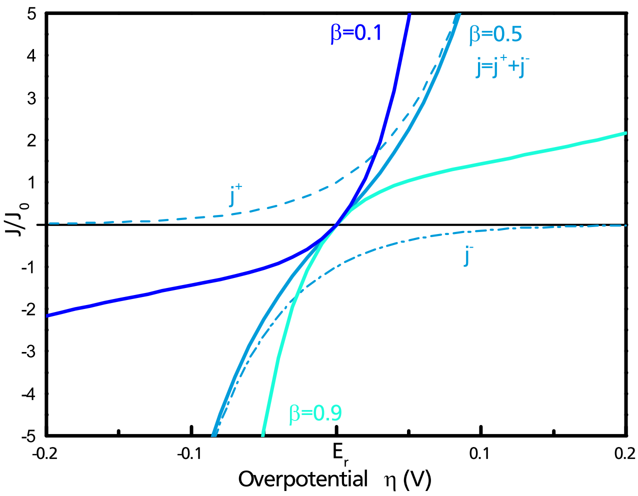

Figure 2.10.: *Current potential behaviour for a redox couple according to the Butler-Volmer-equation 2.29. The half reactions (j^+ and j^-) are displayed as dashed lines, the total net current j as solid blue line [15, 49].*

with the overpotential η, and

$$E_r = \frac{RT}{nF}\left[\ln\left(\frac{k^+}{k^-}\right) + \ln\left(\frac{c_{Ox}}{c_{Red}}\right)\right] \tag{2.26}$$

the rest potential. Equation 2.26 is obviously identical to the Nernst equation (eq. 2.13) for $E_0 = \frac{RT}{nF}\ln\left(\frac{k^+}{k^-}\right)$.
With this, equations 2.23 and 2.24 change to

$$j^-(\eta) = -j_0 \cdot \exp\left(-\beta\frac{nF\eta}{RT}\right) \tag{2.27}$$

$$j^+(\eta) = j_0 \cdot \exp\left((1-\beta)\frac{nF\eta}{RT}\right) \quad . \tag{2.28}$$

The total net current $j(\eta)$ is the sum of cathodic and anodic current

$$\begin{aligned} j &= j^+ + j^- \\ &= j_0\left[\exp\left((1-\beta)\frac{nF\eta}{RT}\right) - \exp\left(-\beta\frac{nF\eta}{RT}\right)\right] \quad , \end{aligned} \tag{2.29}$$

the famous Butler-Volmer equation [15].
The resulting current voltage behaviour of the redox reaction is displayed in figure 2.10. First, for the symmetric case ($\beta = 0.5$), where the half reaction currents are displayed as dashed, and the net current as solid line. Second, for two asymmetric cases ($\beta = 0.1$ and 0.9). Apparently, for large enough overpotentials $|\eta| \gg RT/nF \approx 26/n$ mV, one of the exponential terms becomes so dominant, that the other one can be neglected. This gives rise to the Tafel equation for the cathodic

$$\ln(|j|) = \ln\left(|j^-|\right) = \ln j_0 - \eta\frac{nF\beta}{RT} \tag{2.30}$$

or the anodic

$$\ln(|j|) = \ln\left(j^+\right) = \ln j_0 + \eta\frac{nF(1-\beta)}{RT} \tag{2.31}$$

reaction path [15, 49]. The Tafel equation is frequently used to experimentally determine the exchange current density j_0 and the Tafel slope (either $(1-\beta)nF/2.3\ RT$ or $\beta nF/2.3\ RT$) of metal electrodes.

Practical Application Of Tafel Slopes

Many reactions have specific Tafel slopes. One example would be the **HER**, where the **limiting step** can be identified via its characteristic **Tafel slope** [50, 51]:

- **Volmer**: $H^+ + e^- \longrightarrow H(ads)$ (120 mV/decade)
- **Heyrovsky**: $H(ads) + H^+ + e^- \longrightarrow H_2$ (40 mV/decade)
- **Tafel**: $H(ads) + H(ads) \longrightarrow H_2$ (30 mV/decade)

While the HER has only two pathways, those are much **more numerous** for the **OER**, **preventing** a similiar approach [52–55]. See also [56] for an enlightening deduction of the Tafel slopes from first principles.

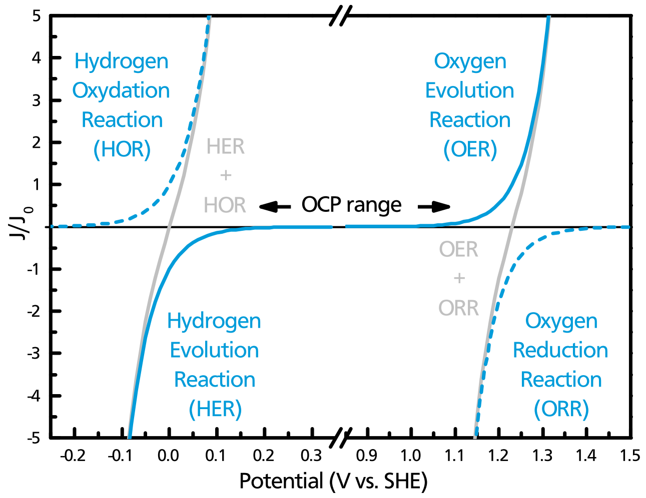

Figure 2.11.: *Depiction of the four redox half reactions for the electrolysis of water. The grey lines display the predicted behaviour after eq. 2.29. Real behaviour deviates though, as some reactions (dashed lines) are limited by an insufficient supply of reactants, it will match the behaviour of the solid blue lines instead [57].*

It has to be kept in mind though, that the Butler-Volmer equation is a rather simple approach, valid for one electron transfer processes only, and only considering the 'electron transfer limitation' of the reaction. Neither tunnelling, nor electronic states from intermediate adsorbates are taken into account. While often accurate for low current densities, other effects come into play for higher current densities or large η. An insufficient supply of reactants to the surface from the solution (or transport of products away from the surface) is called 'diffusion limitation'. Another possibility is the 'reaction limitation', where a chemical reaction, tied to the electron transfer, can not keep up.

Water Splitting CV Explained (Metal Electrode)

The typical current voltage behaviour of water electrolysis, at pH 0, is displayed as solid blue lines in figure 2.11. It consists of a cathodic current for potentials below 0 V vs SHE, identified with the hydrogen evolution, and an anodic current for potentials exceeding 1.23 V vs SHE, identified with the oxygen evolution. Assuming 100 % faradaic efficiency, the currents are directly related to the gas production. Thus, they can be used to calculate the respective amounts produced.

From the Butler-Volmer equation, a different current voltage behaviour would have been expected, due to the participation of HOR and ORR, see grey lines in figure 2.11. While aqueous solutions contain sufficient H^+ and/or OH^- for the HER and OER to proceed without limitation, the amount of dissolved O_2 and H_2 is limited, restricting HOR and ORR. Another consequence is a vague definition of the total rest, or open circuit potential (OCP). While a well defined redox couple, has an equally well defined E_r, see figure 2.10, the OCP for the electrolysis of water will be located somewhere between the E_r values of the hydrogen and oxygen reactions.

The Semiconductor / Electrolyte Interface

In many cases, semiconductor and metal electrodes will behave similar. However, there are some important differences to consider.

Similar to the Fermi level alignment for semiconductor contacts, in sections 2.1 and 2.1, the Fermi level of the electrode and the redox potential of the reactive redox couple in the electrolyte will align. For metal electrodes, the resulting potential drop occurs across the Helmholtz layer, a thin layer (roughly half the diameter of the redox ions in solution) of electrolyte directly at the semiconductor interface [15]. In case of semiconductor electrodes, most of the potential drop will occur in the depletion layer instead. If $n_D \leqslant 10^{19}\,\mathrm{cm}^{-3}$, and for ionic concentrations above 0.01 M the voltage drop in the Helmholtz layer is negligible [58]. Thus, the semiconductor electrolyte contact induces a band bending in the semiconductor, similar to a semiconductor/metal contact.

In case of a n-type semiconductor, the bands will bend upwards at the interface. Thus, under illumi-

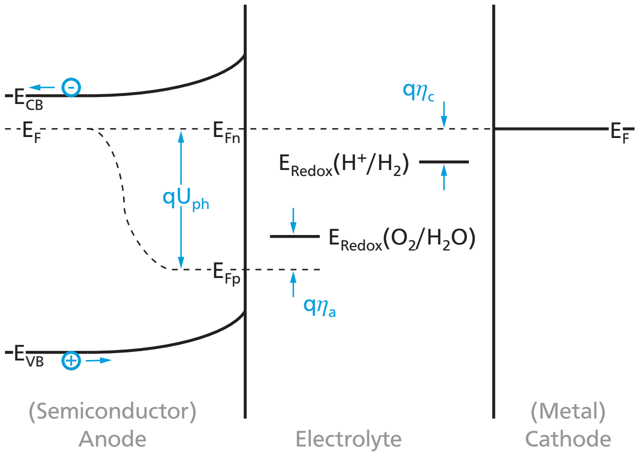

Figure 2.12.: *Band diagram of an n-type semiconductor in contact with an aqueous electrolyte under illumination. The illumination results in a splitting of the Fermi level into quasi Fermi level, E_{Fn} for the electrons and E_{Fp} for the holes. [59]*

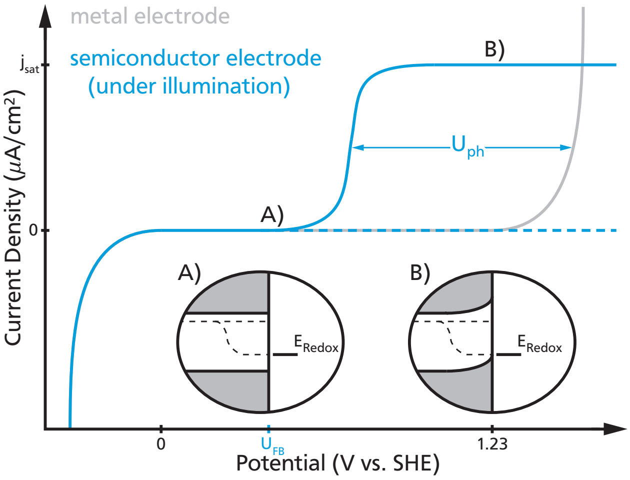

Figure 2.13.: *Current potential curve of an n-type semiconductor under illumination (blue) in comparison to a metal electrode. The generated photovoltage U_{ph} can shift the OER onset to lower potentials, and the current density is limited by the amount of available holes at the interface. In the dark, no holes are available, thus no anodic current (dashed line) [49].*

nation, newly created holes will flow to the semiconductor surface, where they can cross the interface and participate in the OER. Should the hole transfer be inhibited, they will accumulate at the interface. The resulting electric field will oppose further hole flux to the surface, and at some point an equilibrium will be reached. Contrary, the electrons will move into the bulk, which is connected to the (platin) counter electrode, where they will participate in the HER.

The increased number of holes near the surface results in a splitting of the Fermi level (which is no longer in equilibrium), into quasi Fermi levels, one for the holes and one for the electrons respectively, see figure 2.12. In theory, E_{Fp} would then align with $E_{Redox}(O_2/H_2O)$, and E_{Fn} with $E_{Redox}(H_2/H_2O)$. But both reactions consist of more than a single electron transfer step. Therefore the preceding reaction steps will require a certain amount of surplus energy. This is often displayed as overpotentials η_a and η_c for the anodic, respective cathodic reaction.

The Fermi level splitting corresponds to the photovoltage U_{ph} from the semiconductor electrolyte interface. This is another major difference to the metal electrodes, as U_{ph} can substitute part or all of ΔE_{redox}, see figure 2.13, thus shifting the OER onset potential (the potential at which the OER starts), to lower values.

Equation 2.17 can also be written as

$$4\,OH^- + 4\,h^+ \longrightarrow 2\,H_2O + O_2 \quad . \qquad (2.32)$$

In order for the OER to take place at the anode, a sufficient number of holes has to be available. For an n-type semiconductor this is only the case under illumination. Without photon excitation, there will be no hole flux to the surface, therefore no OER, and thus no anodic current, see the dashed line in figure 2.13.

Depending on the illumination intensity, only a limited number of photons will be incoming, and only a part of those will be absorbed close enough to the interface for the holes to reach it and participate in the OER. In contrast to a metal electrode, the anodic current density of a n-type semiconductor will therefore go into saturation at some point. The saturation current density J_{sat} will be corresponding to the hole flux to the surface.

In the above discussion, the semiconductor and the electrolyte were in direct contact, this is called an interface junction. Its behaviour is determined by the interaction of the two constituents. For semiconductor / electrolyte interfaces the charge transfer kinetics are usually described in terms of the Marcus-Gerischer theory [49, 60, 61] assuming electron tunneling processes, see [49] for a comprehensive explanation. For the final situation of this work, a semiconductor / metal / electrolyte junction, charge transfer can be better described by a combination of diode and Butler-Volmer behaviour.

This is in contrast to an embedded junction, an alternative design approach, where the relevant behaviour determining interface is not with the electrolyte, but somewhere within the electrode. Possible examples would be that of an additional catalyst layer, which could also be used to induce a high band bending (and thus a high U_{ph}), or more complex structures like one or more pn/pin junctions for solar cells. Depending on the material systems used, embedded junctions allow a certain amount of custom tailoring in regard to system properties like photovoltage.

3 Experimental Methods

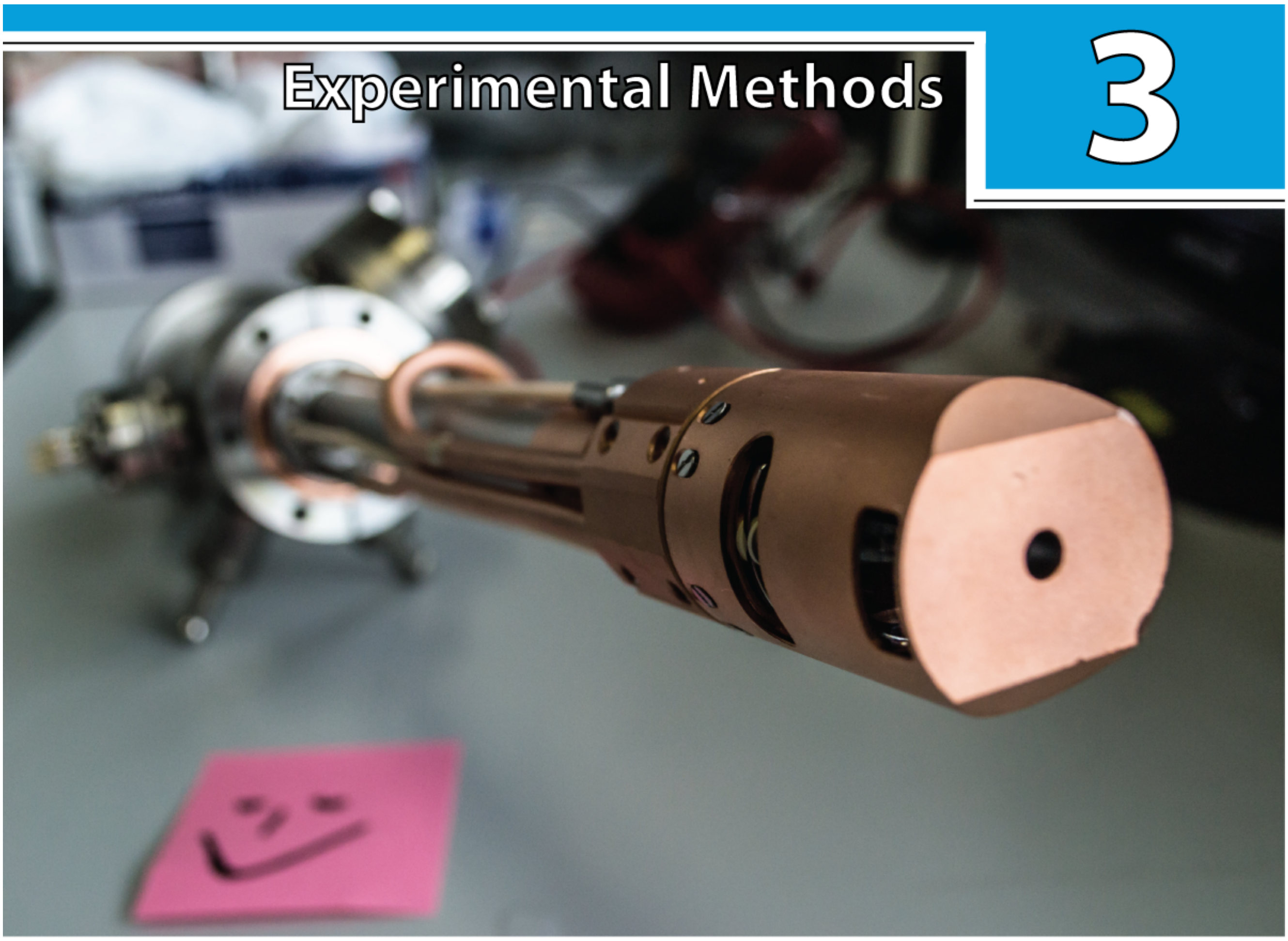

This chapter will supply an overview over experimental methods frequently employed within the context of this work. It is aimed at providing enough information to allow readers without expertise in a specific method to follow the discussion regarding said method. For a more extended and fundamental explanation, a number of suitable literature references are provided.

3.1 Photoelectron Spectroscopy (XPS/UPS)

Photoelectron spectroscopy (PES) is one of the most widely used techniques for surface analysis. It is based on the photoelectric effect, where incident light of sufficient energy causes the emission of free electrons from the sample. Kai Siegbahn and his team in Sweden were the main developers in the early stages of this method, which was rewarded with a physics Nobel prize in 1981 [62]. While PES can supply information on the elemental sample composition, it is most suitable to supply information on the electronic structure, oxidation states and so forth.

Operating Principle

The sample is illuminated with monochromatic light of the energy $E_\lambda = h\nu = hc/\lambda$. Depending on the energy range, PES is often known as: X-ray photoelectron spectroscopy (XPS) for $E_\lambda \approx 10^3$ eV, or ultraviolet photoelectron spectroscopy (UPS) for $E_\lambda \approx 10^1$ eV. Because most spectra were obtained with an X-ray source, XPS will be used in the remainder of this work. Energy transfer during photon absorption is total, due to conservation of energy the electron kinetic energy

$$E_{kin} = E_\lambda - E_{bin} - \Phi \tag{3.1}$$

is directly related to its binding energy E_{bin}, E_λ, and the samples work function Φ. This relation between the samples energy structure and the result-

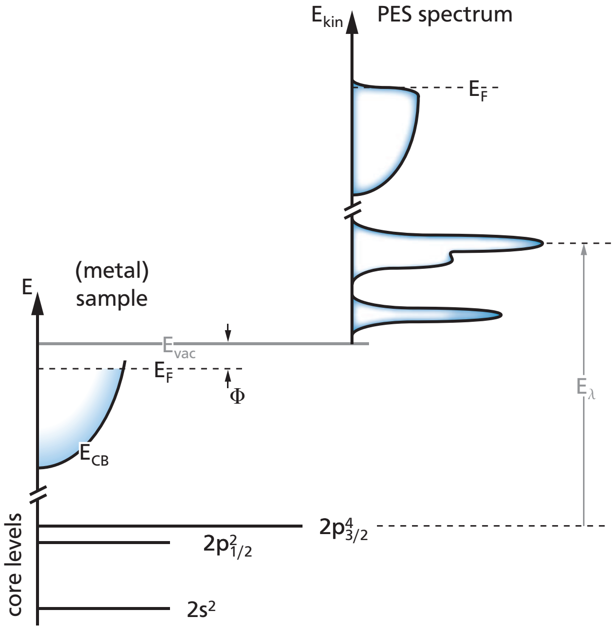

Figure 3.1.: *Diagram of the photo electric effect and the resulting PES spectrum. An electron from an occupied energy level can be excited to an energy state exceeding the vacuum level, thus leaving the sample. Inspired by [63].*

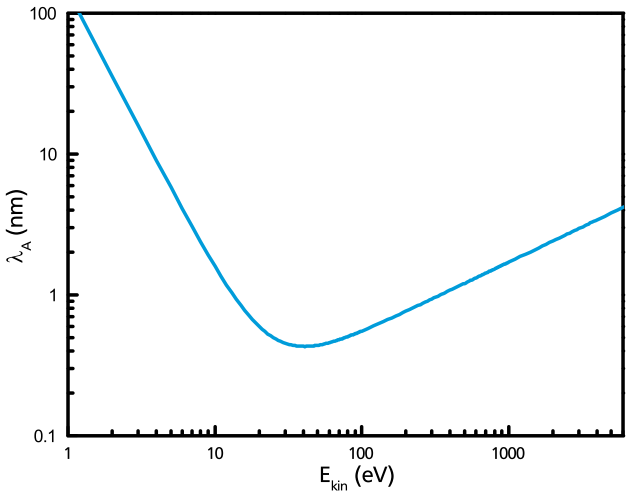

Figure 3.2.: *Inelastic mean free path dependence on the photoelectron kinetic energy. Average behaviour for the elements after equation 3.3 [65].*

ing XPS spectrum, is displayed in figure 3.1. As the sample's Fermi level aligns with that of the spectrometers probe station, it is not necessary to know Φ, instead the spectrometers known work function Φ_S is used. In many cases Φ or Φ_S are therefore not even included in the equations.

An elements electron core levels display a low energy distribution, their position is characteristic for the emitting element and never changes more than a few eV for different oxidation states. The valence band spectrum, is less well defined, exhibiting a broad spectrum, with (oxidation state induced) shifts large enough to make a clear assignment of elements difficult. XPS spectra are often displayed in regard to a binding energy scale .

Stoichiometry Determination

If an electron of element A is emitted as result of irradiation, the measured photoelectron current at the detector is in first order dependent on the respective number of occupied energy states, but other factors have to be considered as well. The total photoelectron current, normally given as counts per seconds (CPS), is

$$I_A(E_{bin}) = K\sigma_A(E_\lambda, E_{bin})\beta_A(E_\lambda, E_{bin})N_A\lambda_A(E_{kin})\mathbf{cos}\theta \tag{3.2}$$

where K is a constant factor representing the experimental set-ups influence, σ_A is the ionization cross section for the absorption of photons with E_λ and electrons of E_{bin}, β_A is the asymmetry factor, N_A the average atomic density of element A for the analysed sample depth (see table 3.2, λ_A the inelastic mean free path of electrons with E_{kin} in the sample, and θ is the angle of emission with regard to the surface normal [64].

After assigning the measured core level peaks to the respective elements, the peak area is corrected for σ_A and λ_A. A comparison of corrected peak areas assigned to different elements, gives information on their respective ratios in the measured volume.

Layer Thickness Determination

Electrons can travel only a short distance in condensed matter, before scattering inelastically, thus

E_{kin} (eV)	**Ni 2p** *634*	**O 1s** *954*	**C 1s** *1204*	**Si 2p** *1386*
$C_{graphite}$ (Å)	11.6	15.8	19.0	21.17
Si (Å)	19.3	26.8	32.2	36.0
SiC (Å)	15.9	21.6	25.9	28.9
SiO (Å)	17.6	24.1	28.8	32.3
am. SiO_2 (Å)	20.9	28.3	33.8	37.6
Ni (Å)	8.9	12.5	15.2	17.1
NiO (Å)	16.3	22.2	26.5	29.6
Ni_2Si (Å)	12.1	16.3	19.4	21.6
RuO_2 (Å)	12.9	17.3	20.6	23.0

Table 3.1.: *Inelastic mean free path length λ_A values for the common (approx.) core level energies in different materials [66]. Kinetic and binding energy are related by $E_{kin} = 1486.74\,\text{eV} - E_{bin}$, where $1486.74\,\text{eV}$ is the photon energy E_λ of the $Al_{K\alpha}$ line.*

λ_A is small. This is the reason, why XPS measurements are so surface sensitive and also why they have to be performed under ultra high vacuum (UHV) conditions. The exact value λ_A is dependent on E_{kin} and the traversed material, its general order of magnitude can be approximated by

$$\lambda_A \approx \frac{143}{E_{kin}^2} + 0.054 \cdot E_{kin}^{1/2} \tag{3.3}$$

for the elements. See figure 3.2 for a graphical presentation of this empirical behaviour found by Seah [65].

In the previous section a homogeneous sample morphology was assumed. Should the sample be heterogeneous instead, the difference in E_{kin} for different core levels will impact the measured photoelectron current, a result of the λ_A energy dependence. Utilising this relation allows the determination of a surface layers thickness, even in the monolayer range. This can be achieved via the numerical solution of the relation

$$\frac{I_A}{I_B} = \frac{N_A}{N_B} \frac{1 - \exp\left(\frac{-d_A}{\lambda_A\left(E_{kin,A}\right)\cos\theta}\right)}{\exp\left(\frac{-d_A}{\lambda_A\left(E_{kin,B}\right)\cos\theta}\right)} \tag{3.4}$$

	N_A mol/cm^3	**N** g/cm^3
$C_{graphite}$ (Å)	0.188	2.26
Si (Å)	0.084	2.34
SiC (Å)	0.161	3.21
SiO (Å)	0.097	2.14
am. SiO_2 (Å)	0.091	2.20
Ni (Å)	0.152	8.91
NiO (Å)	0.179	6.67
Ni_2Si (Å)	0.153	7.40
RuO_2 (Å)	0.157	6.97

Table 3.2.: *Density, normal and atomic, for the materials discussed in the context of this work.*

according to the layer thickness d_A [67]. For a thin layer of A on bulk B, I_A and I_B are the integrated core level line intensities of the respective elements, while $\lambda_A\left(E_{kin,A}\right)$ and $\lambda_A\left(E_{kin,B}\right)$ are the inelastic mean free paths for the two different core level lines ($E_{kin,A}$ and $E_{kin,B}$) in the thin surface layer A.

Should $\lambda_A\left(E_{kin,A}\right) \approx \lambda_A\left(E_{kin,A}\right)$, then eq. 3.4 can be simplified to

$$d_A \approx \lambda_A \cos\theta \cdot \ln\left(1 + \frac{I_A N_B}{I_B N_A}\right) \quad , \tag{3.5}$$

and no numerical solution is needed. The values for λ_A and N_A used within the context of this work are summarized in the tables 3.1 and 3.2.

For further information see [63, 68–70].

3.2 Low Energy Electron Diffraction (LEED)

Low Energy Electron Diffraction (LEED) is a UHV technique for determining the surface structure. This is done by visualising the constructive interference of the electron wave and the two dimensional atomic crystal structure (more precisely the high electron density around the atoms), as displayed in figure 3.3 A). LEED is therefore based on the wave-particle dualism de-Broglie proposed

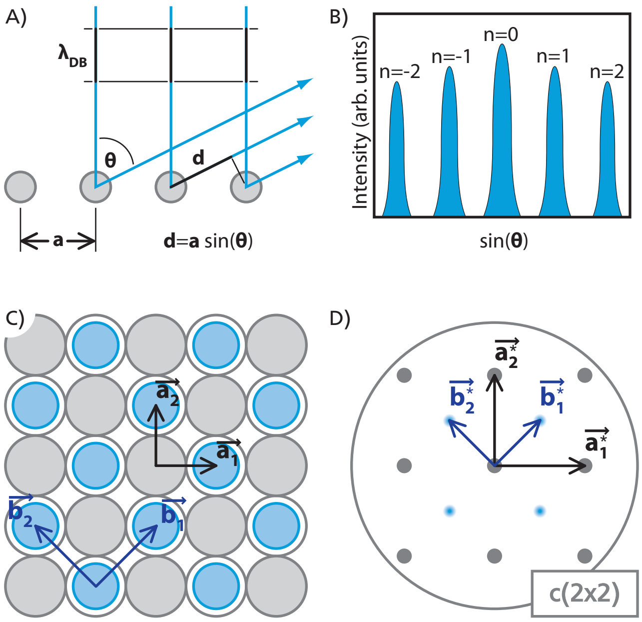

Figure 3.3.: *A) 1D diffraction of the incident electron wave at the crystal lattice, B) 1D spectrum as result of the 'Bragg condition", C) 2D surface structure and translational vectors for the substrate ($\overrightarrow{a_1}$ and $\overrightarrow{a_2}$) and additional adsorbate or reconstruction c(2x2) layer ($\overrightarrow{b_1}$ and $\overrightarrow{b_2}$), and D) resulting LEED pattern in momentum space generated by the reciprocal vectors $\overrightarrow{a_1^*}$ and $\overrightarrow{a_2^*}$ for the substrate and $\overrightarrow{b_1^*}$ and $\overrightarrow{b_2^*}$ for the adsorbate/reconstruction layer.*

in 1924, stating that each 'object' also has wave characteristics.

The basic idea was first employed by accident in 1927 by Davisson and Germer [71]. Further experiments resulted in strong proof for the wave-particle duality theory for electrons [72]. Due to technical difficulties and a lack of theoretical understanding it took about 40 years until LEED could be successfully used to determine atomic positions in the 1960s [73]. With the rise of the semiconductor industry, accompanied by the emergence of commercial UHV systems interest in LEED rose again. In the following years the necessary theoretic groundwork was supplied [73], until LEED for structural determination (as known today) was started in 1974 with Van Hove [74].

Electrons employed for LEED are normally in the energy range 20 to 200 eV. The resulting inelastic mean free path λ_A depends only weakly on the material A and is typically located between 5 to 10 Å. As the atoms signal intensity contribution

$$I(d) = I_0 \cdot \exp\left(\frac{-d}{\lambda_A(E_{kinA})}\right) \tag{3.6}$$

decreases exponentially with depth d, only the uppermost atomic layers are observable via LEED. The sample volume can therefore be considered as two dimensional, and the resulting 2D scattering conditions are less strict than for three dimensional bodies, as the wave vector perpendicular to the surface is not relevant. A mono energetic energy beam is thus sufficient to observe multiple reflexes from different reciprocal grid points [35].

In order to observe electron diffraction patterns, the electrons 'de-Broglie' wave length

$$\lambda_{DB} = \frac{h}{m \cdot v} = \frac{h}{\sqrt{2mE_{kin}}} \tag{3.7}$$

has to be of the some order of magnitude as the crystal lattice distance a. In above equation h is the Planck constant, m is the objects mass, v its speed, and E_{kin} its kinetic energy (for example in eV), thus λ_{DB} is inversely proportional to the electrons momentum [36]. For an electron beam energy of 90 eV this would amount to a wavelength of 1.3 Å.

As displayed in figure 3.3 A), the electron wave is diffracted at the localized increased electron densities surrounding the lattice atoms. If the reflected wave is conform to the 'Bragg condition'

$$a\sin(\theta) = n\lambda \tag{3.8}$$

for an integer n, constructive interference results in a significant signal intensity increase, which in

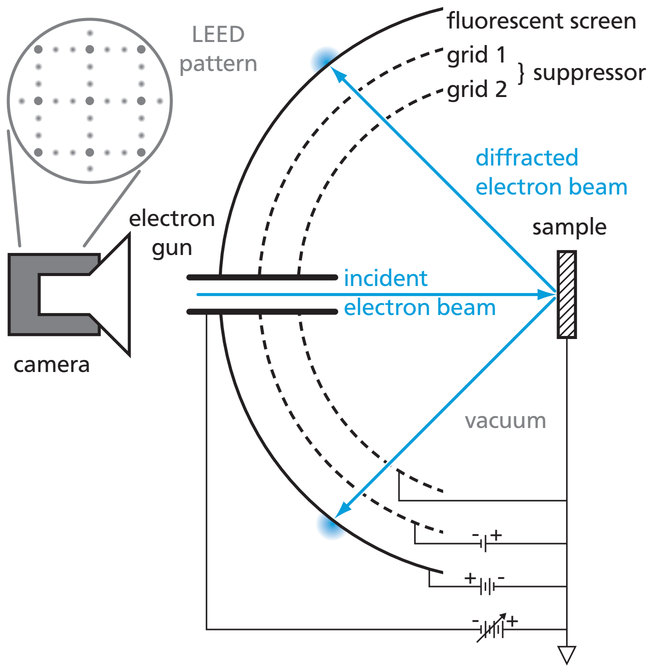

Figure 3.4.: *Schematic setup of a Low Energy Electron Diffraction (LEED) system. The grids repel inelastically scattered electrons. Further grids may be added to shield the sample and fluorescent screen, see [73] for additional information.*

turn gives rise to the observed LEED patterns, as displayed in figure 3.3 B).

The transitioning from one to two dimensions, is best described as the surface structure of a primitive unit cell in real space. This cell is generated by the two translational vectors $\vec{a_1}$ and $\vec{a_2}$. The LEED pattern on the other hand is generated by the associated vectors

$$\vec{a_1^*} = 2\pi\left(\frac{\vec{a_2} \times \vec{n}}{\vec{a_1} \cdot (\vec{a_2} \times \vec{n})}\right) \quad \text{, and} \tag{3.9}$$

$$\vec{a_2^*} = 2\pi\left(\frac{\vec{n} \times \vec{a_1}}{\vec{a_2} \cdot (\vec{n} \times \vec{a_1})}\right) \tag{3.10}$$

in reciprocal or momentum space, where $\vec{n}$ is a vector normal to the surface. Thus $\vec{a_1} \| \vec{a_1^*}$ and $\vec{a_2} \| \vec{a_2^*}$ [73].

In figure 3.3 C) a cubic surface structure with its base ($\vec{a_1}$ and $\vec{a_2}$) is displayed right next to the resulting LEED pattern in momentum space (figure 3.3 D)). As for the real space, the reciprocal pattern is generated according to

$$\vec{g} \equiv h\vec{a_1^*} + k\vec{a_2^*} \quad , \tag{3.11}$$

where h and k are integer numbers.

Additionally to the substrate contribution, a surface adsorbate layer or specific reconstruction patterns of the uppermost atoms can result in further reflexes. In C) and D) this is represented by the blue atoms and the b-vectors. The resulting LEED pattern is a superposition of substrate and adsorbate/reconstruction signal. However, there are other influences to be considered. Stepped surfaces might lead to the split-up of one reflex into many, while rotational domains can result in the extinction of specific reflexes (a popular example would be the 2x1/1x2 reconstruction), and superlattices or surface disorder can give rise to satellite structures around reflexes [73].

A typical LEED experimental setup is displayed in figure 3.4. An electron beam of the desired kinetic energy is directed at the sample. Inelastically and multiple times scattered electrons can be filtered out via a number of grids held at opposing potentials before they hit a fluorescent screen. The resulting pattern on the screen can then be recorded with a suitable camera system. Because of the short inelastic mean free path for low energy electrons a good vacuum is mandatory as most electrons would scatter on the intermediate gas molecules otherwise. For further technical informations on LEED the reading of [73] is recommended.

DAISY Fun (**DA**rmstädter **I**ntegrated **SY**stem for **Fun**damental Research)

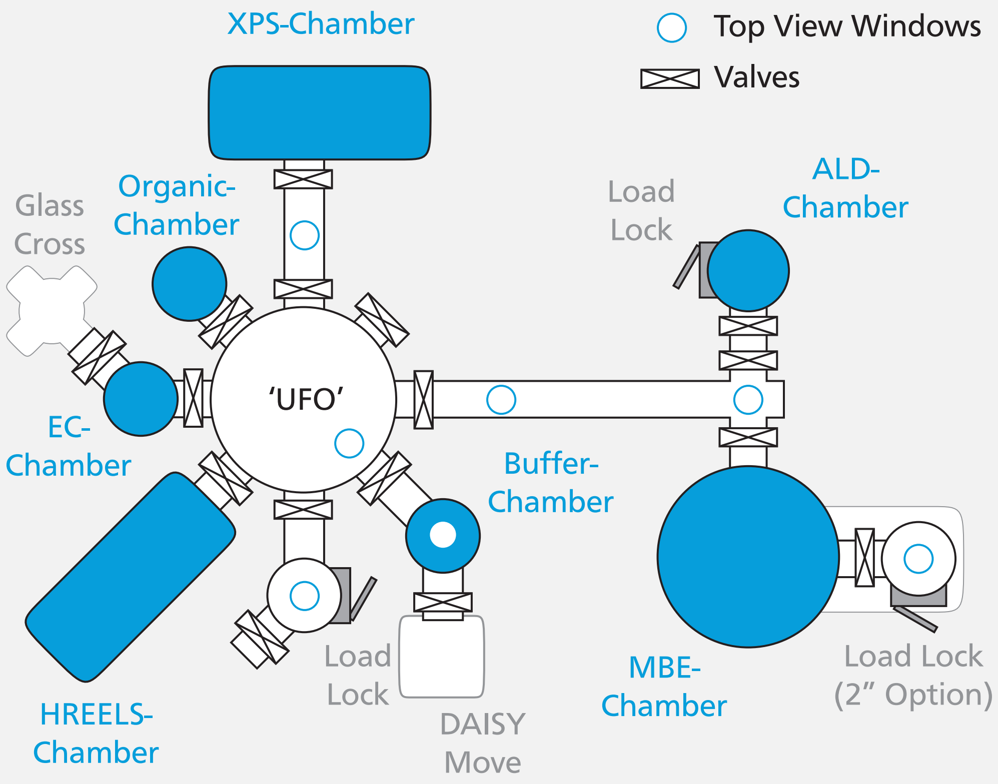

XPS Chamber	XPS	PHOIBOS 150, Focus 500 with XR50M (SPECS)
		$Al_{K\alpha}$ at 1486.74 eV
	UPS	Focus HIS 13
	LEED	BDL 800 IR-LMX (OCI vacuum microengineering)
	Heating	electrom impact heating (up to 700 °C)
		IMPAC IS 120 Pyrometer (400 to 1000 °C)
	Ar Sputter Gun	-
HREELS Chamber	HREELS	Delta 0.5 with LaB6 filament (SPECS)
		electron energy 4 eV, 60° mirror geometry
MBE Chamber	2x Magnetron	-
	2x E-beam Evap.	-
	Heating	-
Organic Chamber	2x E-beam Evap.	-

DAISY Fun (**DA**rmstädter **I**ntegrated **SY**stem for **Fun**damental Research)

Buffer Chamber	Heating	electron impact heating (up to approx. 1200 °C) IMPAC IS 120 Pyrometer (400 to 1000 °C)
	Other	adapter station for 'DAISY Move'
ALD Chamber	-	-
EC Chamber	Electrochemistry	
	Other	adapter station for a glass cross

3.3 UV/Vis Spectroscopy

UV/Vis spectroscopy is a subtype of general absorption spectroscopy in the ultraviolet (10 to 400 nm) to visible spectrum (400 to 700 nm). The sample is illuminated and the transmittance T and/or reflectance R intensity measured. Due to the conservation of energy, both are related via

$$T + R + A = 1 \quad , \tag{3.12}$$

where A is the absorbance [75].

The energy range is sufficient to excite interband excitation of outer electrons, but too high for vibrational states (this would be infrared (IR) spectroscopy), and to low for interband excitations of inner electrons, see figure 3.6 in the next section. Should the band gap be larger than the visible spectrum, no photons are absorbed, and the sample appears transparent. In most cases, UV-Vis spectroscopy is used for the investigation of molecules, as those still have discrete energy states or very narrow bands. Electron transitions between those states results in equally narrow absorption peaks. For macroscopic solids, the band structure is much broader, resulting in equally broad absorption features.

The UV/Vis spectrum, of macroscopic semiconductors, can be used to determine the samples absorption coefficient α and band gap E_{BG}. In the absence of reflectance, transmission through a sample of thickness Δx follows the Lambert-Beer law

$$I = I_0 \cdot \exp(-\alpha \Delta x) \quad , \tag{3.13}$$

where I_0 is the light intensity before, and I after the sample transition. The quantity α is known as the 'absorption coefficient', and measured in cm^{-1} [76].

Plotting the quantity $(\alpha \cdot E_\lambda)^{1/n}$ over E_λ gives rise to a 'Tauc plot' [75, 77]. The value of n has to be chosen depending on the nature of the observed electron transition. It will be

$n = 1/2$ for a direct allowed,
$n = 3/2$ for a direct forbidden,
$n = 2$ for a indirect allowed, and
$n = 3$ for a indirect forbidden transition [78].

Figure 3.5 shows the typical shape of a Tauc plot. The optical band gap can be read off the intercept, between the extended linear plot region and the abscissa.

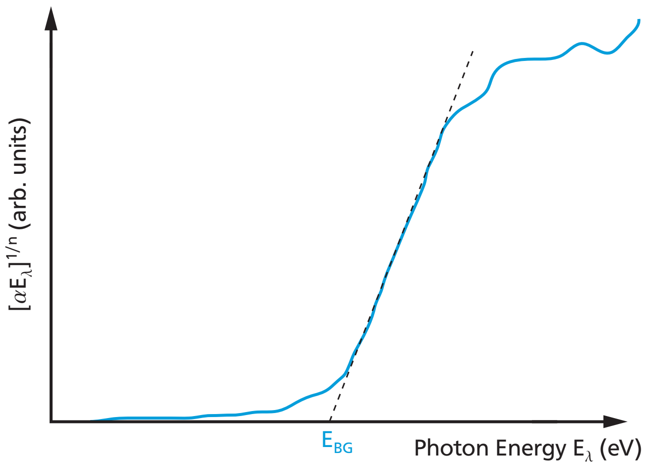

Figure 3.5.: *Theoretic curve shape of a Tauc plot. The intercept of the extended linear region with the abscissa yields the semiconductors optical band gap.*

3.4 Raman Spectroscopy

Raman spectroscopy is based on the Raman effect, a change in photon energy upon inelastic scattering on molecules or solids. The effect was discovered by Sir C.V. Raman, who was awarded a Nobel prize in physics (1928) for this achievement [81].

For Raman spectroscopy a samples reflectance under illumination with monochromatic light, usually from a laser in the visible range, is measured. Three different kinds of reflection are possible, mentioned in the order of their cross section and schematically displayed in figure 3.6: elastic or Rayleigh scattering ($E'_\lambda = E_\lambda$), inelastic Stokes-Raman scattering with phonon creation ($E'_\lambda < E_\lambda$), or inelastic anti-Stokes-Raman scattering under phonon absorption ($E'_\lambda > E_\lambda$).

In absorption spectroscopy, a number of different measures is used. Additionally, to the known wavelength λ and photon energy $E_\lambda = hc/\lambda$, the wave number

$$\nu = \frac{1}{\lambda} \tag{3.14}$$

is defined as the inverse wavelength, and given in cm^{-1}. A Raman spectrum is then comprised of the photon intensity over the photon energy loss in regard to E_λ, the Raman shift $\Delta\nu$. At its origin, the Rayleigh photons result in a dominant peak. The Stokes-Raman scattered photons give rise to a peak structures at $\Delta\nu > 0$, but as the Raman scatter efficiency is low, their intensity can be up to a million times weaker than the reflectance signal of the Rayleigh peak. This is also the reason why the Anti-Stokes-Raman scattered photons are seldom considered, as their cross section is even lower.

Experimental Equipment: UV-Vis

All UV-Vis measurements were performed with a **PERKIN ELMER Lambda 900** UV/Vis/NIR, either in transmission mode or with an Ulbricht sphere.

Figure 3.7 displays a schematic Raman spectrum, with the central Rayleigh peak, and the accompanying Stokes/anti-Stokes peak structure. For clarification, the relation of the four relevant energy measures is displayed as well. It should be mentioned that fluorescence can often be observed in a similar energy range. If present, its higher cross section will make it dominant in the Raman spectrum, burrowing the actual Stokes-Raman modes.

In most cases Raman spectroscopy is non-destructive, and very versatile. It can be used for many applications. Among others, the determination of grain orientation, strain, the degree of crystallinity, or doping levels. In regard to this work, Raman spectroscopy was used for two reasons.

First, the confirmation of the samples polytype. Each SiC polytype has a distinctive number of modes. Starting with two for 3C SiC, and increasing with the unit cell length. A detailed explanation of this phenomenon, along with Raman spectra of the polytypes 3C, 2H, 4H, 6H, and 15R can be found in [82].

Second, the determination of the samples doping concentration n_D. Plasmons, quantized fluctuations in a solids free charge carrier density, can

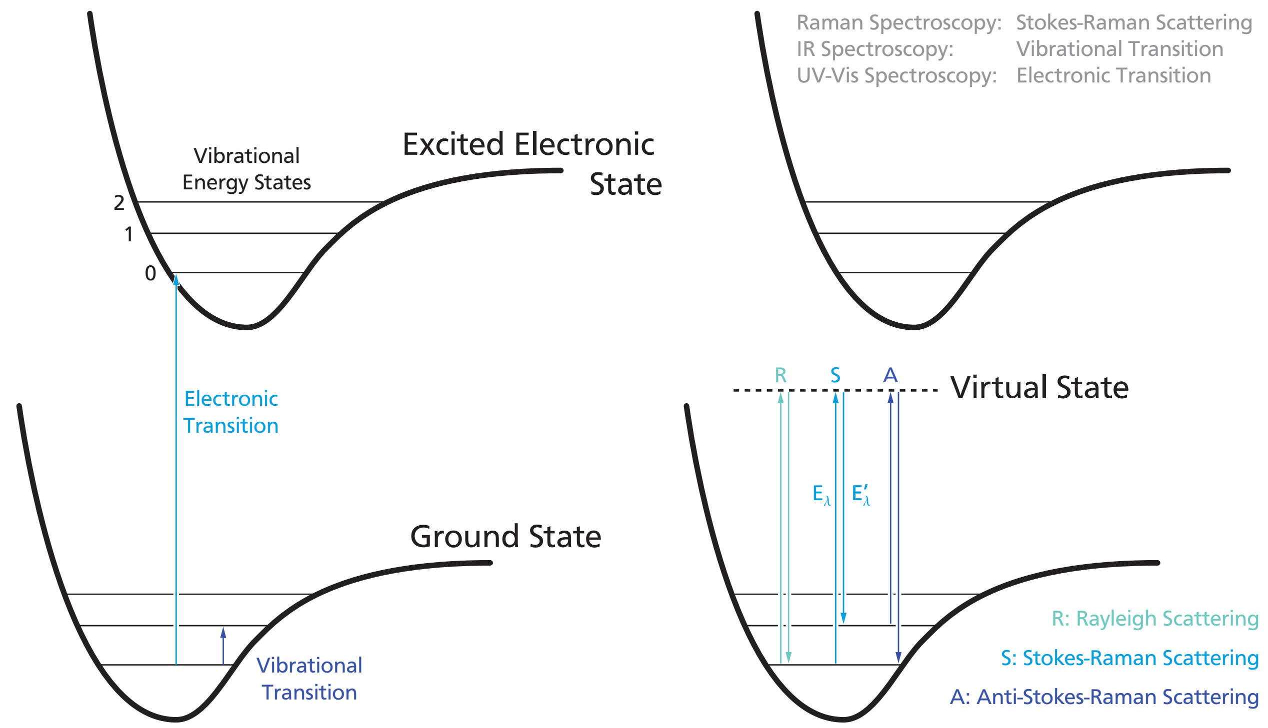

Figure 3.6.: *Schematic representation of the possible electronic and vibrational energy states. Depending on the available energy, different excitation processes will occur. Interband transitions of outer electrons can be observed in the UV-Vis range* ($\lambda \approx 10 - 750\,\text{nm}$, $E_\lambda \approx 124 - 1.65\,\text{nm}$)*, while vibrational transitions are excited via infra-red light* ($\lambda \approx 2.5 - 25\,\mu\text{m}$, $E_\lambda \approx 0.5 - 0.05\,\text{nm}$)*. Raman modes are excited by optical transitions involving a virtual state or by involving the excited state (Resonance Raman).*

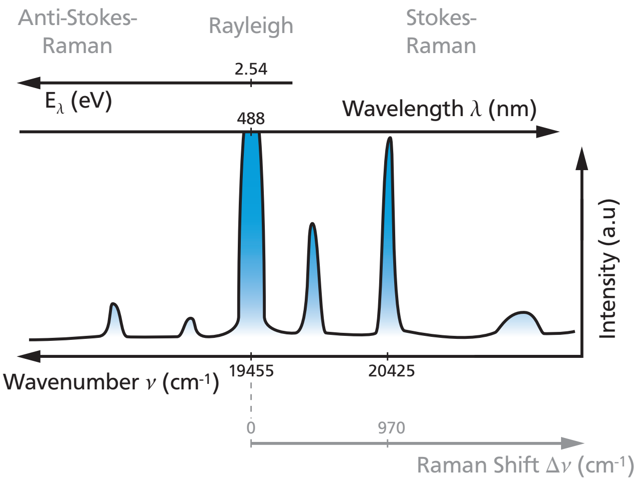

Figure 3.7.: *Schematic Raman spectrum (Stokes-Raman region), for excitation with a* 488 nm *laser, in regard to the four related abscissa units. The elastic Rayleigh peak displays the highest intensity. Anti-Stokes-Raman spectra are seldom used, because the their scatter efficiency is smaller yet than for Stokes-Raman scattering [79].*

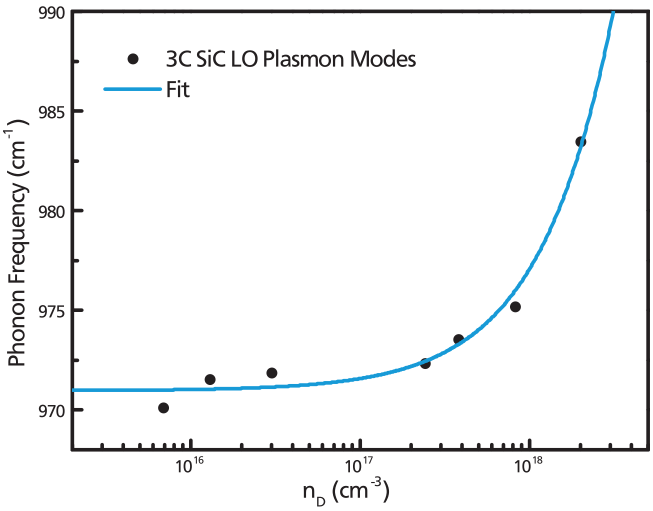

Figure 3.8.: *Raman shift position for the LO plasmon mode of n-type 3C SiC in dependence of the effective carrier concentration* n_D*, after [80].*

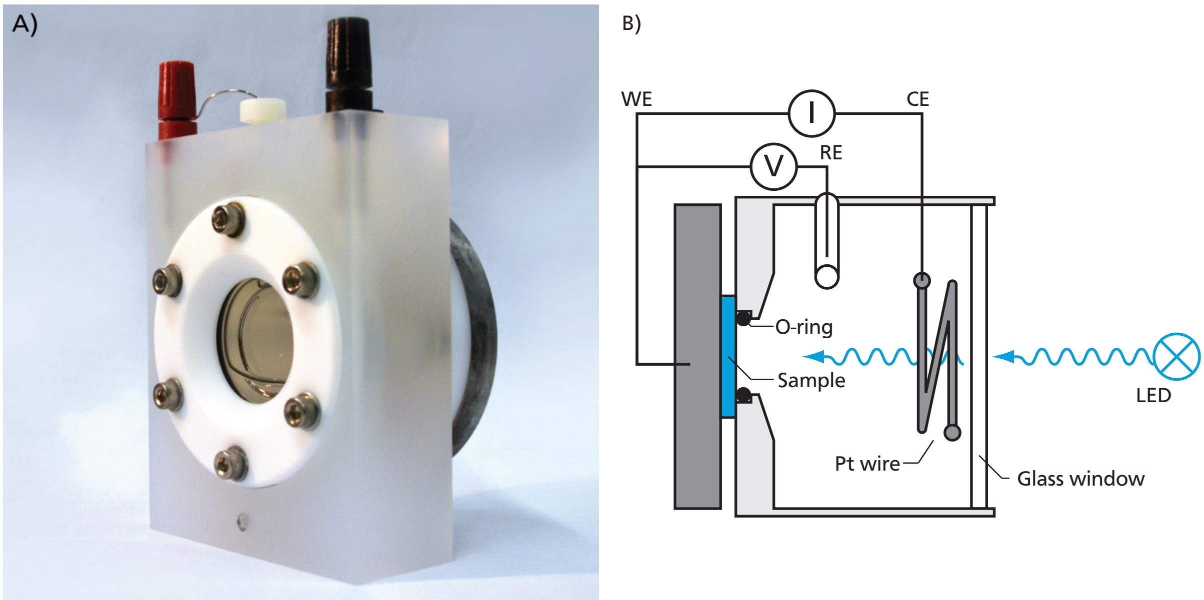

Figure 3.9.: *A) The EC measurements were performed in a PECC-2 (Photo Electro-Chemical Cell) from Zahner-Elektrik GmbH & Co. KG. B) Schematic drawing of the PECC-2 for the measurements in 3-electrode configuration. Current is measured between the sample, at the working electrode (WE), and the counter electrode (CE), while the potential is measured between WE and reference electrode (RE).*

interact with the longitudinal optical phonon, to form a coupled mode. Changes in n_D, and thus the free charge carrier density, will influence the line shape and position of such a LO phonon-plasmon coupled mode (LOPC) [79,82]. The effect has been studied in 3C, 4H, and 6H SiC. Figure 3.8 shows the relation between the LOPC and n_D for 3C SiC, as reported by [80]. While this method is obviously not well suited for cases where $n_D < 10^{17}\,\mathrm{cm}^{-3}$, the accessible doping range coincides nicely with the samples investigated within the context of this work. See reference [81] for further reading on Raman spectroscopy.

3.5 Electrochemistry

Electrochemical (EC) reactions are those where a chemical reaction is somehow related to a electrical current flow, see section 2.2 or [15] for the underlying theory. Electrochemistry includes a multitude of different methods, which provide insights on various sample properties (conductivity, corrosion etc.).

Experimental Equipment: Raman

Measurements were performed on a **LabRAM HR** Raman spectrometer by Horiba Jobin Yvon.

Electrochemical Cell

All presented electrochemical measurements of the samples were performed in a PECC-2 electrochemical cell, see figure 3.9 for a picture and the schematic drawing. The measurements were performed in a three electrode configuration, where the current flow is measured between the sample, at the working electrode (WE), and a platinum wire, the counter electrode (CE), while the potential is measured between WE and the reference electrode (RE). This setup allows an investigation of the half cell reactions at the WE only, without having to consider the electrochemical reactions at the CE. In this case the reference electrode is used as the second half cell, with a known (fixed) potential for measuring the cell potential changes.

Standard hydrogen electrode	(SHE)	$E_{SHE} = 0\,\mathrm{V}$	*activity of H^+ is 1M*
Normal hydrogen electrode	(NHE)	$E_{SHE} \approx E_{NHE}$	*concentration of H^+ is 1M*
Silver chloride electrode	(Ag/AgCl)	$E_{SHE} = E_{Ag/AgCl}$	$+\ 0.197\,\mathrm{V}$
Standard calomel electrode	(SCE)	$E_{SHE} = E_{SCE}$	$+\ 0.241\,\mathrm{V}$
Reversible hydrogen electrode	(RHE)	$E_{RHE} = E_{SHE}$	$+\ 0.0591\,\mathrm{V} \cdot \mathrm{pH}$

Table 3.3.: *Common reference electrodes and their relations to each other. The first step of any EC experiment was a calibration measurement between a RHE and (Ag/AgCl) reference electrode. Then, the later was used for the remaining experimental procedure.*

Experimental Equipment: EC Cell

PECC-2 EC cell from **Zahner-elektrik GmbH & Co. KG**. The cell is made from polychlorotrifluoroethylene (PCTFE), allows the use of different O-ring diameters for sealing, and has a volume of approximately 8 ml.

Reference Electrodes

In a three electrode setup the sample reference is measured relative to a reference electrode, which has a steady, well-know potential. Reference electrodes are normally based on specific redox systems, like (Ag/AgCl), with constant concentrations. A summary of the most common reference electrodes, and their related potentials, can be found in table 3.3.

In the past the SHE, platinum electrode potential in an ideal (theoretical) 1 M acidic solution, was the standard for zero potential. Recently, it is often replaced by the RHE, a pH corrected SHE potential. This makes the comparison between measurements in solutions of different pH much easier, as no further pH correction, according to equation 2.13, is required. If not mentioned otherwise, all EC potentials in this work will be displayed versus RHE (V vs. RHE).

Current Potential Curves

Current potential (IE) curves give the current flow between WE and CE, at a linearly increasing potential relative to RE. The electrical current flow is proportional to the reaction rate, this is called 'Faraday's law', and the IE curve shape can give information on which reactions occur. For simple reactions, and only considering kinetic limitations, the IE behaviour is described by the Butler-Volmer equation 2.29. Special cases of IE curves are, open circuit potential (OCP) measurements, the potential behaviour over time for zero current flow, and cycliv voltammetry (CV) measurements, where the same potential range is measured in both directions. A comparison of IE curves in the dark and under illumination can give information on the photocurrent.

Chopped Light and Transients

Chopped light (CL) measurements are another special IE measurement. The measurement is performed in the dark, and the sample periodically illuminated under controlled conditions. In the available setup, LEDs of varying wavelengths were

Experimental Equipment: Potentiostats

The EC measurements were performed with **ZENNIUM** and **PP221 potentiostats**, both from **Zahner-elektrik GmbH & Co. KG**, the second was used for LED control.

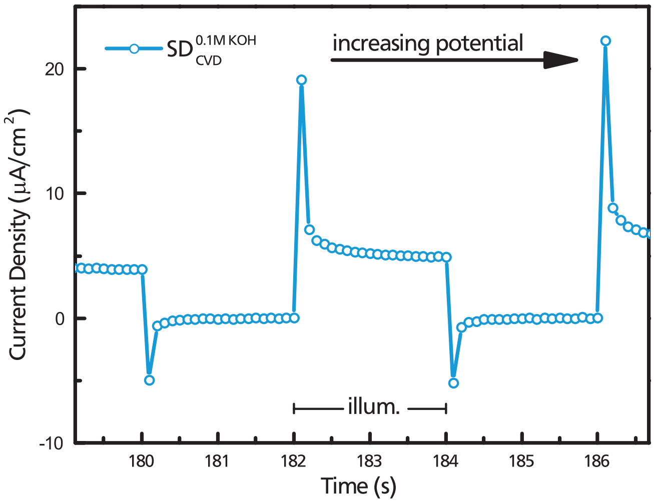

Figure 3.10.: *Chopped light current-time behaviour, close to the onset potential, which shows transient behaviour. The measurement was performed on* SD_{CVD} *in 0.1 M KOH at* 0.62 V vs RHE, *this sample is discussed in chapter 7.*

available. Their intensity was checked with a photo diode. Chopped light measurements allow the determination of the photocurrent by comparing the current behaviour from dark and illuminated intervals. However, the current behaviour over time allows additional insights in the reaction kinetics. Close to the onset potential, the potential vs. RHE where the reaction first occurs, chopped light measurements often display a transient behaviour. This is demonstrated in an example CL measurement displayed in figure 3.10.

Upon illumination, photo generated excitons (electron hole pairs) are separated. In a n-type semiconductor, the holes will flow towards the surface, where they will initially accumulate in case of a hindered charge transfer. This initial current is therefore not the result of a charge transfer across the semiconductor / electrolyte interface, but corresponds to the charging of a capacity. Once a steady state concentration of holes at the surface is reached, an equilibrium is established, and the incoming hole flux to the surface is exactly equal to the holes leaving via interface transfer or recombination [59]. See section 7.3.

Electrochemical Impedance Spectroscopy

Electrochemical impedance spectroscopy (EIS) measurements are performed around a fixed potential U_0, with a small time dependent potential modulation ΔU. The applied total potential can be described by

$$U(t) = U_0 + \Delta U \cdot \cos(\omega t) \quad , \tag{3.15}$$

where ΔU is the modulation amplitude (10 mV is a common value), t the time, and $\omega = 2\pi f$ the angular frequency. An EIS spectrum is composed of the alternating current behaviour (impedance) of the system in dependence of the modulation frequency ω. Examples can be found in figures 3.11 and 3.12.

For evaluation, the electrochemical system is described in form of an electrical circuit, which is called an 'equivalent circuit'. If the equivalent circuit describes the electrochemical reaction correctly, fitting of the measured impedance can yield parameters like the charge transfer resistance, or the depletion layer capacity. Common circuit components are the resistance R, and the capacity C. They are defined as

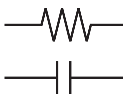

$$Z_R = R$$
$$Z_C(\omega) = -i\frac{1}{\omega C}$$

for an alternating current circuit, where i is the imaginary unit. The total impedance Z of the equivalent circuit is constructed following the same rules as for continuous current, but with above values for the component impedance. Depending on the equivalent circuit, Z can be a complex number.

EIS measurements are either presented as Nyquist or as Bode plot. The first presents the complex part Z_c in dependence of the real part Z_r, while the second displays the total absolute value of $|Z|$ and the phase shift φ over the frequency f. Both values can be obtained from Z_c and Z_r via

$$|Z(\omega)| = \sqrt{Z_r^2(\omega) + Z_c^2(\omega)} \tag{3.16}$$

$$\varphi = \tan^{-1}\left(\frac{Z_c(\omega)}{Z_r(\omega)}\right) \quad . \tag{3.17}$$

All EIS spectra in this work will be displayed as Bode plots.

Selecting the right equivalent circuit for a system is not trivial. Below is a summary of some fundamental circuits and their meaning.

RC: The resistance R_0 in series with a capacity C_1. This equivalent circuit describes an ideally polarized electrode. There is no charge transfer across the electrode / electrolyte interface, only charging and discharging of the capacity C_1. In case of a metal electrode, C_1 would describe the Helmholtz capacity $C_H = \frac{\varepsilon\varepsilon_0}{d_H} \approx 10\,\mu\mathrm{F/cm}^2$ to $100\,\mu\mathrm{F/cm}^2$, for the Helmholtz layer (thickness d_H) [49]. For a semiconductor there is also the space charge capacity of the depletion layer C_{sc} to consider, which will be in the range of $1\,\mu\mathrm{F/cm}^2$ or below. As the two capacities would be in series the total capacity will be

$$C_1 = \frac{C_{sc}C_H}{C_{sc} + C_H} \approx C_{sc} \quad , \tag{3.18}$$

and C_H will be negligible. R_0 describes the mass transfer limitation of the system. The circuits impedance is

$$Z_{RC}(\omega) = R_0 - i\frac{1}{\omega C_1} \quad . \tag{3.19}$$

Figure 3.11 A) displays the equivalent circuit and three sets of component values used to simulate the circuits behaviour. The absolute value of impedance

$$|Z_{RC}(\omega)| = \sqrt{R_0^2 + \frac{1}{(\omega C_1)^2}} \tag{3.20}$$

is displayed in B), and the phase shift

$$\varphi_{RC}(\omega) = -\tan^{-1}\left(\frac{1}{\omega R_1 C_1}\right) \tag{3.21}$$

in C) [83]. Their characteristic curve property dependences on the component values is displayed as well.

(RC): A resistance R_1 in parallel with the capacity C_1. This circuit describes a redox reaction, charging and discharging of the interface capacity C_1, together with the charge transfer across the electrode / electrolyte interface, represented by the transfer resistance R_1. The systems impedance is

$$Z_{(RC)}(\omega) = \frac{R_1}{1 + (\omega R_1 C_1)^2} - i\frac{\omega R_1^2 C_1}{1 + (\omega R_1 C_1)^2} \quad . \tag{3.22}$$

Insertion in equations 3.16 and 3.17 yields [83]

$$|Z_{(RC)}(\omega)| = \frac{\sqrt{R_1^2 + (\omega R_1^2 C_1)^2}}{1 + (\omega R_1 C_1)^2} \tag{3.23}$$

$$\varphi_{(RC)}(\omega) = -\tan^{-1}(\omega R_1 C_1) \quad . \tag{3.24}$$

Similar to the RC circuit, simulations of above results for three data sets are displayed in figure 3.11 D) to F).

R(RC): The combination of the two previous equivalent circuits represents a simple redox reaction in a full EC cell. The systems impedance is

$$Z_{R(RC)}(\omega) = R_0 + \frac{R_1}{1 + (\omega R_1 C_1)^2} - i\frac{\omega R_1^2 C_1}{1 + (\omega R_1 C_1)^2} \quad , \tag{3.25}$$

and a simulation of its phase and impedance are displayed in figure 3.12 B) and C). R_0 is the systems ohmic resistance and R_1 the charge transfer resistance. This circuit gives rise to a characteristic phase shift φ peak, whose position

$$f_{max} = \frac{1}{2\pi}\frac{1}{R_1 C_1}\sqrt{\frac{R_1}{R_0} + 1} \quad , \tag{3.26}$$

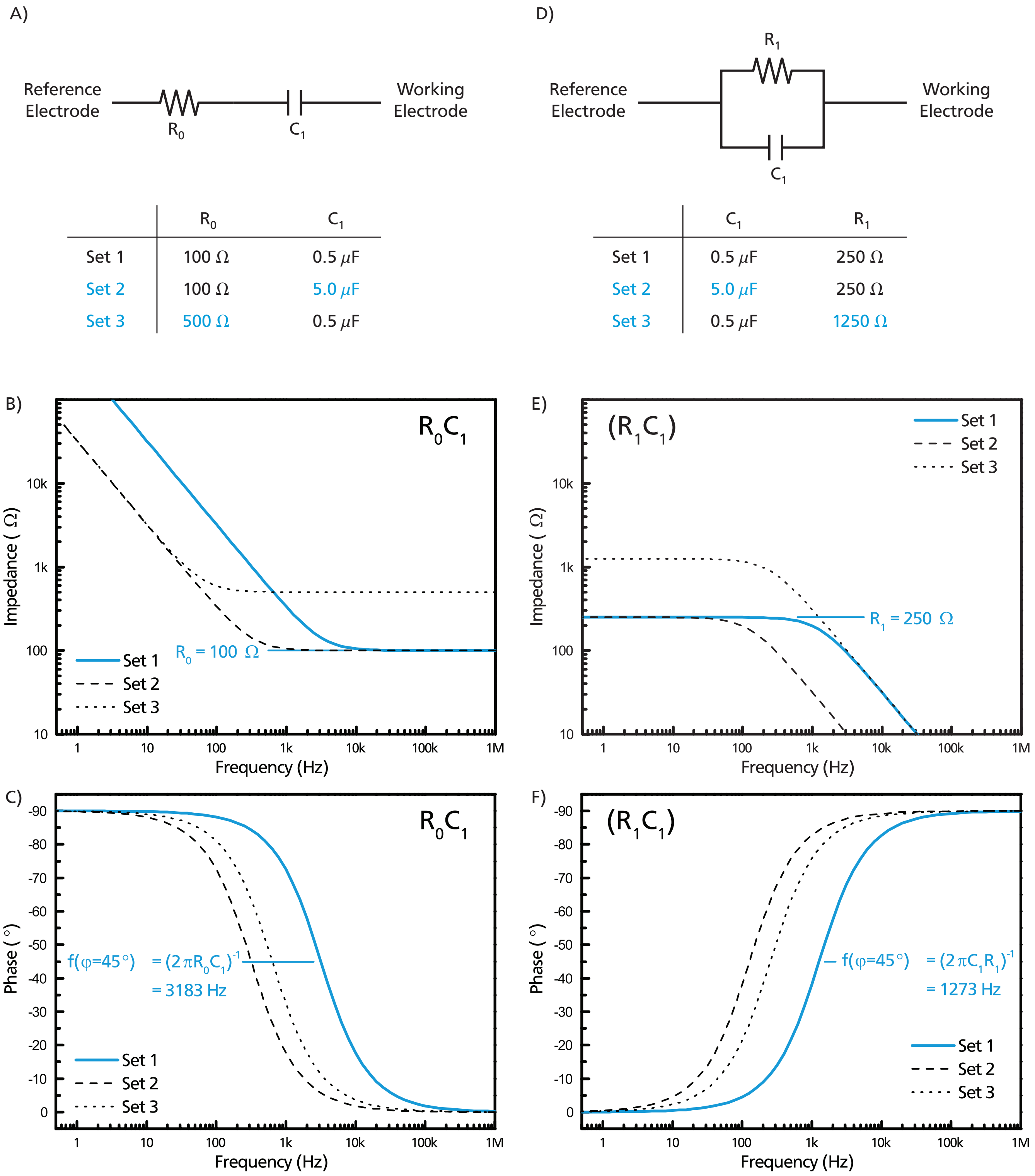

	R_0	C_1
Set 1	100 Ω	0.5 µF
Set 2	100 Ω	5.0 µF
Set 3	500 Ω	0.5 µF

	C_1	R_1
Set 1	0.5 µF	250 Ω
Set 2	5.0 µF	250 Ω
Set 3	0.5 µF	1250 Ω

Figure 3.11.: *Basic RC and (RC) equivalent circuits, for the evaluation of EIS spectra. The displayed impedance and phase shift behaviour (Bode representation), are based on the provided sets of component parameters. Some relations between characteristic curve features and the parameter values are displayed in blue.*

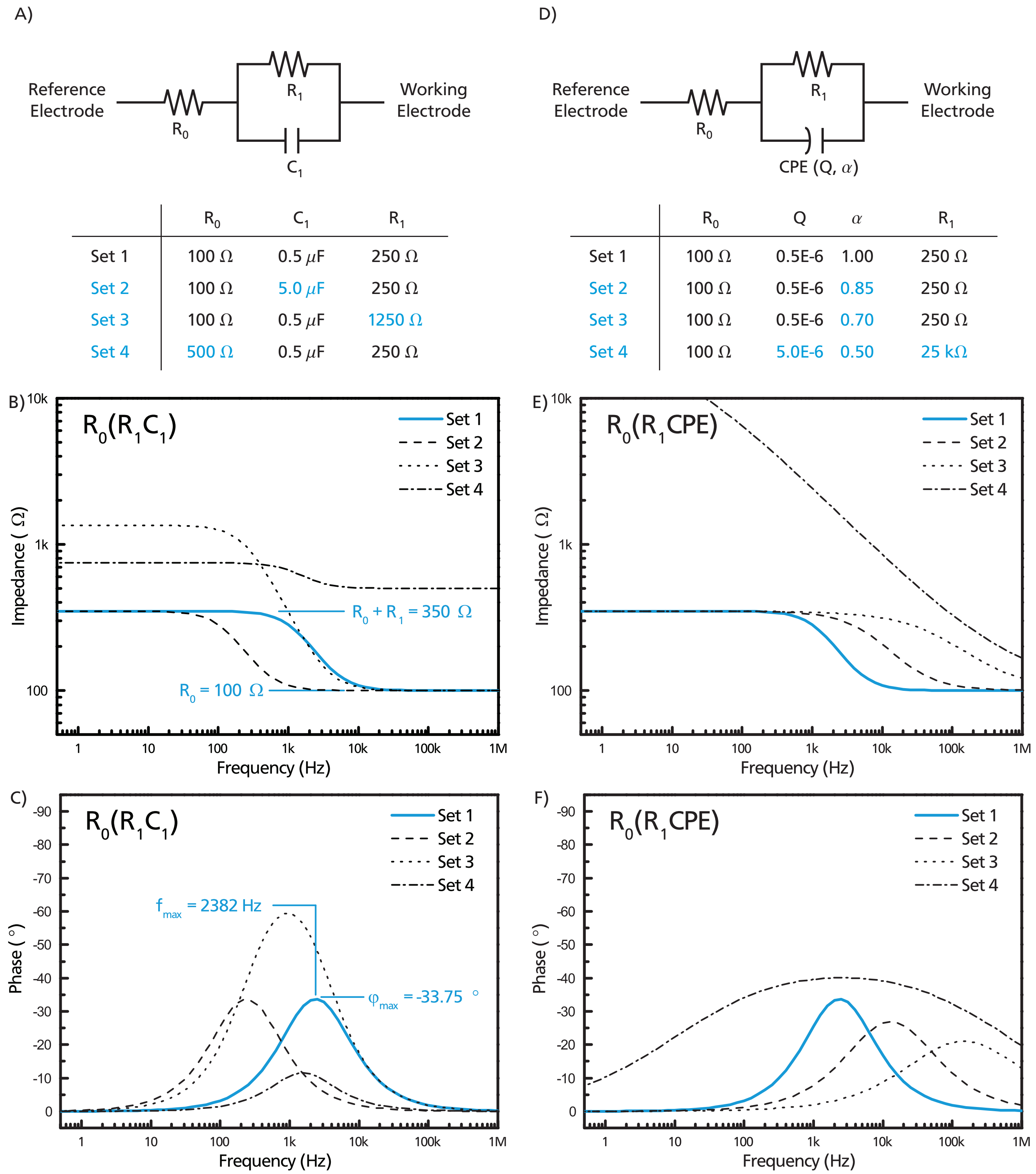

	R_0	C_1	R_1
Set 1	100 Ω	0.5 μF	250 Ω
Set 2	100 Ω	5.0 μF	250 Ω
Set 3	100 Ω	0.5 μF	1250 Ω
Set 4	500 Ω	0.5 μF	250 Ω

	R_0	Q	α	R_1
Set 1	100 Ω	0.5E-6	1.00	250 Ω
Set 2	100 Ω	0.5E-6	0.85	250 Ω
Set 3	100 Ω	0.5E-6	0.70	250 Ω
Set 4	100 Ω	5.0E-6	0.50	25 kΩ

Figure 3.12.: *Basic R(RC) and R(RCPE) equivalent circuits, for the evaluation of EIS spectra. The displayed impedance and phase shift behaviour (Bode representation), are based on the provided sets of component parameters. The equations for* f_{max} *and* φ_{max} *can be found in the text.*

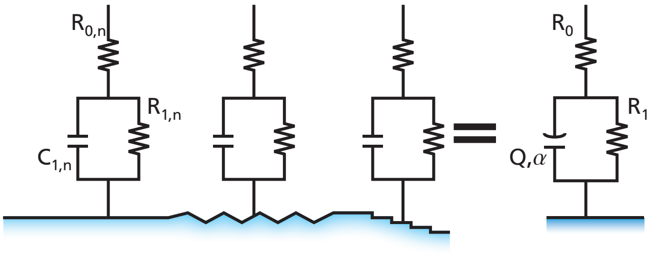

Figure 3.13.: *A large number of parallel R(RC) circuits can be used to model a heterogeneous sample surface. This can either be calculated with a sum function over all circuits, or it is expressed as a constant phase element (CPS) [84].*

and size

$$\varphi_{max} = -\tan^{-1}\left(\frac{R_1}{2(R_0+R_1)}\sqrt{\frac{R_1}{R_0}+1}\right) \quad , \tag{3.27}$$

depend on the component properties [83][1].

Constant Phase Element: (RC) elements can be used to model ideal electrodes, however solid electrodes often display some frequency dispersion in their impedance behaviour. This is the result of a heterogeneous sample surface, which can be thought of as a large number of very small homogeneous sample areas in parallel. See figure 3.13 for a schematic representation of the situation. Using a sum function the systems impedance would be

$$Z^{-1}(\omega) = \sum_n Z^{-1}_{R(RC),n}(\omega) \tag{3.28}$$

$$= \sum_n \left(R_{0,n} + \frac{R_{1,n}}{1+i\omega R_{1,n}C_{1,n}}\right)^{-1} \quad , \tag{3.29}$$

which can also be expressed as a single circuit

$$Z_{R(RCPE)}(\omega) = R_0 + \frac{R_1}{1+(i\omega)^\alpha Q R_1} \tag{3.30}$$

with a constant phase element (CPE) instead of the capacity, where Q and α are the CPE properties. α determines the degree of dispersion, for $\alpha = 1$ a CPE elements is identical to a capacity and $Q = C_1$. See figure 3.12 D) to F) for a graphical display. Lower values of α require an extrapolation of the effective capacity

$$C_{eff} = Q^{1/\alpha}\left(\frac{R_0 R_1}{R_0+R_1}\right)^{\frac{1-\alpha}{\alpha}} \tag{3.31}$$

from the CPE properties [84, 85], see references [83, 86] for further reading on EIS.

Experimental Equipment: Potentiostat

The EIS measurements were performed with a **Interface 1000 Potentiostat/Galvanostat/ZRA** from **Gamry Instruments**.

---

[1] Careful: [83] has a typo in equation (2.148) for f_{max}

4 Photoelectron Spectroscopy Of Cubic Silicon Carbide

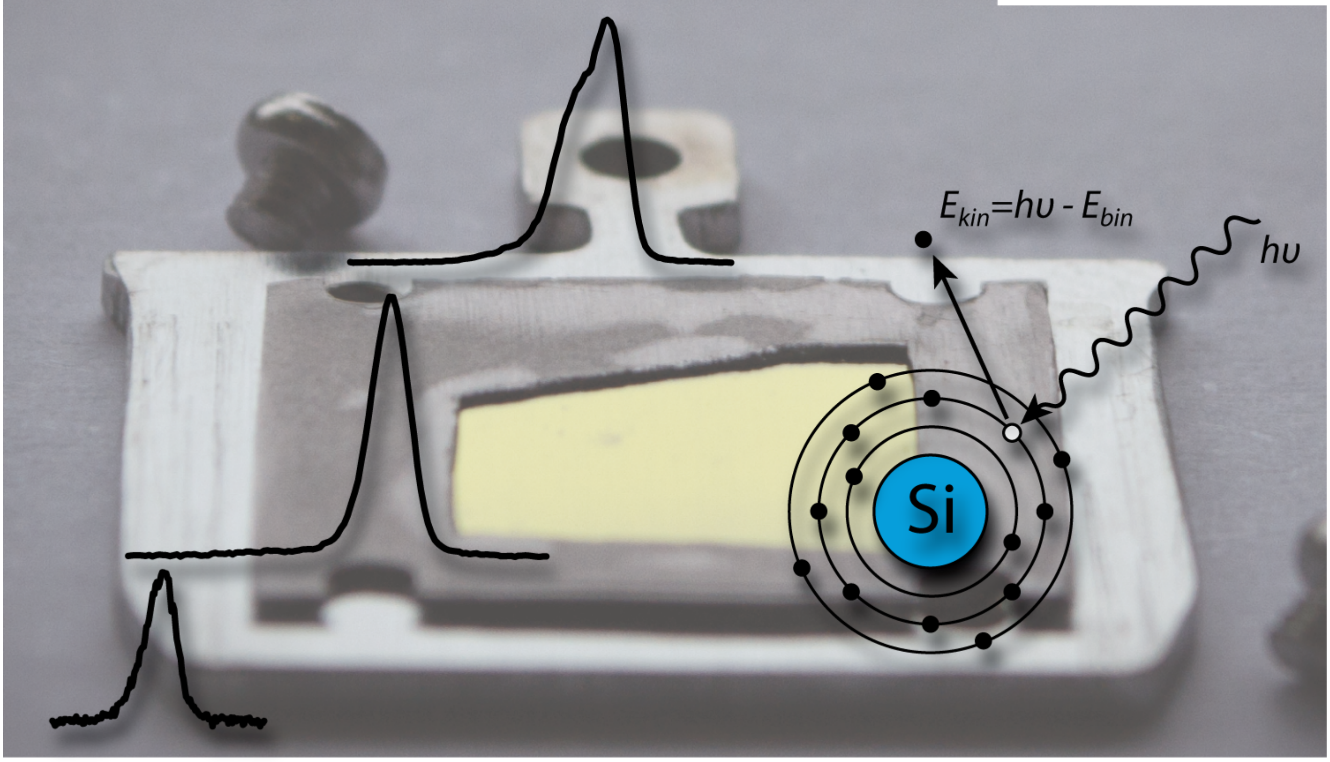

This chapter provides an introduction to photoelectron spectroscopy measurements of cubic silicon carbide. It deals with the identification and interpretation of the relevant peaks, elaborates on the evaluation routine in CasaXPS, and gives a perspective on the information to be gained this way. Employed methods are (angle resolved) XPS and LEED.

4.1 Introduction

X-ray photoelectron spectroscopy (XPS) is a very versatile technique for obtaining information on surface properties. Because of the experimental challenges involved, the first high resolution XP-spectra were not taken before the 1950s. Probably best known for his dedication in advancing the XPS method is Kai Siegbahn (University of Uppsala, Sweden), also due to his well known book from 1967 '*ESCA - electron spectroscopy for chemical analysis*' as XPS was called back then. For his accomplishments regarding XPS he received the 1981 Nobel Prize in physics.

The real breakthrough for XPS came around 1985, when digital instruments and the use of multichannel detectors reduced the measurement time drastically, leading to a significant increase of the use of XPS in material science [68–70, 87]. In the context of this work XPS was used frequently to characterize numerous (mostly) cubic silicon carbide (3C SiC) samples. Therefore this chapter is designed as an introduction to the 3C SiC spectrum, and to give some information on the fitting routines used throughout the rest of this work.

4.2 Experimental Procedure

Most X-ray photoelectron spectroscopy (XPS) experiments discussed in this chapter were conducted on a piece from a (001) 3C SiC grown on a 2" silicon wafer, liberally supplied by Gabriel Ferro (LMI Lyon). Measurements of other samples are used to illustrate specific effects, these are clearly marked in order to prevent a mix-up of data.

The sample was cleaned with isopropanol and aceton for 10 minutes each, in an ultrasonic bath. Afterwards it was oxidized and freed from carbon contaminations in H_2SO_4: H_2O_2=2:1 for 15 minutes, followed by a 10 minute oxide removal step in 40% hydrofluoric acid. See box for the concentrations. After the last etching step, the sample was rinsed with milipore water, dried under nitrogen, mounted on the required sample holder and then introduced into ultra high vacuum (UHV) at the DAISY Fun system within five minutes of the last rinse.

Once there, an XPS measurement was performed. Because some fluorine contamination was detected the sample was then stored in a buffer chamber (at 2×10^{-8} mbar) for three hours, until the fluorine was desorbed. Afterwards angle resolved XPS measurements were performed in order to get a better understanding of the 3C SiC XP spectrum, especially the distinction between surface and bulk species. For this the electron take of angle ω between the surface normal and the detector was varied from 0° to 80°.

For further information on the measurement setup, see chapter 3.

4.3 Results and Discussion

The first measurement performed as part of an XPS analysis is usually a survey spectrum. This is a sensitive (high pass energy), low resolution scan over a large binding energy range. While the low resolution prevents more precise analysis, it does give a good overview of the elemental sample composition and allows the identification of interesting energy ranges to be examined in more detail.

Chemicals Used

H_2SO_4, 96%: VLSIn grade (BASF)
H_2O_2, 31%: VLSIn grade (BASF)
HF, 40%: reag. ISO, reag. Ph. Eur. (Sigma Aldrich)

Sample Nomenclature

In general sample nomenclature in this work will be $\mathbf{A}^{\mathbf{C}}_{\mathbf{B}}$, where

- **A** gives information on the sample **origin or properties** (poly or single domain etc.)
- **B** gives information on the sample **preparation** (cleaning or etching recipe etc.)
- **C** indicates how it was **treated afterwards** (annealed, before of after electrochemical treatment etc.)

The sample discussed in this chapter is $\mathbf{3C_{pir,HF40\%}}$. It is one of multiple samples used to investigate the influence of various etching recipes on surface properties discussed in the next chapter 5.

Elemental electron core level positions do not vary more than a few eV with changes in their oxidation state. In most cases, this allows a clear identification of the elements present. For some element combinations there will be superpositions of different core level peaks (for example the carbon 1s and the ruthenium 3d peak are both located around 284 eV). While this makes the interpretation more difficult it can usually be overcome by using more than one peak per element, or using reference samples with known compositions.

In figure 4.1 the XPS survey spectrum of chemically etched 3C SiC ($3C_{pir,HF40\%}$) is displayed. To the right (at lower binding energies) there are three dominant peaks. These are from electrons of the 2p (101 eV) and 2s (152 eV) shells of silicon, as well as the 1s (283 eV) shell of carbon. Those two ele-

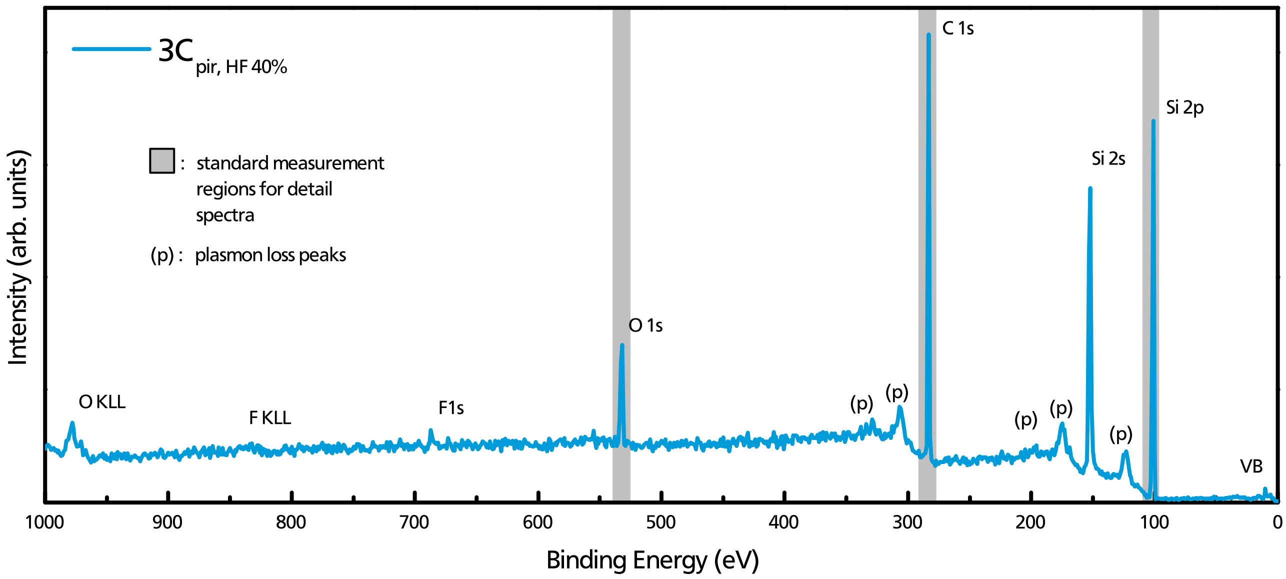

Figure 4.1.: *XPS survey spectrum of chemically etched 3C SiC. From left (high binding energies) to right (low binding energies) the following peaks can be observed: oxygen Auger peak (O KLL) at approx.* 978 eV, *fluorine Auger peak (F KLL) at approx.* 842 eV, *fluorine core level peak (F 1s) at approx.* 687 eV, *oxygen core level peak (O 1s) at approx.* 532 eV, *carbon core level peak (C 1s) at approx.* 283 eV, *silicon core level peak (Si 2s) at approx.* 152 eV, *and silicon core level peak (Si 2p) at approx.* 101 eV. *This spectrum was chosen because there is a fluorine contamination. Normally this should be prevented.*

ments are to be expected in silicon carbide. Each of the peaks displays some plasmon loss features. As only one peak per element is needed for characterisation the Si 2s peak will not be discussed further in this work.

To higher binding energies there are the core level emissions of the oxygen 1s shell (532 eV), and the fluorine 1s shell (687 eV). The oxygen is part of a silicon/carbon oxide termination layer discussed further below and in the next chapter.

This sample was selected especially due to the fluorine contamination, a residue of the hydrofluoric acid (HF) etching procedure, in order to demonstrate where the peak would be located. Normally this kind of contamination can be avoided. But apparently the standardized rinsing procedure was not sufficient to remove the contamination for this etching recipe. However, the amount of fluorine on the sample is very small (0.5 atomic percent), and UHV storage for 3 hours was sufficient for the fluorine to desorb.

Even further to the left the KLL Auger lines of fluorine and oxygen can be observed. They were not employed for evaluation in this work, and will not be mentioned further. Assuming there are no unexpected contaminations, charging effects or other reasons to abort the experiment the survey spectrum is then used to select the desired energy ranges (regions) for the detail spectra. In pure 3C SiC, those are the areas around the O 1s, C 1s and Si 2p core level lines. They have been highlighted with a grey background in figure 4.1.

For a detail spectrum the measurement resolution is increased to 0.05 eV steps. The pass energy is set to a lower values, allowing a better resolution of peak shapes, but consequently decreasing the intensity, and therefore the signal to noise ratio. To counteract this, multiple measurement cycles are performed instead of one single measurement. Averaging over the data from all cycles is then used to reduce the impact of background noise. Most detail spectra in this work will be the result of 10 to 20 cycles.

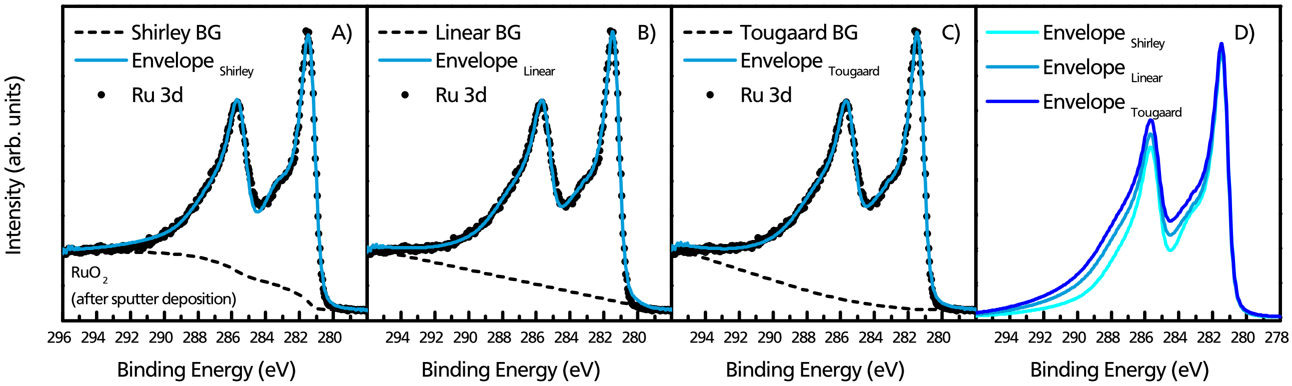

Figure 4.2.: *XPS Ru 3d detail spectra of sputter deposited* RuO_2 *on 3C SiC as example of the background influence on fitting procedures. The three most common background functions: A) Shirley, B) Linear and C) Tougaard were used for fitting the spectra, and the resulting variations of the envelope are displayed in D). The Tougaard background only uses the displayed region instead of the required approx.* 50 eV *and will therefore not be entirely correct.*

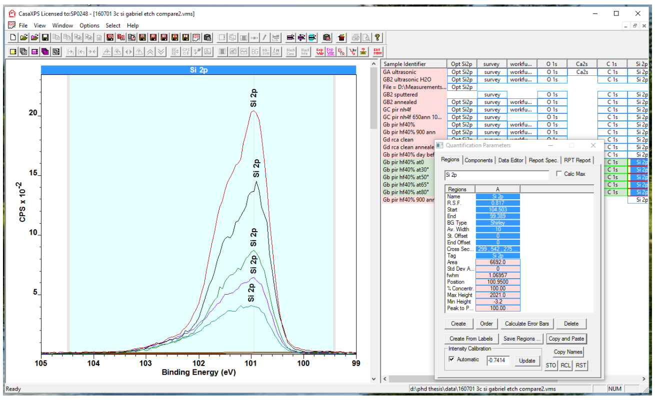

Figure 4.3.: *Screenshot of the CasaXPS [88] software while working on the evaluation of the Si 2p regions for the angle resolved measurements.*

For XPS data evaluation the CasaXPS [88] software was employed, see figure 4.3 for a screenshoot. Before any meaningful evaluation can take place the sample has to be ’fitted’. This process can be divided into the following sub-steps:

1. Definition of a region, the area of interest for evaluation. Peaks or features outside of these regions will not be considered during the evaluation.

2. Selection of the appropriate background function. Inelastic electron scattering can result in a background intensity that is significantly increased to higher binding energies of an emission line [70]. In this case the choice of background can influence the component areas and thus the resulting envelope. The three most common backgrounds (Shirley, Linear and Tougaard, see ’XPS Backgrounds’ box) are displayed in figure 4.2 A) to C) for a Ru 3d line (RuO_2), which will reappear in chapter 9. As can be seen in D) they do result in different envelopes. For 3C SiC the intensity difference is negligible and the choice of background therefore less problematic [70], see figure 4.4 D) to F) If not mentioned otherwise Shirley backgrounds are employed for data evaluation in this work.

3. Creation of artificial line shapes, so called components, in order to model the measured spectrum. The component properties are then used for further evaluation. As a result of the uncertainty principle the basic component line shape is a Lorentzian, where the line width is determined by the core hole state lifetime [89, 90]. Temperature and the impact of analyser and x-ray source result in a additional Gaussian broadening of the line shape [69]. Therefore most peaks are fitted with an adequate number of Voight functions, a convolution of a Gaussian with

a Lorentzian [69, 91, 92]. However, loss process related asymmetric peak shapes (as are common in metals) might require the addition of a tail function.

4. Determining the right amount of components. As enough components allow a perfect fit for any line shape one has to be careful in selecting the appropriate number of spectral species and thus obtain physical valid information. In the most simple case a clean material, where all atoms are in the same oxidation state (they are the same species) should only need one component. If there are more than one species, like bulk and surface, or different chemical environments, more components are necessary. The same is true for doublet splitting, where two components are needed, or for transition metals, whose complex line shapes might require a multitude of components.
5. Adding restraints. Some components have specific relations to each other. For example: It is known that the Si 2p peak is divided into the j=3/2 and j=1/2 species (doublet splitting). Those are 0.6 eV apart, should display a similar full width half maximum (FWHM), and the area ratio is 2:1.

As mentioned above, correct identification of the species present can be tricky. One possibility to help distinguish between surface and bulk species are angle resolved XPS measurements. With increasing take off angle ω the electrons path through the surface layer on its way to the detector is increased. This results in an increase of surface sensitivity with increasing ω. Observing how the peak shape changes with ω allows to distinguish between surface and bulk species.

Figure 4.4 A) to C) shows the relevant detail spectra from the three standard regions - O 1s, C 1s, and Si 2p - of $3C_{pir,HF40\%}$ taken at five different take off angles ω, once all fluorine had desorbed. Spectra D) to F) show the ω=0° measurement with the components and their designation.

XPS Backgrounds

Linear: Easy to implement but physically unrealistic, a linear background results in large errors and should only - if at all - be used if the background is much smaller than the peak.
Tougaard: Valid physical foundation, but requires a region of about 50 eV to higher binding energies of the peak for proper implementation. Thus not frequently used.
Shirley: Based on the assumption that the background results from inelastic electron scattering. Its intensity is therefore related to the peak intensity. No real physical foundation, but sufficiently accurate for most experimental purposes.
For more information on XPS backgrounds see reference [69].

Si 2p region - Due to the doublet splitting this peak is broader than one would expect, see figure 4.4 F). In order to make the ω induced changes more obvious the Si 2p spectrum in figure 4.4 C) was processed by subtracting the j=1/2 components from the measurement data. The effect of this subtrac-

Normalisation Of XPS Peak Intensities

If not mentioned otherwise the **O 1s** and **C 1s** regions in all plots were **normalized** with regard to the **Si 2p** region.
In case of multiple measurements, as in figure 4.4 A) to C) this will be done for each measurement independently. O 1s and C 1s (ω=0 °C) are normalized with regard to Si 2p (ω=0 °C), O 1s and C 1s (ω=30 °C) with regard to Si 2p (ω=30 °C), and so on.

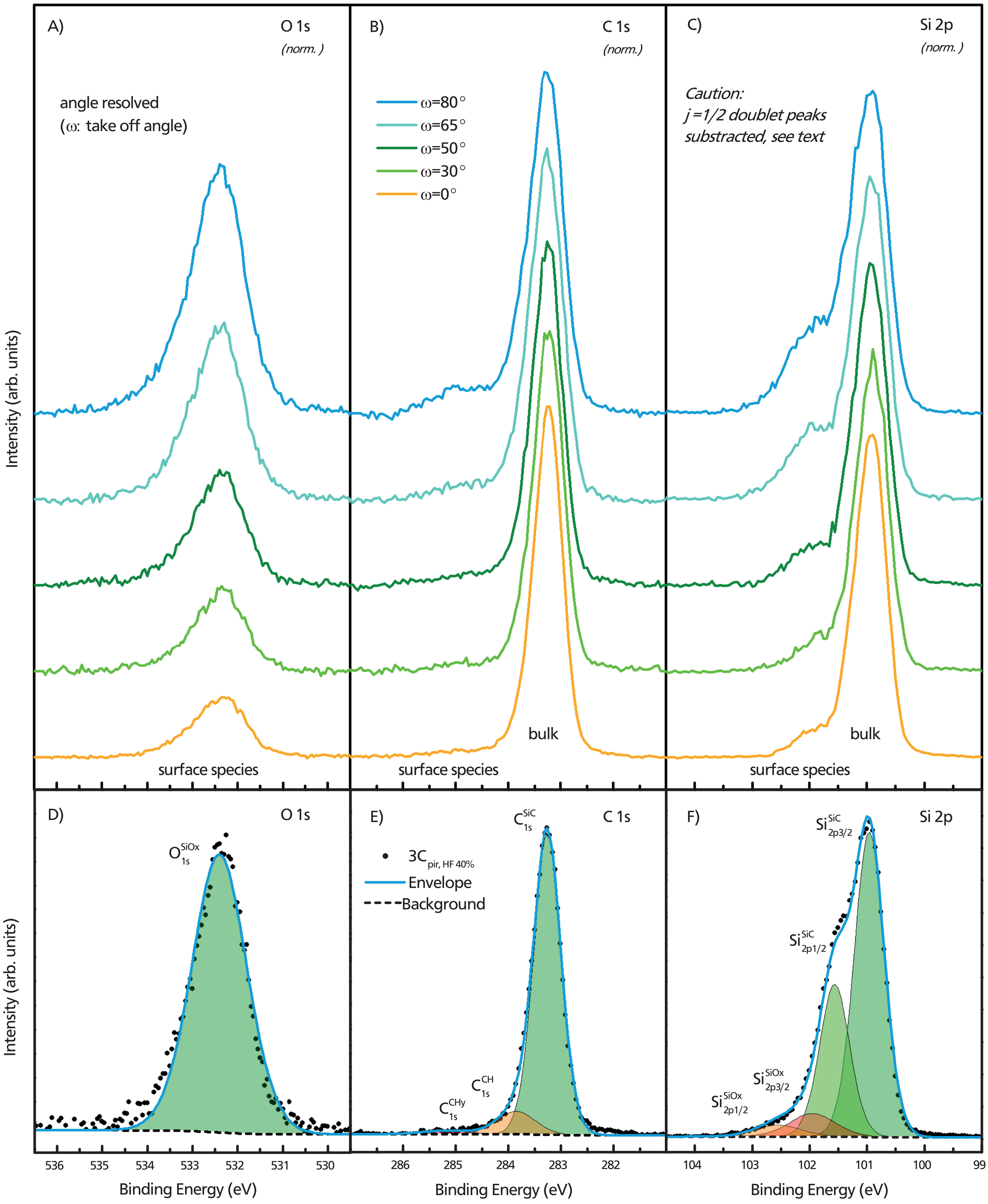

Figure 4.4.: *XP detail spectra of $3C_{pir,40\%}$ O 1s, C 1s and Si 2p regions. A) to C) are angle resolved XPS measurements, where the take of angle ω is the angle between the surface normal and the direction of the detector. A) and B) are normalized with regard to C). C) In order to better show the changes with increasing ω the $Si^{SiC}_{2p1/2}$ and $Si^{SiOx}_{2p1/2}$ components were subtracted from the measurement data. D) to F) display the components employed for fitting the ω=0° detail spectra (colored areas), and the resulting envelope (blue) in comparison to the measurement data (black scatter). Each of the three lower regions is normalized independently.*

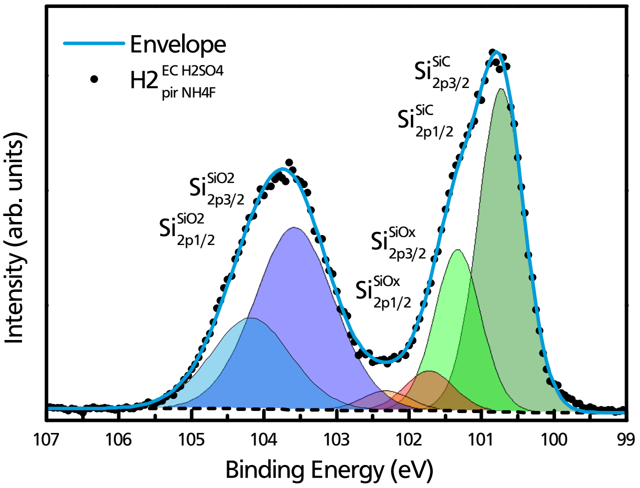

Figure 4.5.: *Si 2p XPS detail spectrum of single domain 3C SiC, after prolonged electrochemical measurements in H_2SO_4 at elevated bias potentials, shows the formation of a SiO_2 layer.*

tion on the line shape is obvious if one compares the ω=0° from C) with F) as both show the same dataset.

There are clearly two different areas in this region. The peak to the right, at 100.96 eV, retains its shape and diminishes in relation to the surface species in the O 1s region. One can therefore assign it to a bulk species, or more precisely the silicon carbide species. Literature provides values from 100.3 to 103.6 eV [93–95] for the 3C SiC $Si^{SiC}_{2p3/2}$ component. As doping concentration, purity or surface termination vary or are not mentioned the wide margin of values is not surprising. But the more recent works on better defined (n-type) samples tend to be around 100.9 to 101.3 eV [94, 95], which is in excellent agreement with this data.

On the other hand there is a strong increase of intensity in the range from 101.5 to 103 eV. Its shape is in good agreement with a single broad species (FWHM of 0.94 to 1.15 eV compared to 0.61 to 0.71 eV for the SiC species), at +0.99 relative to $Si^{SiC}_{2p3/2}$. As this species is shifted to higher binding energies, the respective silicon atoms carry a bigger positive partial charge compared to the SiC bond. Because the only other element present is oxygen the species could either be a silicon carbide compound where the silicon would be bound to one or more other silicon atoms instead to the four carbon atoms, or a silicon-oxide compound. Silicon has a electro negativity of 1.9 compared to 2.55 for carbon. Silicon atoms in a carbon depleted SiC ($SiC_{z<4}$) compound would therefore have a lower partial positive charge then the bulk SiC, and should thus shift to lower binding energies, which is obviously not the case here. Therefore the species has to be some kind of silicon oxide (SiO_x) compound. However, being more specific to the values of x in SiO_x is difficult.

The presence of silicon dioxide (SiO_2) can be excluded, as this peak would be located at higher binding energies around 103.58 eV or +2.88 eV in relation to $Si^{SiC}_{2p3/2}$. See figure 4.5 for the measurement of a single domain 3C SiC sample with a strong SiO_2 component. The SiO_2 formation was the result of prolonged electrochemical measurements in H_2SO_4 at high bias potentials. A binding energy value of 103.58 eV is in good agreement with previous results [93, 94, 96].

Besides silicon dioxide there is little information on other silicon oxide species on the SiC surface. Wheeler mentions 'suboxide' between the SiO_2 and SiC component [93], whereas Iwanowski and Arnault talk of a SiO_x species around 101.8 eV [97, 98]. The properties of the SiO_x component will be further elaborated on in the next chapter.

In conclusion the Si 2p region of 3C SiC is fitted with four to six components: $Si^{SiC}_{2p3/2}$, $Si^{SiC}_{2p1/2}$, $Si^{SiOx}_{2p3/2}$, $Si^{SiOx}_{2p1/2}$, and if required $Si^{SiO2}_{2p3/2}$, and $Si^{SiO2}_{2p1/2}$. See figure 4.4 F).

C 1s region - Similar to the Si 2p region the main peak at 283.25 eV does not change shape with increasing ω. It can be tagged as the silicon carbide bulk component C^{SiC}_{1s}. Previous works state the C 1s 3C SiC position in the range from 282.7 to 286.1 eV [93–95, 99, 100]. But the more recent works on better defined (n-type) samples tend to be around

283.1 to 283.3 eV [94,95], and thus in good agreement with the observed value.

In the range from 284 to 286 eV increased surface sensitivity and the resulting higher surface sensitivity reveal two surface species. The first is located at 285.2 eV and represents some kind of hydrocarbon contamination. As the exact nature of the hydrocarbon is unknown it will be denoted as $\mathrm{CH_y}$. Similar binding energies for hydrocarbon contaminations were reported by Kusonoki [94] for 3C SiC grown on silicon via C_2H_2 beam, and - in relation to the C_{1s}^{SiC} component - by Wee for 3C SiC grown via CVD [99].

Annealing at 900 °C for 10 minutes performed on a similarly prepared sample, presented in the next chapter 5, does not significantly change intensity or position of the second component (the first one disappears). It can be concluded that this second component is not some adsorbate, otherwise it would evaporate at such elevated temperatures under UHV conditions. Due to the (001) orientation of the 3C SiC sample one would expect an equal amount of silicon and carbon atoms in the surface layer.

Therefore the second component, located at 283.67 eV or +0.43 eV is attributed to the surface carbon atoms from the uppermost SiC layer. To the best of the authors knowledge there is no discussion of this species in the literature for (001) 3C SiC. This is probably a result of higher hydrocarbon contaminations superimposing it. In a first attempt it was attributed to a bridging C-O bond, however this interpretation contradicts the 1x1 surface termination witnessed in LEED patterns.

The nature of this bond will be discussed in more detail in the following chapter 5. However, it can be summed up as: HREELS measurements of surface vibrations and the observed atomic ratios for the elements present in combination with the 1x1 surface structure lead to the conclusion that the second component is the result of a C-H bond.

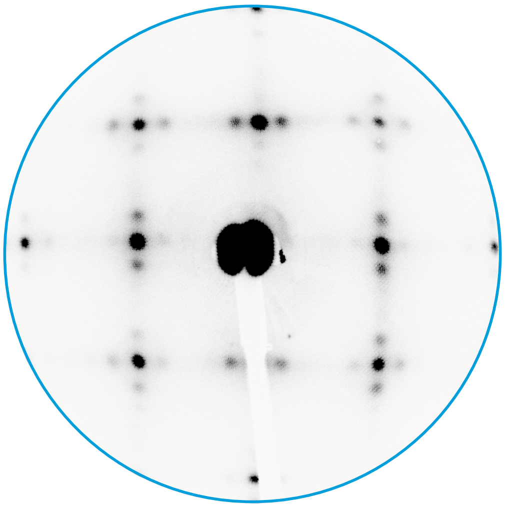

Figure 4.6.: *This LEED pattern of the chemically etched 3C SiC sample* $3C_{pir,HF40\%}$ *shows a 1x1 surface reconstruction with spot splitting as result of disorder in the adsorbate layer. The pattern was taken at* 120 eV.

A similar surface species at $+(0.47 \pm 0.02)$ eV was reported by Seyller [101] for the carbon phase of 6H SiC in case of a hydrogen termination as result of high temperature annealing in ultra pure hydrogen.

Strong surface oxidation of the sample, as in case of $H2_{pir\ NH4F}^{EC\ H2SO4}$ mentioned above for the Si 2p region in figure 4.5, results in the disappearance of the C_{1s}^{Si3CH} species. This kind of treatment thus produces a surface layer entirely made up of $\mathrm{SiO_2}$. In conclusion the C 1s region of 3C SiC is fitted with three components: C_{1s}^{SiC}, C_{1s}^{CH}, and C_{1s}^{CHy}. See figure 4.4 E).

O 1s region - Contrary to the other two regions there is only one broad peak in the O 1s region of the HF etched 3C SiC, see figure 4.4 A). With increasing take of angle ω the intensity of the whole peak grows in relation to the bulk components of C 1s and Si 2p, while retaining the same line shape. This shows that all oxygen present is evenly distributed on the sample surface. Therefore there is no bulk oxygen species.

As most publications on the investigation of 3C SiC with XPS focus on the C 1s and Si 2p regions no reference binding energies for the O_{1s}^{SiOx} component can be provided. In conclusion the O 1s region of 3C SiC is fitted with a single Voigt component: O_{1s}^{SiOx}, which results in a good fit. See figure 4.4 D). Once this model holds (the data is 'fitted'), one can get started on the interpretation. For example: The x in SiO_x can be determined from the corrected component area ratio O_{1s}^{SiOx}:Si_{2p}^{SiOx} to x=0.99. Each surface silicon atom thus has one oxygen atom counterpart, a silicon hydroxide termination.

Considering the whole sample, the termination has therefore to be a mixture of silicon hydroxide Si—OH and carbon hydrogen C—H. The hydrogen in both species can not be observed as hydrogen does not produce a core photoelectron peak. This surface model is in good agreement with the 1x1 termination observed in the LEED pattern. The discussed fitting procedures species identities will be taken as given in the following chapters.

5

Sample Preparation Procedures - Wet Chemical Etching

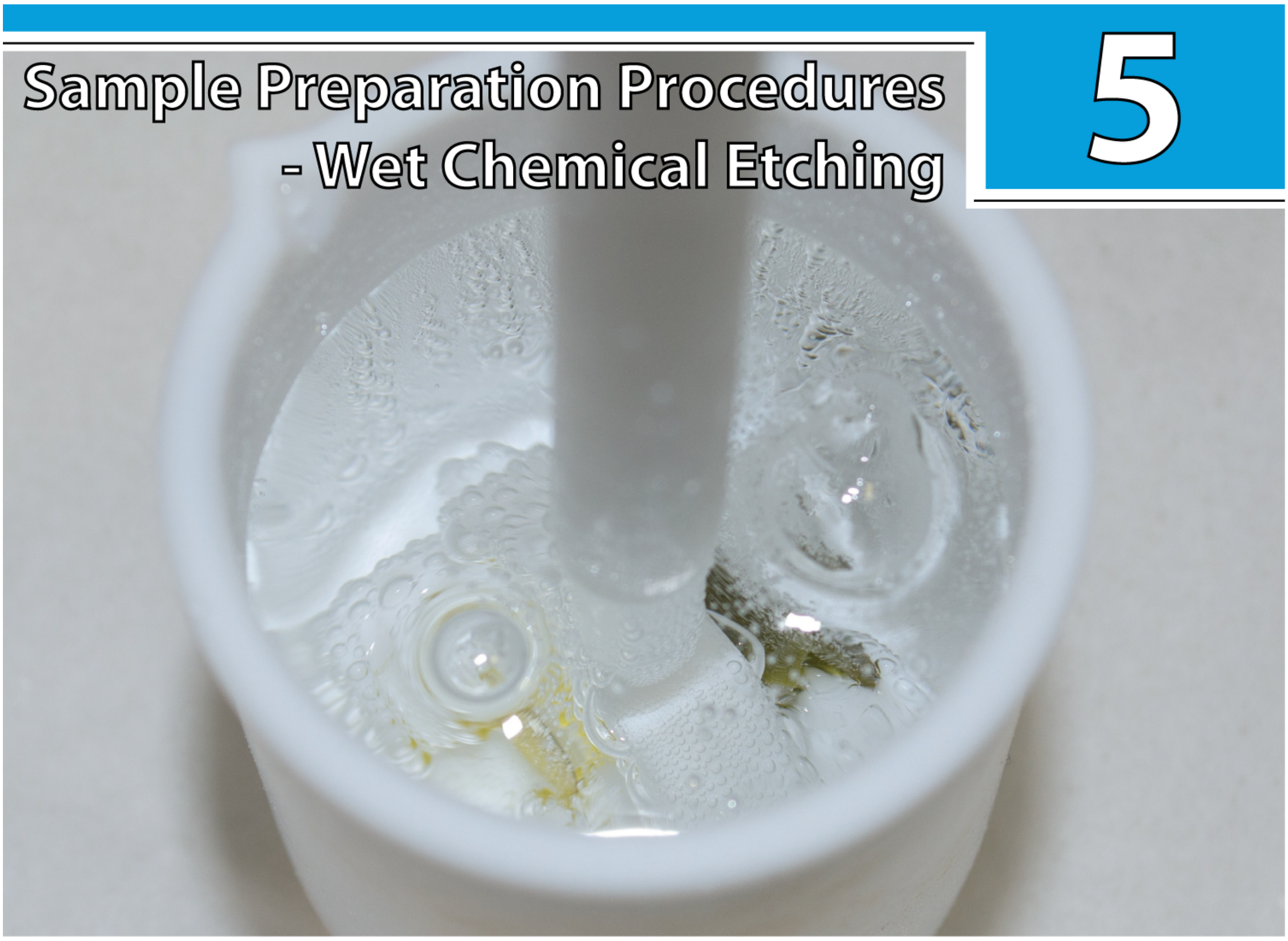

This chapter is mostly focused on wet chemical etching of cubic silicon carbide (3C SiC). The 3C SiC surface properties resulting from the three most promising etching procedures are discussed and compared to an un-etched, and an Ar ion sputtered sample. The employed methods are XPS, LEED and HREELS. In the context of this work wet chemical etching is mainly used for two purposes: First, sample preparation in order to ensure similar sample surface properties on all samples used for UHV and electrochemical measurements, thus ensuring maximum comparability. Second, due to the very limited sample supply (3 single domain samples from Hoya, and each poly crystalline sample is unique) many of the samples had to be used for multiple experiments.

5.1 Introduction

Chemical etching is a widely used technique for sample preparation. It is employed for the removal of hydrocarbons and/or metal traces, the reduction of growth or polishing induced surface roughness, or in producing specific surface terminations [102].

For silicon carbide (SiC) in general different surface preparation methods have been investigated in great detail. From the oxide strip in pure HF [103], HF mixtures like HF:NH_4F:NH_3OH [104], to the standard RCA procedure followed by an oxide removal step in 7:1 NH_4F:HF [105, 106], or an aqua regia etch (about 1:3 HNO_3:HCl) with subsequent HF and NH_4F steps [107, 108], a lot of different methods were tried and the resulting surface properties carefully analysed.

However most of the studies mentioned above are focused on the hexagonal 6H SiC polytype. As, at the time most of the studies were performed, 6H SiC was close to making it to the commercial level for high power electronics, the focus was very understandable. And successful too, as 6H SiC high power electronics are nowadays commercially available.

Research was mainly focused on the polar surfaces with silicon (0001) or carbon ($000\bar{1}$) termination. Most results agreed on the fact that oxide removal via wet chemical etching (with or without previous oxidation step) does not result in an oxide free surface termination. But UHV annealing at temperatures above 900 °C results in oxygen desorption (and possible silicon depletion or graphite formation). If possible, the annealing should be performed under silicon or hydrogen flux, the first being supplied via separate resistive heating or an e-gun evaporator [109, 110]. The resulting surface is oxide free and can, depending on the method used, display a number of different surface recombinations, where $\sqrt{3}\text{x}\sqrt{3}$ is most common.

In general the cubic 3C SiC polytype was investigated less thoroughly than its hexagonal counterparts. Similar to 6H SiC, the relations between surface reconstruction patterns and the annealing temperature (under silicon flux) were studied quite extensively [109–114], while different wet chemical etching procedures are rarely compared.

However, this work is on 3C SiC for direct photoelectrochemical water splitting. Most of the required experiments will be performed ex situ. On top of that, the samples will be in contact with a number of electrolytes for varying durations, possibly while exposed to bias potentials and illumination. While it is not even clear whether or how long an oxide free SiC surface reconstruction would survive ex situ, it is highly unlikely that it would withstand such a treatment for any meaningful amount of time.

As the goal of the surface preparation with regard to further experiments is mainly to provide a clean and reproducible surface, there is little sense in undertaking the extra effort necessary to produce oxide free surfaces. Especially taking into account that many of the performed measurements will be in contact with liquid electrolytes, where a re-oxidation to some degree will occur. UHV annealing can therefore not be the method of choice. Purely wet chemical preparation methods on the other hand are interesting as the are relatively fast and easy to handle. Indeed, a thin, reproducible and well defined oxide layer would have the benefit of being stable in air, thus making the exact timing of ex situ experiments with regard to the sample etching less critical.

The goal for this section, is therefore not to find or affirm a preparation path for a pure SiC surface, but instead find a reliable way of producing reasonable clean and reproducible sample surfaces in order to ensure comparability in the electrochemical experiments. Additionally, it would be of great benefit to keep the preparation routine as simple and fast as possible. Because previous works don't give a lot of information on the sample properties before the UHV annealing steps, this section will present a number of (mostly) wet chemical etching procedures. The resulting surface terminations and properties will be discussed, as will the reasoning behind picking one specific procedure for sample preparation in the context of this work.

5.2 Experimental Procedure

As in the previous chapter, all experiments were conducted on pieces of a two inch (001) 3C SiC on silicon wafer, liberally supplied by Gabriel Ferro (LMI Lyon). The samples were cleaned in an ultrasonic bath for 10 minutes in isopropanol and aceton respectively. Subsequently different etching recipes were applied, see below. Between each step the samples were rinsed with milipore water.

Great care was taken to prevent any kind of contamination. The cleaning was performed in glass beakers, which were cleaned with acetone and isopropanol beforehand. All etching steps were performed employing PTFE beakers, pincers and sample holders, which were previously cleaned with piranha solution (H_2SO_4:H_2O_2=2:1). If not mentioned otherwise all steps were performed at room temperature. After the last etching step, the sample was rinsed with milipore water, dried under nitrogen, mounted on the required sample holder and then introduced into ultra high vacuum (UHV) at the DAISY Fun system within five minutes of the last rinse. Preparation procedures were as follows:

- $\mathbf{3C_{cleaned}}$ - only the above mentioned acetone/isopropanol cleaning was performed.
- $\mathbf{3C_{pir,NH4F}}$ - the sample was oxidized and freed from carbon contaminations in H_2SO_4: H_2O_2=2:1 (piranha) for 15 minutes, followed by a 10 minute oxide removal step in NH_4F.
- $\mathbf{3C_{pir,HF40\%}}$ - piranha etch was followed by a 10 minute oxide removal step in 40% HF.
- $\mathbf{3C_{RCA}}$ - the standard RCA cleaning procedure was employed. First, a 10 minute organic and particle cleaning step in NH_4OH: H_2O_2:H_2O=1:1:5 at 80 °C. Second, a 10 second oxide removal step in 5% HF. Third, a 10 minute ionic cleaning step in HCl:H_2O_2: H_2O=1:1:5 at 80 °C. Fourth, a 10 second oxide removal step in 3% HF.
- $\mathbf{3C_{sputter}}$ - $3C_{cleaned}$ was sputtered with argon ions for 10 minutes in the XPS chamber of Daisy Fun, base pressure $p_{XPS} = 5 \times 10^{-10}$ mbar. The sputtering was performed with 99.999% pure argon, at 5×10^{-6} mbar, 10 mA ion current and 1 kV acceleration voltage.

After introduction to the integrated system, the samples were characterised by photoelectron spectroscopy (XPS), low energy electron diffraction (LEED) and in one case high resolution electron energy loss spectroscopy (HREELS). Further information on the measurement setup and parameters is supplied in chapter 3.

Chemicals Used

H_2SO_4, 96%: VLSIn grade (BASF)
H_2O_2, 31%: VLSIn grade (BASF)
HCl, $\geqslant$ 37%: TraceSELECT (Sigma Aldrich)
HF, 40%: reag. ISO, reag. Ph. Eur. (Sigma Aldrich)
HF 5%: VLSI Selectipur (BASF)
HF 3%: diluted from 40% HF
NH_4F, 40%: semiconductor grade VLSI Puranal (ALDRICH)
NH_4OH, 28-30%: ACS grade (Sigma Aldrich)

Once the characterisation was completed all samples (except $3C_{cleaned}$, as it was sputtered to produce $3C_{Ar\ sputtered}$) were then annealed for 10 minutes. Annealing was performed via electron impact heating in the buffer chamber, which had a base pressure of $p_{buffer}=2 \times 10^{-8}$ mbar. The Temperature was determined via an IMPAC IS 120 pyrometer focused on the molybdenum sample holder. Subsequently the previous measurements were repeated. In the sample nomination annealed samples will be tagged with an elevated 900 °C as in $3C^{900\,°C}_{pir,HF40\%}$, indicating the annealing temperature.

5.3 Results and Discussion

This section deals with the surface properties produced by the presented procedures. The survey spectra of the discussed samples are displayed in figure 5.1. Overall appearance is similar to the 3C SiC spectrum discussed in the previous chapter 4, with oxygen, carbon and silicon being the only or dominant elements present. However some disparities are observed as well.

$3C_{sputtered}$ shows a reduced oxygen content and implanted argon (Ar 2p at 242 eV) from the sputtering process.

$3C_{pir\ HF40\%}$ features a small fluorine contamination (F 1s at 686 eV). Apparently the applied rinsing

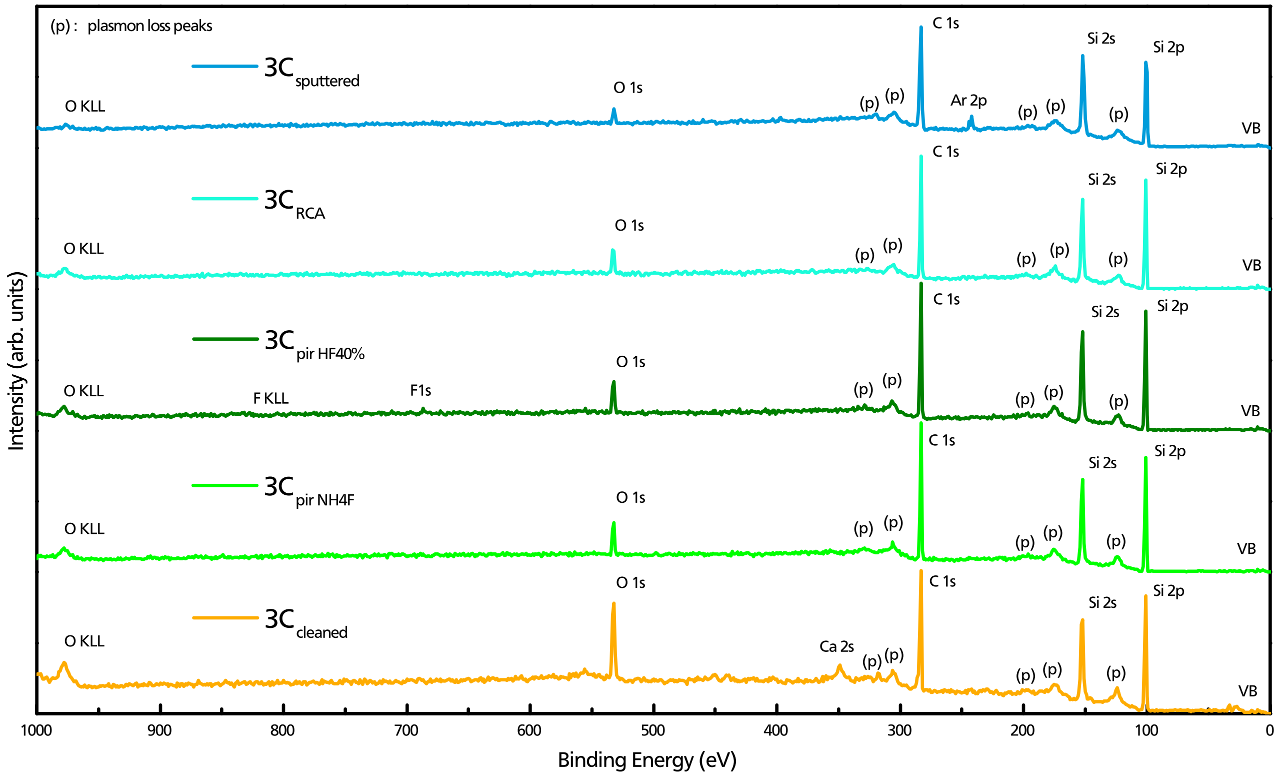

Figure 5.1.: *XPS survey spectra of the five discussed samples.* $3C_{sputtered}$*: shows the lowest oxygen content and embedded Ar from the sputtering.* $3C_{RCA}$*: no contaminations.* $3C_{pir\,HF40\%}$*: small fluorine contamination.* $3C_{pir\,NH4F}$*: no contamination.* $3C_{cleaned}$*: calcium and hydrocarbon contamination.*

procedure is not sufficient for removing all fluorine.

$3C_{cleaned}$ displays a much stronger oxygen peak and calcium contamination (Ca 2s at 349 eV). As the milipore water used in the cleaning procedure was highly pure, this has to be some older contamination that acetone, isopropanol and milipore water could not remove completely.

$3C_{RCA}$ and $3C_{pir\,NH4F}$ both show the desired behaviour, with no contaminations and a roughly similar amount of oxygen.

For a more detailed discussion detail spectra of the O 1s, C 1s and Si 2p regions recorded for the five samples prior and post annealing are presented in figure 5.2. The annealing was performed for two reasons. First, in order to evaluate whether some part of the O 1s and C 1s signals is due to adsorbates, which should at least partially desorb at elevated temperatures. Second, as part of the back contact fabrication process, see next chapter 6, involves an identical annealing process, it seemed reasonable to investigate its influence on the sample surface properties. For evaluation the spectra were fitted with CasaXPS, as discussed in chapter 4. The resulting peak positions and full width half maxima for the main components are provided for the un-annealed samples (full lines).

Wet Chemically Etched - $3C_{pir\,NH4F}$, $3C_{pir\,HF\%}$, and $3C_{RCA}$ are the three wet chemically etched samples. The surfaces of the wet chemically etched samples $3C_{pir\,NH4F}$, $3C_{pir\,HF40\%}$, and $3C_{RCA}$ are very clean, especially considering that they were prepared ex situ. Apart from the fluorine contamination in $3C_{pir\,HF40\%}$ there are no elements besides oxygen, carbon and silicon to be found. At perpendicular take off angle ω the C 1s region displays very weak organic contamination species, which amount to less then a tenth of a monolayer. Use of the fitting parameters discussed in the previous chapter results in excellent fits for all three datasets

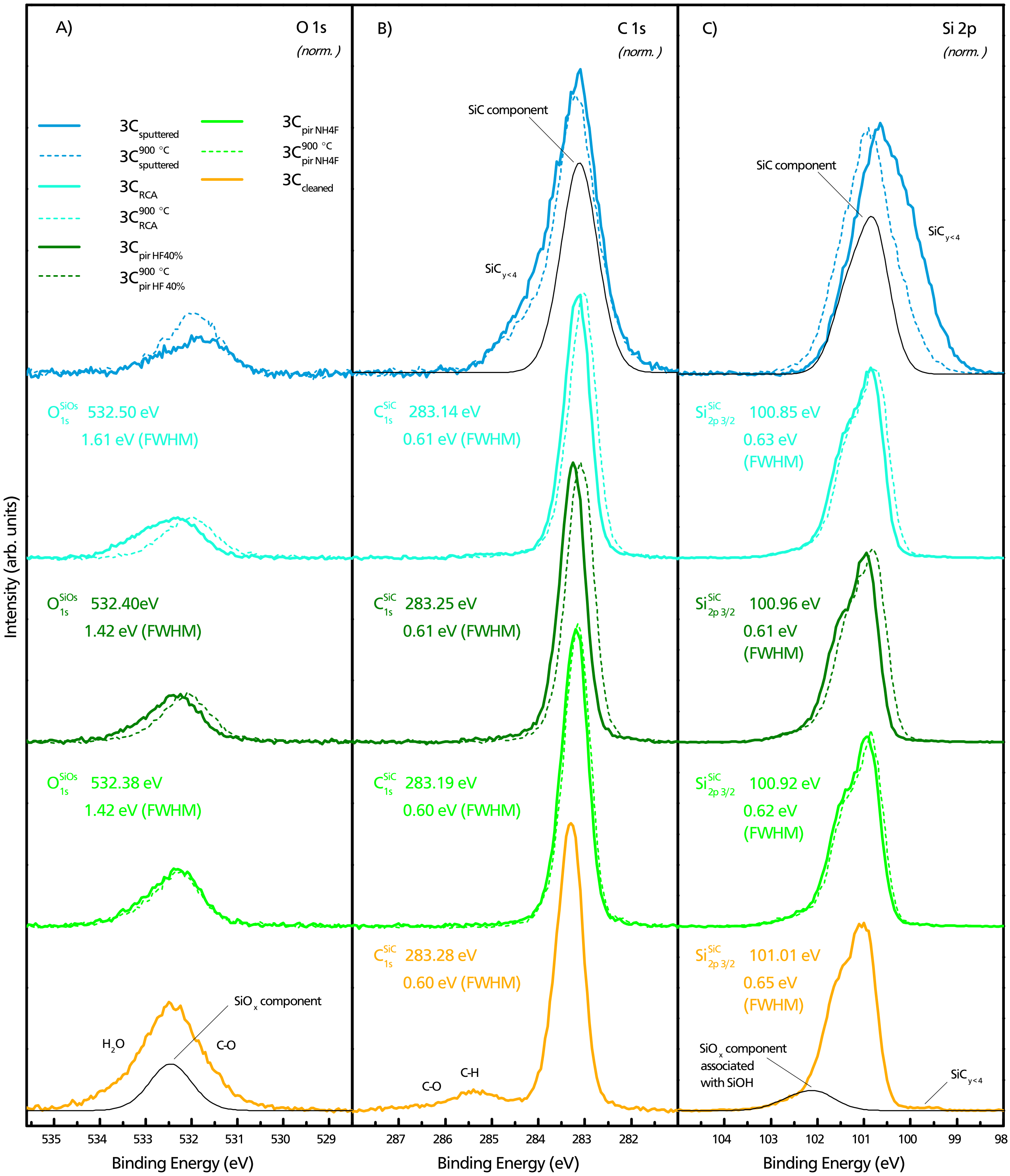

Figure 5.2.: *XP detail spectra of the O 1s, C 1s and Si 2p regions for 3C SiC after five different surface treatments (solid lines). After the XPS measurement all samples (with the exception of* $3C_{cleaned}$*) were annealed. While the subsequent measurements (dashed lines) show no major changes in sample composition, small shifts (about 70 to 350 meV) to lower binding energies occur. The obvious exception being the sputtered sample. Provided positions and FWHMs are for the main components prior to annealing.*

(as well as for the three annealed samples). In the Si 2p region one can observe the silicon carbide bulk Si_{2p}^{SiC} and a silicon oxide surface species Si_{2p}^{SiOH}. There are no traces of SiO_2 on the samples. Taking doublet splitting into account this results in a total of four components for the Si 2p region.

On the other hand the O 1s regions display only one single symmetric peak each. It is assigned to the surface oxide species O_{1s}^{SiOH}. The O_{1s}^{SiOH}:Si_{2p}^{SiOH} ratios of 1.13 ($3C_{pir\,NH4F}$), 0.99 ($3C_{pir\,HF40\%}$), and 1.07 ($3C_{RCA}$) indicate a Si—OH or hydroxide termination for the surface silicon atoms. A superposition of a small contamination contribution not considered in the fit for the O 1s regions of $3C_{pir\,NH4F}$ and $3C_{RCA}$ is the most likely explanation for the ratios greater than unity.

The C 1s regions is made up of the bulk silicon carbide peak C_{1s}^{SiC}, a surface carbon peak C_{1s}^{CH} assigned to SiC surface carbon atoms bound to hydrogen and some very small contributions from organic contaminants. The resulting surface termination would be an alternation of SiOH and CH ligands, where each surface SiC atom is either bound to one hydrogen atom for the SiC carbon or a hydroxide group for SiC silicon.

In order to confirm this, one can take a look at the surface species ratio. As the (001) 3C SiC surface should provide the same number of surface SiC silicon and carbon atoms one would expect the surface species ratio C_{1s}^{CH}:Si_{2p}^{SiOH} to be unity for all three samples. The values of 1.05 ($3C_{pir\,NH4F}$), 1.00 ($3C_{pir\,HF\%}$), and 0.98 ($3C_{RCA}$) are in excellent agreement with this assumption.

Additionally, one can investigate the atomic surface bonds via vibrational absorption losses in High Resolution Electron Energy Loss Spectroscopy (HREELS). The spectrum in figure 5.3 shows the single (FK1) and double (FK2) excitation of Fuchs-Kliewer (FK) surface phonons [115]. While called surface phonons, the FKs are completely determined by bulk properties [116] of ionic crystals. For silicon carbide literature states their positions with ca. (116 ± 1) meV for FK1 and thus ca. 232 meV for FK2, indifferent of the respective polytype [113, 116–118]. This is in good agreement with the determined positions of 116 meV (FMHM is 22 meV) for FK1 and 231 meV (FMHM is 28 meV) for FK2.

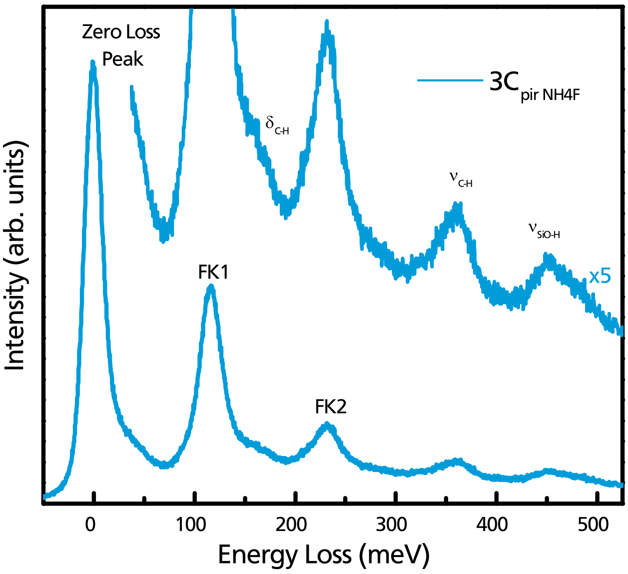

Figure 5.3.: *HREELS spectrum of $3C_{pir\,NH4F}$ shows the single (FK1) and double (FK2) excitation of Fuchs-Kliewer surface phonons for SiC. The presence of ν_{C-H} stretching vibrations, δ_{C-H} bending modes, and ν_{Si-O-H} stretching vibrations gives further evidence on the proposed surface termination.*

Two more sharp absorption features can be observed. The first at 354 meV (FMHM is 29 meV) is in good agreement with the position reported for carbon hydrogen stretching vibrations ν_{C-H} around 353 meV [119, 120]. Corresponding bending modes δ_{C-H} for the C—H bond are frequently reported in the range from 155 to 192 meV [116, 120, 121]. Figure 5.3 exhibits a very broad matching structure in this region The second absorption feature is located at 455 meV (FMHM is 38 meV). This is in excellent agreement with the oxygen hydrogen stretching vibration in the SiO—H bond ν_{SiO-H}, reported in the range of 453 to 456 meV [122, 123].

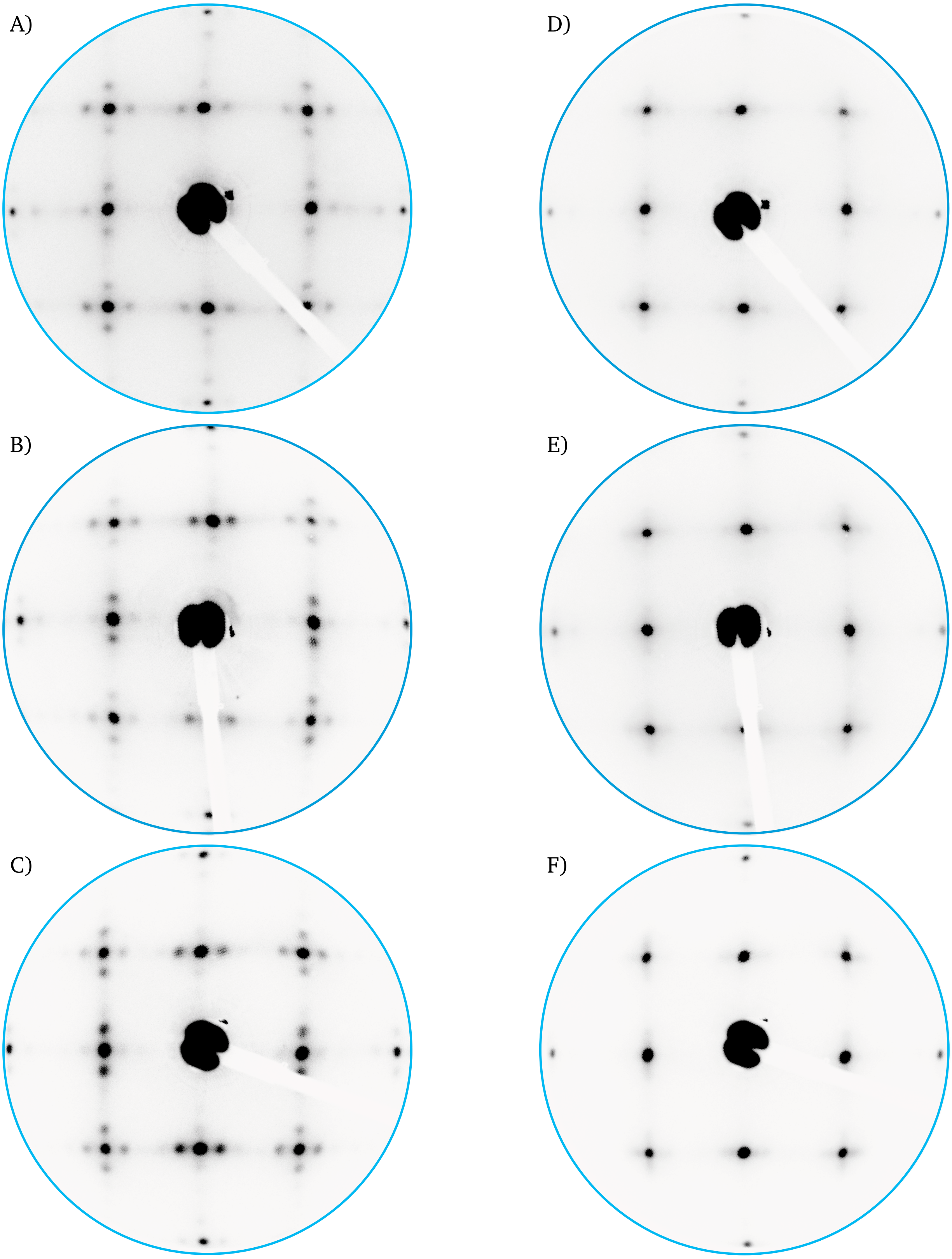

Figure 5.4.: *LEED patterns for wet chemically etched samples A)* $3C_{RCA}$*, B)* $3C_{pir\ HF40\%}$*, and C)* $3C_{pir\ NH4F}$ *before annealing show a 1x1 reconstructed surface pattern with satellite structures accompanying the undisplaced integral spots, indicating a certain disorder in the surface structure. The annealed samples D)* $3C^{900\,°C}_{RCA}$*, E)* $3C^{900\,°C}_{pir\ HF\%}$*, and F)* $3C^{900\,°C}_{pir\ NH4F}$ *show no satellites and should therefore display a much higher degree of surface order. Measurement parameters: beam energy 120 eV, filament current of 2.8 A and a screen voltage of 5 kV.*

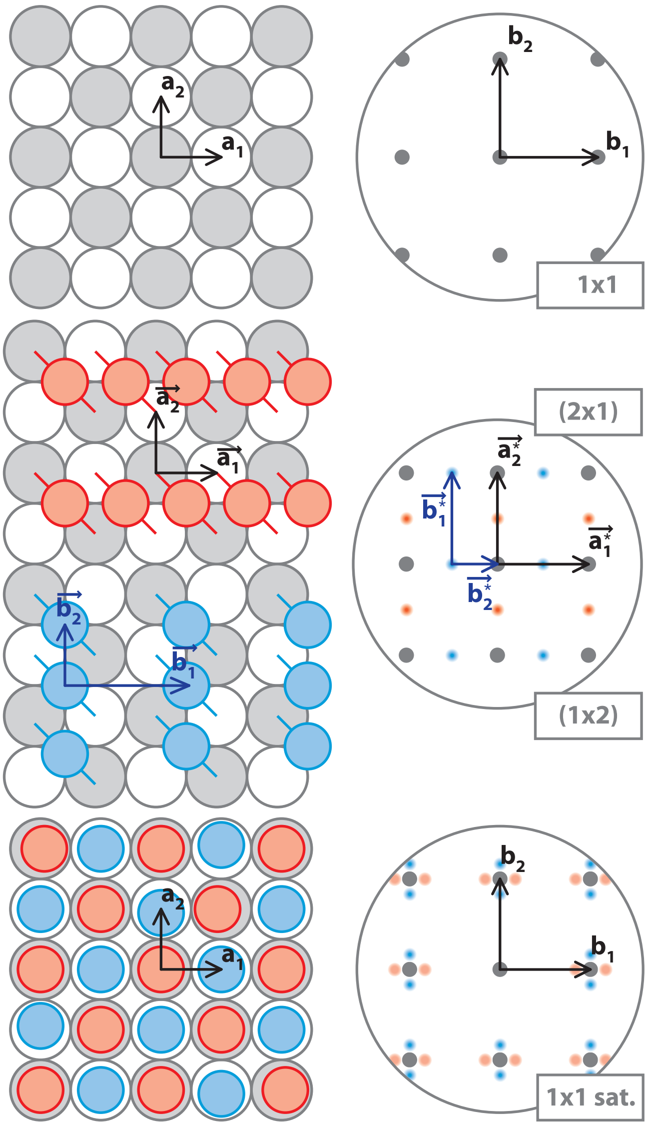

Figure 5.5.: *Relationship between the surface structure (left), also known as direct lattice, and the reciprocal lattice (right) reproduced in LEED patterns [73]. White and gray circles indicate the 3C SiC substrate layer, while the red and blue circles represent the surface atoms. In this case either hydrogen and the hydroxide group or bridging oxide.*

As there are no absorption features for ν_{Si-H} around 259 meV [116, 124], this further confirms the proposed CH/SiOH termination.

Finally one can take a look at the surface reconstruction via low energy electron diffraction (LEED) patterns recorded right after the XPS measurements, see figure 5.4. They look pretty much identical for all three samples, and show a cubic 1x1 recombination surface structure with accompanying satellite spots.

LEED spot splitting of integral-order spots is generally assigned to a certain 'waviness in a surface layer' [73]. Here it most likely indicates a certain mismatch between the 3C SiC substrate and the hydrogen/hydroxide termination layer. The resulting long wavelength buckling gives rise to the satellite spots [73].

Figure 5.5 displays the relation between surface termination and the reciprocal patterns observed via LEED. A surface termination with a bridging oxide would result in a 2x1 / 1x2 surface termination. Comparison of the resulting theoretical LEED patern with those in figure 5.4 shows no congruency, thus further confirming the proposed Si-OH / C-H termination.

Annealing results in the disappearance of the satellite spots, and thus the associated disorder in the surface layer. This goes hand in hand with a reduction of the O_{1s}^{SiOH}:Si_{2p}^{SiOH} ratios to 0.93 ($3C_{pirNH4F}^{650\,^{\circ}C}$), 0.83 ($3C_{pirHF\%}^{900\,^{\circ}C}$), and 0.81 ($3C_{RCA}^{900\,^{\circ}C}$). Furthermore a shift to lower binding energies occurs in all three regions.

It is known, that annealing under UHV conditions is a possible procedure for oxygen removal. For example Johansson et al. reported the complete removal of surface oxygen after annealing a (0001) 6H SiC sample at temperatures of 950 °C and above [106]. As is obvious from the O 1s detail spectra of the annealed samples (dashed lines) in figure 5.2, the performed annealing did not result in a complete removal of oxygen from the surface, but instead a slight reduction. In relation to Si_{2p}^{SiC} the amount of oxygen on the sample post annealing is reduced by 21 % for $3C_{RCA}$, 13 % for $3C_{pir\,HF40\%}$, and 9 % for $3C_{pir\,NH4F}$. However, the last value should be considered with caution, as the annealing temperature was only 650 instead of 900 °C.

The overall peak shapes remain similar pre- and post-annealing. In case of hydrogen terminated

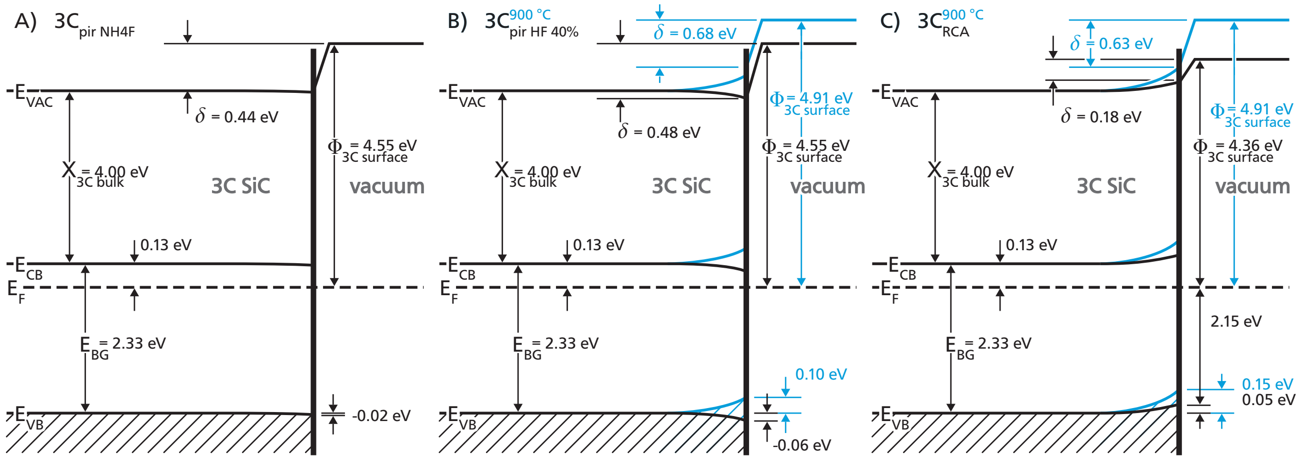

Figure 5.6.: *Band structure diagrams of 3C SiC in a UHV environment directly after wet chemical etching (black) for three different etching procedures A) to C) and the annealing induced changes (blue). The two etching procedures at room temperature A) and b) result in identical surface properties with a slight upward band bending, while the RCA C) procedure results in flat band conditions. However, annealing the samples B) and C) eradicates the differences and increases the surface dipole significantly.*

silicon, the surface termination tends to break down at temperatures around 450 °C and above [125, 126]. A similar breakdown of the CH bonds was not observed, as the component remained stable in spectral shape and intensity.

The XPS measurements in relation with some basic physical properties of 3C SiC allow the construction of band diagrams displaying the 3C SiC/vacuum interface, see figure 5.6. Equations 2.4 and 2.2 yield the distance of 0.13 eV between Fermi level and conduction band minimum $E_F - E_{CB}$ for the bulk 3C SiC with $n_D = 1.1 \times 10^{17}\,\mathrm{cm}^{-3}$. The doping concentration n_D was determined from the Raman spectrum of a sample prepared similarly to $3C_{cleaned}$, see figure 5.7. Because the depth of information for Raman spectroscopy exceeds the epitaxial 3C SiC layer thickness, the spectrum consists of a superposition from the silicon substrate and the 3C SiC Raman signals ($3C_{cleaned}$: blue). A Raman spectrum of a pure silicon sample (Si_{ref}: black) was normalized to the Si main peak at 520.7 cm^{-1} of $3C_{cleaned}$ and subtracted in order to obtain the pure 3C SiC signal, which in turn was used to determine n_D, see section 3.4.

This information was combined with the surface work function $\Phi_{3C\,surface}$, which was determined from the secondary electron edge in figure 5.8 A) and the distance between valence band and Fermi level $E_F - E_{VB}$ from figure 5.8 B). Using $E_{BG} = E_{CB} - E_{VB}$, the later allows a comparison of the measured $E_F - E_{CB}$ from the XPS to the calculated 0.13 eV.

Examination of the resulting band diagrams for the un-annealed samples (black) in figure 5.6 shows that there is no discernible difference in whether NH_4F A) or HF B) was used for the oxide removal. Within the margin of measurement accuracy (0.05 eV) both procedures produce the same band structure. There, both samples display a slight downward band bending of −0.02 to −0.06 eV at the surface, and the hydrogen/hydroxide termination produces a surface dipole δ of 0.44 to 0.48 eV.

As a matter of fact the band bending is so small, that at least for $3C_{pir\,NH4F}$ it makes more sense to speak of a flat band situation. For the surface dipole calculation an electron affinity $\chi_{3C\,bulk}$ of 4.0 eV was assumed, as reported by Philipp [127] and Pelletier et al. [128]. Contrary, the RCA procedure C) results in slight upward band bending of 0.05 eV and a notably lower surface dipole δ of 0.18 eV.

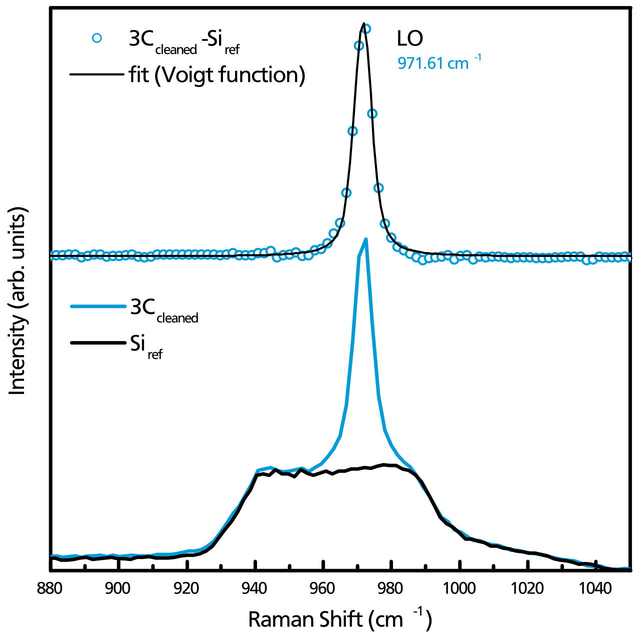

Figure 5.7.: *Raman spectrum of a similarly to* $3C_{cleaned}$ *prepared sample. Due to the higher depth of information for Raman spectroscopy, the spectrum is composed of a superposition of the silicon substrate and the epitaxial 3C SiC Raman signal (*$3C_{cleaned}$*: blue). Subtraction of a pure silicon sample Raman spectra (*Si_{ref}*: black), normalised to the Si peak at* $520.7\,\mathrm{cm}^{-1}$*, yields the pure 3C SiC signal, which was then used to determine the LO position of* $971.61\,\mathrm{cm}^{-1}$*. This corresponds to a doping concentration of* $n_D = 1.1 \times 10^{17}\,\mathrm{cm}^{-3}$.

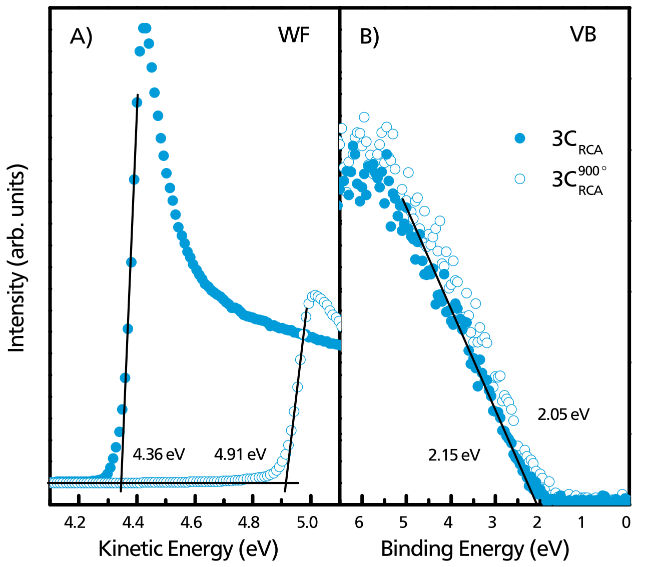

Figure 5.8.: *XPS spectra for A) the secondary electron edge (the applied 3 V bias voltage has already been subtracted) and B) a part of the valence band of RCA wet chemically etched 3C SiC, prior (full circles) and post (open circles) annealing. The black lines show the linear fits employed in determining the work function and the valence band edge.*

The reason for any band bending at the surface has to be the presence of surface states acting as acceptors (upward band bending) or donators (downward band bending) respectively. A possible explanation for the differences between the un-annealed $3C_{RCA}$ on the one and $3C_{pir\ NH4F}$ and $3C_{pir\ HF40\%}$ on the other hand would therefore be surface morphology.

The LEED pattern for $3C_{RCA}$ in figure 5.4 is the most homogeneous one, this is especially apparent in the diagonal spots. Additionally, $3C_{RCA}$ has the lowest Si_{2p}^{SiOH}:Si_{2p}^{SiC} ratio (0.10 compared to 0.12 for $3C_{pir\ NH4F}$ and $3C_{pir\ HF40\%}$), implying less 3C SiC atoms at the surface. Both phenomena indicate a lower degree of surface roughness, which should result in less respectively different surface defects and thus surface states.

This difference in surface morphology is further confirmed by the surface dipole behaviour. Careful reconsideration of the data revealed that the changes in O_{1s}^{SiOH} binding energy do not match the other components exactly. If all peaks in a sample shift in the same way, this is either due to some kind of surface charging or a change in the Fermi level, as the binding energy origin (Binding Energy of zero) is the Fermi level. However if peaks shift differently this is due to chemical changes.

In order to make the difference more obvious the O_{1s}^{SiOH} peak positions were set in relation to the $Si_{2p3/2}^{SiC}$ bulk component. As displayed in figure 5.9, the components O_{1s}^{SiOH} for the NH_4F and HF oxide removal are located 431.44 to 431.46 eV to higher binding energies of $Si_{2p3/2}^{SiC}$. The chemical bond between hydroxide group and 3C SiC sur-

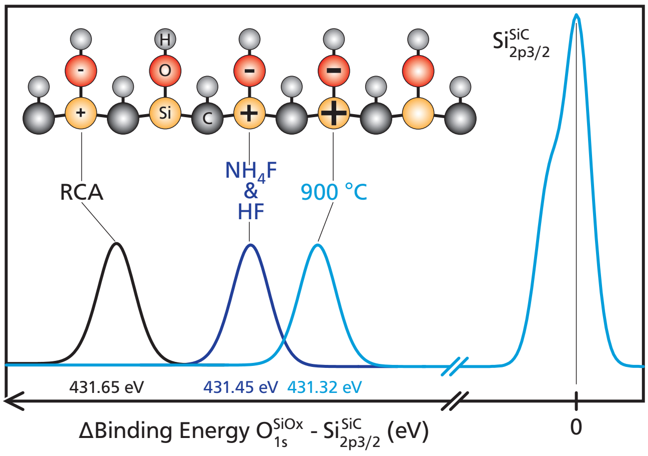

Figure 5.9.: *Graphical representation O_{1s}^{SiOH} components binding energy position relative to the $Si_{2p3/2}^{SiC}$ component. The changes in relative binding energy are linked to a variation in the hydroxides partial charging with preparation procedure.*

face should therefore be identical. Contrary, the RCA procedure has given rise to a O_{1s}^{SiOH} component at 431.65 eV, an even higher binding energy. As higher binding energies are a result of more positive, partial charge in the respective atoms (or in the case of oxygen: less partial, negative charge) one can conclude that the RCA hydroxyl silicon bond, for some reason, is less polar then that from the other two procedures. Because the hydroxyl groups themselves are all similar, this has to be the result of their arrangement on the surface, like dangling bonds in between or multiple hydroxyl groups at a single silicon atom. In figure 5.9 this is indicated by smaller '+' and '-' symbols for the partial charges at the respective atoms.

However, as depicted by the blue lines in figure 5.6, upon annealing the band structures from B) $3C_{pirHF40\%}^{900\,°C}$ and C) $3C_{RCA}^{900\,°C}$ align to match perfectly. Now, both samples display an increased upward band bending of 0.10 to 0.15 eV, along with an likewise increased surface dipole of 0.63 to 0.68 eV. Therefore sample annealing resulted in an increase of acceptor surface states. As the number of hydroxyl groups was reduced during the annealing, this suggests that the remaining dangling bonds on surface silicon atoms act as acceptors, catching free electrons and thus reducing the effective doping concentration at the surface. The increased electron density at the dangling bond surface sites would also agree with the increased polarity of the remaining hydroxyl groups for the annealed samples, see figure 5.9. Post annealing the hydroxide O_{1s}^{SiOH} component is located at 431.33 eV for $3C_{pirHF40\%}^{900\,°C}$ and 431.30 eV for $3C_{RCA}^{900\,°C}$. Annealing at elevated temperatures around 900 °C is therefore sufficient to equalize all differences in the used wet chemical etching procedures. Afterwards the surfaces are identical in all aspects accessible with the employed methods.

Cleaned - As the employed cleaning procedure for this sample does not have the potential to lead to any chemical changes of the 3C SiC sample it can be understood as reference. The Si 2p region appears as expected for SiC, peak shape and position are similar to the etched samples, see figure 5.2 bottom in dark red. However there is a small peak to lower binding energies of the Si_{2p}^{SiC} component. Due to the peak position, closer to that of elemental silicon around 99 eV, unsaturated silicon atoms with one or more of the four carbon ligands substituted with another silicon, as leftover from the CVD fabrication process, seems the most likely explanation.

In addition to the already mentioned calcium contamination the C 1s region shows surface contamination from organic compounds with C-H and or C-O bonds. Otherwise the peak shape implies a CH termination for the surface SiC carbon. As mentioned in the beginning, the O 1s region shows a much higher intensity for $3C_{cleaned}$. The higher O 1s intensity is a result of a superposition from adsorbed organics and possibly water with the O_{1s}^{SiOH} component. It does however prevent any meaningful evaluation of O_{1s}^{SiOH}. For comparison the O_{1s}^{SiOH} components contribution to the O 1s region is displayed in figure 5.2 for the case of a O_{1s}^{SiOH}:Si_{2p}^{SiOH} ratio of unity.

sputtered - It is well known that oxides are difficult to remove via argon ion sputtering. Because of the bonds stability rather high energies and/or long sputter durations are required. This frequently results in structural damage on the substrate. Furthermore, the sputtering might result in the incorporation of part of the surface oxygen into the substrate instead of removing it (highly dependent on the sputtering angle). From figure 5.2 it is apparent that this is also true for the oxide layer on silicon carbide.

Even after 10 minutes of sputtering at medium ion energies the oxygen is not entirely removed from the sample surface. While the apparent broadening of the substrate peaks in the C 1s and Si 2p core level lines gives evidence to the structural damage inflicted upon the 3C SiC substrate. The broadening results from the creation of a multitude of different bonding situations replacing the afore well ordered SiC structure. In figure 5.2 the approximated bulk silicon carbide contribution (SiC component) to the sputtered C 1s and Si 2p regions (dark green) are displayed. However, this is just a very rough approximation. Therefore no peak positions etc. were provided.

In this state the 3C SiC will not be of much use for direct photoelectrochemical water splitting. And the annealing induced changes in the spectrum make it clear that the inflicted damage can not be easily healed out with the available methods. Everything taken into account Ar ion sputtering seems to be a poor solution for SiC surface preparation.

5.4 Conclusion

The 3C SiC surfaces prepared by the three most promising wet chemically etching procedures were compared via XPS, LEED, and HREELS. From comparison of those three to a cleaned but not etched sample it was found that none of the three methods lead to any chemical changes in the SiC bulk, but they produced distinctly cleaner sample surfaces. All three methods result in similar 1x1 surface patterns with satellite structures (indicating a certain disorder in the surface layer structure), as observed in the recorded LEED patterns.

Sample Rinsing

Dipping the etched sample in millipore water **does not remove** all carbon and fluorine contaminations from the sample. **Rinsing** the sample with a water spray bottle has proven to be a much **more efficient** way of cleaning the sample after each etching step.

The 1x1 surface structure as result of similar wet chemical etching was already reported from LEED measurements for 6H SiC and (111) 3C SiC [103, 105, 106, 109], as well as for (001) 3C SiC [109, 111]. However the surface atoms participating in this termination were not elaborated on, or simply given as 'ordered partial overlayer of oxygen' [109]. In this work, evaluation of XPS and HREELS spectra compliantly yields a mixed Si—OH / C—H surface termination for all three methods. A similar treatment on pure silicon (without the carbon) results in a hydrogen terminated Si—H surface [129].

Similar mixed surface terminations are know for the III-V semiconductor GaAs, even though it is less ionic than SiC (EN$_{Ga}$: 1.81 / EN$_{As}$: 2.18 compared to EN$_{Si}$: 1.9 / EN$_{C}$: 2.55). Beerbom et al. reported an As—H/Ga—OH termination for water adsorption on a clean GaAs surface under UHV conditions [130], and as result of immersion in 0.02 M KBr before the application of a bias voltage for oxidation [131]. In both cases, the more electronegative compound is H coordinated, while the other features a hydroxyl termination.

Concentrated hydrofluoric acid and ammonium fluoride for oxide striping result in similar surface properties in terms of band bending (close to flat band: −0.02 to −0.06 eV) and surface dipole (0.44 to 0.48 eV). However in case of HF it seems to be more difficult to remove all traces of fluorine from the sample via rinsing, as is apparent from the remaining fluorine contamination after identical rinsing procedures. RCA results in a weak 0.05 eV upward band bending, also close to flat band, and a distinctly weaker surface dipole (0.18 eV). It is assumed that the differences in surface properties can be attributed to $3C_{RCA}$ having a smoother surface, and thus less surface defects than the other two samples.

Jaegermann and Mayer [132] give a distinctly higher surface dipole of 0.85 eV as result of the Si+/Si-OH dipole on (001) silicon. But as silicon carbides covalent silicon carbon bond is strongly polar (see above), it is not surprising that the dipole between the hydroxyl group and the already partially positively charged, and thus electron starved, silicon atom is less emphasized.

Annealing the samples at 900 °C under UHV conditions results in 1x1 LEED patterns without the satellite spots, indicating a better ordered surface structure. This agrees to a partial change in surface termination. Some of the Si—OH bonds dissociate most likely leaving a dangling bond behind, resulting in a slight reduction of overall oxygen on the sample surface (9 to 21 %). Additional annealing leads to an increase in upward band bending and surface dipole as result of newly created dangling bonds. Post annealing $3C^{900\,°C}_{pir\ HF40\%}$ and the $3C^{900\,°C}_{RCA}$ exhibit identical surface properties.

As $3C_{pir\ HF40\%}$ and $3C_{RCA}$ show identical behaviour in electrochemical experiments, the less elaborate piranha/HF procedure is more advantageous. NH_4F and concentrated HF produce identical surface properties However concentrated HF is extremely dangerous and has to be handled very carefully. While still dangerous to the touch, NH_4F is less critical. And as oxide removal with NH_4F results in the most flat band like surface structure, indicating the least amount of defects, almost all wet chemical etching in this work was performed with the combination of piranha solution and ammonium fluoride oxide stripping presented in the experimental setup part of this chapter.

Immersion Procedure

All samples in this chapter were etched by immersing them in a bath of the respective chemicals while on a PTFE mount, as displayed in the upper picture to the right. But for some other samples, notably those with a deposited and annealed back contact, it proved necessary to etch only one side of the sample, less the back contact would be damaged.

This was achieved by placing the sample, with the side to be etched face down, on a droplet of the respective chemical, see bottom right picture. For comparison samples were etched with both methods, but using the same recipe. Evaluation by XPS and LEED showed that the surface properties are identical. However great care has to be taken during the cleaning of the droplet etch PTFE beaker with piranha solution. Remaining carbon contaminants tend to 'swim' on the NH_4F droplet surface and contaminate the sample if not removed beforehand.

6

3C SiC / Nickel Interface For Ohmic Back Contacts

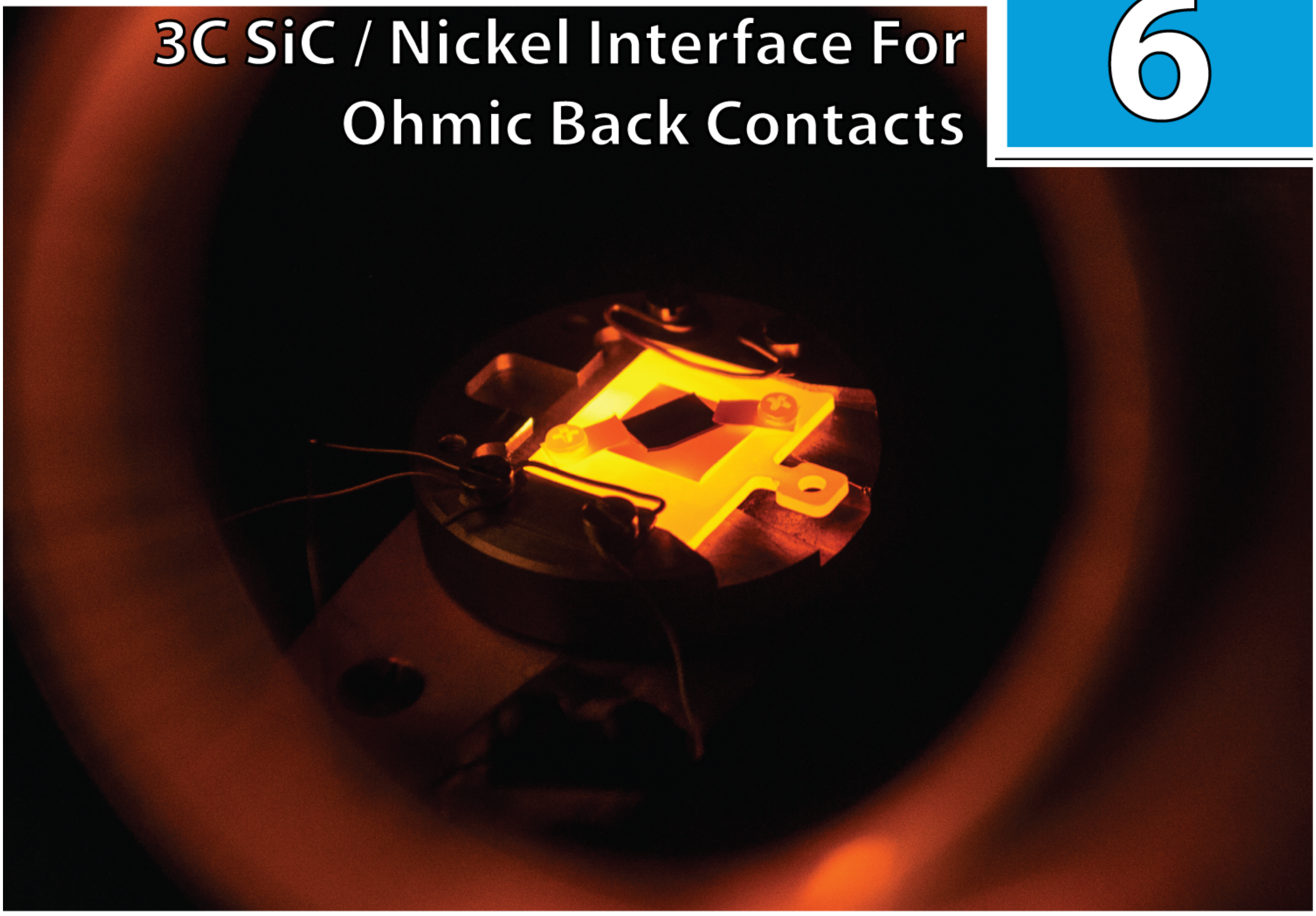

Because all electrochemical measurements require a reliable ohmic back contact to the silicon carbide sample, this chapter investigates the formation of an ohmic contact between 3C SiC and Ni upon annealing at 850 °C. While this contact formation, due to nickel silicide formation, is well known, there were no previous studies on the changes in band structure and Schottky barrier height at the 3C SiC/Ni interface prior and post annealing. The employed methods discussed in the context of this chapter are XPS, UV/vis transmission spectroscopy and LEED.

6.1 Introduction

As mentioned in the introduction silicon carbide (SiC) is a cutting edge material, with a number of impressive material properties. Some of these properties, like the large band gap, high electrical breakdown field (3×10^6 to $2.4 \times 10^7\,\mathrm{V\,cm^{-1}}$) or thermal conductivity [22,23] are the reason for silicon carbides success in high power electronic applications. SiC devices are more efficient, as their drift layers can be considerably thinner, and can be operated at elevated temperatures up to 600 °C. Because the bulk growth of the hexagonal polytypes is much easier to control [33] than for 3C SiC, and because 4H and 6H SiC have higher band gaps of 3.3 eV and 3.0 eV [133], they have been in the focus of application related research for some time.

Over the years a huge selection of material compositions, treatments and evaluation methods have been employed [22,23,134–136] in order to create reproducible SiC Schottky diodes or ohmic contacts to hexagonal SiC. For n-type hexagonal SiC, nickel is the most common contact metal for ohmic contacts. It is a well studied fact that the hexagonal SiC nickel interface exhibits Schottky behaviour after nickel deposition, but the annealing induced formation of nickel silicide results in an ohmic silicon carbide / nickel silicide / nickel contact [22,136].

However, there is a much lower number of studies on the contact bahviour of cubic (3C) SiC. 3C SiC can be produced relatively cheap as thin high quality layers on silicon wafers via chemical vapour deposition (CVD) [137]. Because it is less vulnerable to near-interface traps (NIT) at the SiC/oxide interface [138], shows a higher electron mobility [133], and has a band gap in the visible blue spectrum of 2.3 eV, it is of interest for a number of other applications. Not surprisingly, taking into account the context of this work, one of these applications is direct photoelectrochemical water splitting, where its band gap in combination with its chemical stability make it a promising electrode material [27, 31].

As the annealed nickel contact is known to work for 3C SiC as well [139], but was mostly investigated via Transfer Length Method (TLM) in order to determine the specific contact resistance ρ_c for various surface preparations, annealing temperatures or other contact metals [139–142], it appears reasonable to directly study the Ni / 3C SiC interface properties and band alignments during contact formation via an X-ray photoelectron spectroscopy (XPS) interface experiment.

6.2 Experimental Procedure

All experiments discussed within this chapter were conducted on a (001) 3C SiC sample of $(191 \pm 5)\,\mu$m thickness. The sample was originally grown via CVD by Hoya Cooperation [143]. As piece of an early stage commercial wafer, the sample displays a high level of residual strain distributed inhomogeneously in the crystal volume, and a high planar defect density [143].

Before the interface experiment the sample was cleaned in acetone and isopropanol. Afterwards it was investigated in order to obtain a number of basic informations:

- Raman spectroscopy was performed in order to confirm the polytype and estimate the doping concentration n_D
- Van-der-Pauw Hall measurements were performed in order to confirm the doping concentration n_D
- UV-Vis spectroscopy was performed to allow the determination of the band gap E_{BG}. The measurements were realised in transmission mode as well as utilizing an Ulbricht sphere.

Subsequently the sample was wet chemically etched as discussed in the previous chapter 5, with NH_4F for oxide stripping. Within five minutes after the wet chemical etching the sample was mounted on a molybdenum sample-holder, and then introduced into vacuum at the Darmstadt Integrated System for Fundamental Research (DAISY Fun), see chapter 3. In order to avoid contamination during the annealing process, titanium screws and a tantalum mask were employed to fasten the sample on the sample holder. XPS and LEED measurements were performed at pressures of 4×10^{-9} mbar or below. Additionally a reference measurement on a pure 99.5% nickel foil from Alfa Aesar was performed.

Sample Nomenclature

Within the context of this work a total of three bulk single domain 3C SiC samples was available. The experiments in this chapter were conducted on the first of these samples, hence the name $SD_{\#1}$. As usual the sample preparation will be added as sub-, and the treatment as superscript.

$3C_B^A$: About one micro meter of n-type 3C SiC on a silicon wafer, growth was performed on via CVD.

SD_B^A: Approx. 200 μm thick single domain 3C SiC sample, with no silicon attached.

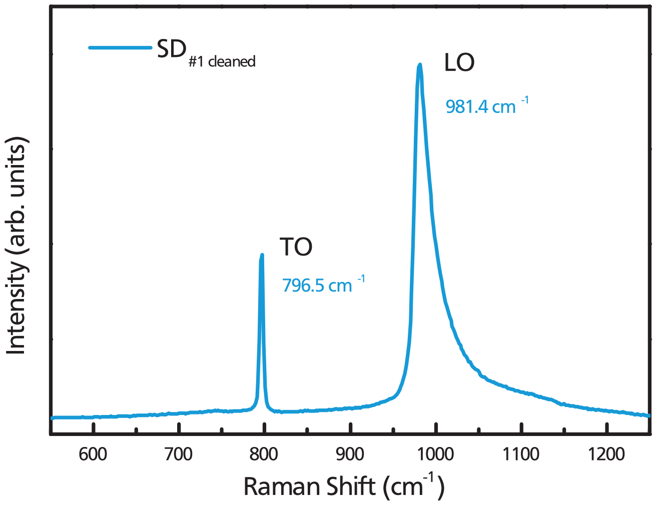

Figure 6.1.: *Raman spectrum of the cleaned (not etched) single domain 3C SiC sample* $SD_{\#1\,cleaned}$. *The utilized light source was a green laser with a wavelength of* 514 nm, *and the spectrometer was calibrated with regard to the* 520.7 cm^{-1} *peak of single crystalline silicon.*

The nickel foil was cleaned in an ultrasonic bath in aceton and isopropanol for 10 minutes each, then introduced into the UHV system within 5 minutes. There, surface contaminations and the nickel oxide surface layer were removed via 15 minutes of argon ion sputtering. Sputtering was performed with 99.999% pure argon, at 4.9×10^{-6} mbar, 10 mA ion current, and 1.5 kV ion acceleration voltage. Subsequently the nickel foil was annealed at 500 °C for five minutes, hence the tag $Ni^{annealed}_{sputtered}$.

Nickel/SiC Interface Experiment

The interface experiment was done by depositioning thin nickel layers on the sample, while performing XPS measurements after each deposition step. Thus giving information on the 3C SiC electronic structure in dependence of nickel layer thickness. All in all six nickel deposition / XPS characterisation cycles were performed, until the 3C SiC signal was almost to low to detect. The nickel deposition took place in the 'MBE' chamber, see chapter 3, via magnetron sputtering at a base pressure of 1×10^{-7} mbar. Sputtering was performed with a 99.999% pure argon flow of 30 sccm at 0.03 mbar and with a total power of 10 W. A Kurt J. Lesker pure 99.99% nickel sputter target was employed as nickel source.

Before each deposition step the nickel target was sputtered at 100 W for about a minute, while the shutter was still closed. This was done in order to remove possible contaminations from the sputter target surface. For the duration of the sputter deposition, the sample was rotated in order to ensure a homogeneous layer growth. In situ transfer between XPS and MBE took place via the 'tube' and 'UFO', at pressures below 3×10^{-9} mbar, see chapter 3.

Contact Annealing

In order to observe annealing induced changes to the substrate signal, the 3C SiC signal had to be measurable. Thus, once the 3C SiC substrate signal was low enough, that an additional nickel deposition step was likely to eliminate all substrate contributions to the XPS spectrum, the interface experiment was stopped. The sample was transferred in situ to the 'buffer chamber', and annealed for five minutes at 850 °C. Annealing was performed via heating of the molybdenum sample holder by electron impact heating. The samples temperature was monitored with a pyrometer. During annealing the chambers base pressure of 4×10^{-9} mbar increased to 1.5×10^{-7} mbar. Post annealing the sample was kept in the buffer chamber for about 15 minutes to ensure it had cooled down. It was then transferred back to the XPS chamber and one final XPS spectrum was taken.

6.3 Results and Discussion

Before $SD_{\#1}$ was etched in preparation of the XPS interface experiment, three other characterisation methods were employed on the cleaned sample in order to gather all information necessary for the

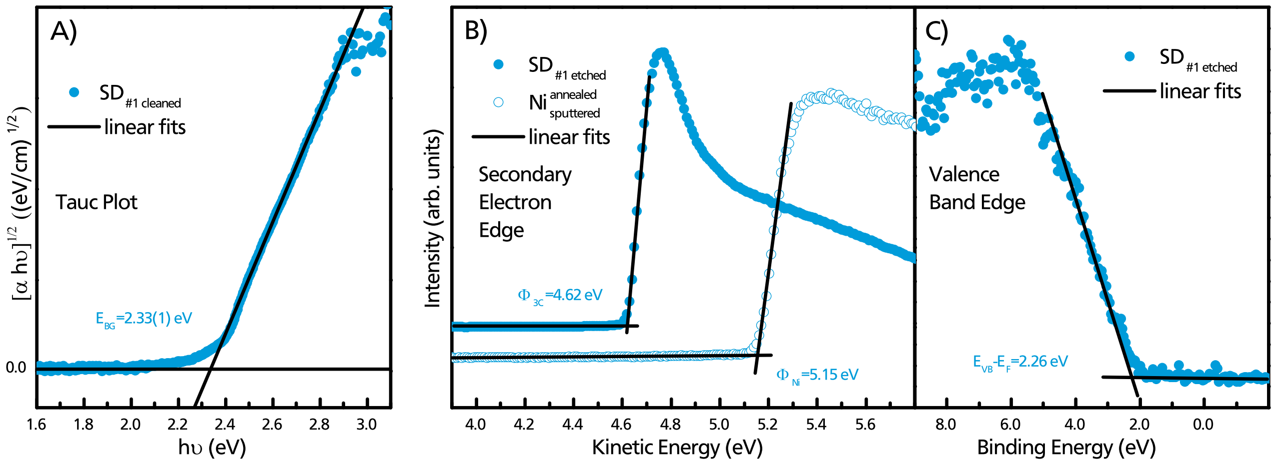

Figure 6.2.: *A) Tauc plot from UV/VIS absorption spectroscopy of 3C SiC before wet chemical etching. As the transition is indirectly allowed:* $n = 2$ *is used to find the band gap* E_{BG}*, B) XP spectrum of the secondary electron edges for* $SD_{\#1\,etched}$ *and the clean* $Ni^{annealed}_{sputtered}$ *used for determination of the work functions* Φ_{3C} *and* Φ_{Ni}*, C) XP spectrum of the valence band edge. The intercept is used to interpolate* $E_{VB} - E_F$*. Please note that B)s and C)s energy scales correlate via* $E_{kin} = h\nu - E_{bin}$*.*

following evaluation. The first was Raman spectroscopy, see figure 6.1 for the recorded spectrum. Raman spectroscopy is a reliable way of identifying the silicon carbide polytype from the number and position of observable modes [82]. For 3C SiC only two modes are reported in the displayed Raman shift range: the transverse optical phonon mode (TO) at 796 cm^{-1} and the longitudinal optical phonon mode (LO) around 972 cm^{-1}. This is in excellent agreement with the observed Raman spectrum for $SD_{\#1\,cleaned}$.

Raman spectroscopy can also be employed to estimate the free carrier or doping concentration n_D of the observed SiC sample [80, 82]. In 3C SiC the TO modes position remains unaffected by changes in the doping concentration, while the LO mode shifts to higher wave numbers with increasing n_D. Furthermore, the LO modes peak shape becomes more asymmetrical with increasing n_D in form of a tail to higher wave numbers. From the observed LO position of 981.4 cm^{-1} a doping concentration of $(1.7 \pm 0.5) \times 10^{18}\,\text{cm}^{-3}$ can be estimated as first presented by Yugami et al. [80] for 3C SiC in 1987. See section 3.4 for further information.

The second characterisation method was a Van-der-Pauw Hall measurement, which yielded a carrier concentration of $(1.3 \pm 0.2) \times 10^{18}\,\text{cm}^{-3}$. Therefore n_D will be assumed as $(1.5 \pm 0.5) \times 10^{18}\,\text{cm}^{-3}$ for the remainder of this chapter.

The third characterisation method was UV/Vis absorption spectroscopy. As literature values on the 3C SiC band gap vary from 2.2 to 2.4 eV [24, 144] it seemed reasonable to determine the band gap for the sample $SD_{\#1}$ experimentally. A possible explanation for the divergent values reported is band gap narrowing in dependence of doping concentration. Values of up to 0.2 eV have been reported [145], therefore the reported divergence seems reasonable.

The absorption coefficient α, determined from the UV/Vis spectroscopy data, was plotted in form of a 'Tauc plot' [75, 77, 78], see figure 5.8 A). In the plot $[\alpha h\nu]^{1/n}$ is given as a function of $h\nu$, where $h\nu$ is the incident lights photon energy. As 3C SiC has a indirect band gap n is two [78]. From the intersect of the extrapolated linear region with the abscissa one can obtain the band gap E_{BG} of (2.33 ± 0.01) eV, this value was also used in the previous chapter.

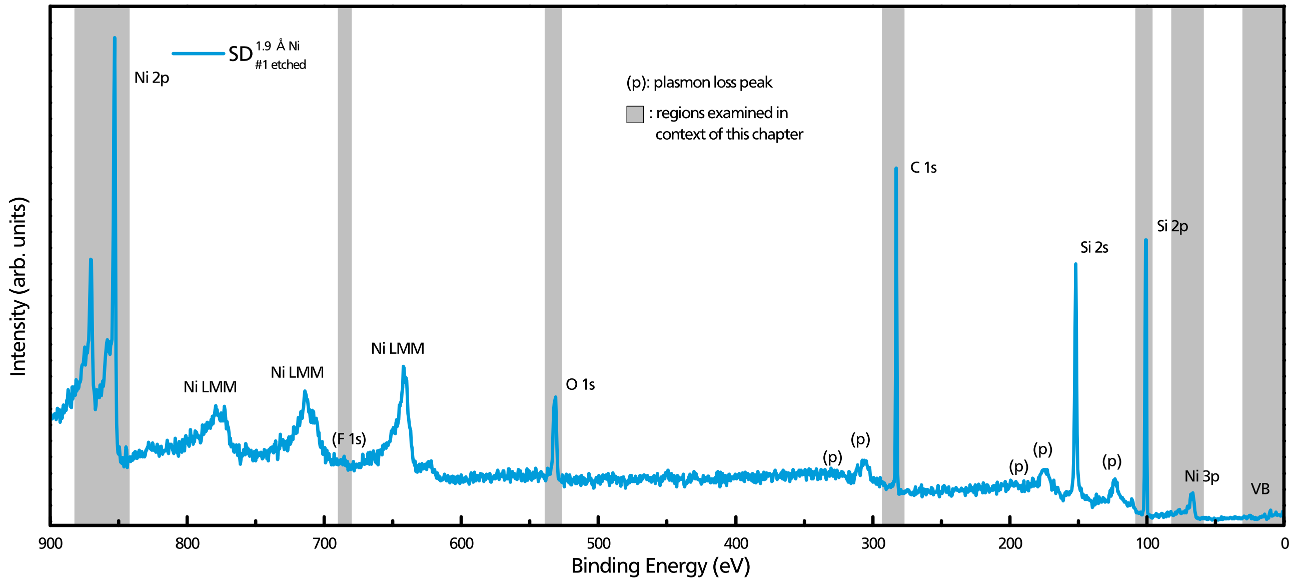

Figure 6.3.: *XPS survey spectrum of the Hoya 3C SiC sample after the second nickel deposition step. Only nickel, oxygen, carbon and silicon are present. Calculations based on the detail spectra component corrected areas state a nickel layer thickness of* (1.9 ± 0.3) Å.

After these initial characterisation steps the sample was wet chemically etched and introduced into the 'DAISY Fun'. The first group of XPS measurements was mostly similar to the results for wet chemically etched 3C SiC reported in previous chapters, and confirmed the presence of oxygen, carbon and silicon. No fluorine was found on the sample.

Because the behaviour of the nickel core level peaks would have to be observed in later experimental steps, two additional regions, Ni 2p and Ni 3p, were measured. All examined regions are highlighted in light gray in the survey spectrum displayed in figure 6.3. This survey was taken after the second nickel deposition step,and provides a good overview of all relevant core level peaks and regions.

In the ideal case (Schottky limit) the contact formation at a semiconductor / metal interface is defined by the difference in work function of the two materials. For nickel, work functions between 5.04 and 5.35 eV have been reported in the past for different crystal orientations [147–150]. Polycrystalline films evaporated under UHV conditions were reported with a surface work function of 5.15 eV [147,149]. This should be comparable to the nickel deposition via sputtering. As a further reference the work function of a clean, annealed nickel foil was extracted from the secondary electron edge, see figure 6.2 B). The resulting value of 5.15 eV for Φ_{Ni} is in excellent agreement. Figure 6.2 B) also shows the secondary electron edge of $SD_{\#1\,etched}$, and the $\Phi_{3C} = 4.62$ eV resulting from the fit.

Furthermore the difference between the upper valence band edge E_{VB} and Fermi level E_F was determined from the valence band edge XPS region displayed in figure 6.2 C). Combined with the band gab E_{BG} of 2.33 eV from the Tauc plot the resulting Fermi level position is $E_F - E_{CB} = 0.07$ eV below the conduction band E_{CB}. One can also calculate this value for the bulk material using equations 2.2, 2.4 and a doping concentration $n_D = (1.5 \pm 0.4) \times 10^{18}\,\mathrm{cm}^{-3}$ (average of Hall and Raman results) to 0.06 eV. This is in excellent agreement with the measured value of 0.07 eV. As bulk and surface show the same $E_F - E_{CB}$, within the margin of error, flat band like conditions on the sample surface can be assumed. From the data presented above a band diagram of the $SD_{\#1\,etched}$

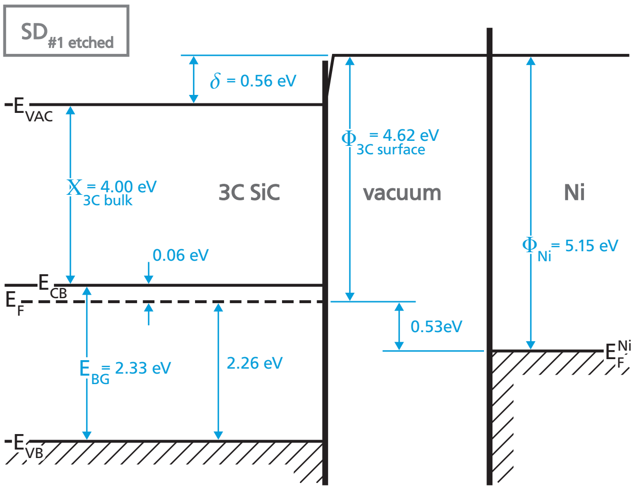

Figure 6.4.: *Band structure diagram for the wet chemically etched $SD_{\#1\ etched}$, with a mixed Si—OH / C—H termination layer, in relation to clean nickel. The diagram was constructed from the performed XPS measurements and a bulk ionisation energy from literature values [127, 128, 146]. Under the assumption of Schottky type behaviour of the Ni 3C SiC interface, an* 0.53 eV *upward band bending and thus a similar peak shift to lower binding energies is to be expected.*

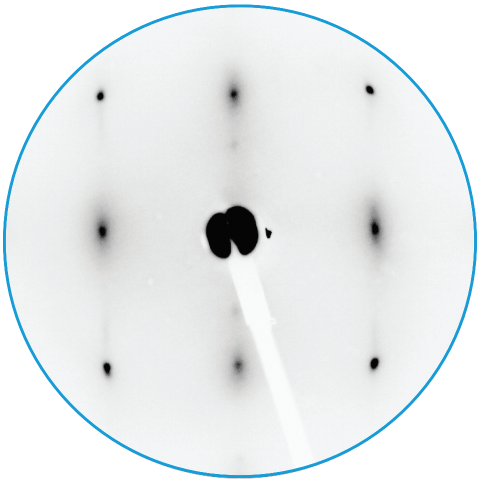

Figure 6.5.: *The LEED pattern of $SD_{\#1\ etched}$ shows the cubic cell with a clear 1x1 reconstructed surface morphology. In contrast to the 3C SiC on Si samples from the previous chapter no satellite spots can be observed after wet chemical etching, even though the sample was not annealed. Measurement parameters: beam energy* 90 eV, *filament current of* 2.8 A *and a screen voltage of* 5 kV.

surface in vacuum was constructed, it is displayed in figure 6.4.

Comparing the band diagram of $SD_{\#1\ etched}$ with the similarly prepared $3C_{pir\ NH4F}$ from the previous chapter shows similar behaviour. Both samples display flat band like behaviour, within the margin of error (—0.02 eV downward band bending for $3C_{pir\ NH4F}$), after treatment with piranha solution and a subsequent NH_4F oxide removal step. Further confirming that this preparation procedure results in a surface without active surface defects. Similar, the observed surface work functions are in reasonable good agreement, with $\Phi_{3C\ surface} =$ 4.62 eV for $SD_{\#1\ etched}$ and 4.55 eV for $3C_{pir\ NH4F}$. The higher deviation in surface dipole ($\delta_{SD} =$ 0.56 eV compared to $\delta_{3C} =$ 0.44 eV) is a result of the difference in doping concentration and the resulting higher Fermi level position for the more strongly doped $SD_{\#1\ etched}$, see figure 5.6 from the previous chapter for comparison. Examination of the respective components from the XPS detail spectra results in a O_{1s}^{SiOH}:Si_{2p}^{SiOH} ratio of 1.10, also similar to the 1.13 observed in the previous chapter for the identical etching procedure. Together with the LEED pattern displayed in figure 6.5, which shows a clear 1x1 termination, a mixed Si—OH / C—H termination can be assumed for this sample as well.

However, in contrast to the previous chapter, this LEED pattern does not display any satellite spots, even though the sample was not annealed. Normally this should be interpreted as proof of a more ordered surface structure, however the first order spots are less defined than for the $3C_x$ samples. So, instead this difference may be due to a more macroscopic difference in sample surface morphology. Figure 6.6 shows Normarski microscopy shots of both sample surfaces. As one can clearly see in B), $SD_{\#1\ as\ is}$ features a lot of steps, which are likely to prevent any macro-surface structures, normally responsible for the appearance of satellite spots, while $3C_{as\ is}$ possess a smoother surface structure.

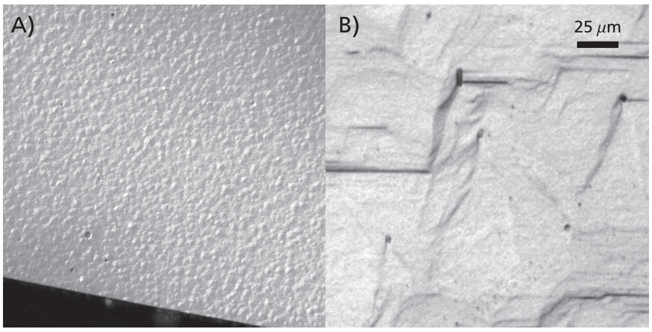

Figure 6.6.: *Normarski microscope pictures obtained for A) $3C_{as\ is}$ and B) $SD_{\#1\ as\ is}$ show the differences in surface morphology. The bulk $SD_{\#1\ as\ is}$ sample shows much larger surface features (steps and terraces) compared to the more evenly distributed $3C_{as\ is}$*

As illustrated in the band diagram in figure 6.4 the variance in work function between the 3C SiC and nickel should result in the formation of a Schottky barrier. The resulting upward band bending, indicated in further diagrams as diffusion potential V_d, should match 0.53 eV. One would then expect a shift to lower binding energy for all core level peaks as result of the reduced energetic distance to the Fermi level. Assuming a Schottky type behaviour of contact formation the barrier height would amount to $\Phi_B = 0.59$ eV.

Nickel / 3C SiC Interface Experiment

The next step was the execution of the actual interface experiment. Increasing amounts of nickel were deposited on $SD_{\#1\ etched}$ by magnetron sputtering. In Figure 6.7 the XPS detail spectra for the Ni 2p, O 1s, C 1s and Si 2p regions taken after each subsequent deposition step are displayed. No normalization was performed, but the Ni 2p is displayed at a quarter of the actual intensity for reasons of clarity. Component peak positions and FWHM are displayed as well for the three components employed for tracking the binding energy shift as result of the band bending on the surface.

The results will be discussed from right to left. As one can see C_{1s}^{SiC} and $Si_{2p3/2}^{SiC}$ both shift to the right (lower binding energies) with increasing nickel layer thickness. If no chemical changes occur on the sample surface all peaks should shift by the same amount, as the band bending affects all SiC components in the same way. Neither peak shows any apparent changes in shape or FWHM, thus chemical changes to the 3C SiC can be ruled out. Observed shifts are 0.33 (C_{1s}^{SiC}) and 0.36 eV ($Si_{2p3/2}^{SiC}$). The 30 meV difference is well within the 50 meV margin of error, thus the shifts are coherent. However from the work function difference in 3C SiC and Ni one would have expected a 0.53 eV shift instead.

One can determine the band bending from the first and last measurement alone. However it is preferable to check the behaviour in between those two extremes. Thus one can ensure that the peak positions converge toward a final value, as well as rule out unexpected side effects.

As increasing amounts of nickel are deposited on the sample surface over the course of the interface experiment, less and less electrons from the silicon carbide surface will be able to pass through the nickel layer without being scattered first. This results in an exponential dampening of the substrate material signal in dependence of the nickel layer thickness d_{Ni}. The nickel layer thickness d_{Ni} was determined by numerical solution of equation 3.4

Pass Energy And FWHM

The SiC components in figure 6.7 all show a 100 meV higher FWHM than in figure 5.2 from the previous chapter. This is a result of the higher pass energy setting (10 eV compared to the 5 eV from the previous chapter) used for the measurements in this chapter. Increasing the pass energy increases the peak intensity, and thus improves the signal-to-noise ratio, but it also broadens the observed peak shapes.

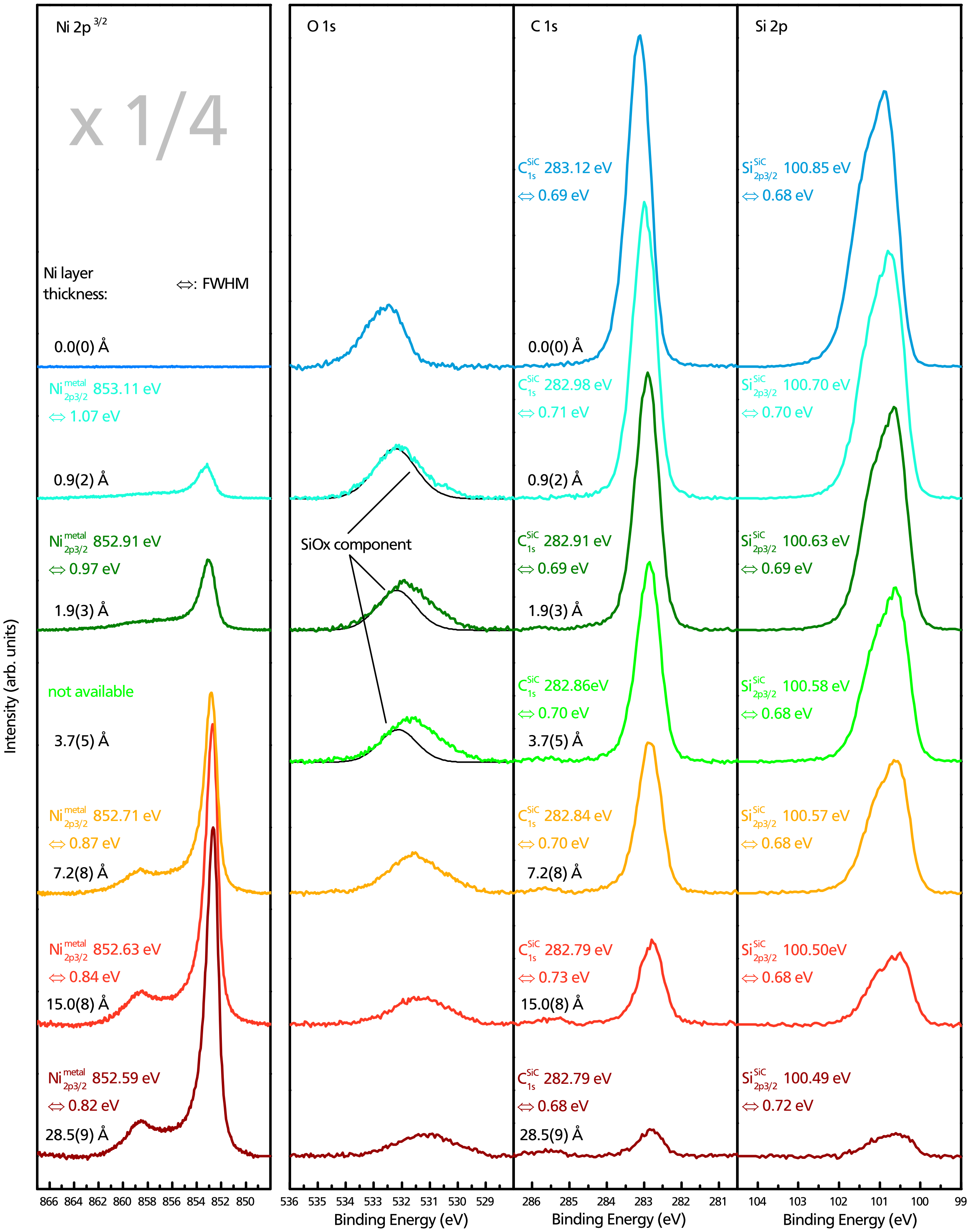

Figure 6.7.: *XPS detail spectra (background subtracted) of* $SD^{x\,Å}_{\#1\,etched}$ *for the various deposition steps as part of the 3C SiC / nickel interface experiment. The spectra were taken with a* 10 eV *pass energy, which explains the about* 0.1 eV *higher FWHM values, compared to the previous chapter. The SiC core level components* C^{SiC}_{1s} *and* $Si^{SiC}_{2p3/2}$ *display a shift of* 0.33 *and* 0.36 eV *to lower binding energies. In the O 1s region one can observe the appearance of an additional nickel oxide species, as is elucidated from the apparent lack of intensity in the displayed* O^{SiOH}_{1s} *component. One detail spectrum (*3.7 Å*) was accidentally overwritten during subsequent experimental steps and could therefore not be evaluated.*

with the corrected peak areas for the Ni 2p and Si 2p regions, see figure 6.7 for the resulting values.

While the C 1s and Si 2p regions display the expected identical dampening, this is less pronounced for the O1s region. Additionally, the O 1s peak exhibits a stronger binding energy shift as well as an increase in FWHM. The assumed O_{1s}^{SiOH} contribution to the O 1s region was estimated from Si_{2p}^{SiOH}, for clarification of the effect it is displayed in figure 6.7 for the first three nickel deposition steps. Two possible explanations seem reasonable.

First, one could argue that some hydroxyl bonds to the surface silicon are broken by the incoming nickel ions. The hydroxyls oxygen could then attach itself to the newly deposited nickel. Thus it would be intermixed or on top of the nickel and therefore less dampened than the 3C SiC bulk signal.

Second, a weak oxygen contamination takes place during nickel deposition. This could for example be caused by a small contamination level somewhere in the argon line.

It can not be said with certainty which of those two effects occur. However, considering the peak shapes and intensities of the annealed sample in the next section, the contamination seems most likely. As the Ni 2p spectrum does not display the typical multiplet splitting for NiO, nor the increased satellite intensity for $Ni(OH)_2$ but instead the known metallic nickel shape, this should not impede the measurements [151, 152].

Contrary to the substrate peaks the nickel signal is bound to increase with d_{Ni}. Actually, because of the high cross section for nickel the signal intensity for the Ni 2p region is only displayed at a quarter of the measured intensity in figure 6.7. Otherwise the substrate peaks would have been hard to read for high d_{Ni}. In the Ni 2p region a clear main peak is apparent, but the characteristic satellite structure for metallic nickel [151, 152] only arises for a nickel layer thickness above (1.9 ± 0.3) Å (less then one monolayer). It is fully present for (7.2 ± 0.8) Å (about three monolayers) of Ni.

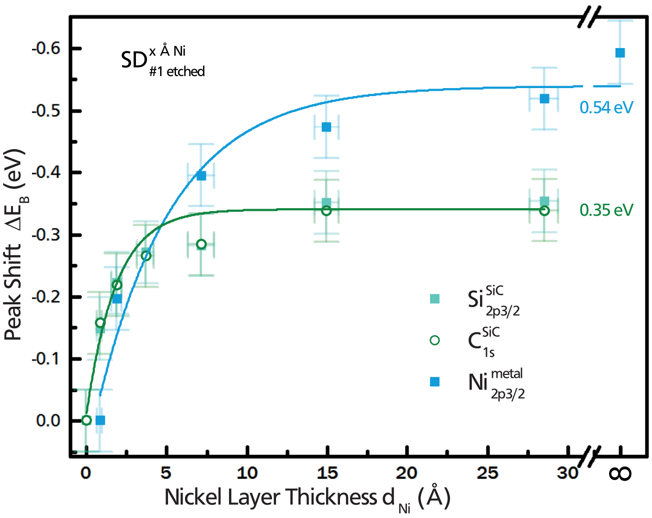

Figure 6.8.: *Diagram of the XPS core level shifts in binding energy as result of nickel deposition. The three components* $Si_{2p3/2}^{SiC}$, C_{1s}^{SiC} *and* $Ni_{2p3/2}^{metal}$ *all show a shift to lower binding energies with increasing* d_{Ni}. *The peak shifts in dependence of nickel layer thickness can be described quite adequately by an exponential function, yielding total peak shifts of* 0.35 eV *for the 3C SiC substrate and* 0.54 eV *for the nickel.*

Above results are graphically summarized in figure 6.8. Fitting the data points with an exponentially function yields a shift of 0.35 eV for the substrate species $Si_{2p3/2}^{SiC}$ and C_{1s}^{SiC} (cyan and dark green). As the function clearly converges on that value additional nickel deposition would not result in further band shifts. This shift is the result of the upward band bending from the Fermi level matching, in other words the formation of a Schottky contact. However, as the work functions exhibit a 0.53 eV difference, a more pronounced band bending was expected.

It stands to reason that further band bending was prevented because the Fermi level was pinned due to defect states in the interface layer. From the observed band bending it can be concluded that these surface states have to be located about 0.41 eV below the conduction band edge E_{CB}. With increasing d_{Ni} more electrons flow from the 3C SiC to the nickel as a result of the Fermi level matching. This results in the formation of a region without or at least a reduced amount of free electrons, the depletion layer. The electron depletion in turn, gives rise to an increase in distance between E_{CB} and E_F^{3C}. At some point, the Fermi level E_F^{3C} will be aligned with the energetic position of the defect states.

To start with, the defect states are all occupied, as they were located below the Fermi level. But once the Fermi level sinks beneath the defect state position some of them will be ionized. The remaining, positively charged ions will cause a potential drop δ_{DS} at the interface [153]. If the defect state density is high enough no further changes in the 3C SiC Fermi level will occur, as additional surface states are ionized instead. Thus, the Fermi level is pinned. Above situation is graphically displayed in the band diagram for the 3C SiC nickel contact in figure 6.9. Whether the defect states and the resulting Fermi level pinning are a result of the Si—OH / C—H termination layer, the various defects in the 3C SiC sample or the interaction with the deposited nickel could not be determined.

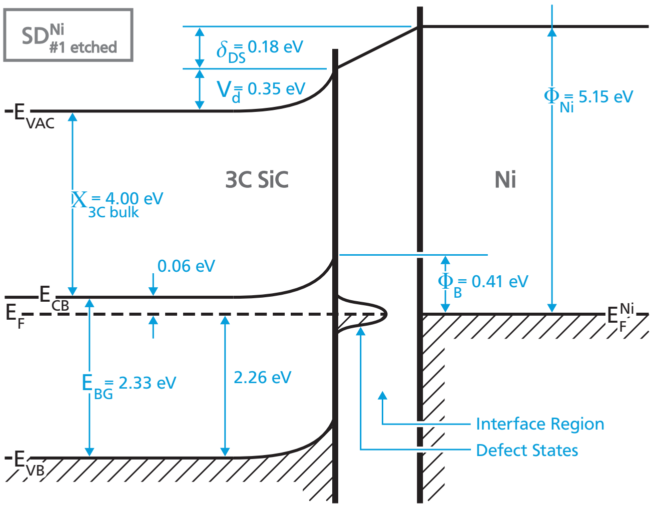

Figure 6.9.: *Band structure diagram for the 3C SiC nickel interface as measured for* $SD^{28.5\,\text{Å}\,Ni}_{\#1\ etched}$. *The diagram was constructed from the performed XPS interface experiment measurements. Reduced band bending of* 0.35 eV *is the result of Fermi level pinning due to surface states, the remaining* 0.18 eV *occur as potential drop* δ_{DS} *across the interface region [153].*

Back in figure 6.8 it is obvious that $Ni^{metal}_{2p3/2}$ exhibits a stronger shift in peak position, 0.54 eV instead of 0.35 eV. This is a result of the 'cluster size effect' as shown for gold by Wertheim et al. in 1983 [154] and recently also for platinum by Klett et al. [155]. For the first nickel deposition steps there will be no closed metal layer, as the sample coverage is less then one monolayer. Instead, there will be a number of nickel clusters or islands. If an electron from one of these clusters is removed due to photoelectron excitation from the incident XPS X-ray radiation, the remaining hole will be subject to a reduced final state screening. As a result the core level peaks of small clusters are shifted to higher binding energies. With increasing cluster size this effect diminishes until it disappears completely for the closed layer [154, 155]. This, in turn, artificially increases the binding energy shift in the nickel emission lines.

Contact Annealing

In order to display ohmic behaviour the n-type (3C) SiC nickel contact has to be annealed [22]. Thus, $SD^{Ni}_{\#1\ etched}$ was transferred in situ to the 'buffer chamber' and heated to 850 °C for 5 minutes under UHV conditions with a base pressure of 4×10^{-9} mbar. While the electron impact heating was active the pressure rose up to 1×10^{-7} mbar. The XPS detail spectra for the Ni 2p, O 1s, C 1s and Si 2p regions are displayed at the bottom of figure 6.10.

At first glance the distinct decrease of the nickel signal attracts the most attention. Pre-annealing, (28.5 ± 0.9) Å of nickel were present on the sample surface. Post-annealing, this is replaced by (3.1 ± 0.3) Å of nickel silicide. The disappearance of about 90% of the nickel is surprising. From the amount of missing nickel one can estimate the Ni

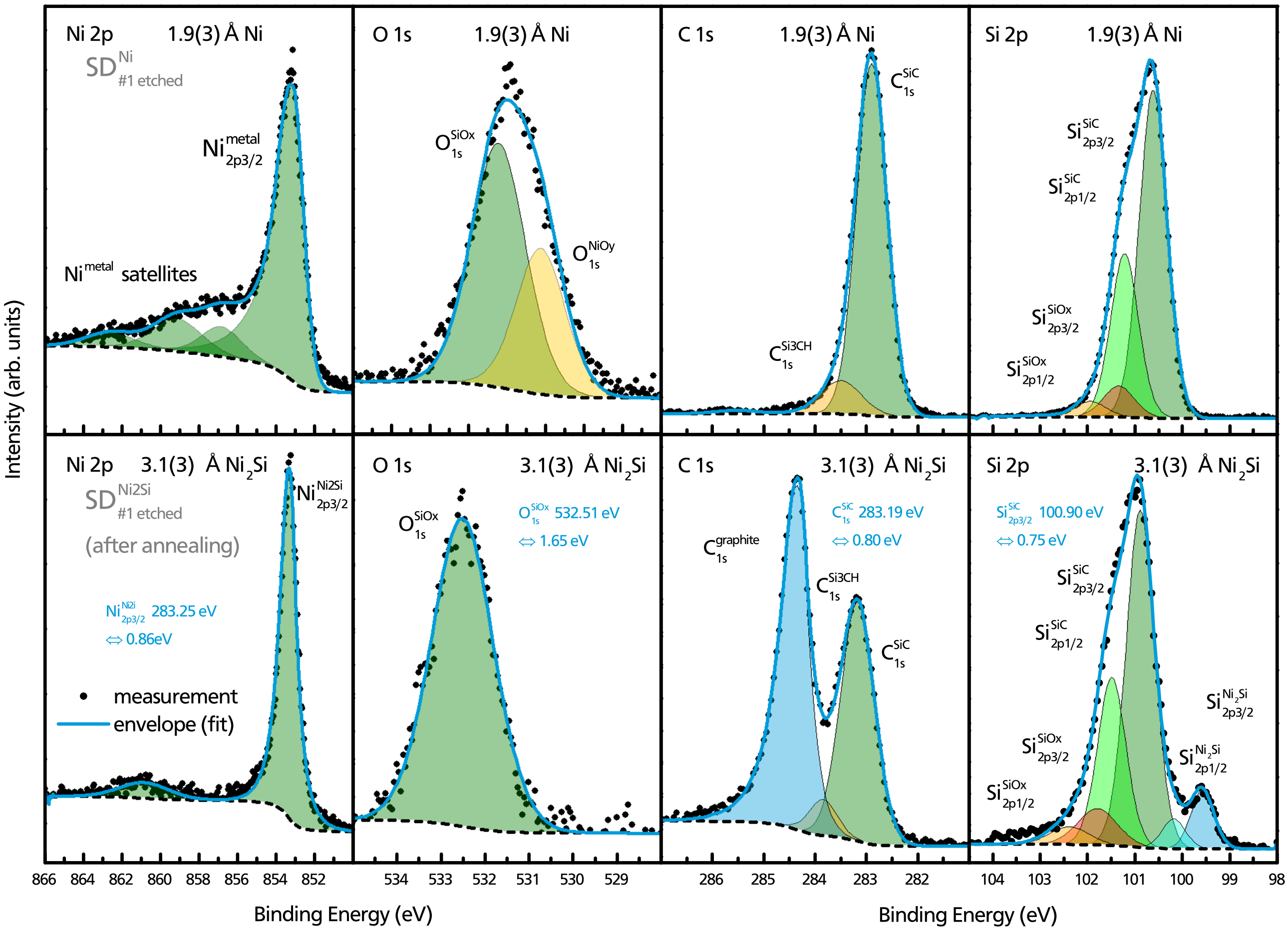

Figure 6.10.: *XPS detail spectra of $SD^{Ni2Si}_{\#1\,etched}$ before (top) and after (bottom) annealing at 850 °C for five minutes. The amount of nickel on the annealed sample is significantly reduced. Therefore XPS detail spectra from a deposition step with a similar nickel content were selected for comparison (top). As result of the annealing all substrate peaks: O^{SiOH}_{1s}, C^{SiC}_{1s} and $Si^{SiC}_{2p3/2}$ reverse the previous shift, observed as result of nickel deposition, and are now located 0.05 eV to higher binding energies than for $SD_{\#1\,etched}$. Ni 2p: the peak satellites disappear, the new peak shape and position indicate Ni_2Si; O1s: the NiO_y species disappears; C 1s: the new species can be tagged as graphite; Si 2p: a matching Ni_2Si species further confirms the presence of nickel silicide. Each region is normalized independently.*

evaporation rate to 1×10^{-9} kg cm^{-2} s^{-1}, only considering the five minutes at 850 °C not the heating and cooling periods. Compared to the maximum molar flux $\dot{\eta}_{max}$ of 6×10^{-11} kg cm^{-2} s^{-1} for Ni at 850 °C it is obvious that the necessary rate can not be achieved by evaporation [156]. At least 925 °C would have been necessary to explain the observed nickel loss as simple evaporation. Neither is the possible formation of nickel oxide an explanation, as nickel oxide has a lower evaporation rate at the same temperature [157].

Instead one could argue, that the nickel loss is the result of nickel diffusion into the 3C SiC. Once it had diffused beneath the XPS measurement depth it would not appear in the XPS spectra any longer. However, in this case the nickel concentration should display a gradient function profile, where the nickel concentration is highest close to the interface and diminishes with increasing depth. This kind of gradient should then give rise to a number of different nickel silicide species in dependence of depth, like $NiSi_2$, NiSi and Ni_2Si. But, as discussed a little bit further down, only Ni_2Si is present, thus nickel diffusion can be ruled out as reason for the nickel deficit.

While not perfect, nickel evaporation seems to be the best explanation. If the temperature measurement with the pyrometer has as much as a 10 % error, the sample temperature would actually be high enough for nickel evaporation to be a reasonable explanation. Should such an uncertainty in the temperature measurement be the reason, it would be similar for all annealing procedures performed in the context of this work, thus not limiting reproducibility.

Because of the reduced nickel amount on $SD_{\#1\,etched}^{Ni2Si}$ the XPS detail spectra from the second Ni deposition step are displayed along with the detail spectra of the annealed sample in figure 6.10. The total amount of nickel on both samples is very close and thus allows a good comparison of the effect.

Besides the signal intensity increase in the Ni 2p region, annealing also results in a change in the nickel peak shape. The satellite peaks characteristic for metallic nickel disappear. This confirms the formation of a new species at 853.25 eV. As it is known that annealing in this temperature range leads to the formation of nickel silicide it may be expected that all remaining nickel is in the form of nickel silicide. The formation of nickel silicides at a silicon nickel interface was studied by Cheung et al. and Cao et al. [158, 159] for Ni layers on bulk Si and vice versa in a broad temperature range via XPS and XRD. In their work it was shown that the Ni 2p peak position is a reliable way of identifying the nickel silicide species, while the corresponding peak in the Si 2p region shows little to no change in its position for the various species.

Comparing the observed peak position at 853.25 eV with the reported values of 853.5 to 853.9 eV for NiSi and 853 to 853.4 eV for Ni_2Si implies that the formed nickel silicide is Ni_2Si [158–160]. This is in good agreement with further studies, which all reported the formation of Ni_2Si for SiC / Ni contacts in this temperature range [136,142,161,162]. Furthermore the rather small FWHM of 0.86 eV is a strong indication that only one nickel silicide species is present.

The presence of Ni_2Si instead of any other nickel silicide species can be double checked via the Ni:Si ratio, as determined from $Ni_{2p3/2}^{Ni_2Si}$ and $Si_{2p}^{Ni_2Si}$. Due to the layered nature of the sample at this stage of the experiment, a thin film correction [67] had to be applied to the component areas before the calculation, see chapter 3.1. As the derived ratio of 1.8:1 is reasonable close the expected value of 2:1, one can consider the presence of Ni_2Si as confirmed. With the nickel silicide species known, the Ni_2Si layer thickness can be calculated according to equation 3.4. The resulting (3.1 ± 0.3) Å resembles about one monolayer.

In the O 1s region, the additional oxygen species O_{1s}^{NiOy} disappears completely. The observed peak shape and position are comparable to $SD_{\#1\,etched}$, but shifted to higher binding energies. From metal contacts to pure silicon it is known, that nickel atoms can diffuse through a thin silicon oxide layer in order to form nickel silicide with the subjacent bulk silicon [163,164]. Similarly, the mixed Si—OH / C—H layer does not inhibit nickel silicide formation.

In the C 1s region one can observe the appearance of a new species at 284.33 eV. From peak position and line shape it would be in excellent agreement with the carbon sp^2 bond, which is characteristic for graphite and graphene [165]. As the peak positions of these two materials tend to overlap in the range from 284.1 to 284.8 eV [166–168] differentiation from peak position alone is impossible. However, an estimate of the carbon layer thickness (equation 3.5) yields about (11 ± 1) Å. This would correspond to ca. three carbon monolayers, thus it is graphite. Furthermore it indicates that the annealing lead to silicon depletion, about two monolayers of SiC Si which were formerly bound to the carbon now forming the graphite layer.

The graphene formation on clean SiC surfaces is well known and actually quite exciting. But it usually occurs at temperatures above 1250 °C [114, 165, 169]. This is not the case in nickel covered SiC though. Instead, graphite formation has been reported for temperatures below 1000 °C [159] as result of carbon atom displacement from nickel atoms during nickel silicide formation [161].

In the Si 2p region one new species comes into existence at 99.56 eV. As discussed above it corresponds well with Ni_2Si. The $Si^{SiC}_{2p3/2}$ core level of $SD^{Ni2Si}_{\#1\,etched}$ is located at 100.90 eV, compared to 100.63 eV for $SD^{1.9\,Å\,Ni}_{\#1\,etched}$ and 100.85 eV for $SD_{\#1\,etched}$. Before the annealing step the sample displayed upward band bending, as the core levels were shifted to lower binding energies than the 100.85 eV for $SD_{\#1\,etched}$, which correspond to a flat band like band alignment. Post annealing the $Si^{SiC}_{2p3/2}$ component is shifted 50 meV to higher binding energies, which corresponds to a downward band bending in the 3C SiC.

As mentioned above, while discussing the necessity of thin film corrections, the sample is a layered system now, with 3C SiC, Ni_2Si and graphite. While it is obvious that the bottommost layer has to be 3C SiC, the order of the remaining two is not quite as self-explanatory.

Both, the Ni 2p and Ni 3p region were measured for $SD^{Ni2Si}_{\#1\,etched}$. The electrons responsible for these peaks exhibit very different kinetic energies, about 634 eV for Ni 2p and 1420 eV for Ni 3p. Because of that their inelastic mean free path lengths λ_A in graphite differ significantly, with values of 11.6 Å for Ni 2p and 21.59 Å for Ni 3p. This means that an overlaying graphite layer would result in a much stronger dampening for the Ni 2p region than for the Ni 3p region. As the Ni_{2p}:Ni_{3p} ratio is 0.71 (opposed to 1.02 before annealing) this is obviously the case. This ratio and the inelastic mean free path lengths from above can be used for a calculation of the overlaying graphite layer thickness via equation 3.5. The resulting graphite layer thickness (8.5 ± 2.6) Å is in good agreement with the (11 ± 1) Å from the $C^{graphite}_{1s}$:C^{SiC}_{1s} ratio using the same equations. It can be concluded that the sample layer order is: (bulk) 3C SiC, Ni_2Si, graphite.

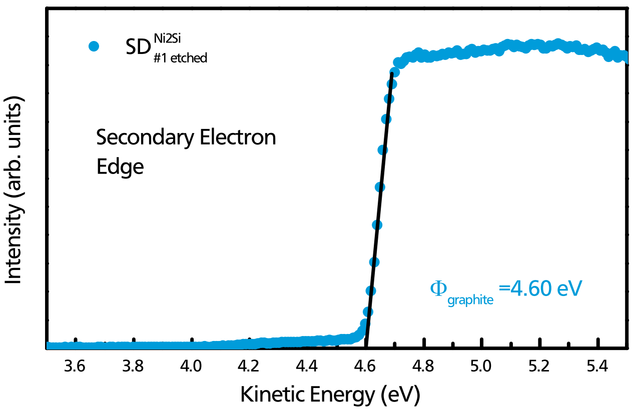

Figure 6.11.: *XPS detail spectrum of* $SD^{Ni2Si}_{\#1\,etched}$*s secondary electron edge. The determined intersect with the abscissa of* 4.60 eV *is in excellent agreement with the work function of graphite.*

Graphite as uppermost layer is further confirmed by the work function observed for the annealed sample, see figure 6.11. As the work function is determined from the very surface, it should only be dependent on the nature of the uppermost layer. The observed value of 4.60 eV is in excellent agreement with literature values of graphite [170].

All the above information can be used to draw a final band diagram of the situation in the annealed sample. This band diagram is displayed in figure 6.12. The most apparent change, compared to the un-annealed sample in figure 6.9, is the reversal of band bending in 3C SiC as result of the 3C SiC / Ni_2Si interface formation. For the 3C SiC / Ni interface the band bending was 0.35 eV upward. Now, for the 3C SiC / Ni_2Si interface it is 0.06 eV downward. Exactly this behaviour is what one would expect from a semiconductor in ohmic contact to a metal.

The obvious explanation for this behaviour is Fermi level matching between 3C SiC (Φ_{3C}) and Ni_2Si (Φ_{Ni_2Si}). While the Φ_{3C} is already known, Φ_{Ni_2Si}

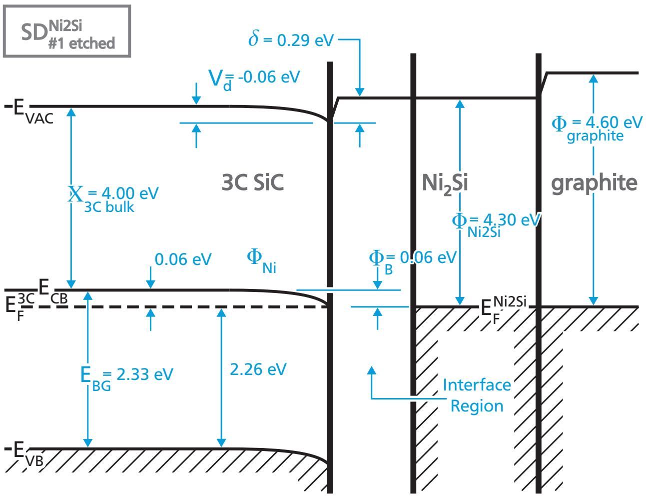

Figure 6.12.: *Band structure diagram of* $SD^{Ni2Si}_{\#1\ etched}$. *Annealing induced nickel diffusion resulted in the formation of* Ni_2Si. *Contrary to the 3C SiC / Ni interface, the 3C SiC /* Ni_2Si *interface shows a* 0.06 eV *downward band bending. This is the characteristic behaviour of an ohmic semiconductor / metal contact.*

can not be determined via XPS as the Ni_2Si is covered by graphite. Biswas et al. examined the nickel silicide work function in dependence of the Ni:Si ratio and reported values between 4.3 eV for Si_2Ni and 4.55 eV for $NiSi_2$ [171]. As discussed above, the nickel silicide species in $SD^{Ni2Si}_{\#1\ etched}$ was identified as Ni_2Si, thus $\Phi_{Ni_2Si} = 4.30$ eV is assumed. This value is 0.32 eV below the 3C SiC surface work function $\Phi_{3C\ surface}$ and electrons from the nickel silicide will flow into the 3C SiC, creating an electron rich interface layer and thus induce downward band bending in the 3C SiC.

With 0.06 eV the observed band bending is lower than the difference in work functions. However, in this case it is to be expected, as the Fermi level reaches the conduction band at this point. Due to the higher density of states in the conduction band the remaining electrons, to be exchanged for Fermi level adjustment, will be localized in an extremely thin layer at the surface. This is basically a dipolar potential and as such will not be observable in XPS. Thus Fermi level alignment is achieved from a combination of diffusion potential (band bending over a measurable depletion layer) and a dipolar potential shift.

In pure silicon nickel / contacts another effect is known to occur. There, nickel silicide formation results in a displacement of dopant atoms. The dopants are further displaced as the silicide front moves, thus creating an accumulation right at the interface. Over the course of the nickel silicide growth this can give rise to a significant increase in doping concentration in the silicon right at the interface [163, 172]. Higher doping concentrations also mean better contacts. However, as only about six monolayers of SiC are transformed into Ni_2Si respective graphite the amount of displaced dopants would not be sufficient to explain the observed effects. Therefore the observed band bending, and thus the ohmic nature of annealed Ni / 3C SiC contacts has to be ascribed to the favourable Fermi level matching between 3C SiC and Ni_2Si.

6.4 Conclusion

This chapter was focused on the investigation of nickel for the production of ohmic contacts to n-type 3C SiC. To the authors best knowledge, there are no comparable studies of the changes in band allocation during nickel contact formation and annealing for 3C SiC. Previous studies were mostly focused on the electrical properties [139–142] or observing the changes in nickel silicide species with temperature [161].

The 3C SiC / Ni contact was prepared in a fashion commonly found in literature. A single domain 3C SiC sample ($SD_{\#1\ etched}$) employed for all experiments in this chapter was wet chemically etched. Subsequent experiments confirmed a clean sample surface, with 1x1 surface reconstruction in form of a mixed Si—OH / C—H termination, and flat band conditions. Upon nickel deposition of up to (28.5 ± 0.9) Å upward band bending was observed as result of Fermi level matching. This behaviour is expected for a Schottky type contact, confirming the numerous reports that un-annealed Ni / 3C SiC contacts are not ohmic. However the observed band bending of up to 0.35 eV remained below the expected value of 0.53 eV. This was ascribed to Fermi level pinning in the 3C SiC as result of surface states.

Five minutes of annealing at 850 °C resulted in the formation of nickel silicide and graphite atop the 3C SiC sample. From the Ni 2p peak position and the observed intensity ratios the nickel silicide species could be determined as Ni_2Si. The new, layered sample structure is: (bulk) 3C SiC, Ni_2Si, graphite. As result of the new 3C SiC / Ni_2Si interface the former upward band bending is changed to 0.06 eV downward band bending. This is the behaviour expected for ohmic contacts. Therefore the ohmic nature of annealed 3C SiC nickel contacts can be identified as a result of the favourable Fermi level matching between 3C SiC and Ni_2Si.

Ohmic Back Contacts To 3C SiC

Method and parameters described in this chapter were also employed to produce ohmic 3C SiC / Ni contacts to all other 3C SiC samples discussed in this work. The only difference being that only one nickel deposition step was performed, instead of multiple separate steps. This single step was performed at higher power (50 W compared to the 10 W employed in this chapter) and an extended duration of about five minutes in order to achieve a higher nickel layer thickness.

6.5 Appendix: TLM Measurements

At a later date the same sample $SD_{\#1}$ was used for determining the specific contact resistance of the annealed 3C SiC / Ni contacts via the transfer length method (TLM). The interface experiment was performed on the original sample surface. Contrary the TLM measurements were performed on the (0.25 μm) polished sample. Otherwise the contacts were prepared following the same preparation procedure discussed in the 'Experimental Procedure' section of this chapter. A simple linear contact pattern, displayed on the top of figure 6.13, was created by using an evaporation mask.

UI Measurements were performed between two adjacent contacts respectively, and the resulting re-

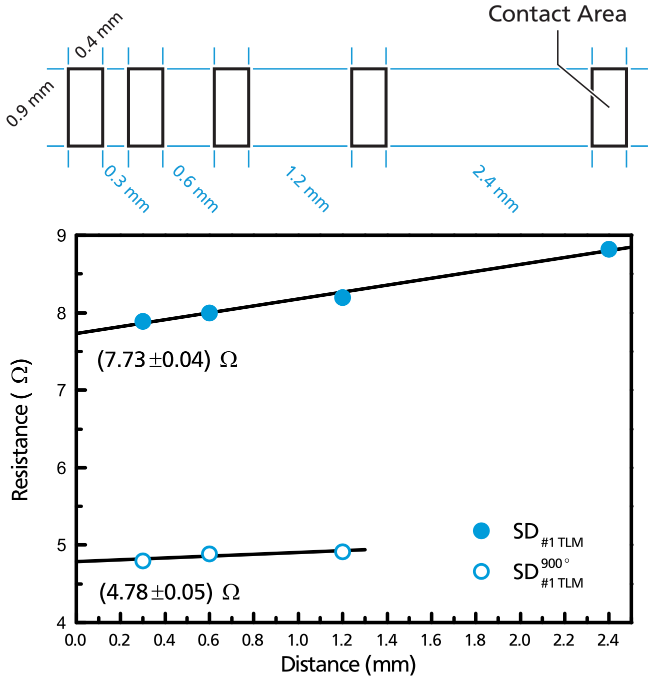

Figure 6.13.: *Top: TLM pattern used for contact resistance determination of $SD_{\#1}$. Bottom: The determined resistance between two adjacent contacts on $SD^{TLM}_{\#1\, polish\, (0.25\,\mu m)}$ were employed for determining the specific contact resistance [62]. Because $SD_{\#1}$ broke during transfer to the annealing chamber, only the four contacts on the left side could be used on $SD^{TLM\; 900\,°C}_{\#1\, polish\, (0.25\,\mu m)}$.*

sistance was plotted over the contact distance, see bottom of figure 6.13. The measured total resistance

$$R_T = R_{sh}\frac{d}{W} + 2R_c \tag{6.1}$$

is a function of the sheet resistance R_{sh}, semiconductor width W, contact distance d and contact resistance R_c [62]. R_T for $d = 0$ can be extrapolated from the ordinate intercept, yielding an R_c of $(3.87 \pm 0.02)\,\Omega$ for the un-annealed and $(2.39 \pm 0.03)\,\Omega$ for the annealed contacts. Considering the contact dimensions this yields a specific contact resistances

$$\rho_c(\text{as is}) = 1.4 \times 10^{-2}\,\Omega\text{cm}^{-2}$$

$$\rho_c(\text{annealed}) = 8.6 \times 10^{-3}\,\Omega\text{cm}^{-2}$$

As one can see, the annealing does result in the expected improvement of ρ_c. However, this study was just intended as a quick survey. Therefore neither the influence of the semiconductor dimensions (the sample was not cut in order to reduce W), nor current crowding at the contact edges or the surface morphology were taken into account [62, 141].

The annealed 3C SiC / nickel contact has been examined many times by various researches. Almost all them employing TLM, in order to measure ρ_c in dependence of annealing temperature, surface preparation, doping etc. A quick search yielded values from as high as $8.64 \times 10^{-1}\,\Omega\text{cm}^{-2}$ to very low values in the range of $1.4 \times 10^{-5}\,\Omega\text{cm}^{-2}$ [22, 139–142, 173].

As the effective contact area for the water splitting experiments in the next chapters will be approximately one square centimetre, the resulting resistance from the contact will be negligible in comparison to the approx. $100\,\Omega$ contribution from the electrolyte. There it is more important that the back contact exhibits ohmic behaviour in the investigated potential range, in order to prevent it from influencing the electrochemical impedance spectroscopy (EIS) measurements. Because the annealed contact shows ohmic UI behaviour in the range from -2 to +2 V this will be sufficient.

7

Single Domain Bulk 3C SiC For Water Splitting Applications

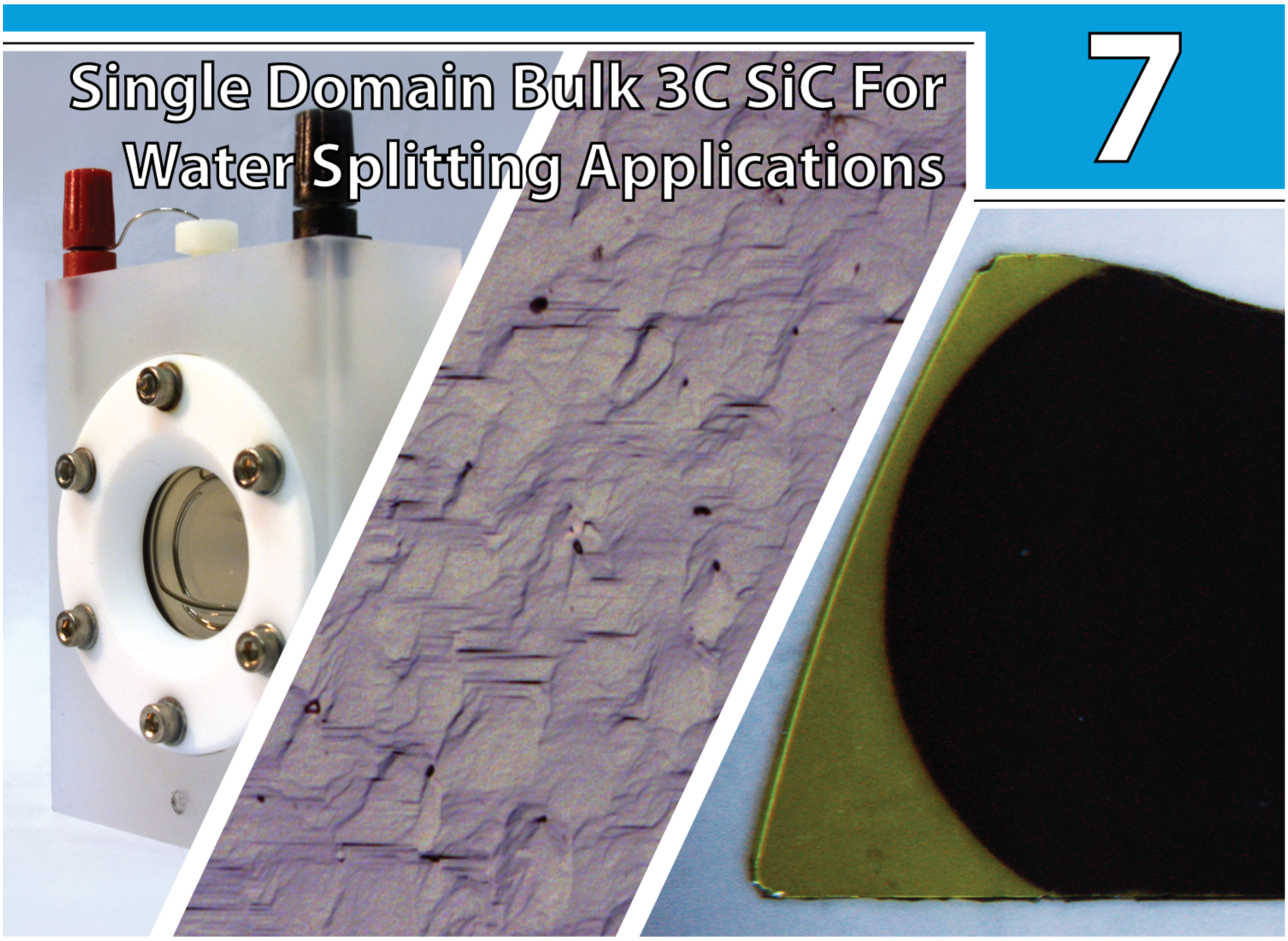

The main topic of this work is 3C SiCs suitability for direct photoelectrochemical water splitting. As single domain 3C is the simplest case, neither substrate interfaces nor grain boundaries have to be taken into account, it will be discussed first in context of the two available samples $SD_{\#1}$ $SD_{\#2}$. The more complex cases can be found in the following chapters. Therefore this chapter will give an introduction to the presentation of electrochemical data, along with its interpretation and conclusions drawn in regard of 3C SiCs performance. Applied measurement methods are XPS, UV-Vis spectroscopy, Raman spectroscopy and a number of electrochemical techniques like cyclic voltammetry, chopped light measurements, impedance spectroscopy and others.

7.1 Introduction

This chapter will be the first to directly deal with the actual topic of this work: the eligibility of cubic silicon carbide (3C SiC) for direct photoelectrochemical water splitting. It will therefore include some introductions regarding electrochemical (EC) measurements, their evaluation and interpretation. The following chapters all deal with EC data and will build upon the foundation established within this chapter.

A multitude of effects can influence EC measurements. In order to minimize those, this first EC chapter will deal with single domain bulk 3C. As there are no additional interfaces, grain boundaries or catalyst overlayers to be considered this simplest case will be discussed first. From there, the following chapters will deal with more complex systems: 3C SiC on substrates in chapter 8, and catalyst heterostructures in chapter 9.

7.2 Experimental Procedure

This chapter is focused on the electrochemical characterisation of (001) single domain cubic silicon carbide (3C SiC) samples. Two samples were

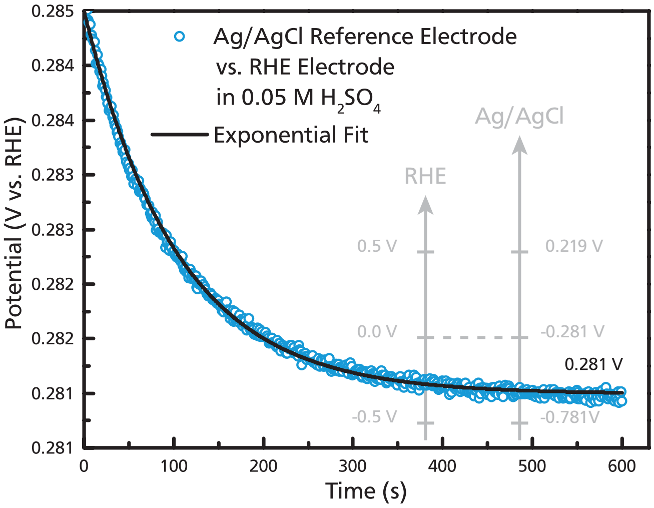

Figure 7.1.: *Open circuit potential (OCP) at zero current of a silver / silver-chloride (Ag/AgCl) reference electrode versus a reducible hydrogen electrode (RHE) used for calibration. The relation between the RHE scale and the reference electrode is displayed in light gray.*

investigated, the first $SD_{\#1}$ is $(191 \pm 5)\,\mu$m, the second $SD_{\#2}$ is $(152 \pm 5)\,\mu$m thick. Both samples discussed were grown via CVD by Hoya Cooperation [143]. As part of an early stage commercial wafer, the sample displays a high level of residual strain distributed in-homogeneously through the crystal volume, as well as a high planar defect density. Before the electrochemical characterisation an ohmic (annealed-) nickel back contact was deposited on the sample backside according to the procedure described in chapter 6.

Sample Nomenclature

Most experiments discussed in this chapter were performed on $\mathbf{SD}_{\#2}$. For electrochemical measurements the **sample preparation** will be added as **subscript** as before. As no further treatment (like annealing etc.) occurred over the course of the experiments, the **superscript** is used to supply the **electrolyte** employed for the measurements, as in $\mathbf{SD}_{\#2}^{\mathbf{0.05M\ H2SO4}}$.

OCP, EIS, CV and Chopped Light (Zahner)

Most electrochemical measurements were performed with a Zahner potentiostat. The only exception were series impedance measurements, which were mostly performed at a Gamry setup, see chapter 3.5.

Previous to any electrochemical experiment the sample was prepared as required. For most experiments this means it was etched with piranha solution and submitted to a subsequent oxide removal step in ammonium fluoride in order to supply a clean and comparable surface, as described in chapter 5. In order to prevent damage to the back contact, droplet instead of immersion etching was performed.

Each electrochemical experiment was started with the calibration of the reference electrode. All experiments discussed in this chapter were performed with Ag/AgCl reference electrodes. For the calibration about 25 ml of the chosen electrolyte were given into a clean glass beaker and bubbled with nitrogen in order to remove dissolved oxygen. Both, the Ag/AgCl and a reducible hydrogen electrode (RHE) were then placed in the bubbled electrolyte and the open circuit potential (OCP) between them was recorded as displayed in figure 7.1. The OCP measurement was performed for 10 to 20 minutes or until the potential remained constant and the obtained saturation value was then used to select the appropriate measurement ranges for the remaining measurements of this experiment. This relation between the potentials versus the Ag/AgCl and the RHE electrodes can also be seen in figure 7.1 (light grey).

During the reference electrode calibration the EC cell parts were thoroughly cleaned with millipore water, subsequently the cell was assembled with the sample inside. Once the calibration was complete, the electrolyte used for the calibration was bubbled with nitrogen once more and funnelled into the electrochemical cell. The EC cell was then mounted in the measurement setup at a fixed distance from the selected LED.

LEDs of different wavelengths and intensities were available, if not noted otherwise a blue LED with a peak wavelength of 455 nm was employed. Finally, the reference electrode was inserted, the potentiostat connected, and a light-tight cover was placed over the EC cell, in order to prohibit external light from influencing the measurement.

EIS for Mott-Schottky (Gamry)

The series EIS measurements for the Mott-Schottky plots were performed with a Gamry setup. Sample preparation was identical, but the 'Experimental EC Mott Schottky Procedure' was performed instead of the 'Experimental EC Standard Procedure'.

Experimental EC Standard Procedure

1. Reference Electrode **Calibration**
2. Open circuit potential (**OCP**)
3. Electrochemical impedance spectroscopy (**EIS**)
4. Chopped light measurement
5. Cyclic voltammetry (**CV**) in the **dark**
6. **OCP** with **illumination** pulse

Experimental EC Mott Schottky Procedure

1. Reference Electrode **Calibration**
2. Open circuit potential (**OCP**)
3. Automated (**EIS**) series
   step width: 0.05 V with 30 s breaks
   frequency range: 0.5 to 10 000 Hz

For further details and information on the experimental methods and employed equipment see chapter 3.

7.3 Results and Discussion - On the Measurement Methods

EC Measurements: Necessary Corrections

While the investigated electrode and its interfaces are to be investigated, a possible contribution from the measurement setup has to be considered as

Assembling The EC Cell Correctly

While **assembling** the **EC cell** prior to any experiment a number of common **mistakes** can **impair** the subsequent measurements:

1. If the **O-ring** is not positioned correctly, **leakage** of the electrolyte can occur. Should the leaked electrolyte touch the EC backplate there is a **short**, this is equivalent to a (small) resistor in parallel to the sample.
2. While funnelling the electrolyte into the EC cell, care has to be taken to **avoid air bubbles** on the **sample surface**. As those would reduce the reactive sample surface area in contact with the electrolyte, depending on the amount of bubbles a substantial **decrease in current** can occur.
3. **Air bubbles** can also stick to the **tip** of the **reference electrode** while it is introduced into the EC cell. This results in totally **random behaviour** of the **current voltage** relation, as the reference electrode is essentially isolated from the sample.

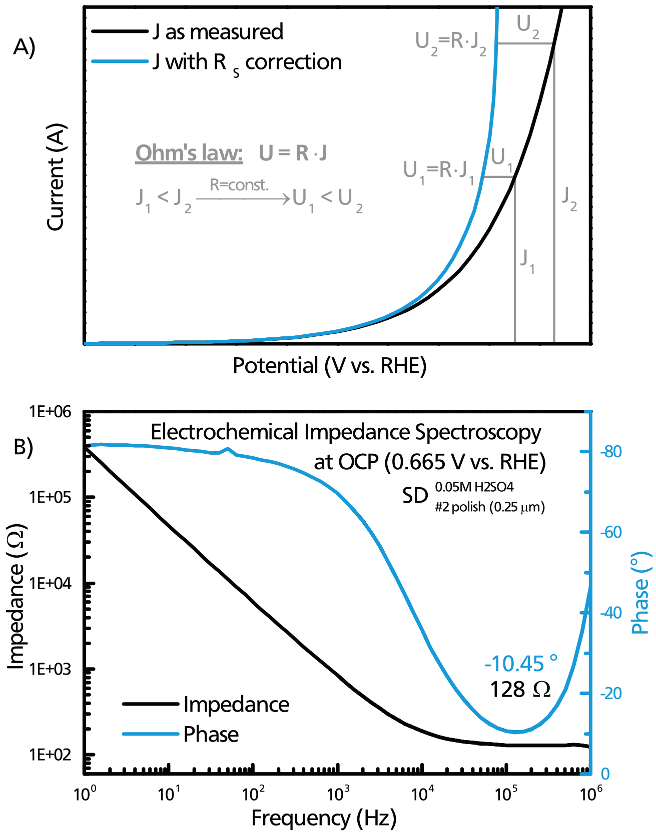

Figure 7.2.: *A) How Ohm's law affects the data upon voltage drop correction for R_S B) Bode plot of the $SD_{\#2}$ EIS measurement used for the determination of $R_S = 128\,\Omega$. The obtained R_S values were used to correct for the setup resistance in the subsequent measurements. See text for a discussion of the correction and the reason for the rising phase at high frequencies.*

well. It will exhibit a total resistance R_S, most of it a contribution of the electrolyte. The actual value will be dependent on the cell geometry. However, the measurements should be corrected for the voltage drop over R_S, in order to ensure comparability between measurements in different experimental setups or with various electrolytes.

Once R_S is known, the voltage drop can easily be obtained from

$$U = R \cdot J \tag{7.1}$$

Ohm's law, where U is the voltage drop occurring for the current J passing through a resistance R. The correction effect on current voltage curve is displayed in figure 7.2 A). In the anodic regime the correction results in a shift to lower potentials. Because R_S is constant a higher current density J will result in a stronger shift. The experimental setups serial resistance R_S (R_0 in chapter 3.5) can be obtained via electrochemical impedance spectroscopy (EIS) at high frequencies, assuming the setup can be represented accurately by a Randles cell as equivalent circuit.

Figure 7.2 B) shows the EIS measurement performed for $SD_{\#2}$ at open circuit potential (0.665 V vs RHE) in 0.05 M H_2SO_4. The obtained R_S of 128 Ω was used for potential corrections in all subsequent measurements. A similar procedure was repeated for all the EC experiments discussed in this work. However, the resulting shifts are rather small. For a current density of $100\,\mu\text{A/cm}^2$ it would amount to 0.012 V

Contrary to the expected behaviour the phase in figure 7.2 B) rises again for high frequencies. This has nothing to do with the 3C sample, but can instead be traced back to the reference electrode. The thin membrane at the tip of the reference electrode has a certain impedance as well, and gives rise to this behaviour. One can prevent this effect by placing a platinum wire next to the reference electrodes tip and connect it via a small capacitance (20 nF to 100 nF) to the reference electrode [28, 174]. Control measurements, performed with this setup in place, showed that the 3C SiC samples have no features in this frequency range, thus the effected high frequency region can simply be ignored. Therefore further measurements were performed without the platinum wire/capacity setup, as the correct placement proved to be quite difficult and time consuming.

Photocurrent Response Measurements

As the 3C SiC samples $SD_{\#1}$ and $SD_{\#2}$ are both n-type they are suitable for the oxygen evolution reaction (OER) in the anodic region, see chapter 2.2

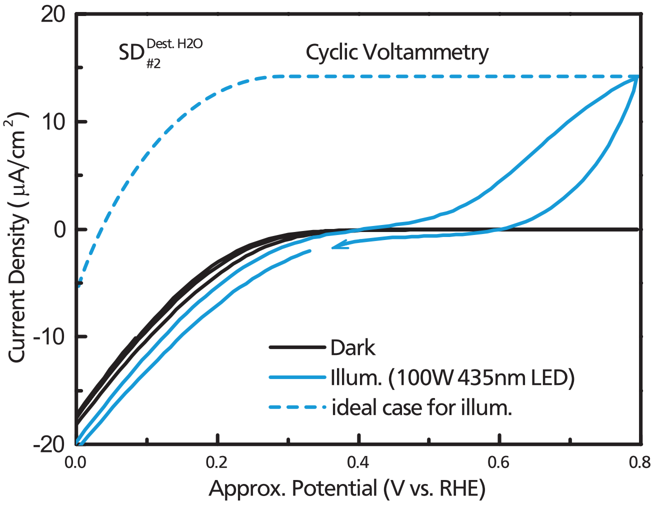

Figure 7.3.: *CV of $SD_{\#2}$ in the dark and under illumination in comparison to the approx. shape of the ideal curve under illumination. As the experiment was performed in dest. water, the (V vs. RHE) should only be understood as an approximate value.*

for general information on the direct photoelectrochemical water splitting process. A very first test measurement on $SD_{\#2}$ is displayed in figure 7.3. It was not performed while following the standard experimental procedure, and the cyclic voltammetry measurements (CV) was performed in distilled water, in order to affect the sample as little as possible. The chosen electrolyte might result in pH changes over the course of the measurement, thus preventing a precise conversions to V vs. RHE, but it is sufficient for a first impression of the overall electrochemical behaviour of 3C SiC.

As expected, there is no anodic current in the dark, as there are no holes which could take part in the OER, see equation 2.15. This curve is called the dark current. However, under illumination with a blue LED, there clearly is a photocurrent, as the CV curve shows a positive/anodic current for potentials exceeding 0.2 V vs RHE. This is the result of photo-generated holes participating in the OER. It is obvious though, that the observed curve is quite different from the ideal curve expected for such a setup, where the photocurrent onset should be far in the cathodic regime. Ideally the curve would then saturate before the origin, making maximum use of all photogenerated holes without the need for an external bias potential. As will be discussed later in this chapter, this deviation is the result of insufficient photovoltage.

CV measurements performed under constant illumination give information about the steady state photocurrent. While this is the relevant value for devices, as they are intended to run continuously for an extended duration, CV does not show some aspects of the process, which are of interest in understanding the problems of this system. This is why the data in this chapter was mostly generated from chopped light measurements, see figure 7.4. As shown, a single chopped light measurement allows the determination of both, steady state photocurrent $J^{s.state}$ and the dark current J^{dark}. Furthermore it gives information on the onset photocurrent J^{onset} and the kinetic processes taking place.

The chopped light measurements were performed with two second light pulses. This interval works well for most of the measurement range, providing sufficient data points, while giving the system enough time to settle into its final state, before the pulse ends. And then again before the next pulse starts. However, for potentials exceeding approx. 1.4 V vs RHE the two seconds of darkness are no longer sufficient for the system to reach equilibrium. This is obvious from the dark current (white areas in figure 7.4) in this potential range still changing rapidly, before the next light pulse hits. For correction, the measurement was repeated with the same parameters, but completely in the dark, yielding a significantly lower dark current.

In the dark, no holes are available for the OER, thus, the dark current should be zero. The occurrence of a positive net current in the dark indicates the presence of a parasitic reaction, most likely anodic dissolution or oxidation of the 3C SiC sample.

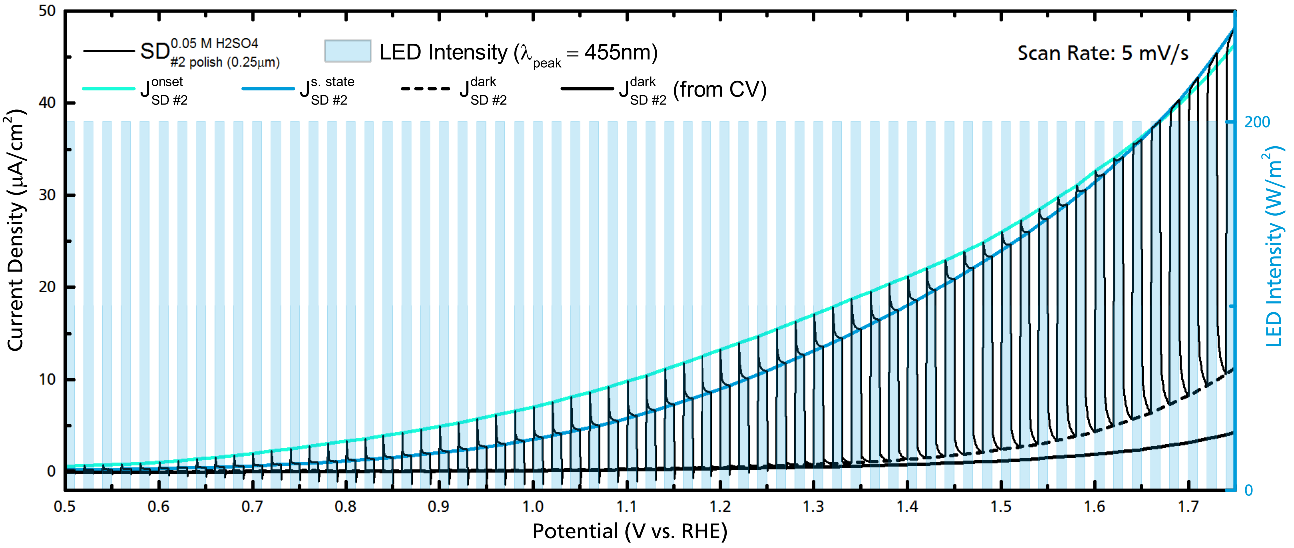

Figure 7.4.: *Detail of an electrochemical chopped light measurement, performed on the polished* (0.25 µm) $SD_{\#2}$ *in* 0.05 M H_2SO_4*. The chopped light measurement was used to determine the onset photocurrent* ($J^{onset}_{\#2}$*: light blue), steady state photocurrent* ($J^{s.state}_{\#2}$*: blue) and the dark current* ($J^{dark}_{\#2}$*: black dash). For comparison of the dark currents a CV measurement in the dark was added* ($J^{dark}_{\#2}$*: black). The scan rate for both measurements was* 5 mV/s.

Illumination might increase the parasitic reaction rate further. Thus, the observed current densities in a potential range, where a significant dark current contribution is observed, have to be considered with caution. A part of it might be the result of photocorrosion, a subject discussed further below.

Chopped Light Transients

As mentioned before chopped light measurements can provide some insight on the kinetics and how those change with varying potential. While the kinetics of electrochemical reactions are more frequently investigated via measurements with rotating ring disk electrodes [58, 175, 176] or intensity modulated photocurrent spectroscopy (IMPS) [177–179], some of those insights can be approximated from chopped light measurements. Figure 7.5 displays the current response (transients) over time for six light pulses at different potentials, excerpts from figure 7.4. They all display a step increase of current upon illumination, a result of photogenerated hole electron pairs being separated, with the holes moving toward the surface and the electrons toward the bulk.

Once an equilibrium between hole generation and loss (either through recombination or transfer into the electrolyte) is formed, the current increase stops at the onset current (J^{onset}). Should the arrival of new holes at the surface exceed the transfer across the interface (J_{tr}), holes will accumulate at the surface. The increased hole density will induce a responding electron flux to the surface, where holes and electrons recombine (J_{rec}), see figure 7.6 for a schematic presentation [59]. At some point another equilibrium is reached and the steady state current ($J^{s.state}$) remains constant.

This recombination current is responsible for the characteristic current decrease following the onset peak observed in figure 7.5. As a result of recombination the current is reduced to less than half the J^{onset} value at lower potentials near photocurrent onset. The effect decreases at more anodic potentials. For a more detailed evaluation one can model the time dependent behaviour of the above system, where only interface transfer and recombination

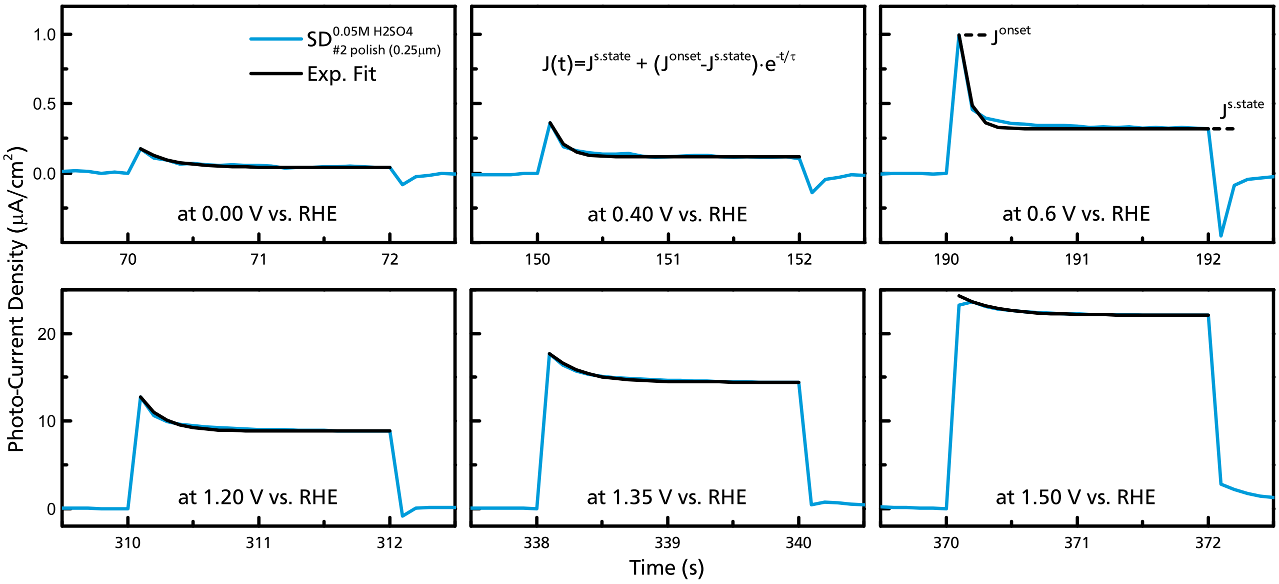

Figure 7.5.: *Some examples of the transient photocurrent response for the polished* (0.25 μm) *$SD_{\#2}$ in 0.05 M H_2SO_4. The sample was illuminated at* 200 W/m^2 *with a blue LED* ($\lambda_{\text{peak}} = 455$ nm) *for two second intervals and at various applied potentials in the context of a chopped light measurement. An exponential fit, according to equation 7.2 was used to determine the time constant τ from the transients line shape. The temporal resolution* (0.1 s *steps) of the measurements, will result in a certain inaccuracy regarding the value of J^{onset}.*

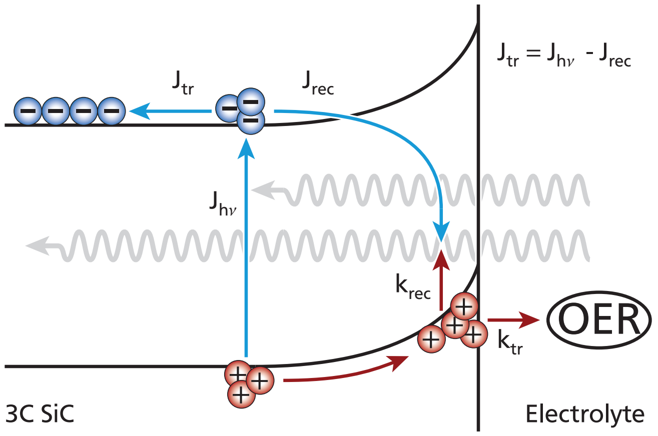

Figure 7.6.: *Graphic of the equilibrium between charge transfer and recombination at the 3C SiC / electrolyte interface under illumination. $J_{h\nu}$, J_{tr} and J_{rec} are current densities, while k_{tr} and k_{rec} describe the corresponding rate constants.*

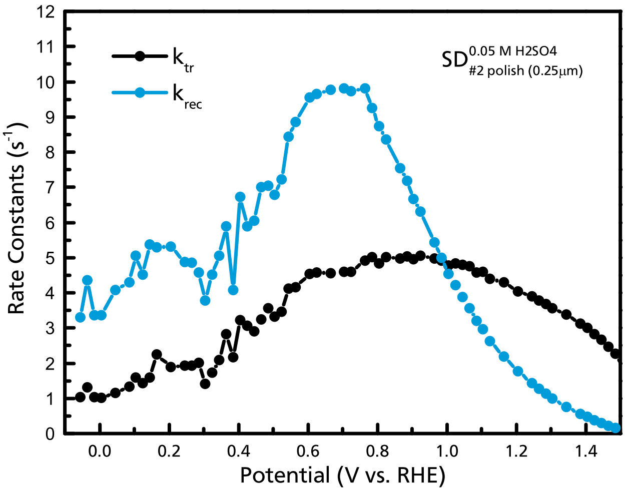

Figure 7.7.: *Rate constants for interface transfer (k_{tr}) and recombination (k_{rec}) in $SD_{\#2}$. Determined via fitting the time dependant transients of the chopped light response according to equations 7.2 to 7.4.*

near the surface are considered [59,177,180]. The time dependent decrease in current $J(t)$ following the onset peak is then given by

$$\frac{J(t)-J^{s.state}}{J^{onset}-J^{s.state}}=\exp(-t/\tau) \quad , \tag{7.2}$$

where t is the time and

$$\tau=(k_{tr}+k_{rec})^{-1} \tag{7.3}$$

is the time constant. Equations 7.2 and 7.2, in combination with

$$\frac{J^{s.state}}{J^{onset}}=\frac{k_{tr}}{k_{tr}+k_{rec}} \tag{7.4}$$

the current relation eq. 7.4, allow an approximation of the transfer (k_{tr}) and recombination (k_{rec}) rate constants from the exponential fits displayed in figure 7.5.

The obtained k_{tr} and k_{rec} values are displayed in figure 7.7 as a function of the applied potential. Both rate constants are comparable to those reported for hematite (α—Fe_2O_3) in magnitude [59]. Further evaluation is difficult due to lack of detailed information on the energy positions of the various oxygen evolution reaction steps, and changes to the band bending (and thus depletion layer) in the semiconductor, which will be discussed later. Additionally, it is likely that the applied model (k_{tr} and k_{rec} only) is too simple. Other reaction paths, such as recombination and interface transfer via surface states, have to be included [178, 180]. For more information about possible models and the resulting time dependant differential equations, a study of the work by Ponomarev and Peter is recommended [180].

Nevertheless, one can draw some conclusions from this. For example, k_{rec} increases until approx. 0.8 V vs RHE, where a steep decrease occurs. In order for recombination to occur, both electrons and holes have to be available in close proximity, here most likely the 3C SiC / electrolyte interface. Assuming the applied bias potential drop occurs in the semiconductor, this would result in the concentration of free electrons in the conduction band to decrease with increasing bias potential, while the band bending increases.

Likewise, changes in k_{tr} are due to the density of states overlap between the hole quasi Fermi levels and the energy position of the first OER step. From the k_{tr} shape one could then argue, that this first step and the quasi Fermi level are aligned at approx. 0.9 V vs RHE. The k_{tr} decrease at higher potentials would then be a result of the difference between those two levels opening up again, at higher applied potentials. A limitation of suitable transfer sites could also result in a k_{tr} decrease for higher current densities.

Keeping the above considerations in mind, the following discussion will refer mostly to the onset and steady state current density, as their difference (or similarity) will give adequate information about the degree of recombination occurring at specific potentials. And as Laurence M. Peter, one of the pioneers in this area of research, wrote in 1990: "*...interpretation of photocurrent transients remains highly controversial after nearly a decade of investigation...*" [178].

7.4 Results and Discussion - OER With 3C SiC

As the comparison of multiple datasets of chopped light measurements is rather confusing, only the net photocurrent will be displayed. An example of this presentation is supplied in figure 7.8, which shows the full data range (only a part was displayed in fig. 7.4). The two blue lines give the corrected onset (J^{onset*}) and steady state ($J^{s.state*}$) photocurrent density for the polished (0.25 μm) $SD_{\#2}$ in 0.05M H_2SO_4, while the black line displays the dark current density (J^{dark}). Corrected means that the dark current at the respective po-

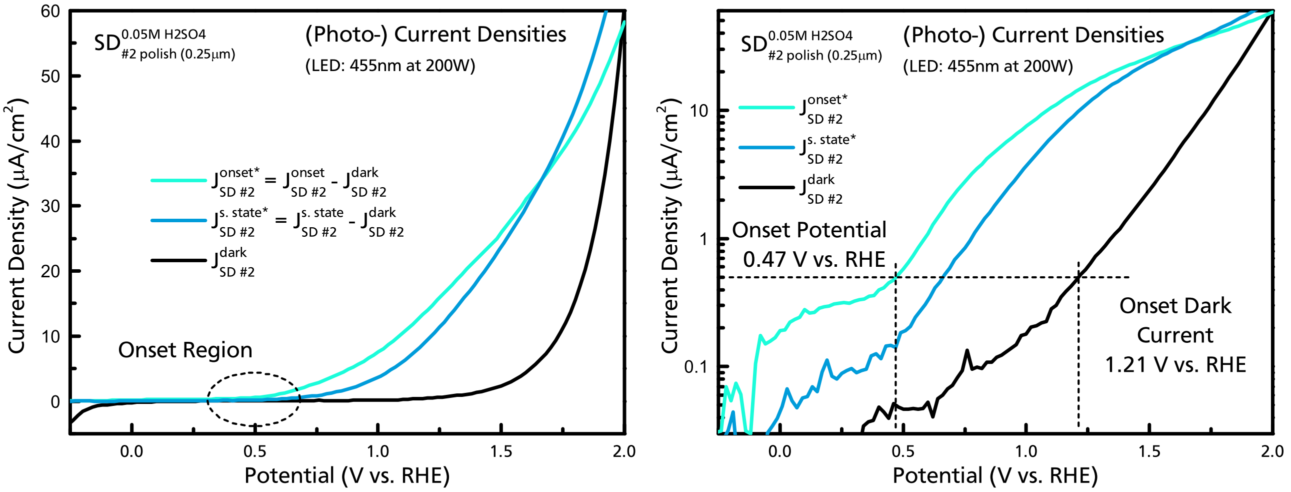

Figure 7.8.: *Corrected onset (J^{onset*}) and steady state ($J^{s.state*}$) photocurrent density for the polished* (0.25 μm) *$SD_{\#2}$ in 0.05M H_2SO_4. The same data is displayed for the current density in linear (left) and logarithmic (right) scale. From the starting point of the linear segment the photocurrent onset potential of* 0.47 V vs RHE *was determined, along with* 1.21 V vs RHE *for the dark current.*

tential has been subtracted from the photocurrent density ($J^{onset*} = J^{onset} - J^{dark}$ and $J^{s.state*} = J^{s.state} - J^{dark}$). Figure 7.8 gives the same data in linear (left) and logarithmic (right) scale for the current density. As the logarithmic scale allows a better examination of the onset region it will be used for most plots in the following discussion.

Onset- Photocurrent/Region/Potential

Onset Photocurrent describes the photocurrent density of the peak at the beginning of a chopped light illumination period. See J^{onset} in figure 7.5.

Onset Region describes the potential region where the current voltage behaviour in the dark and under illumination first starts to deviate. See figure 7.8 (left).

Onset Potential describes the actual potential where the photo-response and thus the OER starts to occur. The are numerous approaches on how this values is to be defined exactly (specific current etc.). Here defined as potential for $J^{onset*} = 0.5\,\mu\text{A/cm}^2$. See figure 7.8 (right).

Quantum Efficiency

The main values of interest will be the potential at which the OER starts to occur (onset potential), and then the photocurrent density at a given potential exceeding the onset potential.

The 'onset potential', is a common, but ill defined term in EC. As the curve shape is exponential, there is no clear intersection, neither can the rest potential E_r be used, as there is no information on the rate of the ORR. A common solution is the definition of a specific current density as onset potential in order to refer to the potential dependence. Here the onset potential will be defined as the potential, where the exponential (linear in a log scale plot) curve region shows a current density of 0.5 μA/cm^2. The lower the onset potential, the better.

Quite the opposite is true for the photocurrent density. However, in order for $J^{s.state*}$ to yield meaningful information, on the 3C SiC efficiency, it has to be considered in relation to the incident light. A higher light intensity will most likely result in higher photocurrents. For comparability, the quantum efficiencies should be considered instead.

Even then, the applied potential will strongly impact the obtained efficiencies. For an objective assessment of the performance, energy efficiency would be the best solution, see chapter 10.

There are two different definitions for quantum efficiency, the first being external quantum efficiency

$$\mathrm{EQE} = \frac{\text{current}}{\text{lightpower}} = \frac{\text{\# of electrons}}{\text{\# of photons}} \qquad (7.5)$$

, gives the ratio of charge carriers measured (photocurrent density) in relation to the amount of photons reaching the sample. The second is the internal quantum efficiency

$$\mathrm{IQE} = \frac{\text{current}}{\text{absorbed light}} = \frac{\text{\# of electrons}}{\text{\# of abs. photons}} \qquad (7.6)$$

and is defined as the ratio of measured charge carriers and photons actually absorbed in the sample. First, the reflection loss due to the whole experimental setup has to be considered. Because the angle of incidence is 90°, the Fresnel equations yield

$$R = \left(\frac{n_1 - n_2}{n_1 + n_2}\right)^2 \qquad (7.7)$$

for the reflectance [75]. From this, the reflection losses of an air/glass/electrolyte/ 3C SiC system can be approximated to 13 %, as displayed in figure 7.9. Considering the original intensity of 200 W/m^2, this means 174 W/m^2 at the 3C SiC surface. Using the photon energy

$$E = \frac{hc}{\lambda} = \frac{1240\,\mathrm{eV\,nm}}{\lambda[\mathrm{nm}]} = 4.37 \times 10^{-19}\,\mathrm{J} \qquad (7.8)$$

for a wavelength of 455 nm. One can determine the number of incident photons per cm^2

$$I_0 = \text{\# of photons} = \frac{P_\lambda}{E} = 3.98 \times 10^{16}\,\mathrm{s}^{-1}\,\mathrm{cm}^{-2} \qquad (7.9)$$

from the light intensity at the 3C SiC surface $P_\lambda = 1.74 \times 10^{-2}$ W/cm^2.

If each of those would be absorbed, form an electron-hole pair participating in the OER reaction and assuming a Faradaic efficiency of 100 % the resulting photocurrent should be 6.37 mA/cm^2. The maximum photocurrent measured for $SD^{0.05\ M\ H2SO4}_{\#2\ polish\ (0.25\mu\mathrm{m})}$ was 72.4 μA/cm^2.

Therefore the internal quantum efficiency

$$\mathrm{IQE}^{0.05\ \mathrm{M\ H2SO4}}_{\#2\ \mathrm{polish}\ (0.25\mu\mathrm{m})}(2\,\mathrm{V\ vs\ RHE}) = 0.011 \qquad (7.10)$$

, even at a high bias potential, is a very small value of 1.1 %. This value should be considered with caution, as part of that current could stem from sample degradation, which clearly occurs at this potential, as the dark current is nearly as high as the photocurrent. At lower bias potentials the IQE gets even worse. Measured without any bias voltage, as would be ideal, it is 0.003 % for the onset current, thus neglecting recombination. The IQE for the steady state is one order of magnitude worse.

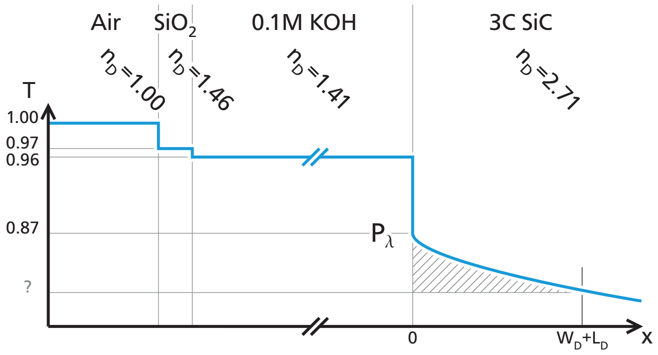

Figure 7.9.: *Schematic of reflection losses in the EC setup according to equation 7.7. The refractive indexes used are from literature [181, 182].*

In order to improve the 3C SiC performance, one first needs to identify the problem. While the high onset potential at 0.47 V vs RHE is responsible for the low IQE without bias potential, the overall photocurrent is way below expectations.

Hole Flux to the Surface

There are two possible circumstances, which could explain the low photocurrent. First, the number of holes reaching the surface is already low. Second, a sufficiently large number of holes reaches the surface, but instead of participating in the OER, they recombine. Considering the approximated recombination rates from figure 7.7, the recombination rate constant k_{rec} never exceeds approximately four times k_{tr}. If recombination alone would cause the problem, the expected IQE should therefore have been 20 % or above.

Thus, the hole flux to the surface has to be investigated further. As photons are absorbed in a semiconductor, they create an electron-hole pair (exciton) by exciting an electron from the valence into the conduction band. The probability of this absorption taking place is given by the absorption coefficient α, which is related to the incoming photon flux I_0, and the photon density $I(\Delta x)$ at the penetration depth Δx, via the Lambert-Beer equation

$$I(x) = I_0 \exp(-\alpha x) \tag{7.11}$$

(reflection losses already taken into account). The 3C SiC samples considered are n-type, any holes from photo excitation will be minority charge carriers. As such they have a short lifetime and will soon recombine with the much more numerous electrons from the conduction band. Two situations have to be considered.

First, the photon could be absorbed near the surface, in the depletion layer. Due to the number of electrons in the depletion layer being 'depleted', the probability of recombination is much reduced. The built-in potential will further aid in electron hole separation, forcing the hole towards the sample surface, where it can participate in the OER. Hence, holes created within the depletion layer width W_D are considered to reach the surface in popular models of charge separation.

Second, a photon is absorbed somewhere in the 3C SiC bulk. As there is no potential driving it into a specific direction it will diffuse at random until, at some point, it recombines, at which point it is essentially lost for the OER reaction. Should the random diffusion happen to move it into the depletion layer, it will behave like the previously discussed holes from there on, and participate in the OER.

The hole flux through the depletion layer was first calculated by Gärtner in 1959 for the case of an n-type semiconductor in contact with a transparent metal contact at the illuminated side [183]. This equation

$$J_{tot} = qI_0\left[1 - \frac{\exp(-\alpha W_D)}{1+\alpha L_p}\right] + \frac{qp_{no}D_p}{L_p} \tag{7.12}$$

is also valid for the n-type 3C SiC in contact with an electrolyte and gives a good estimate of the total amount of holes actually reaching the 3C SiC / electrolyte interface J_{tot}. The first term of equation 7.12 describes the photocurrent, where q is the elementary charge, I_0 the photon intensity at the 3C SiC surface, W_D the depletion layer width, α the absorption coefficient at the the respective wavelength (monochrome illumination assumed) and L_p is the hole diffusion length. The second term describes the dark current contribution. As it is significantly smaller than the photocurrent contribution in most cases it can be neglected [37]. Previous works on photoelectrochemistry used only the simplified version

$$J_{tot} = qI_0\left[1 - \frac{\exp(-\alpha W_D)}{1+\alpha L_p}\right] \tag{7.13}$$

of equation 7.12, when discussing the hole or electron flux, calling it the 'Gärtner equation' [37, 49,

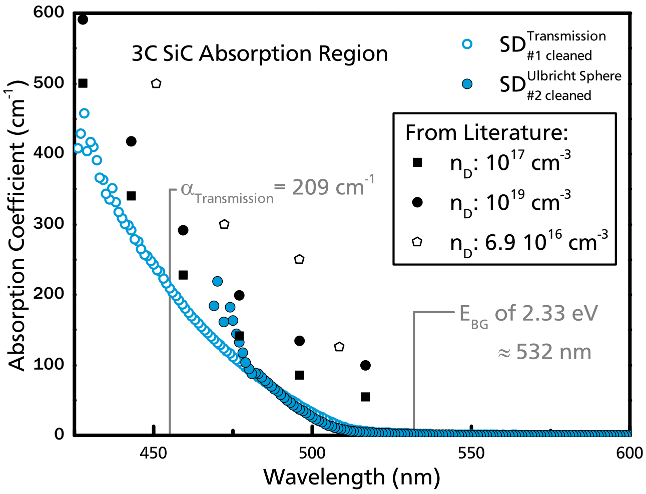

Figure 7.10.: *Absorption coefficient α for $SD_{\#1}$ and $SD_{\#2}$, determined via UV/vis absorption spectroscopy. At the LED wavelength of* 455 nm *α was determined to be* $(209 \pm 2)\,\mathrm{cm}^{-1}$ *for $SD_{\#1}$. For comparison literature values were added: n_D of* $1 \times 10^{17}\,\mathrm{cm}^{-3}$ *and* $1 \times 10^{19}\,\mathrm{cm}^{-3}$ *[184], n_D of* $6.9 \times 10^{16}\,\mathrm{cm}^{-3}$ *[185].*

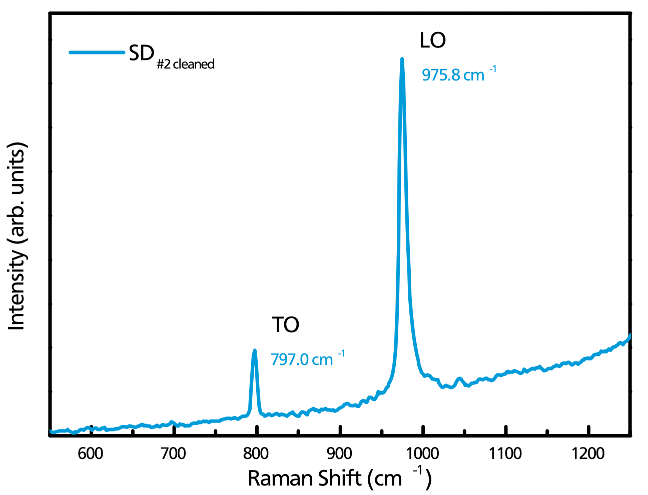

Figure 7.11.: *Raman spectrum for the cleaned (not etched) $SD_{\#2}$. The measurement was performed with a green laser* (514 nm) *and the spectrum was calibrated in regard to the* 520.7 cm^{-1} *Si peak. A doping concentration n_D of* $(8 \pm 3) \times 10^{17}\,\mathrm{cm}^{-3}$ *can be approximated from the LO mode position [80, 82].*

58, 59, 183]. I_0 is already known, therefore α, W_D and L_D have to be determined in order to perform the calculations for comparison.

Absorption Coefficient α

The absorption coefficient α can be determined via UV-Vis absorption spectroscopy. Figure 7.10 displays the values of α for $SD_{\#1}$ and $SD_{\#2}$ as a function of wavelength. Measurements were performed in transmission geometry for $SD_{\#1}$ and with an Ulbricht sphere for $SD_{\#2}$. As we assume monochrome illumination at $\lambda = 455\,\mathrm{nm}$, the respective α value is of interest at this point. Because the light has to pass the sample twice in the Ulbricht sphere setup, the $SD_{\#1}$ measurement shows 100 % absorption at wavelengths below 480 nm ($\alpha = 95$). While this prevents the determination of $\alpha_{\lambda=455\,\mathrm{nm}}$ for $SD_{\#2}$ directly, the conformity between $SD_{\#1}$ and $SD_{\#2}$ is adequate to use the $SD_{\#1}$ value of

$$\alpha = (209 \pm 2)\,\mathrm{cm}^{-1} \tag{7.14}$$

instead, without leading to larger uncertainties. In fact, UV/Vis absorption spectroscopy measurements performed on a similar bulk 3C sample (SD_{CVD}, discussed in section 8) show identical values for α (transmission: 211 cm^{-1}, Ulbricht sphere: 195 cm^{-1}). Linear extrapolation, from the literature data displayed in figure 7.10 results in higher values of: 256, 327 and 458 cm^{-1} for α [184, 185].

Depletion Layer Width W_D

The extend of the depletion layer, its width

$$W_D = \sqrt{\frac{2\varepsilon_0\varepsilon_S(V_d - U)}{qn_D}} \tag{7.15}$$

depends on the doping concentration n_D, the diffusion potential V_d and the applied potential U [37]. As in chapters 5 and 6, n_D can be approximated via Raman spectroscopy [80, 82]. Figure 7.11 shows the appropriate Raman spectrum obtained for $SD_{\#2}$. A green laser with 514 nm wavelength was employed for the measurement, and the setup was calibrated with regard to the 520.7 cm^{-1} line of single crystalline silicon. The observed LO mode position of 975.8 cm^{-1} corresponds to a doping concentration of

$$n_D = (8 \pm 3) \times 10^{17}\,\text{cm}^{-3} \quad . \tag{7.16}$$

Using 8.8542×10^{-12} F/m for the vacuum permittivity ε_0, $\varepsilon_S = 9.72$ for the static dielectric constant of 3C SiC [40], and 1.6×10^{-19} C for the elementary charge q, equation 7.15 changes to

$$W_D = \sqrt{V_d - U[\text{V}]} \times 3.667 \times 10^{-8}\,\text{m} \quad , \tag{7.17}$$

only depending on the total band bending $V_d - U$. However, $V_d - U$ is unlikely to exceed one or two volts, thus the depletion layer width will be in the range of 70 nm or below.

Because the band bending, and thus V_d is a result of the semiconductor electrolyte contact it can not be measured externally. Any measurements would have to be performed on the electrolyte covered 3C SiC surface. While ambient pressure XPS might allow such measurements, U would have to be given with regard to the same equilibrium state, the band bending V_d was measured for. This would induce a huge margin of uncertainty, as the OCP, as possible reference point - is rather undefined between HER and OER. Therefore, some kind of reference for the band situation with regard to the applied potential is required.

$SD_{\#1}$ & $SD_{\#2}$ Doping Concentrations

The two single domain samples obviously have slightly different doping concentrations.

$\mathbf{SD}^{\mathbf{Raman}}_{\#1}$: $(1.7 \pm 0.5) \times 10^{18}\,\text{cm}^{-3}$
$\mathbf{SD}^{\mathbf{Hall}}_{\#1}$: $(1.3 \pm 0.2) \times 10^{18}\,\text{cm}^{-3}$
$\mathbf{SD}^{\mathbf{Raman}}_{\#2}$: $(0.8 \pm 0.3) \times 10^{18}\,\text{cm}^{-3}$
$\mathbf{SD}^{\mathbf{Mott-Schottky}}_{\#2}$: 5.6 to $8.4 \times 10^{18}\text{cm}^{-3}$

Flat-Band Potential From Mott-Schottky Plots

As the total band bending at a given applied potential $V_d - U$ is a result of the charge transfer at the semiconductor electrolyte interface, it can not be measured without this contact. Therefore only electrochemical methods should be considered for its determination, and the method of choice are Mott-Schottky plots.

As discussed in chapter 3, Mott-Schottky plots can be used to determine the flat band potential (no band bending) from the 3C SiC surface capacity C_{SC}. C_{SC} in turn is obtained from the evaluation of electrochemical impedance measurements (EIS) with regard to an adequate equivalent circuit. Figure 7.12 shows the equivalent circuit used at the left side and an example EIS measurement (scatter) along with the resulting fit (lines). The obtained fitting values for the equivalent circuit are presented along the right side. Above measurement was performed on the polished (0.25 μm) $SD_{\#2}$ in a pH 10 buffer solution. Similar measurements were performed in 0.05 M H_2SO_4, pH4 and pH 7 buffer solution, as well as in 0.1 M KOH.

As can be seen, the EIS measurement shows one broad phase shift peak, with the expected decrease in impedance over the same frequency range. This behaviour is roughly similar to a resistance in series with a resistance and capacity in parallel (R(RC)), which is normally used to describe a single electrochemical reaction [86]. However, the displayed phase shift peak is broader than for a pure R(RC) equivalent circuit. Measurements at other potentials and in different electrolytes display an even higher deviation.

This is the result of an inhomogeneous sample surface, where areas with varying properties (as result of macroscopic defects, different surface morphology, surface recombination effects due to de-

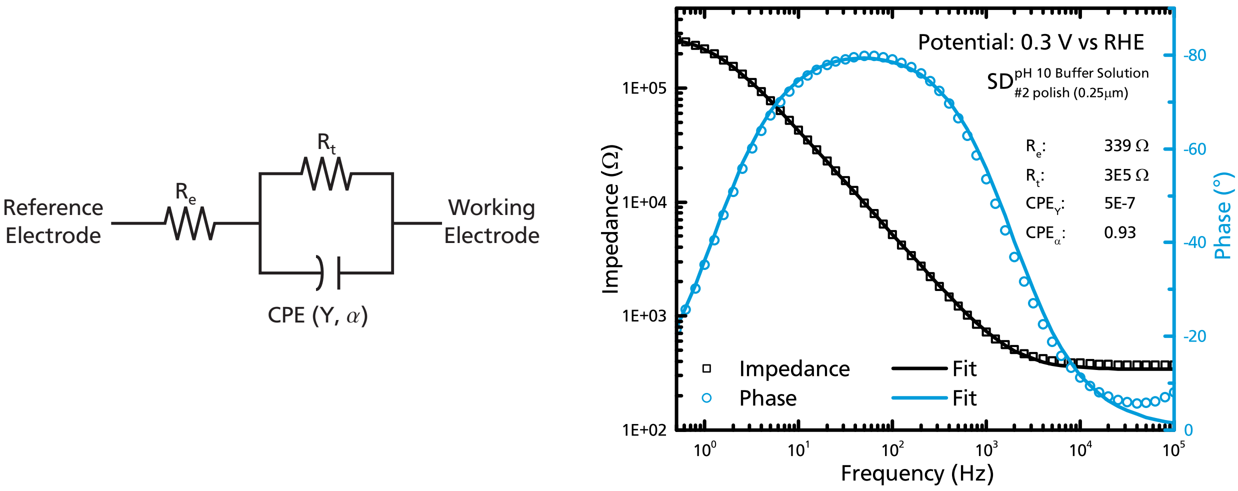

Figure 7.12.: *Left) Randles cell with constant phase element (CPE) as equivalent circuit employed for evaluation of the Right) EIS measurement (Bode plot) performed on the polished* (0.25 μm) *$SD_{\#2}$ in a pH 10 Buffer solution. The obtained information was used to estimate the effective capacity of* 2×10^{-6} F/cm^2 *according to Brug and Hirschhorn [84, 85].*

fect states etc.) would result in different equivalent circuit parameters for each separate area. The observed impedance behaviour of the sample is a superposition of the separate areas and the correct equivalent circuit would be a parallel connection of numerous R(RC) elements, one for each area. This can be factored in via a constant phase element (CPE), see chapter 3. R_e describes the total setup resistance, which is mostly a result of the electrolyte, while R_t represents the charge transfer resistance between the 3C SiC surface and the electrolyte.

While improving the data fitting, CPEs do not provide the desired semiconductor capacitance C_{SC} directly. It can be approximated from the equivalent circuit parameters, as discussed by Brug and Hirschorn [84,85]. The resulting effective capacity

$$C_{eff} = Y^{1/\alpha}\left(R_e^{-1}+R_t^{-1}\right)^{(\alpha-1)/\alpha} \approx C_{SC} \qquad (7.18)$$

should be a reasonable approximation of C_{SC}.

Determination of C_{SC} over a certain potential range allows the determination of the flat band potential via Mott-Schottky plots. The relation between surface capacity

$$C_{SC} = \frac{\varepsilon_0\varepsilon_S}{W_D} = \sqrt{\frac{q\varepsilon_0\varepsilon_S n_D}{2}}\left(V_d - U - \frac{2k_BT}{q}\right)^{-1/2} \qquad (7.19)$$

and applied bias potential U is well known from solid state semiconductor physics [37]. It makes sense to relate U to a readily available value. Therefore, it is generally discussed in relation to V_d for solid state interfaces, and in relation to the flat band potential U_{FB} in electrochemistry. Thus, equation 7.19 changes to

$$C_{SC} = \sqrt{\frac{q\varepsilon_0\varepsilon_S n_D}{2}}\left(U - U_{FB} - \frac{2k_BT}{q}\right)^{-1/2} \qquad (7.20)$$

[176]. Transposing yields

$$\frac{1}{C_{SC}^2} = \frac{2}{q\varepsilon_0\varepsilon_S n_D}\left(U - U_{FB} - \frac{2k_BT}{q}\right) \qquad (7.21)$$

, the Mott-Schottky relation. Which can be used to determine U_{FB}, as $1/C_{SC}^2$ becomes zero for $U \approx U_{FB}$.

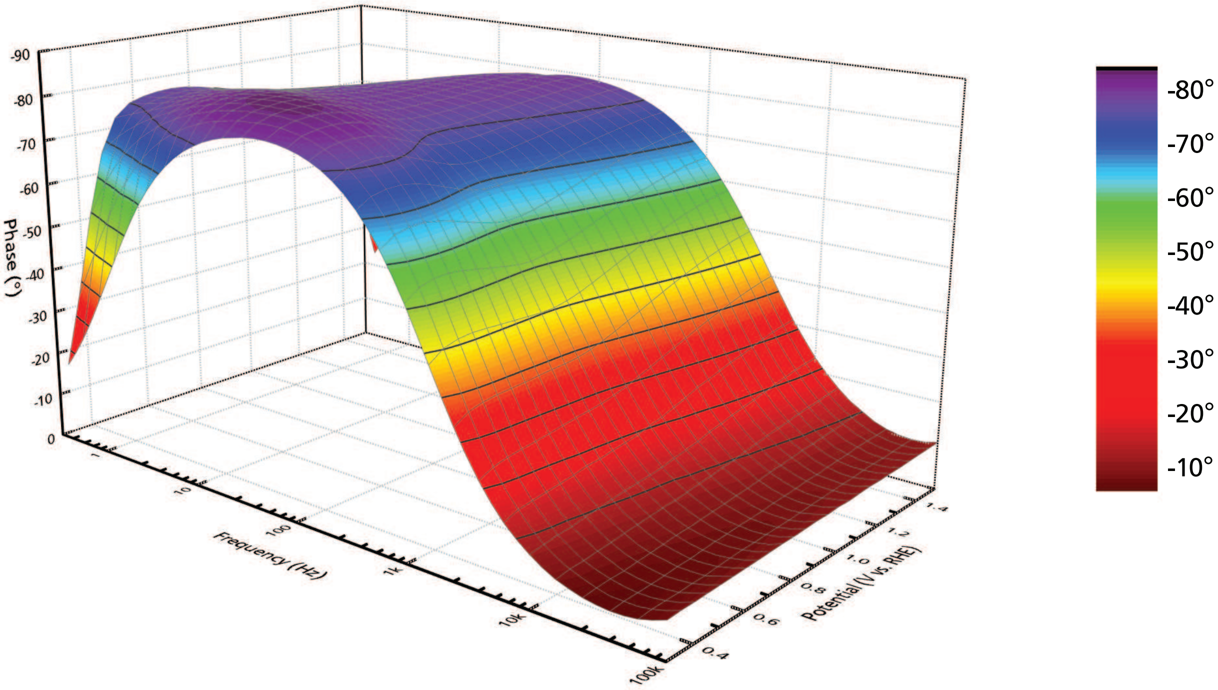

Figure 7.13.: *Phase components (Bode plot) from EIS measurements performed on* $SD^{pH10\,Buffer\,Solution}_{\#2\,polish\,(0.25\mu\mathrm{m})}$. *Measurements were performed in the dark, every* 0.05 V vs RHE *and evaluated with the CPE-Randles equivalent circuit from figure 7.12. The broad peak shape shifts to higher frequencies with increased bias potential, indicating a decrease in the surface capacity, as expected.*

	U_{FB}	U_{OCP}	$\frac{\mathrm{d}(1/C_{SC}^2)}{\mathrm{d}U}$	n_D
0.1M KOH	0.52 V vs RHE	0.85 V vs RHE	1.72 μF V cm^{-4}	8.5×10^{18}cm^{-3}
pH10 Buffer	0.60 V vs RHE	0.67 V vs RHE	1.85 μF V cm^{-4}	7.8×10^{18}cm^{-3}
pH7 Buffer	0.58 V vs RHE	0.67 V vs RHE	1.40 μF V cm^{-4}	10.4×10^{18}cm^{-3}
pH 4 Buffer	0.59 V vs RHE	0.62 V vs RHE	1.81 μF V cm^{-4}	8.0×10^{18}cm^{-3}
0.05M H_2SO_4	0.52 V vs RHE	0.75 V vs RHE	2.58 μF V cm^{-4}	5.6×10^{18}cm^{-3}

Table 7.1.: *Data obtained from the Mott-Schottky measurements displayed in figure 7.14. The flat band potential* (U_{FB}) *was obtained from the x-axis intercept, the open circuit potential was measured before the EIS measurements were performed, the slope* ($\frac{d(1/C_{SC}^2)}{dU}$) *was obtained from the linear fit and used to calculate the corresponding doping concentration* n_D *according to equation 7.23.*

Figure 7.13 displays the phase shift from a Mott-Schottky experiment, consisting of numerous EIS measurements in a potential range from 0.3 to 1.5 V vs RHE. With increasing potential the broad peak shape is shifted to higher frequencies, indicating a decrease in surface capacity, see figure 3.12 in chapter 3. Exactly the expected behaviour, as C_{SC} should decrease with increasing W_D. Furthermore, a strong broadening of the phase shape occurs between 0.6 and 0.7 V vs RHE. This is the region around U_{FB}, where Mott-Schottky-Plots are known to deviate. A result of the approximation

$$\frac{C_{SC}C_H}{C_{SC}+C_H} \approx C_{SC} \tag{7.22}$$

no longer being valid, as C_{SC} is no longer significantly smaller than the Helmholtz capacity C_H around U_{FB} [49, 176]. Surface state participation is also known to result in deviations around U_{FB} [28, 58], indicating the presence of surface states at the 3C SiC/electrolyte interface, see section 7.4.

Figure 7.14 displays five Mott-Schottky plots, obtained for $SD_{\#2\,polish\,(0.25\mu\mathrm{m})}$ in different electrolytes over the whole pH range. The results from the 3D plot in figure 7.13 (pH 10 buffer solution) are displayed in dark green. In all five electrolytes $1/C_{eff}^2$ shows the expected linear behaviour for $U \gg U_{FB}$. As can be seen from the x-axis intercepts, the flat band potentials range from 0.52 to 0.60 V vs RHE, see table 7.1 for the Mott-Schottky evaluation results. This spread could either be the result of measurement deviation or a slightly different interaction of the 3C SiC surface with either the buffer solutions or KOH/H_2SO_4, as each of those two groups yields similar U_{FB}.

In order for U_{FB} to remain constant with regard to the reducible hydrogen electrode, the flat band potential has to change with pH. This is demonstrated in figure 7.15, where U_{FB} is displayed with regard to the standard hydrogen electrode (SHE) instead of the pH corrected RHE. The pH dependence of

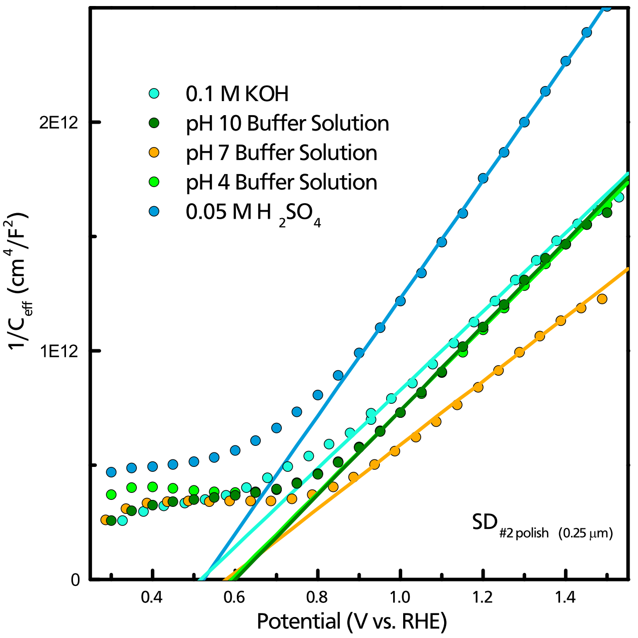

Figure 7.14.: *Mott-Schottky plots for $SD_{\#2\,polish\,(0.25\mu\mathrm{m})}$ in five different electrolytes, performed in the potential range from 0.3 to 1.5 V vs RHE. All plots show the expected linear behaviour, and the linear fits used to determine the x-axis intercept are displayed in the appropriate colours. The resulting U_{FB} can be found in table 7.1. The slope yields a n_D in the same order of magnitude as Raman measurements*

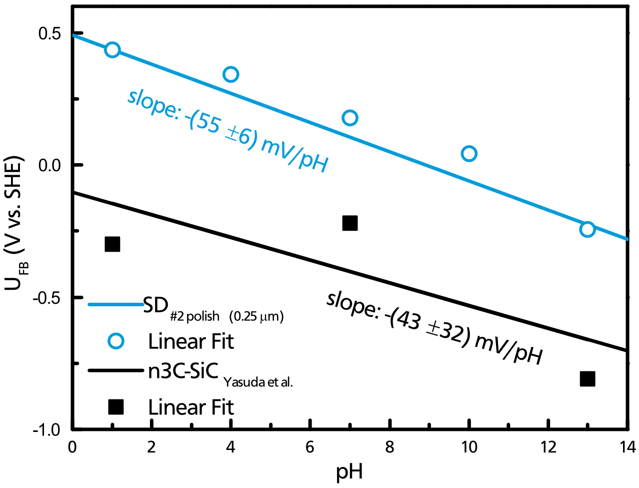

Figure 7.15.: *Flat band potential (U_{FB}) vs. standard hydrogen electrode (SCE) for $SD_{\#2\,polish\,(0.25\mu\mathrm{m})}$ in comparison to the only other Mott-Schottky plots for bulk 3C SiC performed by Yasuda et al. (converted from vs. SCE to SHE) [29].*

$SD_{\#2\,polish\,(0.25\mu m)}$ was found to be (55 ± 6) mV per pH unit. A pH dependence of U_{FB} usually is the result of an proton/hydroxil absorption/desorption equilibrium at the semiconductor/electrolyte interface, and the resulting change in the potential drop over the Helmholtz layer [28]. The observed value is almost identical to the expected 59 mV per pH unit for ionic semiconductors. While no such dependency would be expected for an inert covalent semiconductor without oxide termination.

For comparison, a pH dependancy of: 33 mV/pH was reported for silicon (with a thin oxide layer) [186], 40 mV/pH for 6H SiC (apparently with a Si-OH termination) [28], and (36 ± 27) mV/pH could be approximated for 3C SiC (no information on surface termination) [29]. The high pH dependency indicates a high surface reactivity. Any surface reactions are most likely to take place via the Si-OH surface bonds or surface/defect states [28, 187].

There is only one other report of bulk n-type 3C SiC flat band potentials in regard to pH. Yasuda et al. investigated a 303 μm 3C SiC sample with a doping concentration of $2 \times 10^{19}\,\mathrm{cm}^{-3}$ [29]. An approximation of their results is displayed in figure 7.15 for comparison. They observed U_{FB} at potentials from 0.46 to 0.73 V below what was observed in this work. A lower U_{FB} is desirable, as it should indicate a higher band bending and thus photovoltage at the same bias potential.

One possible explanation for the significant difference would be a sample surface of better quality. As discussed in section 7.4, $SD_{\#2}$ displayed a approx. 0.15 V lower U_{FB} before it was polished. On the other hand Yasuda et al. performed voltage-capacity measurements at one frequency only. This technique assumes an ideally capacitive interface, described by R_e in series with the capacitance only, instead of the CPE element needed for almost all real surfaces [83]. While the method is fast and easy to use, no equivalent circuit fitting required, the underlying assumption can result in major shifts in slope and derived U_{FB} for different frequencies [83, 188, 189].

Lasia reported a difference of almost 0.5 V in U_{FB} and about a factor 4 in slope between measurements performed at the same sample but with varying frequencies [83]. The most probable explanation seems to be a combination of both effects: a better surface quality and a shift due to the single frequency measurements.

The derivative with respect to the potential U of equation 7.21 yields the slope

$$\frac{\mathrm{d}(1/C_{SC}^2)}{\mathrm{d}U} = \frac{2}{q\varepsilon_0\varepsilon_s n_D} \tag{7.23}$$

of a Mott-Schottky plot. Obviously it can be used to determine the samples doping concentration. The slopes in figure 7.14 indicate a doping concentration in the range from 5.6×10^{18} to $10.4 \times 10^{18}\,\mathrm{cm}^{-3}$, see table 7.1, about one order of magnitude above the value obtained from the LO Raman mode of $8 \times 10^{17}\,\mathrm{cm}^{-3}$. An uncertainty of about one order of magnitude is generally accepted in the doping concentrations obtained via Mott-Schottky plots, as only n_D at the surface is measured, where surface states, pinning or surface roughness (and the resulting increased surface area) can all influence the obtained results [190].

Hole Diffusion Length L_p

Finally the hole diffusion length L_p is the last unknown quantity.

$$L_p = \sqrt{D_p \tau_p} \tag{7.24}$$

gives the distance a minority carrier (hole) will travel in a certain direction during its life time τ_p in n-type 3C SiC [37, 49]. D_p is the hole diffusion

	μ_n (cm^2 V^{-1}s^{-1})	μ_p (cm^2 V^{-1}s^{-1})
Lebedev [133]	≤ 1000	≤ 40
Hudgins [23]	$300-900$	$10-30$
Kona [39]	$615-710$	$19-22$
$SD^{Hall}_{\#1}$	51.6 ± 0.2	-

	τ (ns)
Sun [194]	8200
Scajev [193]	$18-300$
Grivickas [192]	$0.5-150$
Ichimura [191]	3300

	L_p (μm)
Lebedev [195]	1.5

Table 7.2.: *Literature values of the 3C SiC electron and hole mobility (μ_n and μ_p), and the lifetime τ. There is a huge spread between the reported mobility values, witness to an equally large spread in 3C SiC quality. While this argument stays valid for the lifetime as well, the huge spread is mostly due to different recombination paths being observed.*

coefficient, which is related to the hole mobility μ_p via

$$D_p = \left(\frac{kT}{q}\right)\mu_p \tag{7.25}$$

, the Einstein relation [37,49]. From the literature values presented in table 7.2 and equation 7.24 L_p can be estimated to lie between 113 nm and 29 μm [23, 39, 133, 191–194]. However, it should be noted that the values for μ_p were all obtained for p-type SiC. Lebedev et al. estimated the hole diffusion length in n-type 3C SiC via electron beam induced current, they obtained a value of 1.5 μm for L_p [195].

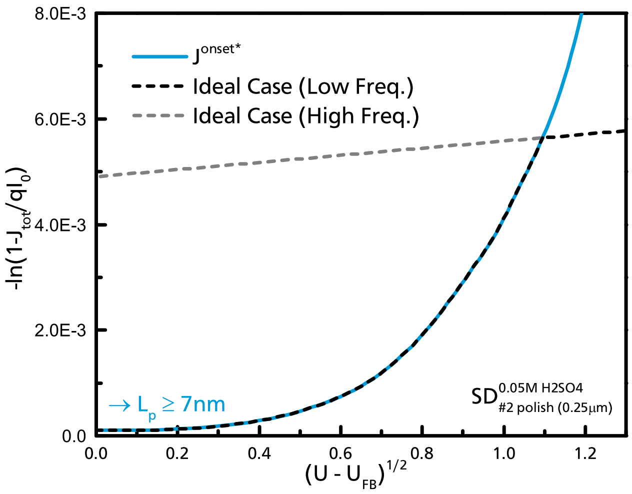

Figure 7.16.: *Representation of the photo current according to equation 7.26. Blue shows the measured data from $SD^{0.5M\ H2SO4}_{\#2\ ploish\ (0.25\mu\mathrm{m})}$. The dashed lines represent the expected behaviour, as described by Peat et al. [196] for higher (grey) and lower (black) frequencies. $U_{FB} = 0.52$ V vs RHE.*

The hole diffusion length can also be determined via electrochemical methods. Peat et al. [196] proposed a determination from the observed photocurrent

$$-\ln(1-\frac{J_{tot}}{qI_0}) = \alpha\sqrt{\frac{2\varepsilon_0\varepsilon_S}{1n_D}}\sqrt{U-U_{FB}} - \ln(1+\alpha L_p) \tag{7.26}$$

, a transposition of the Gärtner equation (eq. 7.13). Assuming the absence of a recombination current, a plot of $-\ln(1-\frac{J_{tot}}{qI_0})$ over $\sqrt{U-U_{FB}}$ should produce a linear curve shape, with a slope in proportion to α. The intercept with the y-axis at $\sqrt{U-U_{FB}} = 0$ could then be used to determine L_p. Peat et al. employed illumination in the kHz regime in order to obtain a recombination free photo response (similar to the grey dashed line in figure 7.16). Their measurements at 60 Hz displayed an exponential curve progression close to U_{FB}, which changed to linear at higher bias potentials, so a linear extrapolation of the data could be used (similar to the black dashed line in figure 7.16). As F^{onset*} corresponds to a 10 Hz measurement, a similar deviation is to be expected for the $SD_{\#2}$ data.

Figure 7.16 displays the onset photo current from $SD^{0.5M\ H2SO4}_{\#2\ polish\ (0.25\mu\mathrm{m})}$, which does not exhibit linear be-

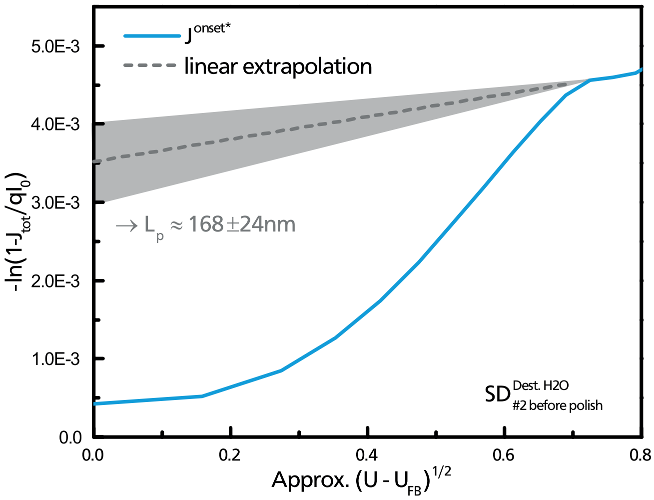

Figure 7.17.: *Measured data from* $SD^{Dest.H2O}_{\#2\,before\,polish}$ *in blue. The curve shows the expected linear region needed for the determination of* L_p *according to equation 7.26. From the intercept of the linear extrapolation with the ordinate an* L_p *of* $(168 \pm 24)\,\mathrm{nm}$ *was approximated. However, there is a high degree of uncertainty regarding the abscissa, see text.*

haviour over the whole $\sqrt{U - U_{FB}}$ range. There are two possible explanations.

First, the lower frequency results in recombination and thus a deviation from the ideal linear behaviour (dashed grey line) over the whole measurement range. As shown previously (see figure 7.7), recombination for $SD^{0.5M\,H2SO4}_{\#2\,polish\,(0.25\mu\mathrm{m})}$ becomes negligible for potentials exceeding 1.6 V vs RHE, thus a linear section would be expected for the measurement in figure 7.16 (black dashed line for the expected case).

Second, a linear section in figure 7.16 would correspond to a mostly constant value for J^{onset*} for high potentials, which would be related to the incoming hole flux at the surface. This is clearly not the case for $SD^{0.5M\,H2SO4}_{\#2\,polish\,(0.25\mu\mathrm{m})}$ (see figure 7.8). The most likely explanation for this behaviour is the occurrence of a second reaction, superimposing the OER, like dissolution of the 3C SiC, this will be discussed in the next section.

In conclusion, no value for L_p can be determined for $SD^{0.5M\,H2SO4}_{\#2\,polish\,(0.25\mu\mathrm{m})}$ from figure 7.16, because the missing linear section does not allow a linear extrapolation, which would then intersect the ordinate (grey dashed line). It can only be concluded that L_p has to be greater than 7 nm, which is the L_p corresponding actual intersect of the curve with the ordinate.

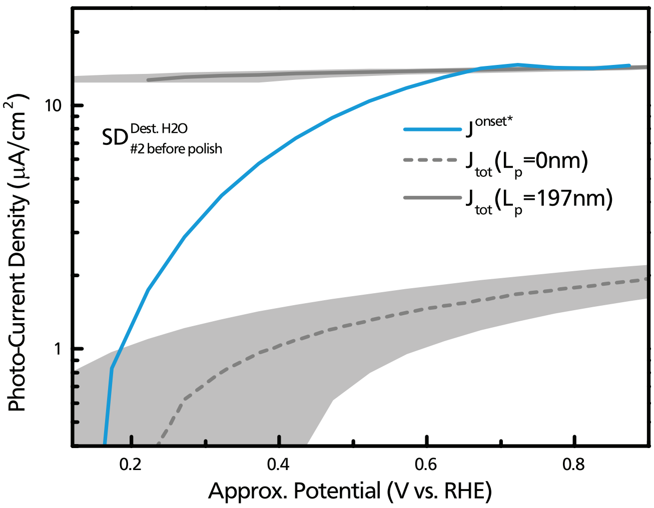

Figure 7.18.: *Photocurrent from a test measurement of* $SD^{Dest.H2O}_{\#2\,before\,polish}$ *in dest. water before the sample was polished. The potential vs. RHE is prone to deviations, but the photocurrent goes into saturation while no dark current occurs. Fitting of the saturation* J^{onset*} *with equation 7.13 (*J_{tot}*) yields* $L_p \approx (197 \pm 3)\,\mathrm{nm}$*. The grey areas represent the margin of error from the* U_{FB} *uncertainty. Light source was a* 435 nm *LED at* $100\,\mathrm{W/m^2}$.

Contrary to the $SD^{0.5M\,H2SO4}_{\#2\,polish\,(0.25\mu\mathrm{m})}$ measurement, an earlier test measurement of $SD^{Dest.H2O}_{\#2\,before\,polish}$ does show the constant J^{onset*} value at potentials exceeding 0.7 V vs RHE. This is a result of the different surface morphology, see section 7.4 for a more detailed discussion. From this measurement, displayed in figure 7.17, a value of $L_p \approx (168 \pm 24)\,\mathrm{nm}$ was approximated, using equation 7.26 and an extrapolation of the short linear section.

However, there are a number of problems here. First, the short linear section results in a larger margin of error. Second, and more problematic, is the uncertainty of the abscissa $U - U_{FB}$. No EIS measurements for a Mott-Schottky plot were performed in this early experiment, U_{FB} is therefore essentially unknown. This is why the data in figure 7.17 is based on the assumption that U_{FB} will be located close to the onset potential, as has been observed for $SD^{0.5M\ H2SO4}_{\#2\ ploish\ (0.25\mu\mathrm{m})}$. As this might result in a strong shift in $U-U_{FB}$, and thus the ordinate intercept, above value should be considered with caution. Furthermore, the measurement was performed in dest. H_2O, thus a significant change in pH over the course of the experiment is likely to occur, further increasing the possible margin of error.

In order to evaluate the severity of those uncertainties an additional approach for the determination L_p was employed. Figure 7.18 shows the data from $SD^{Dest.H2O}_{\#2\ before\ polish}$ in the standard J^{onset*} over (approximate) potential vs. RHE arrangement. The Gärtner equation 7.13 was used to fit the constant J^{onset*} region from 0.7 V vs RHE onward. For the fit a U_{FB} of 0.2 ± 0.2 V vs RHE was assumed, and L_p selected as variable parameter. As can be seen in figure 7.18, the uncertainty in U_{FB} has a huge impact on the photocurrent density for small L_p ($L_p = 0$ is displayed as example).

From the fit a value of (197 ± 3) nm was determined for L_p. The impact of the U_{FB} position is small and gives rise to the 3 nm margin of uncertainty. This value for L_p will be used for the remainder of this chapter.

However, it should be clear that other factors, like recombination, might lead to a much higher margin of error for this value, also there were no control measurements on other samples or employing other methods. If there is an error, the employed method is likely to underestimate the determined value for L_p. As the diffusion length is essentially governed by the 3C SiC bulk properties, the low diffusion length can be interpreted as indication of a high defect density in the 3C SiC bulk.

Photocurrent Approximation

After obtaining all the necessary physical properties of $SD_{\#2}$ the theoretical total hole flux J_{tot} to the 3C SiC / electrolyte interface under illumination can be calculated. The hole flux can be understood as upper limit to the photocurrent density, as the current resulting from the OER can not exceed the supply of holes needed for the reaction. As the whole approximation was undertaken in order to pinpoint the reason for 3C SiCs poor water splitting performance, two scenarios are possible.

1. The photocurrent density is equal to the approximated value. In this case the minority charge carrier supply is the limiting factor.
2. The photocurrent density is significantly below the approximated value. This could either be the result of minority carrier recombination at the 3C SiC / electrolyte interface, or a later onset as result of overpotentials and the available photovoltage.

Figure 7.19 displays J^{onset*}, $J^{s.state*}$ and J^{dark} of $SD^{0.05\ M\ H2SO4}_{\#2\ polish\ (0.25\mu\mathrm{m})}$ with a logarithmic ordinate. The general kinetics of a simple electrochemical reaction can be described via the Butler-Volmer equation (eq. 2.29), see chapter 2.2. As the OER is a 4 electron process, and therefore not simple, the Butler-Volmer equation can still be used to describe the overall behaviour, if one of the reaction steps

Obtained $SD_{\#2}$ Properties

- **α**: 209 cm^{-1} at 455 nm
- **$\mathbf{n_D}$**: $8 \times 10^{17}\ \mathrm{cm}^{-3}$
- **$\mathbf{W_D}$**: 36.7 nm $\times \sqrt{U-U_{FB}[\mathrm{V}]}$
- **$\mathbf{U_{FB}}$**: 0.52 V vs RHE
  polished (0.25 μm) in KOH and H_2SO_4
- **$\mathbf{L_p}$**: 197 nm

is the limiting factor. While there is no information on the OER kinetic steps, the observed current potential behaviour in figure 7.19 is in good agreement with the Butler-Volmer equation. The expected exponential behaviour is apparent from the straight lines in J^{onset*} and $J^{s.state*}$ in the potential range from approx. 0.5 to 1.1 V vs RHE (a result of the logarithmic scale).

At higher potentials a flattening out of the photocurrent density is observed. This is expected, as the OER photocurrent density for an n-type semiconductor is limited by the flux of photoexcited holes to the surface. Indeed, above a certain potential a constant photocurrent density would be expected. At lower potentials, the observed photocurrent density exceeds the expected linear behaviour (dashed lines - linear extrapolation). There are two explanations:

1. As the measurement starts in the cathodic potential range, a small amount of hydrogen is produced initially (see left side of figure 7.8). This would be oxidized in the HOR at higher potentials, superimposing the OER.
2. Surface reactions taking place in this potential range could change the density of surface states, and thus U_{FB}. Which in turn could result in an initial shift of the onset potential.

Besides the measured current densities, the figure also displays the hole flux calculated from equation 7.13 under consideration of the obtained $SD_{\#2}$ sample properties. For exemplification three different values for L_p were plotted, as this value has the biggest influence on the resulting approximation in regard to a possible margin of error. Disregard of L_p (lower limit - grey dashed) obviously results in a hole flux significantly below the observed photocurrent density, while $L_p = 1.5\,\mu$m (upper limit - grey dots) greatly exceeds it.

Finally, using the previously obtained value of (197 ± 3) nm for L_p results in the solid grey line ($J_{tot}(L_p = 197\,\text{nm})$). The calculated current density is of the same order of magnitude as the photocurrent density, which implies that the approximation is rather accurate. For most of the potential range it exceeds J^{onset*} and $J^{s.state*}$, as a upper limit should, until all three lines intersect at about 1.6 V vs RHE.

An intersection at this point is actually in very good agreement with the assumptions made so far. As discussed in the beginning of this chapter, a matching of J^{onset*} and $J^{s.state*}$ means that the chopped light measurement shows no transient behaviour. Thus, there is no, or negligible, recombination and all holes arriving at the 3C SiC / electrolyte interface will participate in the OER.

This is in good agreement with the rate constants from figure 7.7 discussed earlier, where k_{rec} approaches zero at potentials exceeding 1.5 V vs RHE. Without recombination, the measured photocurrent densities should therefore be identical to the incoming hole flux described by J_{tot}. The accuracy of the prediction (in regard to a triplicate intersection) is excellent.

However, at potentials above 1.6 V vs RHE the measured current density exceeds the approximated hole flux to the sample surface. Again, there are multiple possible explanations for this:

First, all photocurrent is a result of the OER. Consequently, the assumed value for L_p has to be smaller than in reality. The real hole flux would then exceed the predicted $32\,\mu\text{A/cm}^2$ for $L_p = 197$ nm. Photocurrent saturation would thus only be achieved at a more anodic potential than the 2 V vs RHE limit of the performed measurement, and the change in the photocurrent density slope would probably be the result of Fermi level pinning, see figure 7.20 C) and E). L_p would have to be approximately 500 nm instead of $L_p = 197$ nm in order to yield the $69\,\mu\text{A/cm}^2$ determined from figure 7.19 at 2 V vs RHE. As previously discussed

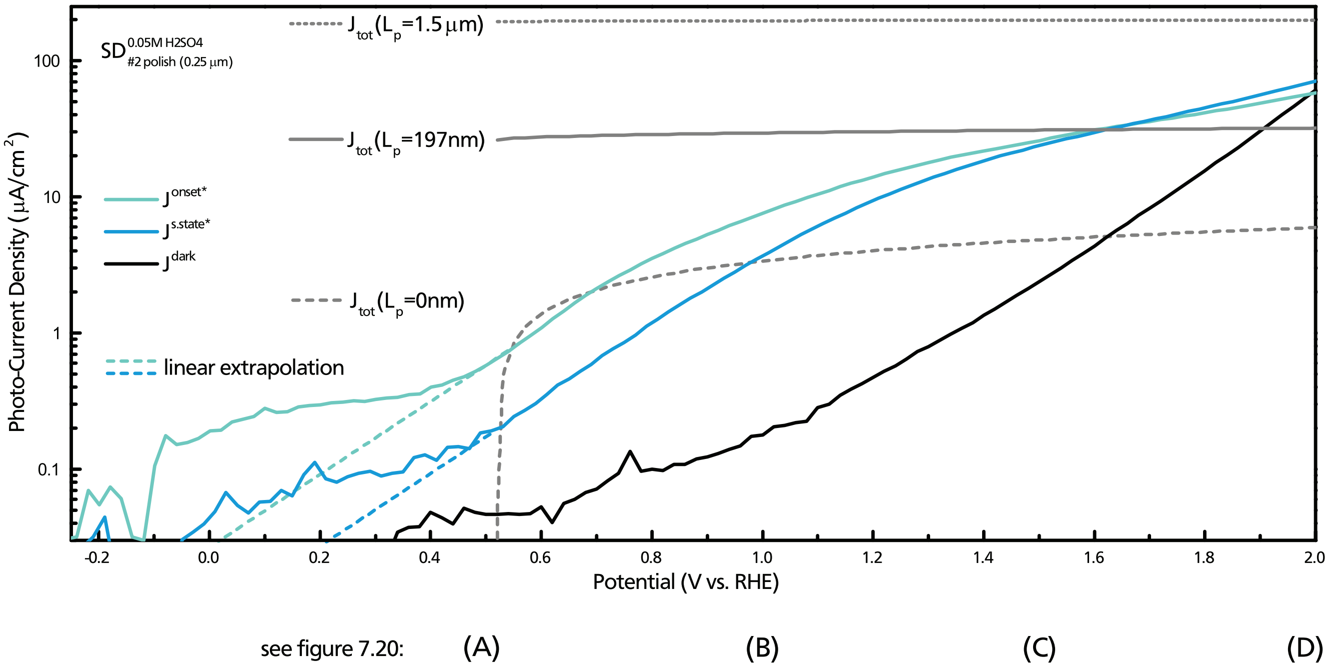

Figure 7.19.: *Photo and dark current density of* $SD^{0.05\,M\,H2SO4}_{\#2\,polish\,(0.25\mu m)}$ *under* 200 W/m^2 *illumination with a* 455 nm *blue LED in dependence of the applied potential. The approximated hole flux to the 3C SiC / electrolyte interface, according to equation 7.13, is displayed in grey for three different values of* L_p*. Assuming* (197 ± 3) nm *for* L_p*, the observed photocurrent would exceed the predicted hole flux to the surface for potentials exceeding approx* 1.6 V vs RHE*, see text.*

an underestimate of L_p is a real possibility with the applied method.

Second, the photocurrent exceeding 32 μA/cm^2 at 1.6 V vs RHE is not the result of the OER. The most probable alternative reaction would a parasitic side reaction like anodic oxidation or anodic dissolution (should the formed oxide prove unstable in the electrolyte for the applied potential) and the proposed reaction pathways would be

$$\mathrm{SiC} + 8\,\mathrm{OH}^- \rightleftharpoons \mathrm{SiO_2} + \mathrm{CO_2} + 4\,\mathrm{H_2O} + 8\,e^- \tag{7.27}$$

$$\mathrm{SiC} + 4\,\mathrm{OH}^- \rightleftharpoons \mathrm{SiO} + \mathrm{CO} + 2\,\mathrm{H_2O} + 4\,e^- \tag{7.28}$$

in an alkaline electrolyte [27, 197, 198]. Onset and rate of the side reaction depend strongly on the surface morphology, see section 7.4, where a rough surface yields an increase of J^{dark}, or the 'as is' SD_{CVD} in figure 8.10 where no (dark) anodic dissolution was observed up to 2 V vs RHE.

The necessary holes for the reaction could either be provided by photo-excitation or defect states in the SiC. Van Dorp et al. used (ultra violet) light to facilitate the oxidation of 4H and 6H SiC at potentials exceeding 1.56 to 1.71 V vs RHE [199, 200]. In theory electrode degradation should be subject to similar restrictions as the OER, meaning that the number of available holes restrict the reaction rate. In reality a mixture of the both explanations seems most likely.

However, if only holes from photo excitation were able to sustain oxidation, then there couldn't be any degradation in the dark, thus there couldn't be any dark current. As the dark current is obviously present, it must be concluded that defect states are also able to supply the necessary holes for the SiC degradation. Then it would also be possible that illumination might initiate the degradation reaction, but not supply all holes necessary for the reaction. One could imagine it as some kind of amplification process.

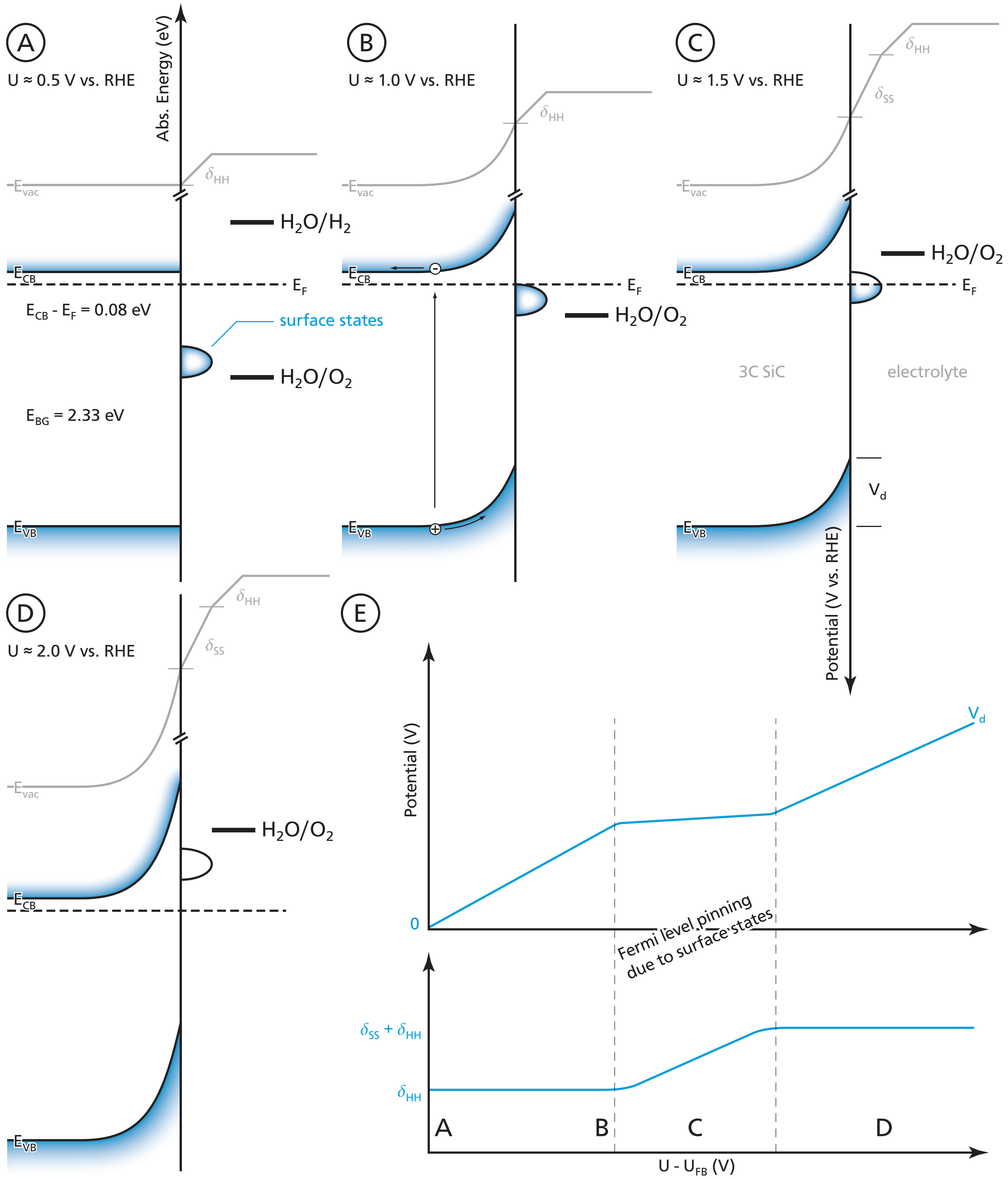

Figure 7.20.: *Approximated band diagram of the $SD_{\#2\,polish\,(0.25\mu\mathrm{m})}$ 3C SiC / electrolyte interface in dependence of the applied bias potential. A value of* 0.52 V vs RHE *was determined for the U_{FB} in 0.1M KOH and 0.05M H_2SO_4 from Mott-Schottky Plots. (A) Flat band: all surface states are occupied, some potential drop across the Helmholtz layer δ_{HH} (B) $U_{FB} + 0.5\,\mathrm{V}$: potential drop occurs in the semiconductor, surface states remain below E_F (C) $U_{FB} + 1.0\,\mathrm{V}$: Fermi level reaches surface states, further potential drop occurs at the interface as δ_{SS} instead of in the semiconductor as surface states are ionized. This changes the position of the H_2O/O_2 redox couple in relation to the semiconductor bands (D) $U_{FB} + 1.5\,\mathrm{V}$: Once all surface states are empty any additional potential drop will - again - occur in the semiconductor (E) Schematic graph of the diffusion potential (V_d) changes with bias potential U and the impact of Fermi level pinning. See text for more details.*

Knowledge of the flat band potential allows the construction of the 3C SiC band diagram in dependence of the applied potential (relative to the reference electrode). The diagrams are displayed in figure 7.20 for 4 different potential regions.

Region (A): Describes the flat band like situation at U_{FB}, there is no band bending and thus no diffusion potential V_d. Possible surface states at the 3C SiC/electrolyte interface are all below the Fermi level and thus occupied. This interface also gives rise to the Helmholtz layer as charged species from the electrolyte adsorb on the electrode surface, which in turn gives rise to a step in the vacuum energy level at the interface. Excitons (photoexcited hole electron pairs) will not be separated, as there is no electric field to do this, and thus will recombine shortly after their creation. Therefore there will be little to no photocurrent observable.

Region (B): For a more anodic potential than in (A) most of the additional potential is dropped across the depletion layer at the 3C SiC/electrolyte interface. This gives rise to upward band bending equal to the diffusion potential V_d. In region (B) the applied potential is not sufficient to move the Fermi level beneath the surface state energy, thus all surface states remain occupied. In this, and all the following potential regions, the electric field V_d will separate any excitons created in the depletion layer. Holes will be moved towards the semiconductor/electrolyte interface, while electrons will be moved into the bulk towards the back contact and a photocurrent will be observed. As more anodic potentials will supply more energy in order to facilitate the reaction the current density will increase with higher anodic potentials.

Region (C): At even more anodic potentials than (B) the Fermi level will eventually cross the energy position of the surface states. As it does so, some of the formerly occupied surface states will be ionized, thus creating positively charged ions, which give rise to a potential drop δ_{SS} at the semiconductor surface. This Fermi level pinning will also result in a change of the relative positions of the surface states and the OER potential. While occupied surface states remain, a more anodic potential will not increase V_d, as it did in region (B), but instead ionize more surface states, and thus increase δ_{SS}. This relation between V_d and δ_{SS} is also displayed in figure 7.20 (E). The photocurrent density in this region will behave similarly to region (B). However, as V_D does not increase with U as result of Fermi level pinning the increase of photocurrent density with more anodic potentials might be stalled or progress slower than in (B).

Region (D): Once all surface states are ionized any additional bias potential will drop across the depletion layer, as it did in region (B), again. A further increase of the anodic potential will result in a higher photocurrent density, until all incoming holes at the surface are able to cross over into the electrolyte and participate in the OER (or electrode oxidation). At this point the photocurrent density will go into saturation and a further increase of the bias potential would not yield any improvements.

The above considerations can be briefly summarized as follows:

- The low absorption coefficient α, means that light absorption does not only occur close to the interface but also further in the bulk.
- The high doping concentration n_D results in a small depletion layer. This in combination with the rather
- low minority carrier diffusion length L_p means that most photogenerated holes will be located to far away from the 3C SiC/electrolyte interface as to reach it. Thus preventing them from participating in the OER, as their energy is lost upon recombination with the majority charge carriers in the bulk.
- A high number of defects (either as result of the - as of yet - imperfect growth procedure

or formed during the photo-oxidation of the electrode) result in Fermi level pinning, thus reducing the available photovoltage and resulting in a later onset potential, see section 7.4.

- It stands to reason that the transfer of charge carriers from the electrode to the electrolyte will be further impaired through the lack of catalyst on the electrode surface.

The later problems (surface states, overpotential and maybe flat band position) might be solved by adequate surface preparation, higher quality samples, or the addition of a thin catalyst layer. Contrary, increasing the absorption properties is almost impossible. While an increase of W_D and L_p might increase the hole yield, the actual absorption coefficient can not be increased, thus severely limiting 3C SiC efficiency.

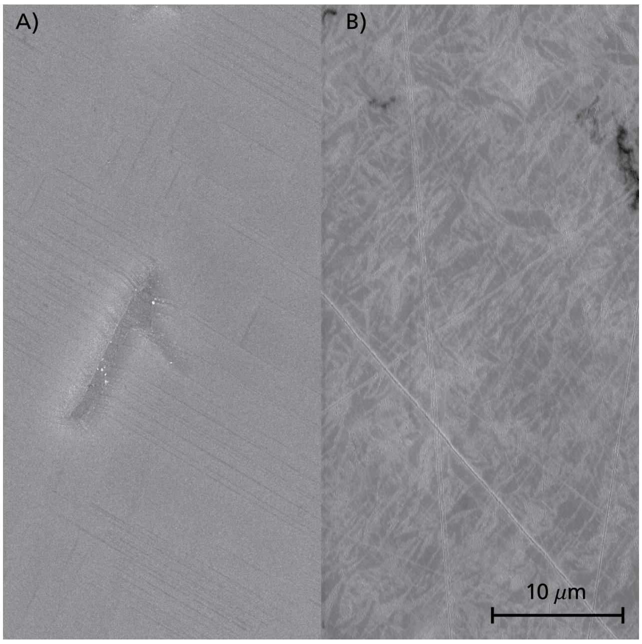

Figure 7.21.: *HREM shots of the $SD_{\#2}$ surface. A) displays the unpolished sample surface, while B) displays it after the 6 μm polishing step.*

Influence of Surface Morphology

As discussed in the previous section, one of the major limiting factors is the high recombination current at potentials below approx. 1.5 V vs RHE. There are two main factors governing the recombination rate. First, recombination centres, mostly defects in the band gap, which increase the probability of recombination. Second, an accumulation of minority charge carriers at the 3C SiC surface as result of slow charge transfer will also result in an increased recombination rate, and thus current. This is to be expected and correlated to the formation of recombination centres, as the photocorrosion of the semiconductor will directly compete with the OER. However, defects could also have a positive influence as a charge transfer from the SiC to the electrolyte via surface defect states could possibly increase the charge transfer rate.
In order to investigate the influence of surface defects on the OER of 3C SiC $SD_{\#2}$ was measured with two different surface morphologies:

1. $SD_{\#2\,polish\,(0.25\mu\mathrm{m})}$
   $SD_{\#2}$ was polished with diamond suspension of decreasing average size. The last step was performed with 0.25 μm diamond grains. This is the same sample preparation as was discussed previously in this chapter.

2. $SD_{\#2\,polish\,(6\mu\mathrm{m})}$
   As above, but the polishing procedure was stopped after the 6 μm step. Figure 7.21 B) clearly shows the resulting scratches and unevenness of the surface.

All samples were etched with piranha solution and NH_4F before EC measurements. It can be expected that a rougher surface should also result in a higher surface defect concentration. Figure 7.21 displays HREM pictures of the $SD_{\#2\,as\,is}$ and $SD_{\#2\,polish\,(6\mu\mathrm{m})}$, clearly showing the difference in surface morphology. Aside from the different surface preparations,

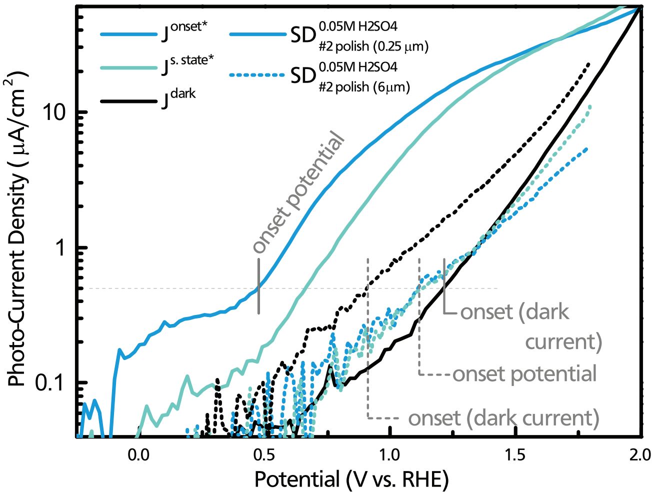

Figure 7.22.: *$SD_{\#2}$ photo- and dark current densities obtained for two different surface preparation procedures. The measurement procedures were identical.*

the measurement procedures for the polished samples were identical. Figure 7.22 displays the resulting photo- and dark currents for both samples.

$SD^{0.05\,M\,H2SO4}_{\#2\,polish\,(0.25\mu\mathrm{m})}$ (solid lines) displays the previously discussed onset potential at 0.47 V vs RHE. For comparison, the dark current only reaches a current density of 0.5 μA/cm^2 at the dark current onset of 1.21 V vs RHE. However, the dark current increases faster with the applied bias potential, and around 2 V vs RHE J^{dark} and the photocurrent densities J^{onset*} and $J^{s.state*}$ are about equal, before that the photocurrents are always significantly larger than J^{dark}.

For $SD^{0.05\,M\,H2SO4}_{\#2\,polish\,(6\mu\mathrm{m})}$ (dotted lines) the opposite holds true. The dark current exceeds the photocurrent density over the whole measurement range. Therefore it also reaches the 0.5 μA/cm^2 threshold at 0.91 V vs RHE (dark current onset) before the photocurrent at 1.13 V vs RHE (onset potential). Over the whole potential range J^{onset*} and $J^{s.state*}$ are almost identical, thus there is no transient behaviour.

It stands to reason, that an increased number of surface defect states will result in an increase of recombination (and thus transient behaviour) at lower potentials where the charge transfer is kinetically impaired. This should then result in a transient behaviour, which is not observed in the measurement. A possible explanation might be that the observed photocurrent is a product of increased oxidation under illumination.

The question arises, why does a rougher surface result in a shift of the onset potential to higher potentials? As mentioned before, it can be assumed that the rougher, defect rich surface will display an increased amount of surface states. For a perfect semiconductor / electrolyte interface, without surface states, a change in potential will result in an immediate change in the number of ionised dopant atoms in the semiconductor, as the potential drop occurs across the depletion layer and the Fermi level position is shifted. Because the total charge of the ionised dopant atoms changes, so does the total capacity of the semiconductor, this behaviour is described by the Mott-Schottky equation 7.21.

This behaviour is impaired by the presence of surface states. At a potential below U_{FB} all acceptor surface states will be occupied, resulting in a total charge of Q_p^{SS}, see figure 7.20 (A). While they remain fully occupied the measured capacity will follow the Mott-Schottky relation, although the intersect is shifted, as all or part of the potential drop will occur across the surface states in the Helmholtz layer. See figure 7.23.

At some point, increasing the potential will result in an emptying of those acceptor surface states (similar to figure 7.20 (C)), effectively pinning the Fermi level and preventing, or decreasing, changes of the capacity with potential until all surface acceptor states are empty, and the capacity is equal to that of the surface state free interface at the same potential. Further increase of the potential, results in a ionisation of donator surface states, thus the Fermi level remains pinned. Only once all of them are empty, resulting in a total charge of Q_n^{SS}, will the Fermi level unpin, and the capacity follow the Mott-Schottky relation again [201].

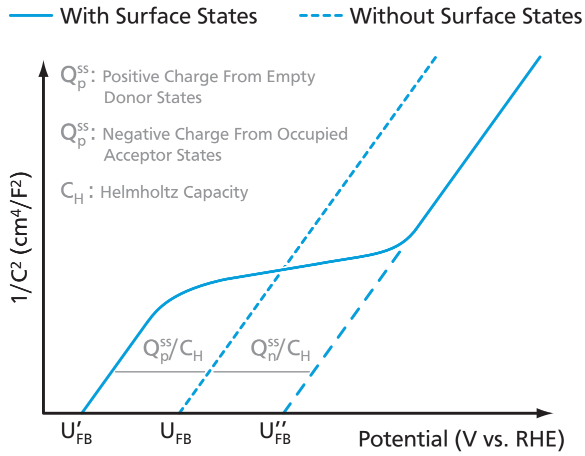

Figure 7.23.: *Diagram for clarification of surface state imposed changes on the shape and flat band position in a Mott-Schottky plot. Surface states can pin the Fermi level. In this case all or part of the applied potential is dropped across the Helmholtz layer, as surface states are ionised without changing the capacity according to the Mott-Schottky relation [201].*

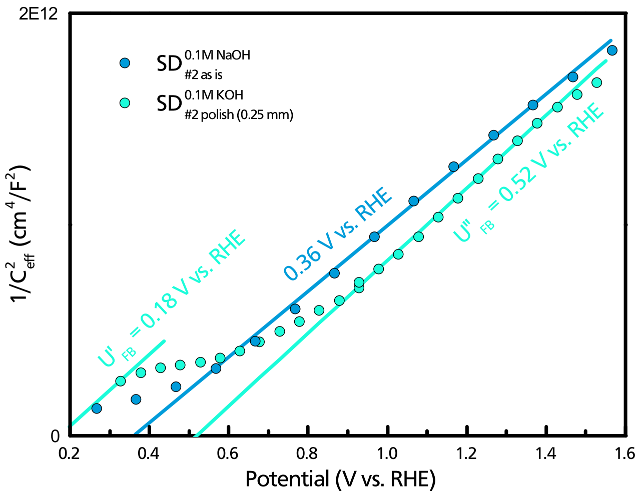

Figure 7.24.: *Mott-Schottky plot of $SD_{\#2}$ with two different surface preparations. The polished sample exhibits the characteristic s-shape for surface state participation, indicating a shift of U_{FB} to higher potentials. This is in good agreement with the 'as is' measurement, where a lower amount of surface states, and thus a smaller shift, is to be expected.*

The presence of both acceptor and donator surface states results in a characteristic s-shape, as displayed in figure 7.23 by the full, blue line. From the above explanation it should be obvious that an higher amount of surface states will result in a larger shift of the measured U_{FB} in regard to the ideal U_{FB}.

Figure 7.24 displays two Mott-Schottky plots measured on $SD_{\#2}$ with different surface preparations. The measurement performed on the polished sample exhibits the characteristic s-shape, as result of both, acceptor and donator surface states being present. Therefore the obtained flat band potential of 0.52 V vs RHE will not be the actual U_{FB} but rather a U_{FB}” located at a higher potential due to Fermi level pinning from surface states, see figure 7.23.

This is in good agreement with the curve progression of the 'as is' sample, which yields a U_{FB} of 0.36 V vs RHE. As such it is located at a lower potential, as would be expected for a sample with a reduced surface state concentration. It is entirely possible that $SD^{0.1MNaOH}_{\#2asis}$ is subject to a certain, but smaller shift as well. From the s-shape position of $SD^{0.1MKOH}_{\#2polish(0.25\mu m)}$ it can be concluded that U_{FB} without surface state participation should be located in the range from 0.18 (U'_{FB}) to 0.52 V vs RHE (U_{FB}”). However, this is still far from the U_{FB} position of approximately −0.1 V vs RHE Yasuda et al. reported for their single frequency Mott-Schottky measurement of an n-type 3C SiC bulk sample [29].

As there is no illumination, and thus no photogenerated holes, the increased dark current of $SD^{0.05\,M\,H2SO4}_{\#2\,polish\,(6\mu m)}$ has to be related to an oxidation of the electrode surface. In order to confirm this assumption XPS measurements of both polished samples were performed after the identical EC treatment. Figure 7.25 A) to C) display the resulting core level detail spectra. While both samples exhibit a strong oxygen signal in A), the signal for $SD^{0.05\,M\,H2SO4}_{\#2\,polish\,(6\mu m)}$ is approx. four times larger than for the smoother sample. Similarly, the Si 2p sil-

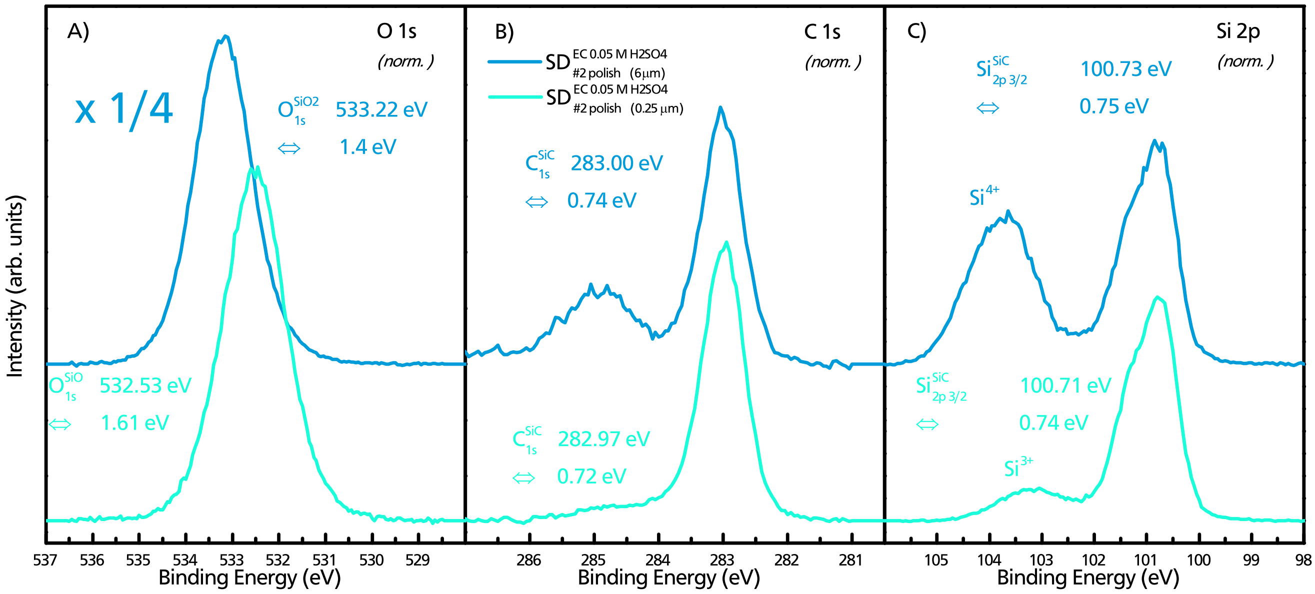

Figure 7.25.: *XPS detail spectra of the polished samples* $SD^{0.05\,M\,H2SO4}_{\#2\,polish\,(x\,\mu m)}$ *after the standard electrochemical measurement procedure was performed in 0.05 M* H_2SO_4*. Obviously the rougher surface results in stronger oxidation and the formation of a* SiO_2 *layer, instead of the SiO layer observed for the* 0.25 µm *surface preparation. The peak intensities were normalized in regard to* $Si^{SiC}_{2p3/2}$.

icon oxide signal in C) is much more pronounced for the rougher sample as well.

The peak positions can be used to determine the silicon oxides oxidation states. For $SD^{0.05\,M\,H2SO4}_{\#2\,polish\,(6\mu m)}$ a O^{SiO2}_{1s} position of 533.22 eV and a $Si^{SiO2}_{2p3/2}$ of 103.58 eV were determined. This is ingood agreement with the 4^+ oxidation state, corresponding to a SiO_2 layer. Literature values deviate from 533.2 to 533.4 eV for the O 1s, and 102.7 to 104 eV for the Si 2p peak, though [202–204]. While $SD^{0.05\,M\,H2SO4}_{\#2\,polish\,(0.25\mu m)}$ displays a 3^+ or Si_2O_3 bond, with binding energy positions of 532.53 eV for O^{SiO}_{1s} and 103.08 eV $Si^{SiO}_{2p3/2}$. Also in reasonably good agreement with the literature values around 532.5 eV and 102.7 eV [202, 205].

From Si 2p oxide peaks, it is obvious that the SiO_2 layer should be considerable thicker than the Si_2O_3 layer. The Si^{SiOx}_{2p}:Si^{SiC}_{2p} ratio and equation 3.5 were used to calculate the Si_2O_3 and SiO_2 layer thickness. And indeed, the SiO_2 layer is, with (28 ± 1) Å, almost four times thicker than the (7.8 ± 0.7) Å Si_2O_3 layer. Supporting the interpretation of increased corrosion in form of oxidation for $SD^{0.05\,M\,H2SO4}_{\#2\,polish\,(6\mu m)}$. For both oxidised samples, the C^{SiC}_{1s}:Si^{SiC}_{2p} ratio increases from 1.01 (for the etched samples) to 1.30 for $SD^{0.05\,M\,H2SO4}_{\#2\,polish\,(0.25\mu m)}$ and 1.46 for $SD^{0.05\,M\,H2SO4}_{\#2\,polish\,(6\mu m)}$ as result of silicon depletion caused by the oxidation process, as former SiC Si atoms are now part of the oxide over layer.

Comparing the measurement results makes it obvious that the surface morphology plays a major role in the photo response. Increasing surface disorder results in a photocurrent onset at higher potentials, indicating that a defect rich surface seriously hinders the charge transfer kinetics and OER via an increase of recombination. From the behaviour of $SD^{0.05\,M\,H2SO4}_{\#2\,polish\,(6\mu m)}$ it has to be concluded that this hindrance can reach a level were the OER is rendered ineffective and photo corrosion becomes the dominant effect. This is supported by the increased oxidation rate for the rougher sample surface observed via XPS. No positive effects of increased surface defect densities, like a possible improvement of interface charge transfer via surface states, were found.

Influence of Electrolyte and pH

There is vast number of possible electrolytes for direct photoelectrochemical water splitting. Most experiments are performed either in weak aqueous acid or weak aqueous base. The choice of electrolyte can influence the flat band potential (in cases of low surface reactivity) and has a major influence on chemical side reactions, such as sample decomposition or oxidation potentials. For example, diluted hydrofluoric acid can be used as electrolyte in order to prevent the formation of an oxide layer during electrochemical experiments, as the oxide is constantly etched away [27]. As illumination at sufficiently high potentials will increase the anodic dissolution, it can be used for etching patterns etc. [197, 198].

In order to investigate the electrolyte influence on the OER for 3C SiC, the sample was measured in 0.05 M H_2SO_4 and 0.1M KOH respectively. The measurement procedures were otherwise identical. As discussed in a previous section, U_{FB} is identical for both electrolytes, the 3C SiC band edges are therefore expected to be in a similar position with regard to OER for both electrolytes. Therefore an identical behaviour in terms of the OER is to be expected. From examination of the resulting photo- and dark currents in figure 7.26 it is obvious that the overall behaviour is almost identical, as expected.

As both samples display a significant dark current for potentials exceeding approx. 1.2 V vs RHE some kind of sample degradation has to occur, and because the dark currents are similar the same should hold true for the degradation reaction rates. In order to investigate the nature of this degradation, $SD_{\#2\,polish\,(0.25\,\mu\mathrm{m})}$ was examined via XPS before and after each of the two electrochemical experiments. All resulting core level detail spectra are displayed in figure 7.27, only oxygen, carbon and silicon were present on the sample.

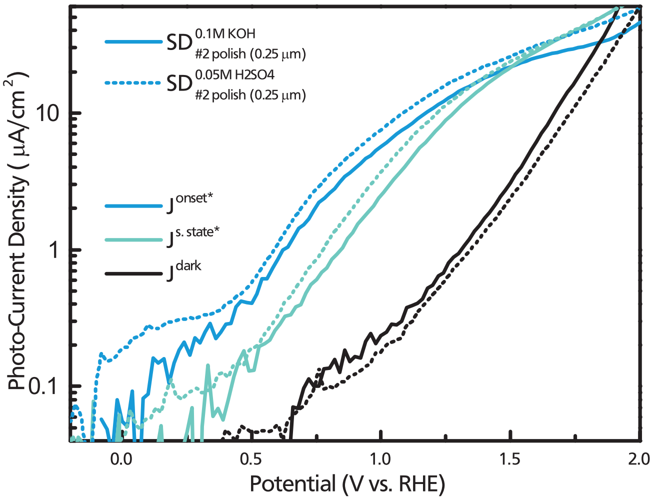

Figure 7.26.: *Photo- and dark current densities for $SD_{\#2\,polish\,(0.25\,\mu\mathrm{m})}$ in 0.1 M KOH and 0.05 M H_2SO_4. Apart from the electrolyte, measurement procedures were identical. Within the expected margin of error for electrochemical measurements, the two measurements can be considered as identical, as expected (at least where the onset potential is concerned), because of their identical U_{FB}.*

Etched: The polished sample $SD_{\#2\,polish\,(0.25\,\mu\mathrm{m})}$, was then etched in piranha solution and NH_4F (dark green). It behaves similar to the previously discussed cases in chapter 6, with the exception of an 140 meV energy shift to lower binding energies and an increase to FWHM from 0.7 to 0.75 eV. Additionally the polished sample exhibits a three times higher oxygen amount on the surface, probably a result of adsorbed water. All above deviations can be assigned to additional surface roughness and defects inflicted during the polishing procedure (and in case of the oxygen content, the shorter time span in vacuum before the XPS measurement). The $Si_{2p}^{SiC}/C_{1s}^{SiC}$ ratio is 1.01.

0.1 M KOH: After EC measurements in 0.1 M KOH all core level peaks exhibit a 140 eV shift to higher binding energies, thus restoring flat band conditions. The FWHM is restored to 0.7 eV as well. No new species can be observed, neither are there changes to the intensity ratios. As no new chemical compounds were found, it has to be concluded

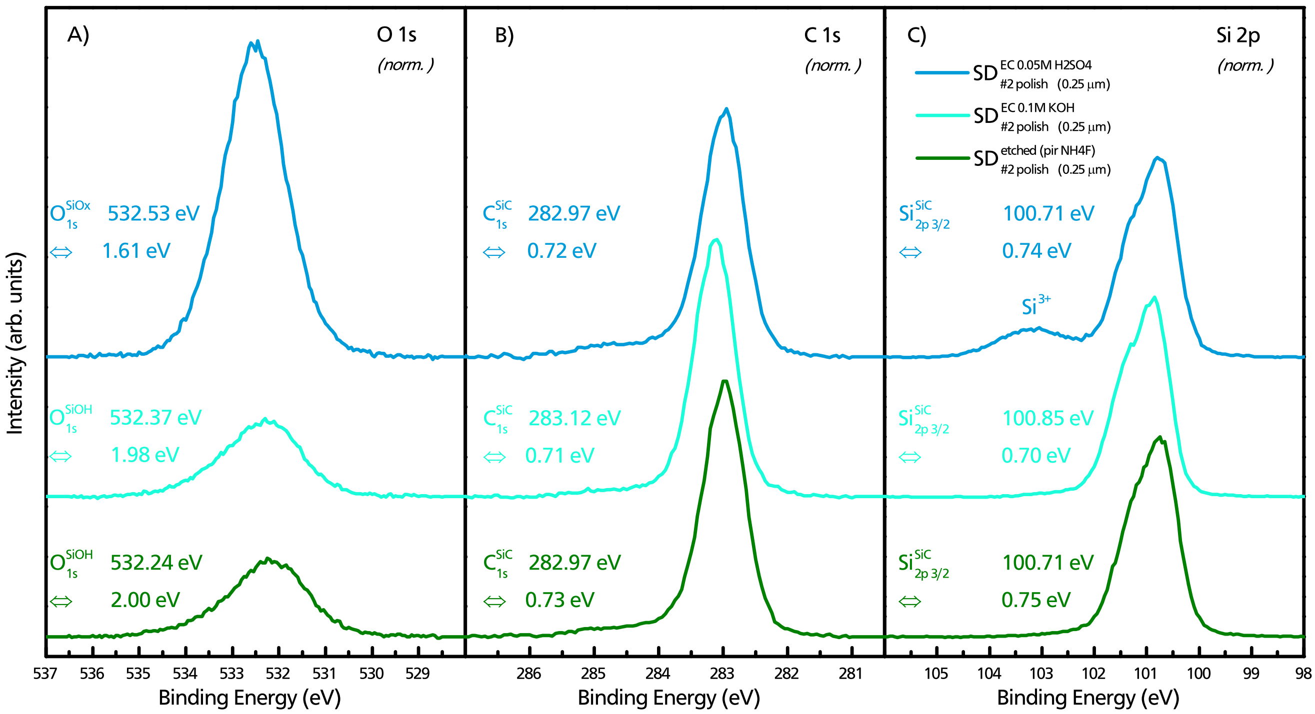

Figure 7.27.: *XPS detail spectra of* $SD_{\#2\,polish\,(0.25\mu m)}$ *for the etched sample and after the standard electrochemical measurement procedure was performed in 0.05 M* H_2SO_4 *respectively 0.1 M KOH. Apparently electrochemical measurements in KOH cause anodic dissolution (no additional species) in 3C SiC, while* H_2SO_4 *results in oxidation (oxide peak in Si 2p, increase in O 1s).*

that the observed dark current results from anodic dissolution of the 3C SiC electrode in KOH.

Anodic dissolution of SiC in general is known, and can be used for photoelectrochemical patterned etching, but the electrolyte of choice is normally diluted HF [197, 198]. Van Dorp et. al investigated the chemical stability of 4H-SiC in 0.05 to 0.5 M KOH at room and elevated temperatures [199, 200]. They proposed light driven oxidation of the SiC sample at anodic potentials exceeding 1.56 to 1.71 V vs RHE and subsequent dissolution at lower potentials. As those parameters are in excellent agreement with the observed 3C SiC behaviour it can be assumed that the reactions are similar. The discussed changes in the XPS detail spectra are therefore related to the removal of the topmost 3C SiC layers, along with at least some of the polishing induced defects.

Experimental Sequence For $SD_{\#2}$

1. polished (0.25 μm)
2. etched / EC in 0.05 M H_2SO_4 / XPS
3. etched / XPS
4. EC in 0.1 M KOH / XPS

0.05 M H_2SO_4: EC measurements in 0.05 H_2SO_4 did not cause peak shifts, and the 3C SiC bulk components peak shapes remain mostly unchanged. However, a new species appears in the Si 2p spectrum at 103.08 eV. From the peak position it can be concluded that this species does not correspond to SiO_2, which is located at approx. 103.6 eV (see section 7.4), but Si^{3+} (Si_2O_3) [203,206,207]. From the Si_{2p}^{Si2O3}:Si_{2p}^{SiC} ratio and equation 3.5 a total oxide layer thickness of (7.8 ± 0.7) Å was calculated. Assuming the surface oxide layer is mostly Si_2O_3, as indicated by the binding energy, the O_{1s}^{Si2O3}:Si_{2p}^{Si2O3} ratio should be approx. 1.5, but instead it is 4.17 ± 0.01. This is probably the result of an increased amount of adsorbed water on the sample

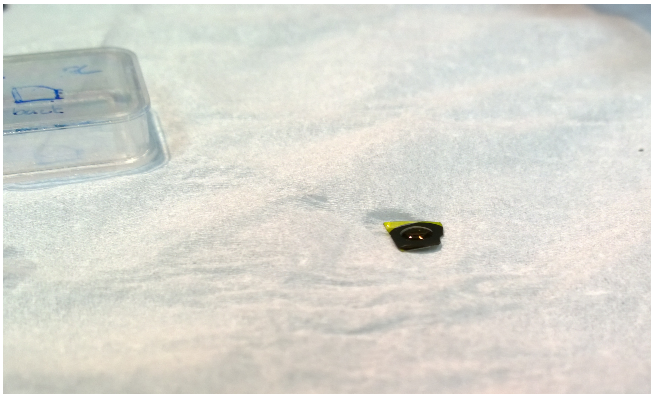

Figure 7.28.: *Picture of $SD_{\#2}$ after the electrochemical experiment in H_2SO_4. The sample was rinsed with distilled water after the experiment. From the way the water sticks only to the area previously exposed to H_2SO_4 its hydrophilic nature is obvious.*

surface, as the sample was hydrophilic after the EC experiment, as opposed to hydrophobic after the etching procedure. See figure 7.28, for a picture of the hydrophilic sample directly after the H_2SO_4 experiment. Furthermore, the C_{1s}^{SiC}:Si_{2p}^{SiC} ratio changes to 1.3, a result of surplus carbon not longer bonded as SiC at least partially overlaying the bulk signal.
Even though sample degradation clearly occurs, both in acidic and base electrolytes, it has to be noted that it only occurs at higher bias potentials and then at low rates (following from the low oxide layer thickness in H_2SO_4) compared with other semiconductors, for example silicon, where oxidation occurs faster and at lower potentials.

7.5 Conclusion

In the context of this chapter the general suitability of 3C SiC for water splitting, or more precisely the oxygen evolution reaction, has been investigated. Chopped light measurements were used to obtain the photocurrent density, which amounted to 70 μA/cm^2 at 2 V vs RHE for $SD^{0.5M\ H2SO4}_{\#2\,polish\,(0.25\mu\text{m})}$. This corresponds to an internal quantum efficiency of 1.1 %. As this is much lower than desired, the 3C SiC sample properties (mostly $SD_{\#2}$) were thoroughly investigated, and the obtained information was used to estimate the hole flux to the 3C SiC / electrolyte interface according to the Gärtner equation.

For L_p = 197 nm only about 0.5 % of the incoming photons is absorbed close enough to the 3C SiC surface to reach the interface and participate in the OER. This corresponds to a photocurrent density of 32 μA/cm^2 at 1.6 V vs RHE, assuming the exceeding current density is a result of photo corrosion. For L_p = 500 nm this number would increase to the aforementioned 1.1 %.

Because $SD_{\#2\,polish\,(0.25\mu\text{m})}$ has a rather high n_D of 8×10^{17} cm^{-3}, in combination with a low L_p of 197 nm, only the holes created in the uppermost 240 nm will participate in a photo-oxidation reaction. At the same time, 3C SiC has a rather poor absorption coefficient, a consequence of the large band gap in combination with its indirect nature. For comparison, the 3C SiC samples from this chapter feature an α of approximately 209 cm^{-1} for $\lambda = 455$ nm, while pure silicon has an α of approximately 2200 cm^{-1} [208], more than one order of magnitude higher. In order to increase the hole flux to the surface, and thus the efficiency, there are two approaches.

First, the harvesting depth could be increased, allowing holes from deeper within the bulk to reach the surface and participate in the OER. This could be obtained by the use of more pure and low doped 3C SiC, a doping concentration of 1×10^{14} cm^{-3} would result in a 5 μm W_D and should ensure an efficiency exceeding 10 %. However, this would also increase the sample resistance. The same is true for a reduced defect density, as this would increase L_p and thus the harvesting depth. Both approaches are feasible, and will be discussed in the next chapter 8.

Second, an increase in α would increase the number of electron hole pairs created within the harvesting depth, thus increasing the efficiency. However, a materials absorption coefficient is a direct consequence of its band structure and can not be altered. The only solution would be the addition of dyes or nano dots, to create alternative excitation pathways. While those approaches are very interesting, especially a two step excitation for 3C SiC, the associated efforts would go beyond the scope of this work.

The maximum photocurrent is only half of the problem, though. Ideally the OER should be running at maximum efficiency without an additional bias voltage. In theory, the OER onset should be located at 1.23 V vs RHE plus the overpotential η required for electrons to be transferred from the 3C SiC, to the electrolyte via the Si—OH/C—H surface. In reality, saturation (due to limited hole supply) is reached at 1.6 V vs RHE, while the OER starts around 0.5 V vs RHE. From this a photovoltage of about 1 V can be approximated. This could be improved by a better sample surface, as a reduction of surface states will result in a reduced shift of the flat band potential, thus increasing the photovoltage. Another approach would be an additional p-type 3C SiC or high work function catalyst layer on top, in order to create a buried junction instead of the interface junction used so far. This approach will be discussed in chapter 9.

Indeed, surface preparation seems to be critical to obtaining feasible 3C SiC electrodes. A rough, defect rich surface results either in a later onset of the OER or can prevent it completely, resulting in a much earlier onset of the sample degradation as indicated by a high dark current, even at lower potentials. On the other hand, a well defined defect free (or poor) sample surface results in an early OER onset, and a higher corrosion potential, as indicated by a later dark current onset. In case of the unpolished sample surfaces, no dark current was detected at all. Because the electrolyte pH apparently does not change the band positions relative to the redox potentials (same U_{FB} regardless of pH) the electrolyte can be selected purely in regard to sample degradation. For the samples polished with 0.25 μm diamond suspension, acidic electrolytes resulted in the formation of a thin silicon oxide film on the surface, while alkaline electrolytes result in a slow dissolution of the SiC electrode. However, without the polish induced defects, a 3C SiC surface is astonishingly inert to degradation.

In conclusion, it can be said that 3C SiC, while very durable, has problems to deliver high efficiency water splitting due to its material properties. However it might be possible to overcome some of these problems, as will be investigated in the following chapters.

8

Improving 3C SiC: Hole Flux To The Surface

The low hole flux to the 3C SiC surface is the result of a high doping concentration and low hole diffusion length. In order to improve the efficiency, approximately five micrometers of low n_D 3C SiC was grown on a single domain sample (similar to $SD_{\#1}$ and $SD_{\#2}$) via CVD. Investigation of the sample was conducted in a similar fashion to $SD_{\#1}$ and $SD_{\#2}$ in the previous section, and an photocurrent increase by a factor of 18 was observed. Applied measurement methods are XPS, absorption spectroscopy, Raman spectroscopy and electrochemical methods.

8.1 Introduction

The investigation of the single domain samples $SD_{\#1}$ and $SD_{\#2}$ in the previous chapter yielded a very low photocurrent, in the range of $30\,\mu\text{A/cm}^2$, and thus an equally low direct photoelectrochemical water splitting efficiency for 3C SiC. A detailed analysis of the sample properties allowed a comparison of the expected influx of holes to the surface, via the Gärtner equation (eq. 7.13), with the measured photocurrent. This allowed to draw conclusions on why the n-type 3C SiC performed so poorly with regard to the oxygen evolution reaction (OER).

The first problem is recombination at the 3C SiC / electrolyte interface. While the $SD_{\#2}$ photocurrent onset is located close to the flat band potential (U_{FB}=0.52 V vs RHE, U_{onset}=0.47 V vs RHE), the maximum photocurrent (all incoming holes are transferred across the interface) is not reached until approximately 1.65 V vs RHE. This is assigned to recombination of holes at the surface via surface states, in combination with low transfer rates across the interface.

However, the main problem are not the losses due to recombination, but the low percentage of photo generated holes making it to the surface in the first place. Considering the incoming photon flux ($200\,\text{W/m}^2$ at 455 nm), a photocurrent of $6370\,\mu\text{A/cm}^2$ would be possible if all photons

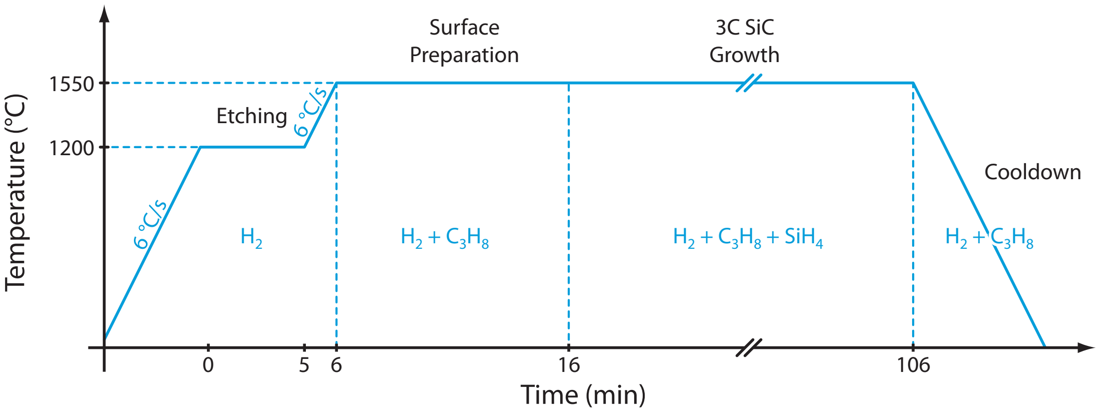

Figure 8.1.: *Experimental parameters of the low* n_D *CVD growth on a single domain (001) 3C SiC sample from Hoya. The growth was performed by Kassem Alassaad (Univ. Lyon) [209], and the sample will be listed as* SD_{CVD}.

could be harvested, and no recombination occurs. The observed maximum photocurrent for $SD_{\#1}$ and $SD_{\#2}$ is approx. 0.5 % of that. As indirect semiconductor 3C SiC displays a relatively low absorption coefficient α (209 cm^{-1} at 455 nm for $SD_{\#2}$), holes from deep inside the 3C SiC bulk have to be able to reach the surface in order to harvest a meaningful percentage of the incident light. This would require a thick depletion layer and/or large hole diffusion length. Because of the high doping concentration and defect density neither of the two properties are near the desired values in the single domain 3C SiC samples investigated so far.

The obvious solution would be the use low n-type 3C SiC bulk samples of better quality (meaning less defects and thus a higher hole diffusion length). Unfortunately, it has proven very difficult to grow high quality bulk 3C SiC. At the moment, there is no supplier who would be able to produce a sample of the desired properties.

However, 3C SiC layers of great quality can be grown via chemical vapour deposition (CVD) on substrates. This approach is widely used. Either with silicon substrates, which are cheap but limit the operation temperature to below the Si melting point at 1414 °C [137, 209]. Alternatively hexagonal SiC substrates can be used. They allow growth at higher temperatures, thus increasing the growth rate, and have nearly identical lattice constants, thus preventing strain through the sample. As the hexagonal SiC surface allows two different orientations of growth, twinning is a serious problem, though. The typical composition is (111) 3C SiC on (0001) SiC [209–211].

Therefore a third single domain n-type (001) 3C SiC sample from Hoya cooperation was used as seed for epitaxial layer growth via CVD. The resulting layer should improve the hole flux to the surface, while bulk 3C SiC / CVD 3C SiC should not drastically alter the overall sample behaviour in the electrochemical experiments.

8.2 Experimental Procedure

This chapter is focused on SD_{CVD}. The sample is similar to $SD_{\#1}$ and $SD_{\#2}$, from the previous chapter, but with an additional epitaxial layer of a lower doping concentration on top.

Low $\mathbf{n_D}$ 3C SiC Layer via CVD

An n-type (001) single domain 3C SiC sample from Hoya cooperation, was used as seed for an epitaxial 3C SiC layer grown via chemical vapour deposition (CVD). The CVD was performed at the Laboratoire des Multimatéaux et Interfaces in Lyon, with the kind support of Prof. Gabriel Ferro. Kassem Alassaad, who has obtained a high degree of expertise on the 3C SiC growth via CVD over the course of his PhD. project [209], was so kind as to perform the actual experiment.

After methanol cleaning in an ultrasonic bath, with subsequent ethanol dip, the sample was dried under argon gas flow. Subsequently, SD_{CVD} was introduced into the experimental setup via the airlock, which was then flushed with argon for 10 minutes in order to remove the air. As nitrogen atoms like to be incorporated into SiC as n-dopant, the amount of introduced nitrogen had to be kept as low as possible. From the airlock, the sample was transferred into the hydrogen filled reactor.

The following experimental procedure is graphically depicted in figure 8.1. From 700 °C upward the temperature was measured by pyrometer. Once 1200 °C were reached the sample temperature was held constant for five minutes. This hydrogen etching is meant to further clean the surface and remove the natural oxide surface layer. Subsequently, the temperature was increased to the working temperature of 1550 °C, and the incident gas was changed from pure H_2 to H_2 and propane (C_3H_8). The 10 minute surface preparation step is needed to prevent droplet formation, which could then result in whisker growth later on. Once the silane (SiH_4) was added to the gas mixture, the actual growth process started. After one hour of growth, the silane supply was stopped and the reactor cool down process was initiated.

Experience values gained from the setup indicate the growth of about 5 μm 3C SiC with a n-doping concentration around $1 \times 10^{17}\,\mathrm{cm}^{-3}$. For more information on the 3C SiC CVD growth process a study of [209] is highly recommended.

Sample Preparation and Characterisation

Before the CVD epitaxial layer growth, the SD_{CVD} surface was examined via differential interference contrast microscopy (DIC) also known as Nomarski optical microscopy [212]. This was repeated after the growth process.

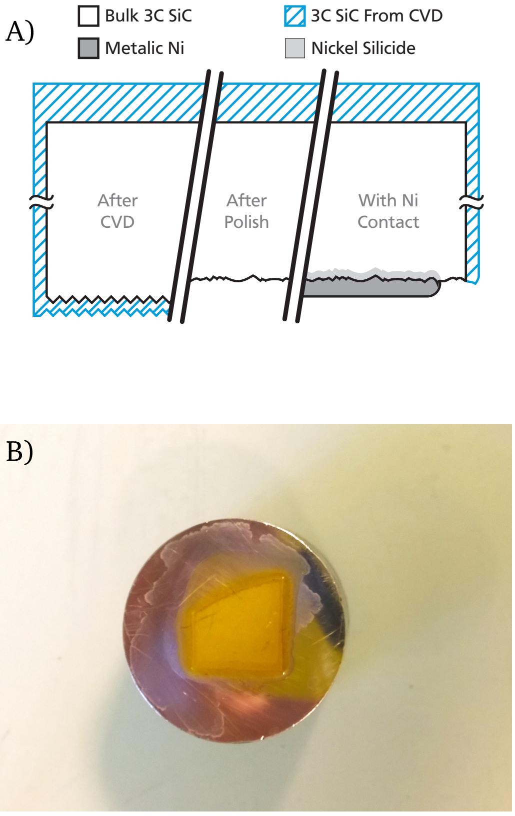

Figure 8.2.: *A) Cross section diagram of SD_{CVD} after the lower n_D layer was grown via CVD, after the backside was polished (0.25 μm) in order to remove newly grown 3C SiC from the contact area, and with the annealed Ni back contact. B) Picture from SD_{CVD} glued to a metal holder with resin, ready to be polished.*

In order to remove a possible low n_D layer from the sample backside (the contact side), the backside was polished with diamond suspension (down to 0.25 μm), see figure 8.2. The sample was then thoroughly cleaned with methanol and isopropanol in order to remove any remnants of the resin.

Subsequently, UV/Vis and Raman spectroscopy were performed in order to determine the absorption coefficient α and the doping concentration n_D of the bulk 3C SiC. Absorption spectroscopy was performed both, in transmission and with an Ulbricht sphere.

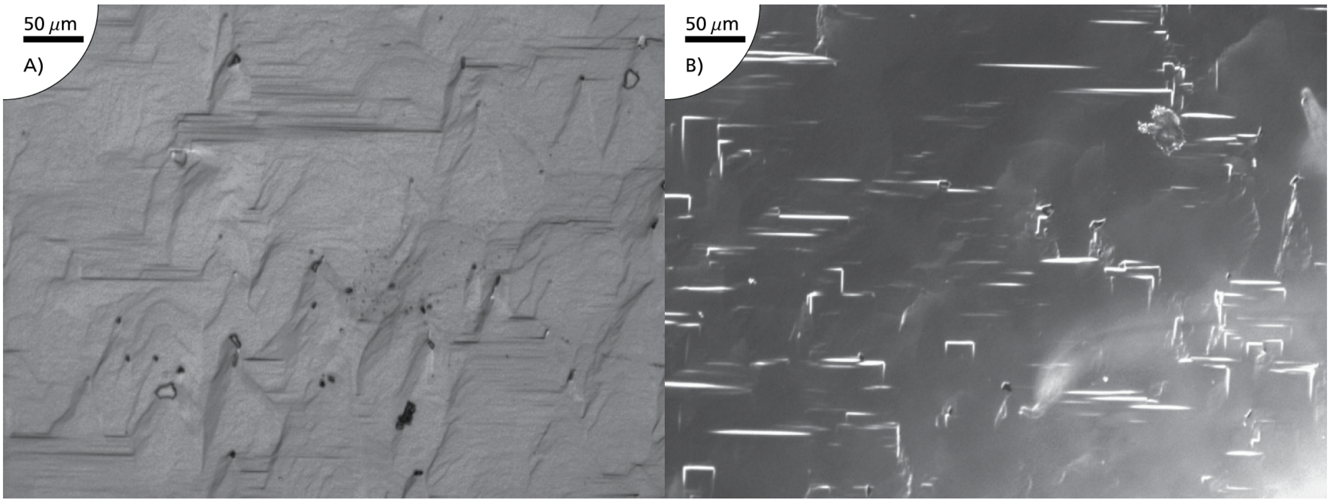

Figure 8.3.: *Nomarski microscopy pictures of SD_{CVD}. Measurements were obtained A) before and B) after the epitaxial layer growth via CVD.*

The samples was etched with piranha solution and NH_4F, as described in chapter 5. Once introduced into the UHV system, XPS and LEED measurements of the front were performed and it was briefly extracted from the UHV setup in order to flip it over and mount it onto an molybdenum sample holder for annealing. After reintroduction to the UHV setup, the nickel back contact was deposited as described in chapter 6.

In the following, the sample was used for electrochemical experiments, similar to those described in chapter 7, with the Zahner and Gamry setups. Prior to each EC experiment, the sample front surface was droplet etched with piranha solution and NH_4F, see chapter 5.

8.3 Results and Discussion

The general investigation was performed in a similar fashion to the previous chapter. However, the more complex sample structure will prohibit some of the methods previously used from providing meaningful results.

Epitaxial n$^-$ 3C SiC Layer Properties

Nomarski microscopy pictures of SD_{CVD} were taken before and after the CVD growth, see figure 8.3 A) and B). Pre growth A), the sample surface exhibits a lot of steps from the growth process, which might give rise to additional surface defect states, as atoms on the step front will exhibit dangling bonds. Additionally, various micropipes disturb the propagation of the step growth fronts, resulting in V-like formations. Post growth B), the sample surface appears much smoother. While there are still steps present, they are almost all either straight or rectangular, as one would expect for cubic (001) growth. It stands to reason, that the plain surface and the reduced number of visible defect sites should result in less surface defect states, and thus less recombination and a photocurrent onset at lower potentials.

SD_{CVD} was also investigated via UV/Vis absorption spectroscopy, after the CVD growth. The resulting absorption coefficient α is displayed in figure 8.4, both for transmission geometry and an Ulbricht sphere. The obtained values from 195 to 211 cm^{-1} at 455 nm are in good agreement with the 209 cm^{-1} for $SD_{\#1}$. As the measurement provides information on the whole sample thickness,

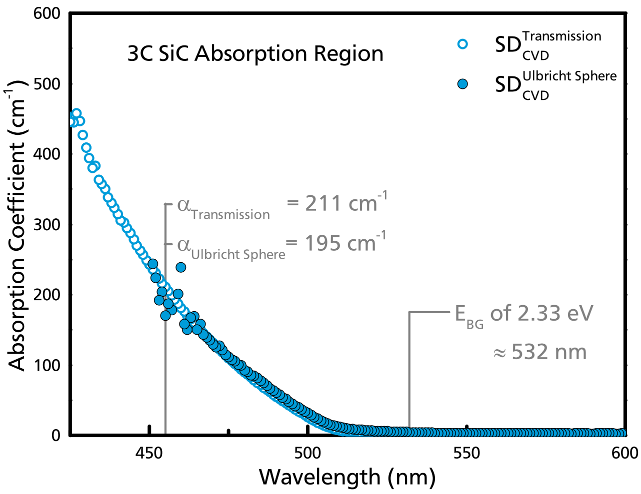

Figure 8.4.: *3C SiC absorption coefficient α from UV/Vis measurements, performed in transmission and with an Ulbricht sphere. The obtained values of* 195 *and* 211 cm^{-1} *for a* λ *of* 455 nm *are in good agreement with* 209 cm^{-1} *obtained for* $SD_{\#1}$.

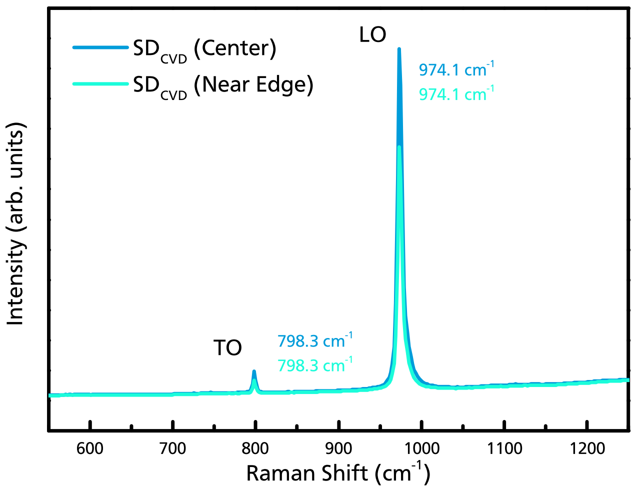

Figure 8.5.: *Raman spectrum obtained for* SD_{CVD} *at two different locations show identical peak positions. The excitation light source was a blue laser at* 488 nm*, which results in a penetration depth* $\delta = 1/2\alpha$ *of approximately* 750 μm *[213].*

the obtained α will be a result of the bulk 3C SiC. However, it is highly unlikely that the CVD layer should exhibit any meaningful deviations from the bulk α.

While Raman spectroscopy can be used to approximate a 3C SiC samples doping concentration, it presents a similar challenge for the layered sample, as for the UV/Vis measurements. The effective penetration depth $\delta = 1/2\alpha$ of the Raman laser depends on the 3C SiC absorption coefficient for the excitation lasers wavelength [213]. Even for the lowest laser wavelength available (488 nm), the resulting penetration depth is in the range of 750 μm. Therefore classic Raman spectroscopy will mostly yield information on the 3C SiC substrate. Where the LO position of 974.1 cm^{-1} indicates a doping concentration of $n_D = (5.1 \pm 2.5) \times 10^{17}$ cm^{-3}. While the epitaxial 3C layer contribution is superimposed by the asymmetrical LO overshoot, the modes of other polytypes should be in discernible intensities [82, 213]. Because of the non-existence of such additional lines it can be assumed that only 3C SiC was grown on the seed sample.

In another approach, the epitaxial layers n_D can be approximated via XPS measurements of the front surface. Assuming piranha/NH$_4$F etching results in flat band potential, as was the case in previous chapters, the core level peak positions can be used to determine the energetic difference between the Fermi level and the conduction band, and thus n_D can be calculated via equation 2.2. Figure 8.6 displays the Si 2p region of SD_{CVD}, in comparison to that of $SD_{\#1\,as\,is}$ from chapter 6 (flat band and $n_D = 1.5 \times 10^{18}$ cm^{-1}).

The lower binding energy of $Si_{2p3/2}^{SiC}$ for SD_{CVD}, would then result in $E_F - E_{CB} = 0.15$ eV. This is in good agreement with the valence band spectrum, displayed in figure 8.7. Both, the XPS and UPS measurements yield 2.18 eV within the margin of error for $E_{VB} - E_F$. Considering a band gap of 2.33 eV this corresponds to $E_F - E_{CB} = 0.15$ eV. With equation 2.2, this yields a doping concentration of 4.2×10^{16} cm^{-3} for the epitaxially grown 3C SiC layer. According to equation 7.15, this results in a four fold increase of

$$W_D = 160\,\mathrm{nm} \cdot \sqrt{U - U_{FB}} \tag{8.1}$$

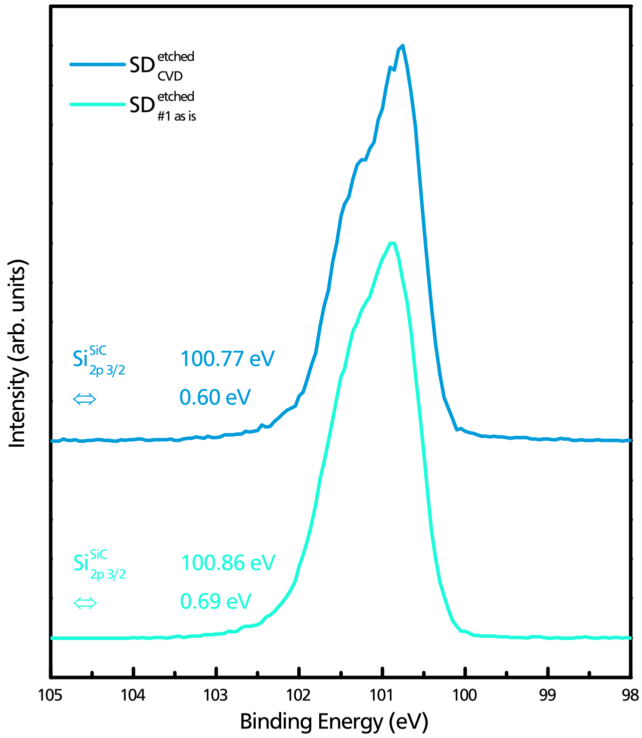

Figure 8.6.: *XPS Si 2p detail spectra of SD_{CVD} in comparison to $SD_{\#2\ as\ is}$. Both samples were etched with piranha solution and NH_4F prior to the XPS measurements. The better resolution of the spin orbit splitting for SD_{CVD} is the result of a lower pass energy of* 5 eV*, in contrast to the* 10 eV *for $SD_{\#2\ as\ is}$.*

, the depletion layer width, compared to $SD_{\#1}$ and $SD_{\#2}$. But it is still far from the desired multiple micrometers, necessary to harvest a meaningful percentage of the incident light. Therefore, hope has to be based on a significantly increased hole diffusion length L_p, as result of a reduced defect density in the CVD grown epitaxial layer.

Apart from the previously discussed shift to lower binding energies, as result of a lower n_D, XPS measurements exhibit similar behaviour to $SD_{\#1}$ and $SD_{\#2}$. Only the elements oxygen, carbon, and silicon are present, see XPS survey in figure 8.8, and the C_{1s}^{SiC}:Si_{2p}^{SiC} ratio is 1.01. No fluorine remnants from the etching procedure were observed.

In addition to XPS, LEED measurements were performed on SD_{CVD}. The resulting pattern is displayed in figure 8.9. It clearly shows the cubic crystal structure and a 1x1 surface reconstruction.

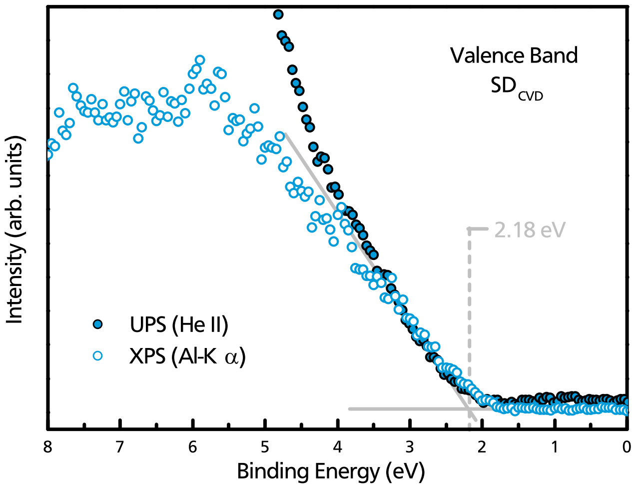

Figure 8.7.: *Valence band spectrum of SD_{CVD}. XPS (E_{pass} = 20 eV) and UPS (He II line) measurements are in good agreement on the VB onset. The valence band onset from linear extrapolation is also in good agreement with the $Si_{2p3/2}^{SiC}$ position, which were used to approximate the epitaxial layers doping concentration n_D.*

Contrary to $SD_{\#1}$ and $SD_{\#2}$ the un-annealed SD_{CVD} does not exhibit any satellite features. This, in combination with the sharpness of the spots indicates an extremely well ordered surface morphology. Ideally this will go hand in hand with the epitaxial layer being equally defect free.

Water Splitting Performance

The idea behind the production of SD_{CVD} was to create a low n_D epitaxial layer on top of the 3C SiC bulk sample, as this would result in an increased W_d, which would result in an increased hole flux to the surface, which - finally - would result in an increased efficiency. Figure 8.10 displays the chopped light measurement performed on SD_{CVD} (blue) in comparison to the $SD_{\#2\ polish\ (0.25\mu m)}$ measurement (black). Both measurements were performed in 0.1 M KOH, and the sample preparation was identical.

The differences between photocurrent densities will be discussed later on the basis of logarithmic

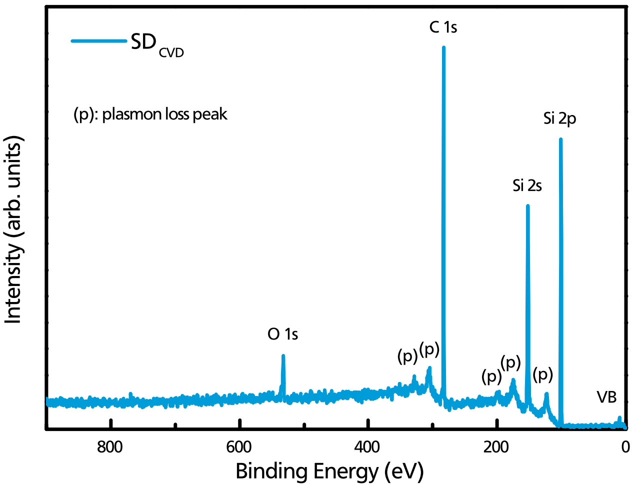

Figure 8.8.: *XPS survey spectrum of SD_{CVD}. Only the elements oxygen, carbon, and silicon are present. Overall behaviour is similar to $SD_{\#1}$ and $SD_{\#2}$, but for the core level shift to lower binding energies.*

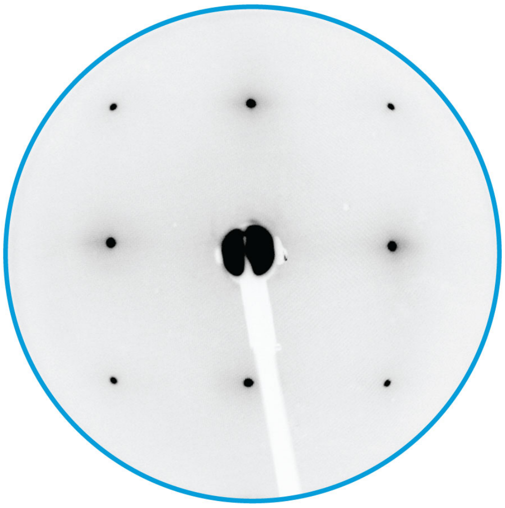

Figure 8.9.: *LEED pattern of SD_{CVD} shows the (001) sample orientation and 1x1 surface termination. The observed spots are the sharpest obtained for any of the examined un-annealed 3C SiC samples in this work. Measurement parameters: beam energy* 90 eV*, filament current* 2.8 A*, and a screen voltage of* 5 kV.

photocurrent density plots. However, three differences should be noted right away.

First, the greatly increased current density. At 1.8 V vs RHE, $SD_{CVD}^{0.1\,KOH}$ displays a current density of 579 μA/cm^2 (compared to 62 μA/cm^2 for $SD_{\#2\,polish\,(0.25\mu\mathrm{m})}^{0.1\,KOH}$, without subtracted dark current).

Second, the absence of dark current. Similar to $SD_{\#2\,as\,is}$ no dark current (and thus no degradation) occurs, but this time the measurement range was greatly increased (by 0.9 V vs RHE).

Third, the current density clearly goes into saturation, showing exactly the expected behaviour due to hole flux limitation.

It was attempted to determine the flat band potential in a similar fashion to $SD_{\#2\,polish\,(0.25\mu\mathrm{m})}$ in the previous chapter. The phase component of the resulting Bode plots are displayed as 3D plot in figure 8.11. While the behaviour is comparable for lower potentials, there is a strong deviation in the remaining measurement range.

From 0.45 V vs RHE upward, a second RC component appears, thus making an evaluation with a CPE-Randles cell as equivalent circuit (see figure 7.12 to the left) impossible. For demonstration, the EIS spectra of $SD_{\#2\,polish(0.25\mu\mathrm{m})}^{0.1M\,KOH}$ and $SD_{CVD}^{0.1M\,KOH}$ are displayed in the figures 8.12 and 8.13. A R(RC)(RC) equivalent circuit was used for a very rough approximation of the component values. If the second RC component is the result of the buried n-/n 3C SiC junction, $R_2 \ll R_1$ means that almost the entire potential drop still occurs at the 3C SiC / electrolyte interface.

At potentials exceeding 1.0 V vs RHE the curve shape indicates a possible third RC couple at frequencies exceeding 1 MHz. The greater number of RC couples, and thus the more complex shape of the EIS measurements, is a direct result of the different, more complex sample structure. Where $SD_{\#2\,polish\,(0.25\mu\mathrm{m})}$ only had a single electric field region (the depletion layer), $SD_{CVD}^{0.1M\,KOH}$ has up to three.

The EIS measurement at potentials above 0.45 V vs RHE might be simulated with an R(RCPE)(RCPE)(RCPE) equivalent circuit. However, in such an circuit the physical meaning of the additional components would not be clear, making their determination obsolete. Additionally, the increas-

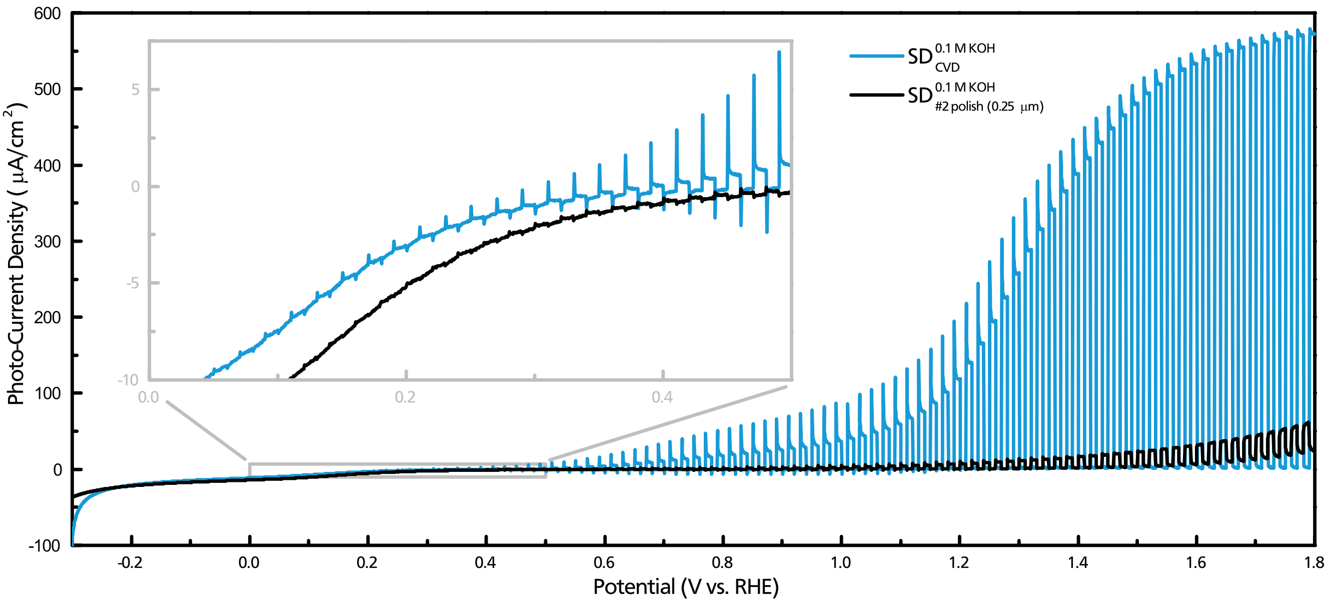

Figure 8.10.: *Electrochemical chopped light measurement of SD_{CVD} (blue) in 0.1 M KOH under illumination with a 455 nm LED at 200 W/m². The sample was droplet etched prior to the EC measurement. There is no discernible anodic dark current over the whole potential range, and the photocurrent displays the expected saturation for higher potentials.*

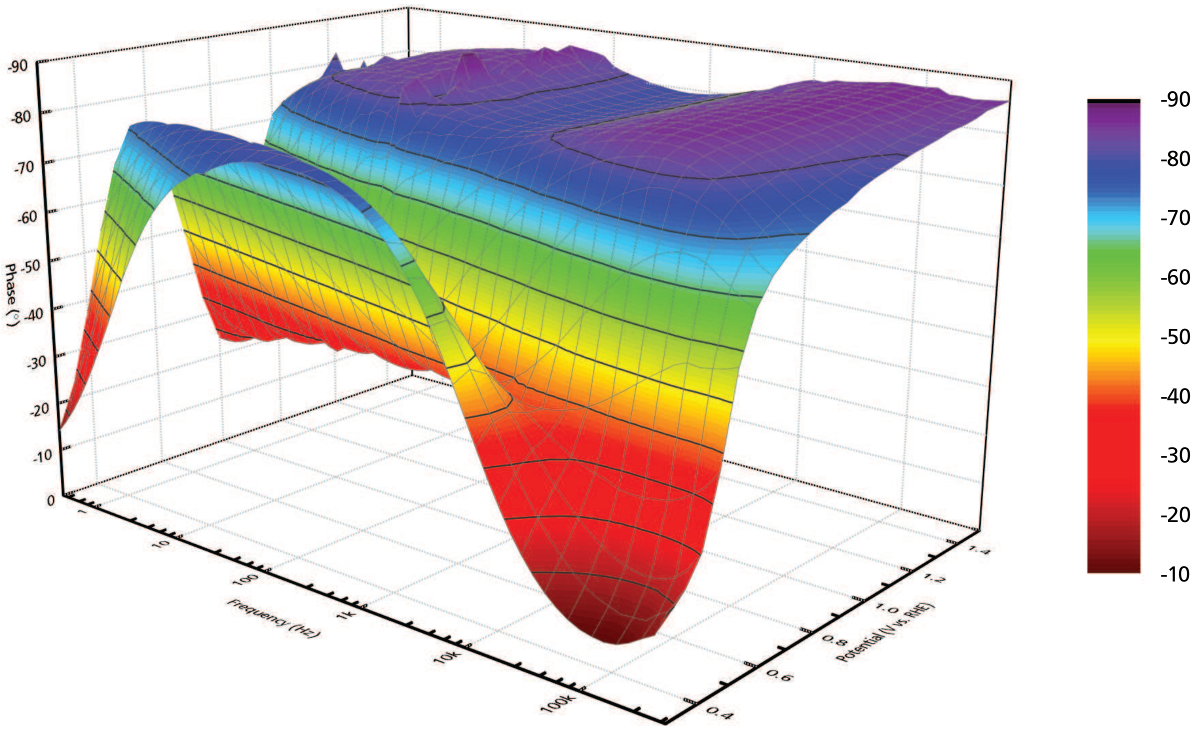

Figure 8.11.: *3D plot of the phase shifts from EIS Bode plots, performed on SD_{CVD} in 0.1 M KOH. While the behaviour is similar to $SD_{\#2}$ at low potentials, it deviates drastically at higher potentials. The shape, with two to three maxima, indicates at least two to three R-C or R-CPE couples, a result of the more complex sample structure.*

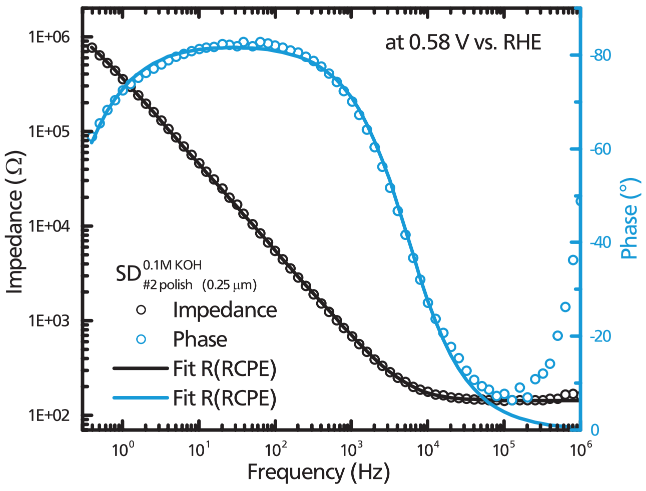

Figure 8.12.: *EIS spectrum of $SD^{0.1M\,KOH}_{\#2\,polish(0.25\,\mu m)}$ at 0.58 V vs RHE. A single R(R CPE) equivalent circuit results in a good fit. Different potentials mainly result in a shift of f_{max} via the changing capacity of the depletion layer at the semiconductor / electrolyte interface.*

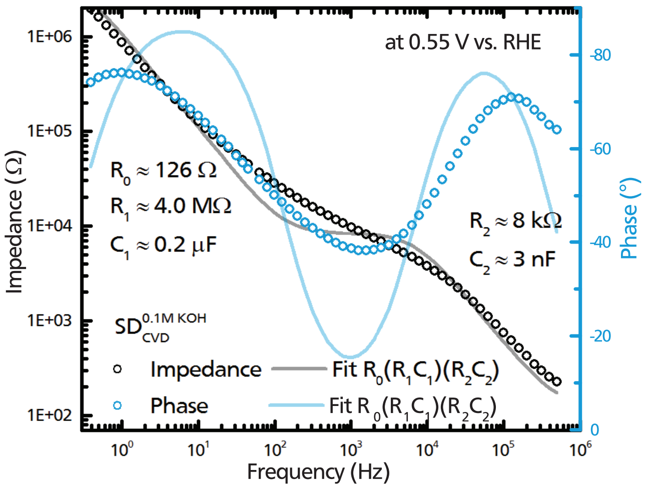

Figure 8.13.: *EIS spectrum of $SD^{0.1M\,KOH}_{CVD}$ at 0.55 V vs RHE. A single R(R CPE) equivalent circuit is no longer sufficient for the evaluation. For potentials exceeding 0.45 V vs RHE, the EIS curve shape depends strongly on the applied bias potential.*

ing degrees of freedom due to the higher number of components endangers the reproducibility of the fitting process, as multiple combinations might result in similar results.

Therefore, only the first three EIS measurements (from 0.3 to 0.45 V vs RHE) of $SD^{0.1\,KOH}_{CVD}$ were evaluated with a R(RCPE) equivalent circuit, see figure 7.12 to the left. Their resulting capacities are displayed as Mott-Schottky plot in figure 8.14, together with the $SD^{0.1M\,KOH}_{\#2\,polish\,(0.25\,\mu m)}$ results from the previous chapter. While those three points behave as would be expected for the sample, it should be kept in mind that the low number of points and the complex system do not allow more that educated guesses.

The three data points form a line. Linear extrapolation allows the determination of 0.26 V vs RHE for U_{FB}. This would be within the potential range for a surface state free 3C SiC sample stated in the previous chapter. The observed flat band position is close to the lower limit discussed in section 7.4 in context to the surface state participation. Therefore, and despite the low number of data points, the observed U_{FB} is very reasonable.

Secondly, there is the slope $\frac{\mathrm{d}(1/C_{SC}^2)}{\mathrm{d}U}$ to consider. It was used to extract the samples n_D, according to equation 7.23. Here, the $SD^{0.1\,KOH}_{CVD}$ Mott-Schottky plot yields an n_D about 20 times smaller than for $SD^{0.1M\,KOH}_{\#2\,polish\,(0.25\,\mu m)}$. This ratio is identical to the doping concentrations of the two samples obtained from XPS and Raman measurements. In both cases, the Mott-Schottky plots yield approximately one order of magnitude larger values for n_D, than the other methods. Assuming the obtained U_{FB} value is correct, the photocurrent onset of $SD^{0.1\,KOH}_{CVD}$ should be at lower potentials than for $SD^{0.1M\,KOH}_{\#2\,polish\,(0.25\,\mu m)}$.

Figure 8.15 displays the photocurrent densities J^{onset*}, $J^{s.state*}$ and the dark current density for two different 3C SiC samples, $SD^{0.1\,KOH}_{CVD}$ and $SD^{0.1M\,KOH}_{\#2\,polish\,(0.25\,\mu m)}$. Over the whole measurement range up to 1.8 V vs RHE $SD^{0.1\,KOH}_{CVD}$ displays zero dark current. This further confirms the relation between the sample surface preparation and degradation made in section 7.4.

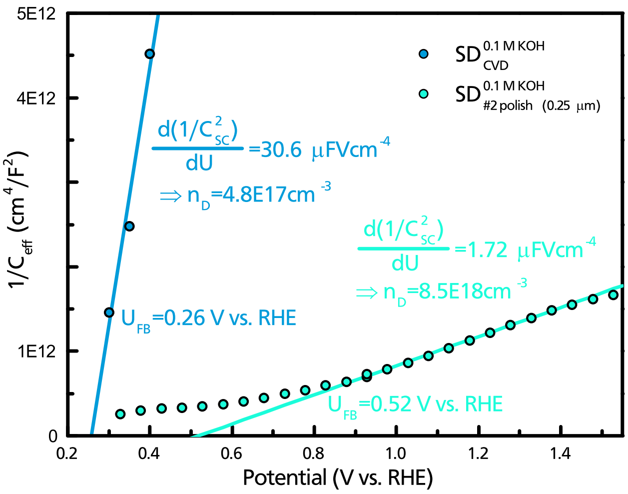

Figure 8.14.: *Mott-Schottky plots from $SD^{0.1\,KOH}_{CVD}$ and $SD^{0.1M\,KOH}_{\#2\,polish\,(0.25\mu m)}$. Fitting with a CPE-Randles cell yields the displayed values for $SD^{0.1\,KOH}_{CVD}$, but can not be employed for higher potentials, as the additional RC components would require a more complex equivalent circuit.*

The onset potential for $SD^{0.1\,KOH}_{CVD}$ at 0.24 V vs RHE is located at significantly lower bias potentials than for $SD^{0.1M\,KOH}_{\#2\,polish\,(0.25\mu m)}$. Its position also agrees perfectly with the rough approximation of the flat band position discussed above. This behaviour is similar to the previous chapter, where U_{FB} and the photocurrent onset where also located at almost the same potential for $SD_{\#2\,polish\,(0.25\mu m)}$ in

- 0.1 M KOH: onset potential of 0.52 V vs RHE and U_{FB} of 0.52 V vs RHE, and
- 0.05M H_2SO_4: onset potential of 0.47 V vs RHE and U_{FB} of 0.52 V vs RHE.

In addition to the earlier onset, $SD^{0.1\,KOH}_{CVD}$ also displays a much steeper slope than $SD^{0.1M\,KOH}_{\#2\,polish\,(0.25\mu m)}$.

3C SiC Tafel Slopes

Obtained from the linear $J^{s.state*}$ regions in figure 8.15:

$SD^{0.1\,KOH}_{CVD}$:	192 mV/decade
$SD^{0.1M\,KOH}_{\#2\,polish\,(0.25\mu m)}$:	513 mV/decade

A steep slope, equivalent to a small Tafel slope, is desirable, as it will obviously result in higher current densities at lower potentials. As the OER is a multi step reaction, it is generally assumed that the observed slope is the result of a single rate determining step (RDS), which has to be at least a factor 100 slower than all preceding steps [55, 214]. The slope can be used to attempt an identification of the RDS. For the HER, the three necessary reaction steps at platinum electrodes (Volmer, Heyrovsky, and Tafel) are quite well documented (120 mV/decade, 40 mV/decade, and 30 mV/decade) [50, 51].

Being a four electrode reaction, the OER - as in our case - is much more complex than the HER though. Over the years, a number of different reaction pathways were proposed, and it is entirely possible for multiple of these reaction pathways to occur in parallel [52–55]. This makes an identification of the RDS for n-type 3C SiC rather difficult, assuming it is a kinetic and not a diffusion limitation process anyway. It can be assumed that the 3C SiC surface does not display a high catalytic activity, as the slopes would be even steeper otherwise. Therefore it would be reasonable to add a dedicated catalyst to improve the OER kinetics and refocus on 3C SiC's main tasks, providing sufficient holes and photovoltage to drive the OER.

Compared to the other sample, $SD^{0.1\,KOH}_{CVD}$ displays a highly increased photocurrent density of 545 to 577 μA/cm^2 in the potential range from 1.6 to 1.8 V vs RHE. In relation to the 29 μA/cm^2, $SD^{0.1M\,KOH}_{\#2\,polish\,(0.25\mu m)}$ displays at 1.6 V vs RHE, this correlates to an increase by a factor of 19. With the assumption that there is no noteworthy recombination at potentials exceeding 1.6 V vs RHE, this means a likewise increase in the hole flux to the surface. As the transmission behaviour of $SD^{0.1\,KOH}_{CVD}$ does not exhibit any noticeable deviations, it can be assumed that α is either identical, or at least comparable to the previously discussed SD 3C SiC

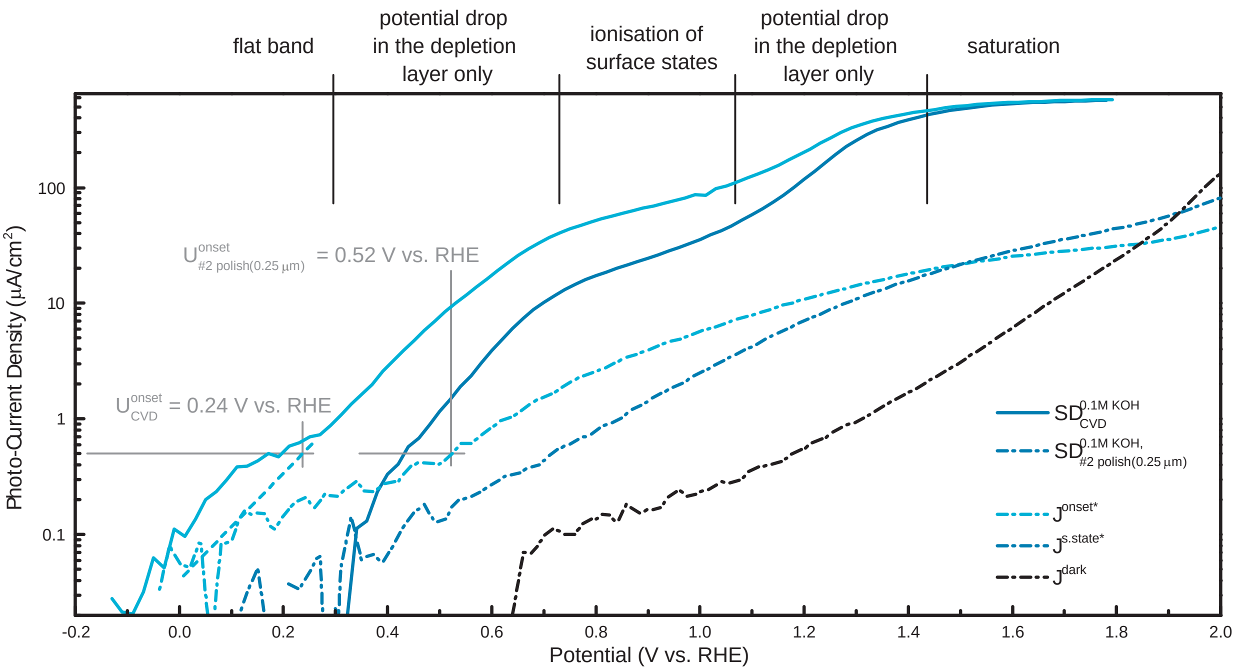

Figure 8.15.: *Photo and dark current density of* $SD_{CVD}^{0.1\,KOH}$ *under* 200 W/m^2 *illumination with a* 455 nm *blue LED, in dependence of the applied potential. Neither sample degradation (dark current), nor photo corrosion are observed (photocurrent goes into saturation). For comparison, measurement results of* $SD_{\#2\ polish}^{0.1M\ KOH}$ (0.25 μm) *(identical light source), and* $SD_{\#2\ as\ is}^{dest.\,H2O}$ (100 W/m^2 *at* 435 nm*) are provided as well.*

samples. Therefore, any difference in the observed photocurrent density has to be the result of an increased harvesting depth, holes from deeper within the bulk being able to reach the sample surface.

Part of this improvement is definitely a result of the reduced doping concentration. Considering the obtained values of n_D, a reduction from 8.0×10^{17} to 4.2×10^{16} cm^{-3}, the difference between $SD_{\#2}$ and SD_{CVD}, would result in an increase of W_D from 36.7 to $160 nm \cdot \sqrt{U - U_{FB}}$. However, the obtained increase by a factor of 4.4 is not sufficient as to explain the observed improvement of the photocurrent density by itself. Instead, the main contribution to the observed increase has to be assigned to the only remaining factor in eq. 7.13, the hole diffusion length L_p

SD_{CVD} & $SD_{\#2}$ Doping Concentrations

The ratios between the n_D values obtained from Mott-Schottky plots is identical to those obtained from other methods.

SD$^{\mathbf{XPS}}_{\mathbf{CVD}}$: 4.2×10^{16} cm^{-3}
SD$^{\mathbf{Raman}}_{\mathbf{\#2}}$: 8.0×10^{17} cm^{-3}
SD$^{\mathbf{Mott-Schottky\ 0.1M\ KOH}}_{\mathbf{CVD}}$: 4.8×10^{17} cm^{-3}
SD$^{\mathbf{Mott-Schottky\ 0.1M\ KOH}}_{\mathbf{\#2}}$: 8.5×10^{18} cm^{-3}

Keeping the above assumption of no recombination at higher potentials in mind, the hole diffusion length can be estimated from resolving the Gärtner equation 7.13 according to L_p. This yields approximately 4400 nm as L_p for the epitaxial layer of SD_{CVD}, a significant improvement compared to the 197 nm found for the original SD bulk samples. As the epitaxial layer is about 5 μm thick, only holes generated in the epitaxial layer will be able to reach the sample surface and participate in the OER.

The second junction, between the epitaxial layer and the bulk, should therefore be mostly irrelevant to the hole harvesting process. This embedded junction will however influence the overall electrode performance via impairing the charge carrier transport across the depletion layer.

Figure 8.15 can be roughly divided in sections where different effects occur, similar to the schematic band diagrams displayed in figure 7.20 (A) to (D) in the previous chapter. For potentials around the U_{FB} of 0.24 V vs RHE there will be no band bending, thus no electric field an only a very small photocurrent (fig. 7.20 (A)). An increase of potential will result in induce the formation of a depletion layer in the 3C SiC at the electrolyte interface. Due to the high resistance in this region the potential drop will occur there almost exclusively (fig. 7.20 (B)). At potentials exceeding 0.73 up to 1.07 V vs RHE the photocurrent slope decreases noticeably, this could be the result of Fermi level pinning due to the ionisation of surface states (fig. 7.20 (C)). From the onset of the slope change the surface states energetic position can be approximated to 0.64 eV below the conduction band edge. This value is made up of the 0.49 eV band banding induced at 0.73 V vs RHE plus the energetic difference of 0.15 eV between Fermi level and conduction band. See figure 8.16 for a schematic representation of the surface state position and the OER and HER potentials for S_{CVD} at U_{FB}.

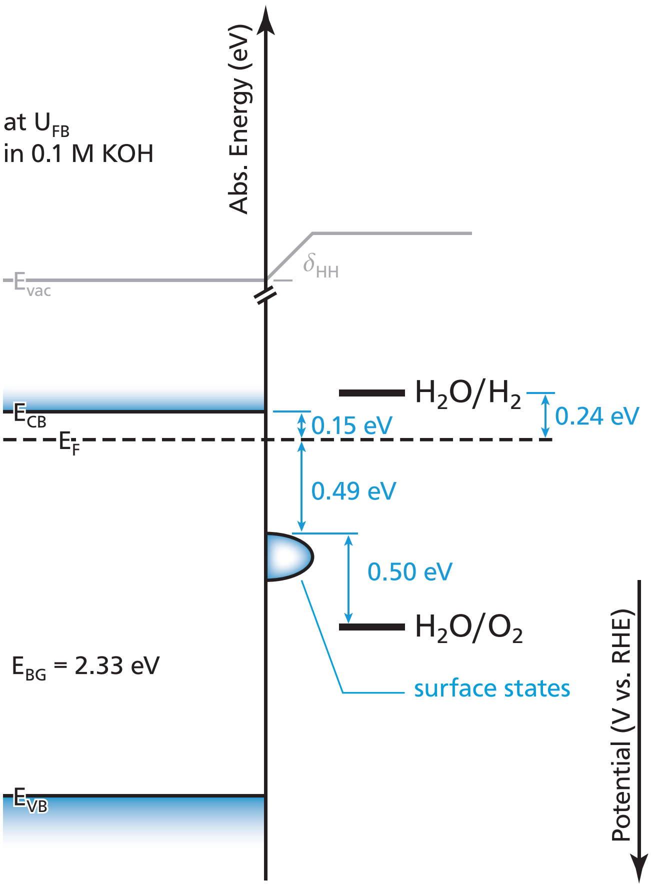

Figure 8.16.: *Band diagram schematic of SD_{CVD} in 0.1 M KOH at the flat band potential (U_{FB}) of* 0.24 V vs RHE. *Assuming the change of slope in figure 8.15 indicates the onset of Fermi level pinning through surface states, those surface states should be located* 0.64 eV *beneath the conduction band.*

8.4 Conclusion

As discussed in the previous chapter, 3C SiC displays a rather low OER efficiency, even at high anodic potentials. From an approximation of the hole flux to the 3C SiC / electrolyte interface, via the Gärtner equation, it could be concluded, that the main problem is the low percentage of light, absorbed close enough to the interface for the generated holes to reach it. A direct result of the low absorption coefficient α. The low α in turn, is the result of the wide 3C SiC band gap in combination with the band gaps indirect nature. This problem was further enhanced by the high doping concentrations (thus, a low W_D) in combination with very low values for hole diffusion length.

In this chapter, it was demonstrated that the hole harvesting depth and thus the hole flux to the surface can be increased by a factor of 19, via the growth of a five micrometer epitaxial 3C SiC layer on an existing SD sample. Most of this increase is the result of a significant improvement in the hole diffusion length L_p from 197 to 4400 nm, but the decrease in doping concentration by a factor of 10 to 4.2×10^{16} cm^{-3} and the resulting increase in W_d are helpful as well.

No dark current was observed up to 1.8 V vs RHE, neither is there any transient behaviour at higher bias potentials. Therefore, it can be assumed that almost all holes reaching the surface participate in the OER. The observed photocurrent of 577 μA/cm^2 at 1.8 V vs RHE corresponds to an internal quantum efficiency of 9.1 % for blue light ($\lambda = 455$ nm).

In addition to the improved maximum photocurrent, the onset potential is also shifted 0.28 V to lower potentials. This is ascribed to the lower number of surface states on the unpolished surface. However, the cell still does not yield sufficient photovoltage to run without an applied external bias. The high Tafel slope indicates a kinetic problem, which is to be expected without the addition of a suitable catalyst.

The performed measurements do not allow a separation of the onset potential position into the impacts of overpotential and photovoltage. Taking into account that many other not catalyst materials require extremely high overpotentials for the OER (glassy carbon 1.24 V, copper 1.27 V, iron oxide 1.27 V), the use of an adequate catalyst material, like nickel or ruthenium oxide, on the 3C SiC surface might be sufficient to allow the OER to take place with at an acceptable efficiency without any bias potential being required. The investigation of 3C SiC / catalyst hetero-junctions will be discussed in the next chapter.

9

Improving 3C SiC:

Charge Transfer And Photovoltage

This chapter will be focused on how the charge transfer across the 3C SiC / electrolyte interface can be improved by the addition of a surface catalyst layer. As a side effect, this layer will change the electrode from an interface junction (where the 3C SiC / electrolyte interaction defines the properties) to a buried junction (properties are defined by the 3C SiC / catalyst interface). The discussed samples are 3C SiC grown via CVD on a silicon wafer. They are parts of the same wafer already used for the wet chemical etching experiments in chapter 5. Applied methods for this chapter are: XPS interface experiments, absorption spectroscopy, and electrochemical methods.

9.1 Introduction

Back in chapter 2, it was shown that the current voltage behaviour of a simple redox reaction can be explained in terms of the applied overpotential η and the exchange current density j_0, as result of the reaction kinetics. Ideally a catalyst should increase the current density at a set overpotential. This will manifest either in a steeper Tafel slope or a higher j_0. The resulting curve shape will then appear as if a shift to lower potentials had occured. In addition to improving the reaction kinetics, a suitable catalyst layer might also protect the surface from corrosion.

The performance of catalysts is mostly studied on inert metal substrates. This setup provides sufficient charge carriers for anodic and cathodic reactions, and the cells rest potential (eq. 2.26) is easily determined, as is the catalysts performance. For measurements on semiconductors substrates additional effects, like the semiconductor resistivity, space charge regions or substrate oxidation have to be taken into account. For characterisation it is common to pick a current density, and report the necessary overpotential for it to be reached. A value of $10\,\mathrm{mA/cm^2}$ is used most frequently, although $1\,\mathrm{mA/cm^2}$ or $10\,\mu\mathrm{A/cm^2}$ can be found as well. Figure 9.1, shows some of the known catalyst

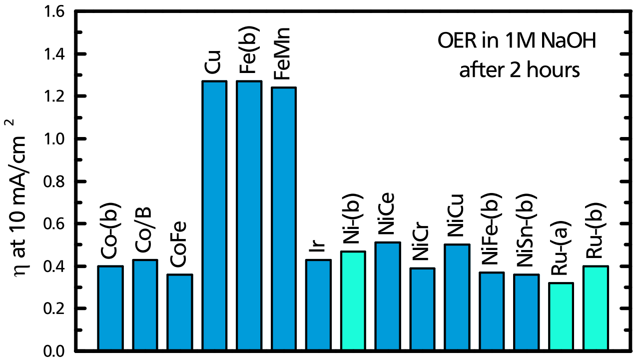

Figure 9.1.: *Overpotentials η for some common OER catalysts. The values are for a current density of* $10\,\mathrm{mA/cm^2}$ *in 1 M NaOH after two hours of OER. (a) and (b) are place holders for oxides, were the exact stoichiometry is unknown [17].*

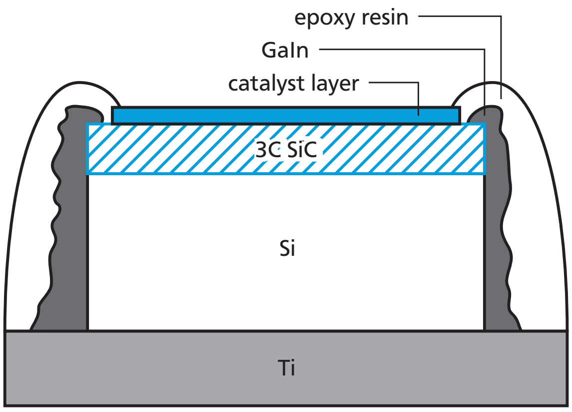

Figure 9.2.: *Cross section schematic of the* $3C_{NiO}$ *and* $3C_{RuO2}$ *samples with a GaIn contact. The samples was etched first, followed by catalyst deposition, and the GaIn contact.*

for the OER, and the necessary overpotentials for a $10\,\mathrm{mA/cm^2}$ current density [17].

The situation gets even more complex for an illuminated semiconductor, where the photovoltage will act as an additional bias potential shifting the OER to lower potentials (see figure 2.13 in chapter 2). In this case the photovoltage will be determined by the 3C SiC / catalyst interface. As the photovoltage is not constant, but depending on the current density, the overall cell performance of the catalyst covered 3C SiC, will be a superposition of the catalysts performance (current density in dependence of overpotential η) and the junctions photocurrent in dependence of photovoltage characteristic (this will be abbreviated as IV in the rest of this chapter). If neither the catalytic performance nor the junctions IV characteristic are known, it is not possible to distinguish their impacts on the overall cell performance.

9.2 Experimental Procedure - Si / 3C SiC

All experiments in this chapter were performed on pieces of the same two inch (001) 3C SiC on Si wafer, already used for the experiments in the chapters 4 and 5, where it was found that the $1.5\,\mu$m 3C SiC layer has a doping concentration of $1 \times 10^{17}\,\mathrm{cm^{-3}}$. Before any experiments were performed the samples were wet chemically etched with Piranha solution and NH_4F. This results in a flat band like situation at the surface, as was discussed in chapter 5. Post etching no traces of contamination were found. Sample nomenclature will follow the known path (for example $3C_{pir,NH4F}$ for a 3C SiC on Si sample after wet chemical etching).

For the electrochemical measurements some kind of electrical contact will be required. Ideally directly to the 3C SiC, in order to prevent any unnecessary impact from the 3C SiC / Si heterojunction and the high resistance silicon substrate. In order to accomplish this, the 3*C* sample was placed on a piece of titanium sheet. Its 3C SiC front was connected to the metal sheet via Gallium Indium eutectic (99.99 % metals basis, 62 % Gallium) by Alfa Aesar. To improve handling and durability the eutectic was covered with epoxy resin, see figure 9.2 for a schematic.

An etched 3C SiC sample, $3C_{etched}$, with the above contact was investigated via the standard EC experimental procedure. This sample's performance will function as reference for the influence of NiO and RuO_2 catalyst layers.

Two different high performance catalyst systems, with low reported overpotentials were selected. The wide band gap semiconductor nickel (II) oxide (NiO), with an overpotential of 0.47 V at 10 mA/cm^2, and the metallic ruthenium (IV) oxide (RuO_2), with an overpotential between 0.32 and 0.40 V.

Si / 3C SiC / NiO

After some initial test, to get the deposition parameters right, the 3C SiC / NiO interface was investigated via an XPS interface experiment. The experimental procedure and equipment for the NiO deposition were mostly identical to those presented in chapter 6, for the $SD_{\#1}$ 3C SiC / nickel interface experiment. However, in order to produce NiO, the gas flow was adjusted to 20 sccm Ar and 1 sccm 99.995 % pure O_2. Before the first deposition, the Ni target was cleaned via sputtering 240 s at 30 W with closed shutters, the actual deposition was performed at 15 W.

The MBE base pressure p_{MBE} was 1.9×10^{-8} mbar, and the accompanying XPS measurements were performed at pressures of 4×10^{-10} mbar or below. Deposition times were 3, 6, 15, 35 and 41 seconds, and the layer thickness was estimated from the relative peak intensities according to equation 3.4.

Afterwards, the sample was stored under UHV conditions for one day, before it was extracted, and equipped with the aforementioned GaIn back contact. It was then introduced into the EC cell, and the standard EC experimental procedure, described in chapter 7, was performed. The measurements were performed in 0.1 M KOH. Because of the eutectic GaIn contact, no post EC XPS measurements were performed.

Si / 3C SiC / RuO2

Similarly, the 3C SiC / RuO_2 interface was investigated with another XPS interface experiment. The experimental procedure was mostly identical to the one in the previous section, but a 99.95 % pure ruthenium target by Kurt J. Lesker was used instead, and the gas flows were 18.5 sccm argon with 1.5 sccm oxygen [215]. As before, the Ru target was cleaned, at 20 W for one minute, before the power was reduced to 10 W, and the shutter was opened for the deposition.

The MBE base pressure p_{MBE} was 2.2×10^{-8} mbar or below, and the accompanying XPS measurements were performed at pressures of 7×10^{-10} mbar or below. Deposition times were 3, 7, 17, 44 and 49 seconds. The layer thickness was estimated from the relative peak intensities according to equation 3.4.

Afterwards, the sample was stored under UHV conditions for two days, before extraction. The GaIn contact was added, and it was introduced into the EC cell. Again, the standard EC experimental procedure was performed in 0.1 M KOH, see chapter 7. Because of the GaIn back contact, no post EC XPS measurements were performed.

9.3 Results and Discussion

Similar to chapter 8, the epitaxial 3C SiC doping concentration can be determined from the XPS measurements via equation 2.2. The necessary $E_{CB} - E_F$ of 0.13 eV was already determined in chapter 5, and the resulting approximation for n_D is 9.3×10^{16} cm^{-3}. This is in excellent agreement with the expected value of 10^{17} cm^{-3} from former experience with the CVD setup, and the resulting depletion layer width would be

$$W_D = 108\,\mathrm{nm} \cdot \sqrt{V_d - U} \quad .$$

Si / 3C SiC

As mentioned above, the more complex cell design prevents any meaningful EIS measurements.

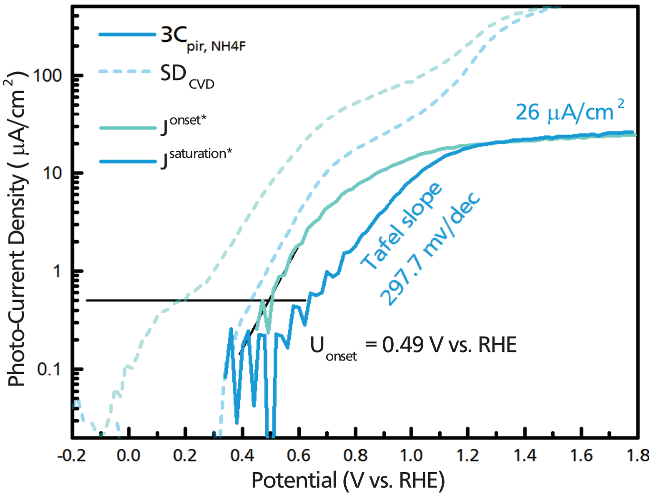

Figure 9.3.: *Photocurrent density for $3C_{pir,\,NH4F}$ in comparison to SD_{CVD}. Both measurements were performed in 0.1 M KOH, with a* 455 nm *LED at* 200 W/m^2. *$3C_{pir,\,NH4F}$ will be the reference behaviour for evaluation of the catalyst impact.*

Therefore, the flat band potential U_{FB} can not be determined via Mott-Schottky plots. While the exact extend of W_D at a given potential will thus remain unknown, it was already shown in the previous chapters, that the hole diffusion length L_p is the dominant factor for the expected photo current density. So far, L_p values between 197 nm for $SD_{\#2}$ and 4400 nm for SD_{CVD} were found.

Assuming an epitaxial layer thickness of 1.5 μm, and further assuming L_p is sufficient to allow all holes generated within the epitaxial layer to reach the surface would result in

$$J_{photo}(\lambda = 455\,\text{nm}) = 197\,\mu\text{A/cm}^2$$

as the expected maximum photocurrent density. This increases to

$$J_{photo}(\lambda = 455\,\text{nm}) = 210\,\mu\text{A/cm}^2 \quad , \qquad (9.1)$$

if the reflection on the 3C SiC / Si interface is taken into account, which will result in part of the light crossing the 3C SiC layer a second time.

Figure 9.3 shows the measured photocurrent density of $3C^{0.1M\,KOH}_{pir,NH4F}$. This measurement will function as reference for the subsequent investigation of the catalyst covered samples. The observed maximum photocurrent density is obviously much lower than the approximated 210 μA/cm^2. A possible explanation would be that not all charge carriers from near the centre of the sample are able to reach the contacts at the sample sides, before recombination. Furthermore, the onset potential is shifted 0.25 V to the right, compared to $3C_{CVD}$. This could either indicate a higher defect density at the sample surface or be a result of a Schottky contact between the GaIn eutectic and the 3C SiC, which induces a opposing built in potential.

While the different back contact prevents a meaningful comparison between the bulk and the epitaxial 3C SiC samples, it should not inhibit a comparison between the three samples investigated within this chapter. As $3C^{0.1M\,KOH}_{pir,NH4F}$ and the two samples with a catalyst layer, $3C^{0.1M\,KOH}_{NiO}$ and $3C^{0.1M\,KOH}_{RuO2}$, only differ in their surface preparation any observed changes should be a result of those surface layers alone. Relative changes in onset potential, Tafel slope etc. can then be used to extrapolate the catalyst layers performance on 3C SiC bulk samples.

Besides a different method of contact formation, the silicon substrate could also influence the measurement by absorbing light and thus providing charge carriers. Due to the straddling nature of the Si / 3C SiC heterojunction, both holes and electrons would have to overcome an energy barrier in order to cross over into the 3C SiC [30, 216]. In order to investigate whether there is any photocurrent contribution from the Si substrate, the photocurrent density of $3C^{0.1M\,KOH}_{pir,NH4F}$ was measured for different wavelengths. Some of those with a wavelength large enough as not to be absorbed in the 3C SiC.

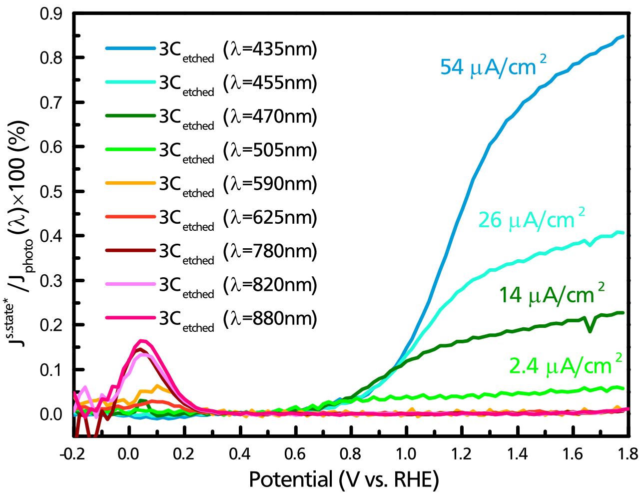

Figure 9.4.: *Measured photocurrent density $J^{s.state*}$ of $3C_{pir,NH4F}$ in relation to the possible current density from the incident photon flux J_{photo} for different LED wavelengths λ.*

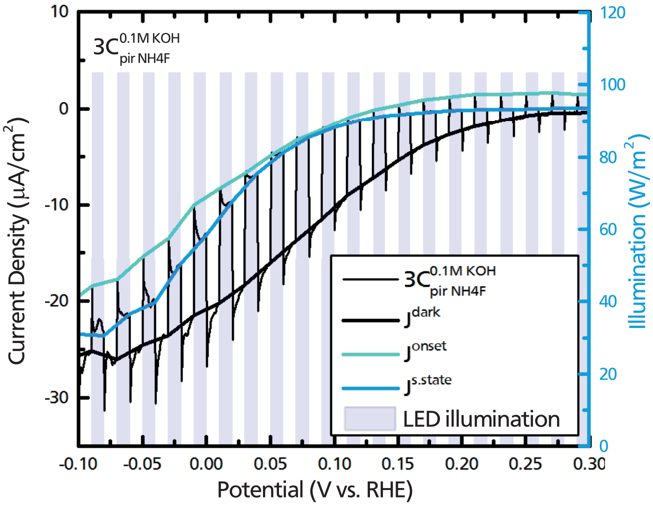

Figure 9.5.: *Current density response of $3C_{pir,NH4F}$ in 0.1M KOH under chopped light illumination with a* 880 nm *LED. While this wavelength is not absorbed in the epitaxial 3C SiC layer it induces a photovoltage in the Si substrate, which in turn shifts the curve to the left.*

The measured steady state photocurrent $J^{s.state*}$ is displayed as percentage of the incoming photon flux in figure 9.4. Wavelengths of 505 nm and below can be absorbed in 3C SiC, and the respective measurements only show the expected behaviour, with the onset potential around 0.49 V vs RHE. The observed $J^{s.state*}$ dependency on λ corresponds very well to the 3C SiC absorption coefficient for those λ, further confirming that the observed photocurrent is an effect of the epitaxial 3C SiC layer only.

For wavelengths exceeding 505 nm, no light should be absorbed in the 3C SiC and no photocurrent is observed in the potential range of 0.5 V vs RHE and above. However, those measurements display a weak anodic current in the potential range from 0.0 to 0.2 V vs RHE. This is a result of a shift of the cathodic onset current to a more negative potential under illumination, see figure 9.5. As the illumination induces a photovoltage in the Si substrate, the curve is shifted to the left, thus $J^{s.state*} = J^{s.state} - J^{dark}$ becomes positive in the area where the photovoltage results in a different current density at a given potential vs. RHE.

Si / 3C SiC / NiO

Nickel oxide exhibits a high dissolution resistance in alkaline solutions [217], and is an efficient catalyst for the OER [17, 218, 219]. NiO is a wide band gap semiconductor, whose band gap is frequently reported in the range from 3.1 to 4.3 eV [220–224]. Even assuming the lowest reported value for E_{BG}, absorption would only have to be considered for incoming light with a wavelength λ of 400 nm or below, and can be neglected for the electrochemical experiments performed with a 455 nm LED.

The last deposition step of the interface experiment was used to determine the NiO properties. At this point, any contributions from the subjacent 3C SiC to the spectrum are negligible. From the valence band spectrum, see figure 9.6, it is obvious that the valence band edge is very close to the Fermi level (binding energy of zero) As the NiO band gap is 3.1 eV or above it can be concluded that the deposited NiO is p-type. This spectrum also confirms that the deposited NiO is not metallic but a semiconductor.

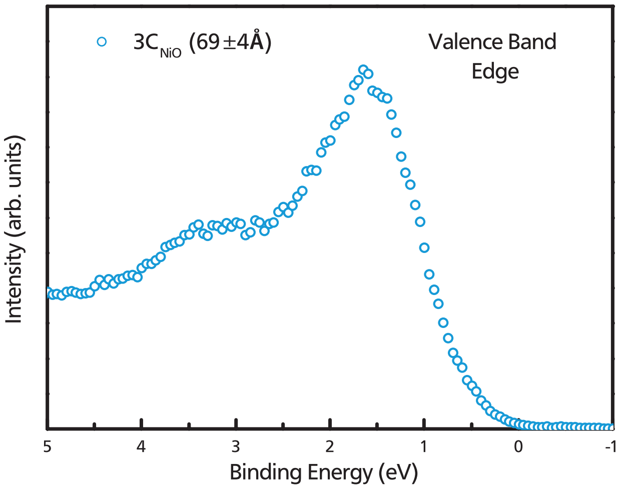

Figure 9.6.: *XPS spectrum of the* 3C$_{NiO}$ *valence band after the last interface experiment deposition step, corresponding to a* (69 ± 4) Å *NiO over layer. Considering the assumed* E_{BG} *of* 3.1 eV*, the observed* $E_{VB} - E_F$ *shows the p-type nature of the NiO.*

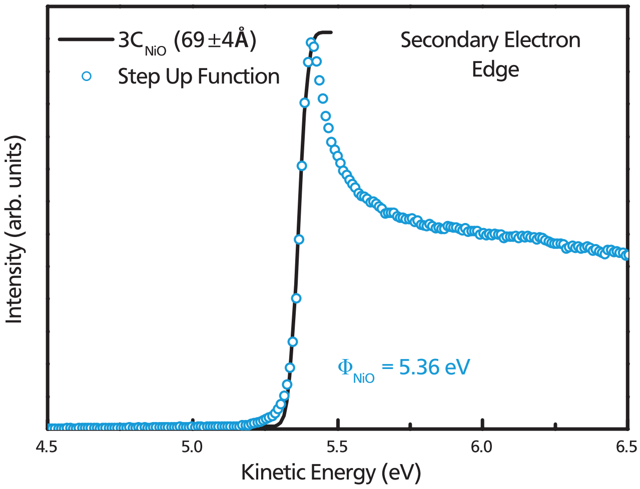

Figure 9.7.: *Secondary electron edge XPS spectrum for* 3C$_{NiO}$ *after the last interface experiment deposition step. While the first deposition steps exhibit strong changes in the surface work function, the final two show identical behaviour. The determined work function for* Φ_{NiO} *is* 5.36 eV.

The (69 ± 4) Å deposition step was also used to determine the NiO work function from the secondary electron edge, see figure 9.7. While the surface work function underwent strong changes during the first deposition steps, the changes decrease with increasing NiO layer thickness, until there is no change between the 42 ± 3 and the (69 ± 4) Å NiO layers. Therefore, this final value of 5.36 eV is taken as the work function of the deposited polycrystalline nickel oxide Φ_{NiO}. This value is in excellent agreement with previous reports, which mostly provide values from 5.0 to 5.6 eV [225–227]. Although the exact value of Φ_{NiO} depends strongly on the preparation method and parameters. Greiner et al. [226] achieved NiO work functions as high as 6.7 eV for in situ oxidised NiO, but found this to be unstable, the value decreasing due to the adsorption of residual gases even under UHV conditions.

XPS interface experiments and their outcomes have been discussed at length in chapter 6, thus the following discussion will be kept short. The relevant XPS detail spectra of the 3C SiC / NiO interface experiment are displayed in figure 9.8. Considering the p-type nature of the NiO layer, and further considering that Φ_{NiO} is significantly higher than the $\Phi_{SiC\ bulk}$ of 4.13 eV, or the $\Phi_{SiC\ surface}$ of 4.55 eV, the interface contact should result in upward band bending (shift to lower E_{bin}) in the 3C SiC and downward band bending (shift to higher E_{bin}) in the NiO.

The observed behaviour corresponds to those assumptions. All obtained shifts in the 3C SiC components ($Si_{2p3/2}^{SiC}$ and C_{1s}^{SiC}) and the NiO main peak ($Ni_{2p3/2}^{NiO}$) are summarized in table 9.1. From the the respective work functions it can be concluded, that the total diffusion potential V_d for an ideal junction between the two materials should amount to 1.23 eV. As both, 3C SiC and NiO, are semiconductors, the band bending will occur in both materials, and their distribution should depend on their respective doping concentrations [37].

While the final band bending of 0.43 eV in the 3C SiC can be clearly determined by comparison of 3C SiC surfaces without and that with a 69 Å NiO layer, this is not the case for the NiO layer. Compared to the first NiO deposition step (2 Å) the $Ni_{2p3/2}^{NiO}$

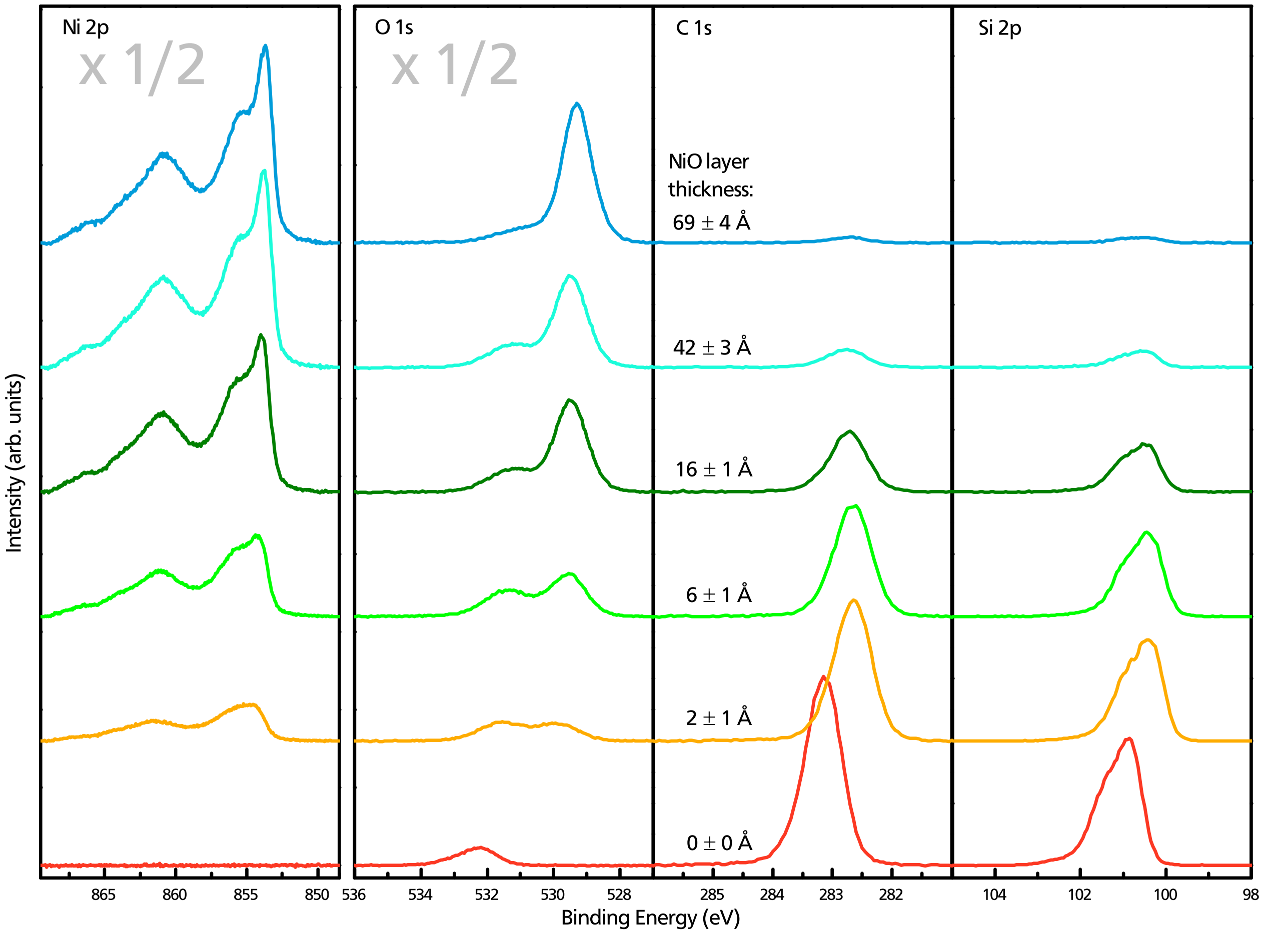

Figure 9.8.: *XPS detail spectra (with subtracted background) of the 3C SiC / NiO interface experiment performed on* $3C_{NiO}$*. All measurements were performed with a* 10 eV *pass energy. The SiC species* $Si^{SiC}_{2p3/2}$ *and* C^{SiC}_{1s} *display a* 0.49 eV *shift to lower binding energies, after the first deposition step. Layer thickness determination was performed via numerical solution of equation 3.4.*

d_{NiO} (Å)	$\Delta Si^{SiC}_{2p3/2}$ (eV)	ΔC^{SiC}_{1s} (eV)	$\Delta Ni^{NiO}_{2p3/2}$ (eV)
0	0	0	-
2 ± 1	-0.48	-0.49	0
6 ± 1	-0.48	-0.48	+0.74
16 ± 1	-0.41	-0.41	+0.65
42 ± 3	-0.37	-0.37	+0.50
69 ± 4	-0.40	-0.45	+0.42

Table 9.1.: *Relative peak shifts of the main 3C SiC and the NiO component. Data was obtained from the 3C SiC / NiO interface experiment presented in figure 9.8.*

component of the final deposition step is shifted 0.42 eV to higher binding energies, which could be a result of the expected downward band bending. However, this shift does not necessarily correspond to the actual band bending in the NiO layer. Part of the observed shifts in binding energy could be ascribed to chemical changes, as the Ni 2p detail spectra for low NiO layer thicknesses do not display the characteristic NiO peak shape, and the first deposition step is less than one monolayer of NiO. Cluster size effects could also influence the measurements [154, 155].

Furthermore, all components display the strongest shifts in binding energy for the first two deposition steps (−0.49 eV for 3C SiC, 0.74 eV for NiO), which then decreases with further NiO deposition, until at least the 3C SiC components stay constant within the margin of error. A possible explanation for this could be an arrangement of the first NiO

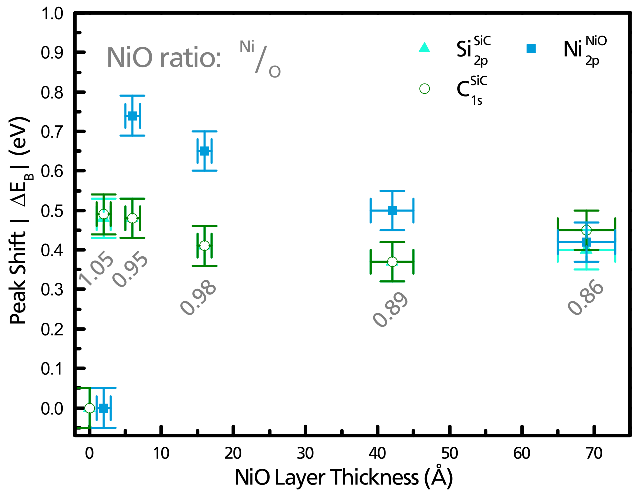

Figure 9.9.: *Absolute values of the binding energy shifts plotted over the deposited NiO layer thickness for* $3C_{NiO}$.

monolayer as an ordered polar structure which could exhibit a build in electric dipole. However, the above considerations prevent a clear statement on the NiO band bending. Therefore the following considerations will take the possible range of 0 to 0.8 eV for V_d^{NiO} into account. The absolute values of the discussed peak shifts are displayed in figure 9.9.

Nickel oxide is commonly found in two configurations, either as nickel (II) oxide (NiO), or as nickel (III) oxide (Ni_2O_3). In the presence of hydrogen nickel (II) hydroxide ($Ni(OH)_2$) is also common, its peak shape and position are very similar to that of Ni_2O_3 [228–232]. The two configurations show a characteristic and distinct curve shape in their XPS Ni 2p core levels. As the deposited nickel oxide displays two distinct peaks in the binding energy range from 852 to 857 eV and has its main peak located at 853.7 eV, see figure 9.8, it can be identified as NiO [151, 152, 232]. This is supported by the stoichiometric information (see figure 9.9) where a Ni:O ratio between 1.05 and 0.86 was found for the NiO species in the O 1s and Ni 2p regions.

The above information in combination with the knowledge of the 3C SiC band diagram from chapter 5 allows the construction of a band diagram for the 3C SiC / NiO interface. Figure 9.10 displays the situation for 3C SiC and NiO separately (A) and in contact (B). Obviously, the contact results in a staggered heterojunction [37]. Therefore, any holes transferring from the 3C SiC into the NiO catalyst layer will loose energy due to the abrupt change ΔE_{VB} in the valence band edge positions at the interface. Which in turn should result in a shift of the OER onset potential to higher potentials, as this energy loss has to be compensated by an additional bias potential.

Because there is no 3C SiC / electrolyte interface, the available photovoltage will be determined by the buried 3C SiC / NiO junction only. The open circuit photovoltage of the junction should be equal to the total diffusion potential $V_d = V_d^{3C} + V_d^{NiO}$. As concluded from the XPS interface experiment, V_d will be in the range of 0.43 to 1.23 eV, depending on the value of V_d^{NiO}. Depending on the junctions form factor, the available photovoltage at higher photocurrent flows will be smaller still. Furthermore the energy loss ΔE_{VB} and the necessary η of 0.15 to 0.25 V for the OER at NiO [218, 219] have to be taken into account as well.

Above considerations have been graphically summarized in form of a flow chart, see figure 9.11. While the mentioned uncertainties do not allow a precise prediction of the potential, necessary to reach a photocurrent density of 10 μA/cm^2, narrowed down to a potential range from 0.84 to 1.64 V vs RHE, or slightly higher (depending on the form factor). Considering that the reference sample $3C_{pir,NH4F}$ exhibited a current density of 10 μA/cm^2 at 0.89 V vs RHE, the NiO layer is actually likely to worsen the onset potential by shifting it to the right.

Figure 9.12 displays the chopped light measurement results of $3C_{NiO}$ in 0.1M KOH under 200 W/m^2 illumination from a 455 nm LED, in comparison to the reference $3C_{pir,NH4F}$ (dashed line), the original chopped light measurement can be found in the ap-

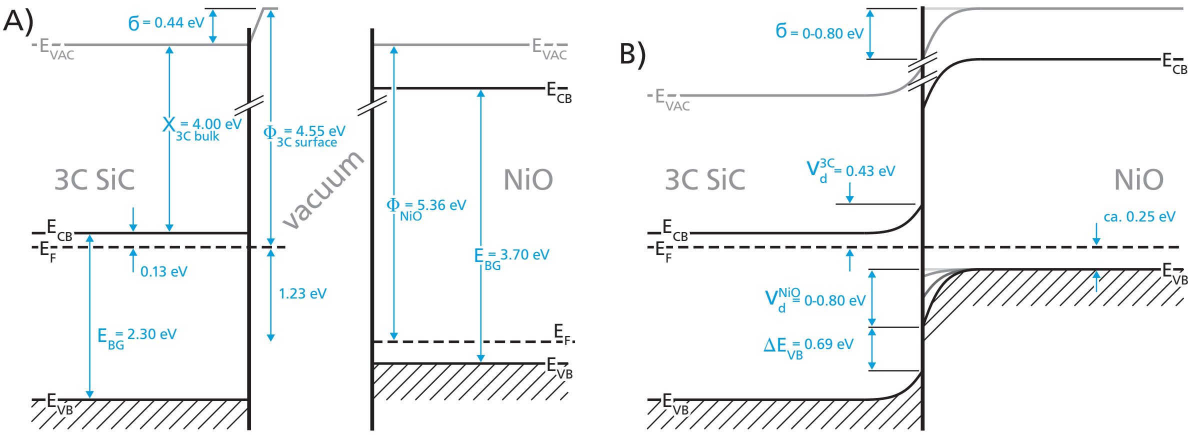

Figure 9.10.: *Band diagram of the 3C SiC / NiO interface (A) before and (B) after contact formation. Because the resulting interface is a staggered heterojunction, where any holes transferring from the 3C SiC to the NiO will lose energy. The NiO band gap was also measured via absorption spectroscopy, see figure A.1 in appendix A.3. As the performed experiment does not allow to distinguish between binding energy shifts due the chemical changes and due to band bending in the NiO (see text)* V_d^{NiO} *can not be determined precisely, which is why a range is supplied in (B).*

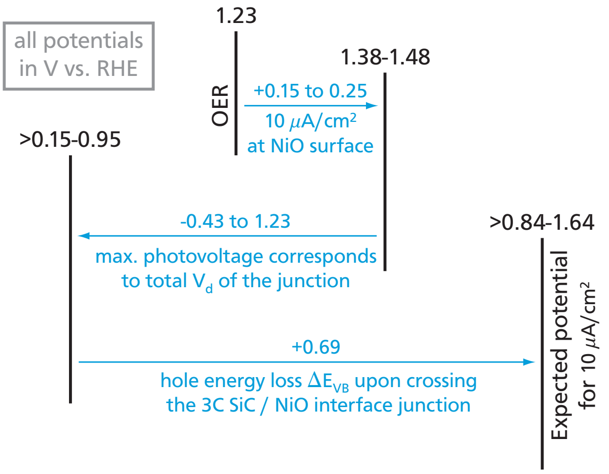

Figure 9.11.: *Flow chart of the reasoning used to approximate the expected potential at which a current density of* $10\,\mu\text{A/cm}^2$ *should occur.*

pendix (figure A.2). The first obvious difference is the large onset potential ($J = 0.5\,\mu\text{A/cm}^2$) shift from 0.49 to 1.54 V vs RHE for $3C_{NiO}$ in comparison to $3C_{pir,NH4F}$. Only a slightly larger bias potential of 1.58 V vs RHE is required for a $10\,\mu\text{A/cm}^2$ current density. This is in excellent agreement with the rough approximation of 0.84 to 1.64 V vs RHE discussed above. From the $U_{10\mu\text{A}}$ of 1.58 V vs RHE it can be concluded that the junction provides a photovoltage of 0.49 to 0.59 V at this current density.

Second, the current density increase with potential is much steeper for $3C_{NiO}$. While the $3C_{pir,NH4F}$ $J^{s.state*}$ displays a Tafel slope of 297.7 mV/dec (0.824 to $8.24\,\mu\text{A/cm}^2$) the nickel oxide covered $3C_{NiO}$ displays a Tafel slope of 31 mV/dec, about one order of magnitude smaller than without NiO for the same current density range. This is in excellent agreement with the reported values of 29 mV/dec for the OER at NiO electrodes [218]. Obviously, the NiO catalyst layer results in a significant improvement of the cells OER kinetics.

Last, the maximum photocurrent density is increased drastically, from 26 to $212\,\mu\text{A/cm}^2$ for $3C_{NiO}$. This is almost exactly the value initially anticipated for the epitaxial 3C SiC on Si $3C$ samples, see equation 9.1. Apparently the buried 3C SiC / NiO junction results in a further extension of the depletion layer, which then prevents recombination during the electron movement to the sample sides.

It should be mentioned, that the $3C_{NiO}$ $J^{s.state*}$ behaves exactly as expected, displaying values of zero until the steep increase at around 1.5 V vs RHE. However, J^{onset*} displays a complex, potential de-

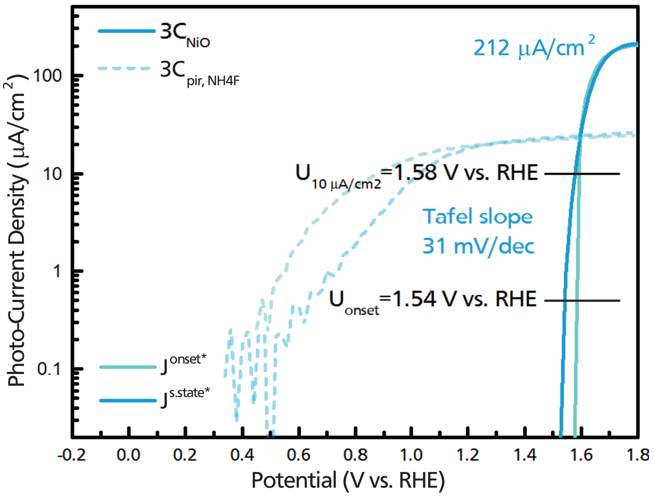

Figure 9.12.: *Photocurrent density for the NiO covered* $3C_{NiO}$ *in comparison to catalyst free* $3C_{etched}$. *Measurements were performed in 0.1 M KOH, the* 455 nm *LED was set to* $200\,W/m^2$. *The chopped light measurement can be found in figure A.2 in the appendix.*

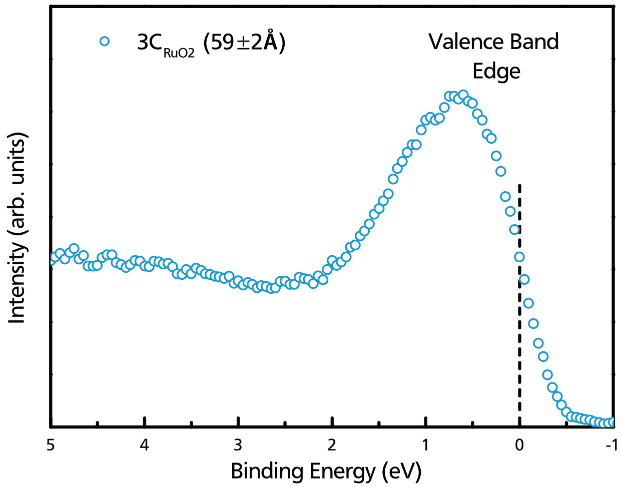

Figure 9.13.: *XPS spectrum of the* $3C_{RuO2}$ *valence band after the last interface experiment deposition step, corresponding to a* (59 ± 2) Å RuO_2 *epitaxial layer. The position of the Fermi level* ($E_{bin} = 0\,eV$) *in the valence band confirms the metallic nature of* RuO_2.

pendent transient cathodic (negative) current behaviour, not displayed in the logarithmic plot. See figure A.2 in appendix A.3 for the linear plot.

Si / 3C SiC / RuO2

Ruthenium oxide has long been the best known OER catalyst, with η values between 0.33 and 0.40 V for a current density of $10\,mA/cm^2$ [17, 219, 233, 234]. For single crystalline ruthenium (IV) oxide, the catalytic performance depends on the RuO_2 orientation, with the (100) surface requiring a lower η than the (110) surface [234]. It is frequently used as a benchmark system for new OER catalysts. Because RuO_2 is metallic, see figure 9.13, band bending will only occur in the 3C SiC, which should allow a more precise prediction of the current potential behaviour.

Similar to the previously discussed buried 3C SiC / NiO junction, the available photovoltage will be defined by the 3C SiC / RuO_2 contact, thus a high Φ_{RuO2} is desirable. Various researchers have reported a wide range of RuO_2 work functions from 4.6 to 6.2 eV [215, 236–238]. Apparently Φ_{RuO2} is correlated to the oxygen concentration during magnetron sputter deposition, where a higher concentrations result in a higher Φ_{RuO2} [215]. The initial deposition steps of the interface experiment result in a work function increase, but the last three steps (15, 37 and 59 Å) display similar values. In figure 9.14 the secondary electron edge of the last deposition step ((59 ± 2) Å) was used to determine the Φ_{RuO2} of 6.65 eV, and thus higher than any reported previously.

Figure 9.15 shows XPS detail spectra of the three regions of interest for the 3C SiC / RuO_2 interface experiment. The components employed for the fitting procedure are displayed as well. Obviously, the C 1s and the Ru 3d core levels are superimposed.

All relevant detail spectra of the interface experiment are displayed in figure 9.16. The spectra are background subtracted, and in order to improve comparability for the reader, the XPS signal from the C 1s / Ru 3d region was separated into the contributions of the respective elements.

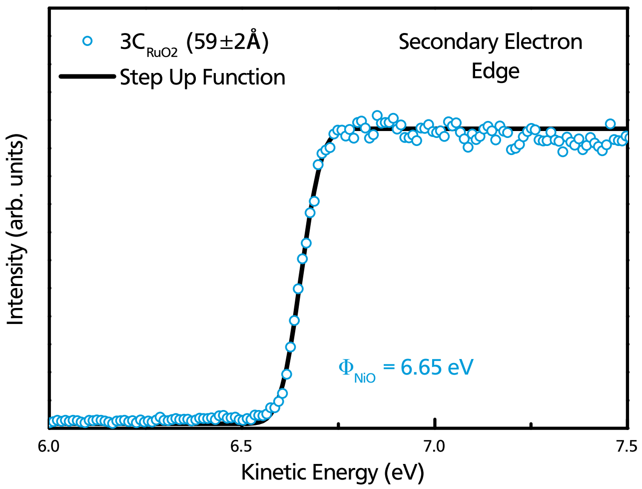

Figure 9.14.: *The* $3C_{RuO2}$ *secondary electron edge XPS spectrum was used to determine the* RuO_2 *work function* Φ_{RuO2} *of* 6.65 eV. *This measurement was performed after the last deposition step of the 3C SiC / RuO*$_2$ *XPS interface experiment displayed in figure 9.16.*

d_{NiO} (Å)	$\Delta Si^{SiC}_{2p3/2}$ (eV)	ΔC^{SiC}_{1s} (eV)	$\Delta Ru^{RuO2}_{3dp5/2}$ (eV)
0	0	0	-
2 ± 1	-0.57	-0.59	0
6 ± 1	-0.48	-0.50	-0.01
15 ± 1	-0.41	-0.42	-0.05
37 ± 1	-0.41	-0.41	-0.02
59 ± 2	-0.41	-0.42	-0.03

Table 9.2.: *Relative peak shifts of the main 3C SiC and* RuO_2 *components. Data was obtained from the 3C SiC / RuO2 interface experiment presented in figure 9.16.*

To produce the C 1s spectrum, all RuO_2 components were subtracted from the measurement data and vice versa for the Ru 3d spectrum. Distinction of the elemental contributions is clear up to the (15 ± 1) Å deposition step. For the final 2 steps the small intensity of C^{SiC}_{1s} results in a higher uncertainty in the component position.

The Ru 3d peak was fitted according to the excellent RuO_2 XPS analysis of Morgan [235]. From the observed $Ru^{RuO2}_{3d5/2}$ position of 282.70 eV, which is in excellent agreement with previously reported values between 282.6 and 282.7 eV, and the peak shape the deposited layer can clearly be identified as RuO_2 [215, 235, 239–241]. This is further reinforced by the stoichiometry, as O^{RuO2}_{1s}:Ru^{RuO2}_{3p} is in the range between 1.7 and 2.2, see below.

Considering the extremely high Φ_{RuO2} of 6.65 eV a strong upward band bending (shift to lower E_{bin}) in the 3C SiC is to be expected. The observed behaviour is in accordance with this assumption, but once again the value of the shift remains below the expectations, and the final shift amounts to a V_d of 0.41 eV. This must be ascribed to Fermi level pinning via defect states at the 3C SiC surface. As the Fermi level was pinned at exactly the same position, approx. 0.41 eV below the conduction band edge, for $3C_{NiO}$ and $3C_{RuO2}$ it can be expected that the defect states, or at least their energy levels, are identical.

Table 9.2 summarizes the relative changes in peak positions of the relevant 3C SiC and RuO_2 components and figure 9.18 provides a graphical presentation. Similar to the previous interface experiment, the initial two deposition steps result in a higher V_d, in this case 0.57 eV, compared to 0.48 eV for NiO, which then changes to a stable but lower value for deposited layers exceeding one to two monolayers.

Again, this could be ascribed to a build-in electric field as result of a special alignment of the first metal oxide monolayer. In this case the RuO_2 chemical composition might also play a role, as the x in RuO_x is 1.7 for the first two deposition steps, before it increases to 2.0 and then 2.2 for the last two deposition steps. Such a high oxygen concentration could lead to the formation of an oxygen layer on the RuO_2 surface. The resulting oxygen dipole could explain the extremely high RuO_2 work function. Alternatively, the number of surface states as result of the metal ion bombardment increases over the first deposition steps, thus increasing the Fermi level pinning.

Above information is also graphically displayed in form of two band diagrams. Figure 9.17 (A) shows

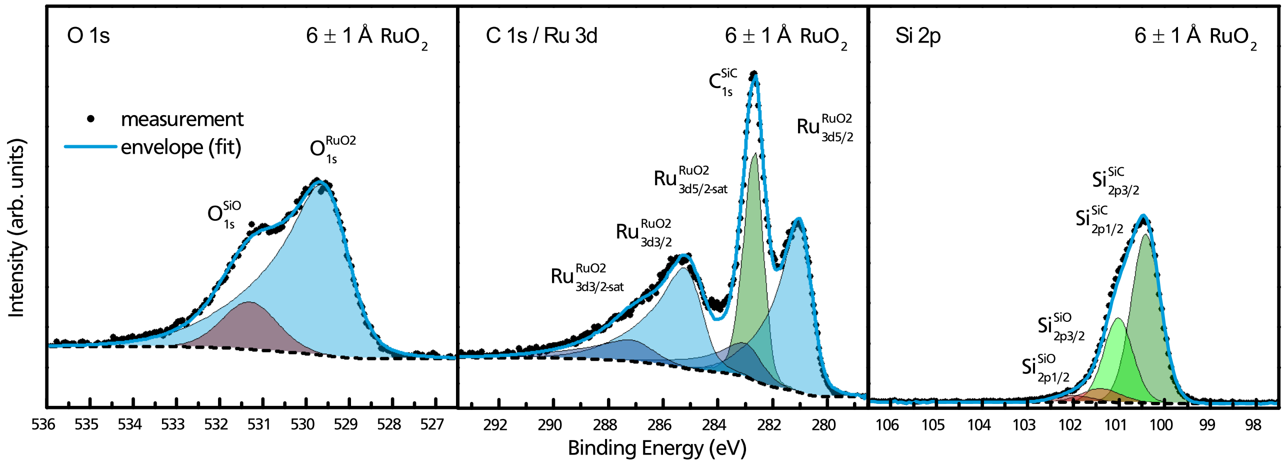

Figure 9.15.: *O 1s, C 1s / Ru 3d, and Si 2p XPS detail spectra of $3C_{RuO2}$ after the second deposition step. The C 1s and Ru 3d core levels are superimposed. In order to facilitate comparison, the information from the performed fits in CasaXPS were used to display the C 1s and Ru 3d spectra separately in figure 9.16.*

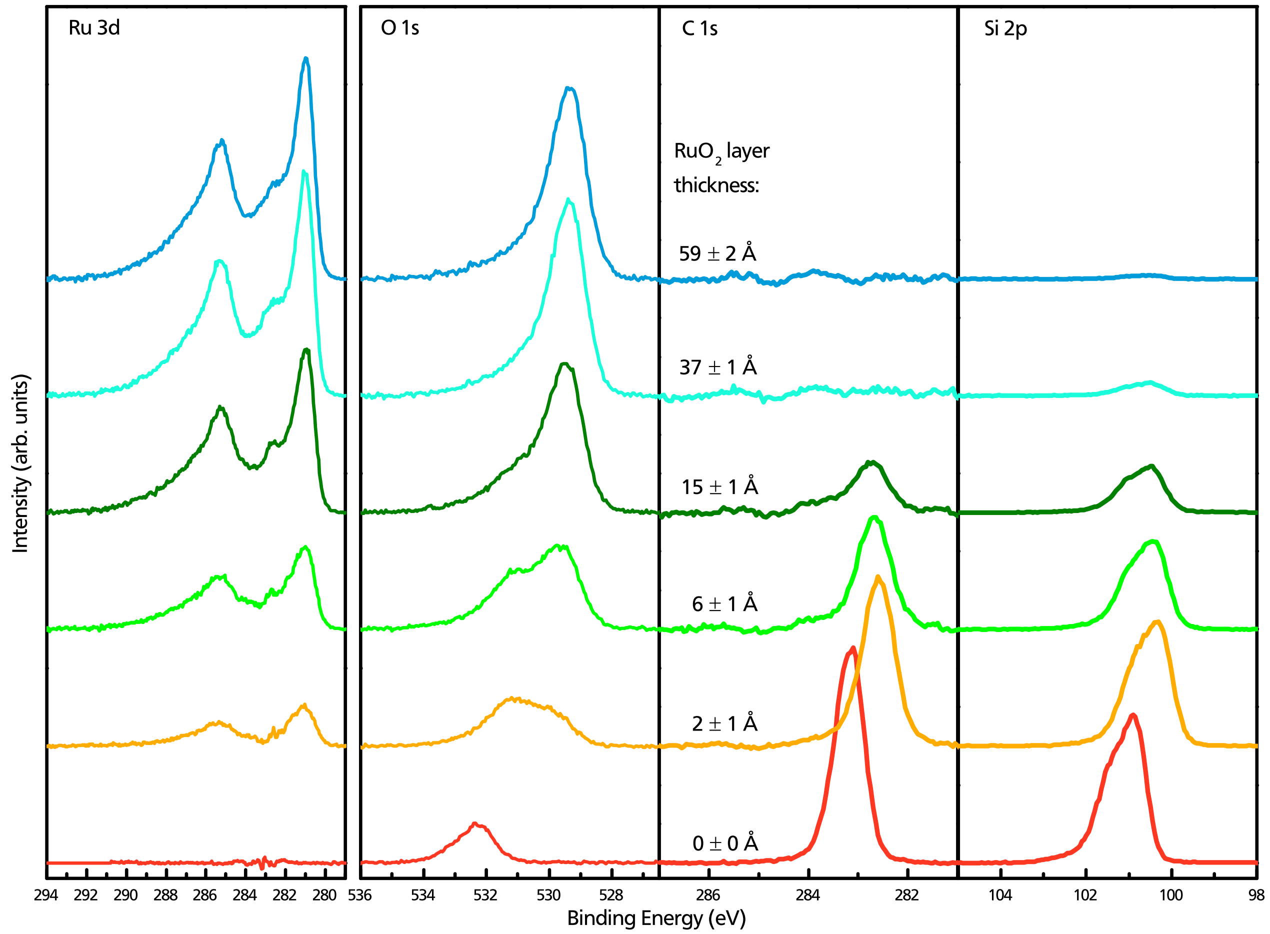

Figure 9.16.: *Background subtracted XPS detail spectra of the 3C SiC / RuO$_2$ interface experiment. The measurements were performed with a pass energy of 10 eV. After the first deposition step ((2 ± 1) Å RuO$_2$) the 3C SiC bulk components were shifted 0.41 eV to lower binding energies. The layer thickness was determined from C^{SiC}_{1s} and Ru^{RuO2}_{3d} via equation 3.5. Note that the additional feature at approx. 283 eV in the Ru 3d spectrum is a satellite feature, and not a leftover from the C 1s subtraction [235].*

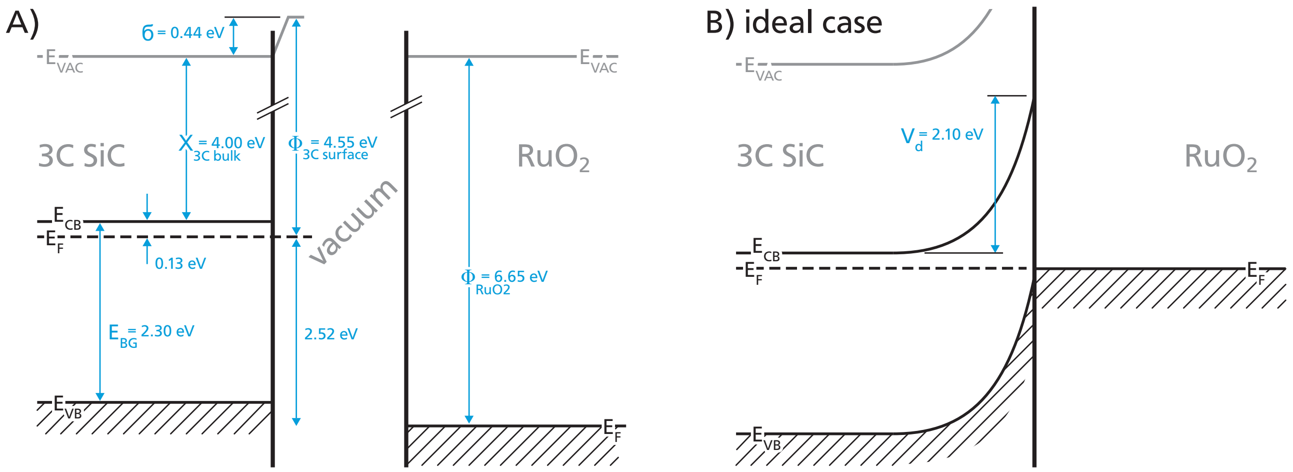

Figure 9.17.: *3C SiC / RuO_2 interface schematic (A) before contact formation and (B) for an ideal contact without surface states and pinning. In the ideal case, the large difference between Φ_{3C} and Φ_{RuO2} would produce a large V_d which could be used to power the OER.*

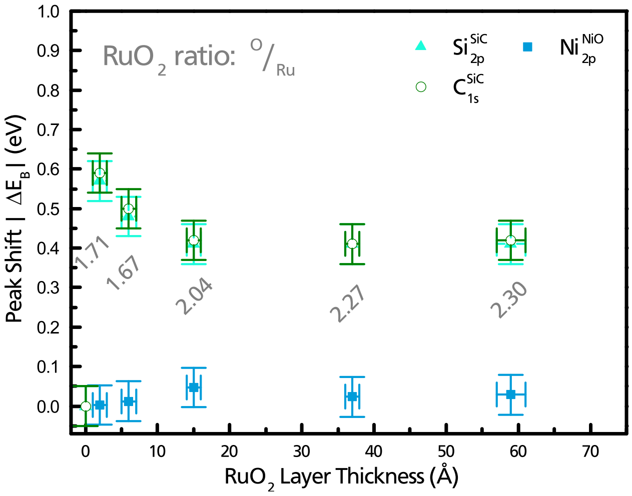

Figure 9.18.: *Absolute values of the binding energy shifts plotted over the deposited RuO_2 layer thickness for $3C_{RuO2}$.*

the initial situation, while (B) demonstrates how the ideal junction between the two materials would look like. Φ_{RuO2} is large enough for the RuO_2 Fermi level to lie below the 3C SiC valence band. In a perfect junction, without surface states or dipole, this would give rise to an upward band bending of 2.1 eV.

This would still be easily sufficient to power the OER, especially considering the low η of RuO_2 for the OER. The junction obviously looks great on paper. However, the 3C SiC / RuO_2 XPS interface experiment only accounted for a V_d of 0.41 eV, which is significantly below the theoretical value of 2.17 eV. As discussed in chapter 6, this reduced V_d is a result of Fermi level pinning via surface states at the 3C SiC / RuO_2 interface. The resulting band diagram of the 'real junction' is displayed in figure 9.19.

Most of the potential drop from the Fermi level aligning therefore occurs in form of an interface dipole δ in a very thin region at the interface. Because the Fermi level is held at a position 0.54 eV (0.41 + 0.13) below E_{CB}, it can be concluded that the responsible surface states are located at this energy. The same band bending was observed for in the 3C SiC / NiO junction, while it is possible that this is pure coincidence, it seems more likely that a similar kind of surface state is responsible for the pinning in both cases.

Similar to the previous section on NiO, the EC behaviour of $3C_{RuO2}$ can be approximated from the available information. See figure 9.20 for the flow chart. For a current density of $10\,\mu A/cm^2$ at a RuO_2 interface an overpotential η between 0.02 and 0.17 V will be required [234,242]. In this case, the only other factor to be considered is the photovoltage, which should be 0.43 V or below. From the above information, the expected potential for a

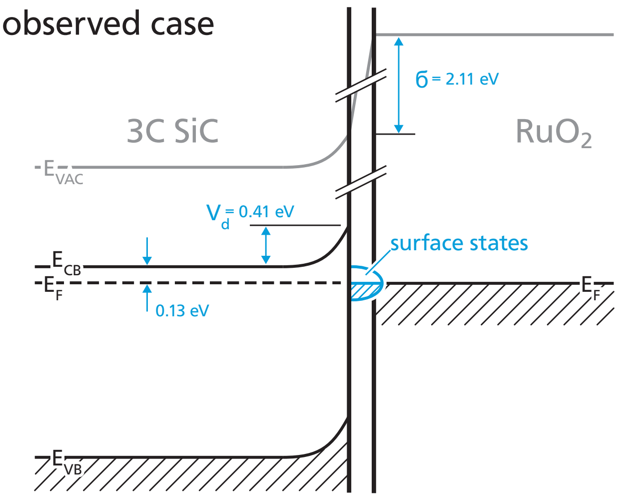

Figure 9.19.: *Band diagram of the 3C SiC / RuO$_2$ junction based on the results of the interface experiment from figure 9.16. Most of the potential difference from the Fermi level alignment seems to drop at the interface via surface states.*

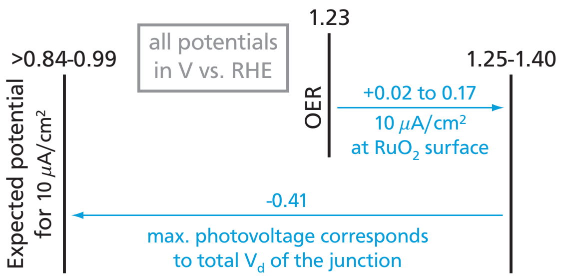

Figure 9.20.: *Rough approximation of the expected potential at which a current density of* 10 μA/cm^2 *should occur for* $3C_{RuO2}$.

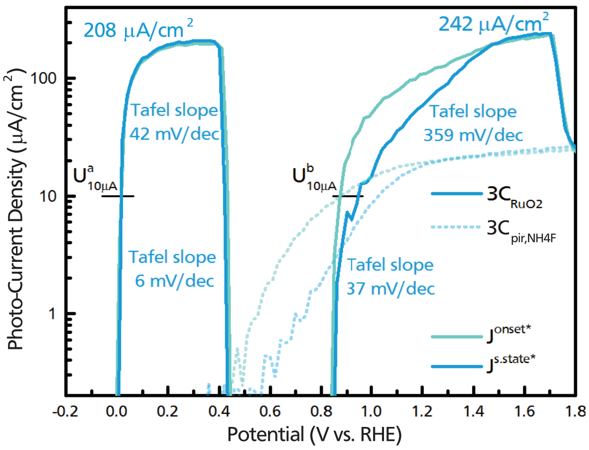

Figure 9.21.: *Photocurrent density for the RuO$_2$ covered* $3C_{RuO2}$ *in comparison to* $3C_{etched}$ *without a catalyst layer. All measurements were undertaken in 0.1 M KOH, and a* 455 nm *LED at* 200 W/m^2 *was employed. The original chopped lght measurement can be found in figure A.3 in the appendix.*

photocurrent of 10 μA/cm^2 from $3C_{RuO2}$ would be in the range from 0.84 to 0.99 V vs RHE.

Figure 9.21 shows the measured photocurrent for $3C_{RuO2}$ in 0.1M KOH under 200 W illumination with a 455 nm LED. The measurement shows a first steep increase at close to 0 V vs RHE ($U^a_{10\,\mu A}$ = 0.02 V vs RHE), which results in a saturation current density of 208 μA/cm^2 from 0.2 V vs RHE upwards, until the photocurrent density drops abruptly to zero at 0.4 V vs RHE. No photocurrent is observed up to 0.84 V vs RHE, where another steep increase occurs ($U^b_{10\,\mu A}$ = 0.94 V vs RHE), which goes into saturation much slower and finally reaches a maximum photocurrent density of 242 μA/cm^2 at 1.7 V vs RHE, before J^{onset*} and $J^{s.state*}$ drop again to values around 25 μA/cm^2.

Repeating the same chopped light scan for a second time afterwards did not produce a comparable result, instead it looked more like the behaviour of $3C_{pir\ NH4F}$ (dotted line in figure 9.21). This indicates that the RuO$_2$ is almost completely removed during the EC measurement. Indeed, an comparative measurement on a similarly prepared sample, but without the GaIn back contact, showed no traces of RuO$_2$, instead of the previously deposited 6 nm layer, after the same EC procedure. Apparently the RuO$_2$ layer is not stable.

There are two possible interpretations for this curve shape.

One: Activation passivation behaviour

The observed overall current potential relation is also similar to the expected behaviour for the formation of a passivation layer. An initial current increase related to the electrode oxidation followed by a steep decrease, as a stable passivation layer is formed (normally an oxide of the electrode material) [15]. Should this oxide be conducting the 'transpassivation' OER will then occur at higher

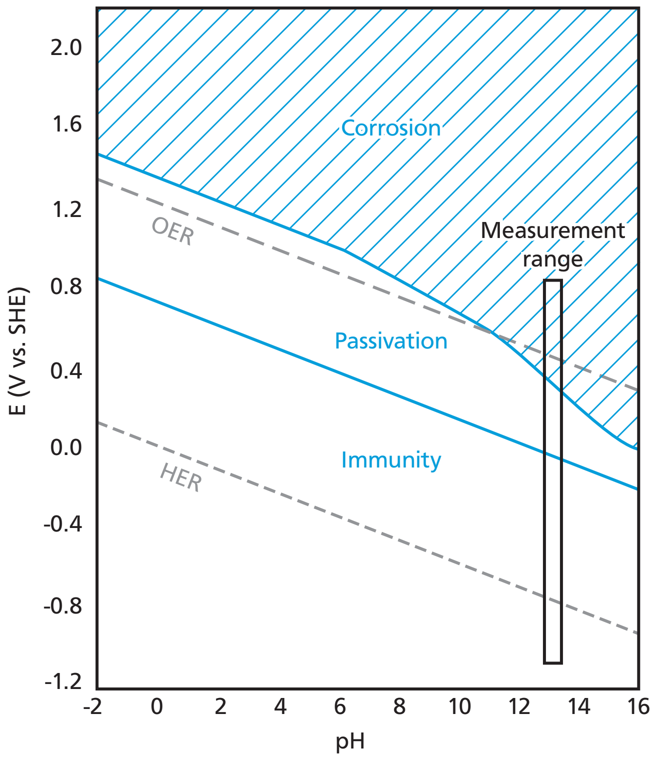

Figure 9.22.: *Theoretical parameter diagram for immunity, passivation and corrosion of Ru, based on the potential-pH diagram of ruthenium. After [243, 244].*

potentials. Thus, the second current density rise would be the result of the OER. In this case the observed OER $U^b_{10\mu A}$ of 0.94 V vs RHE is in excellent agreement with the approximated 0.84 to 0.99 V vs RHE for $3C_{RuO2}$ at 10 μA/cm^2 from figure 9.20.

However, the XPS spectra of $3C_{RuO2}$ clearly show the catalyst layer to be RuO_2 not simply metallic Ru, see figures 9.15 and 9.16. As it is already oxidised, no further oxidation and thus no associated current flow should occur. This is further confirmed from the ruthenium potential-pH (Pourbaix) diagram. For 0.1 M KOH (pH approximately 13) the oxidation

$$\mathrm{Ru} + 3\mathrm{H_2O}{=}\mathrm{Ru(OH)_3} + 3\mathrm{H^+} + 3\mathrm{e^-} \qquad (9.2)$$

of ruthenium should only occur at potentials above 0.74 V vs RHE [243, 244]. Below that, ruthenium is immune to oxidation, see figure 9.22 for a graphical summary of the Ru potential-pH diagram parameters for ’immunity’, ’passivation’ and ’corrosion’. The full diagram and the associated equations can be found in appendix A.3. Therefore, it has to be concluded that the initial current rise is not a result of Ru oxidation either.

Two: Hydrogen oxidation reaction

As for all chopped light measurements, the starting potential was at −0.2 V vs RHE. Before the anodic photocurrent onset at 0 V vs RHE $3C_{RuO2}$ displays an extremely high cathodic current of 2300 μA/cm^2 at −0.19 V vs RHE, see figure A.3 in appendix A.3. This should correspond to an equally high production rate of H_2 at the RuO_2 surface. As can be seen from the potential-pH diagram in figure A.4 it is quite possible to at least partially reduce RuO_2 to metallic Ru at cathodic potentials, which is known to be a good catalyst for the HER [245]. A high hydrogen concentration at the surface would then result in the occurrence of the hydrogen oxidation reaction (HOR), see figure 2.11 and equation 2.14. This is normally inhibited due to lack of reactants. However, the initial H_2 production changed this.

HOR and OER both require holes for the reaction to occur. As the observed photocurrent density will therefore be limited by the hole flux to the surface, both reactions should occur at approximately the same rate, as is observed in figure 9.21. Once the available hydrogen at the surface is used up the reaction will stop abruptly, as is the case at 0.4 V vs RHE, and the current density will drop to zero until the OER starts at a higher potential.

Integration of the total current flow over the appropriate potential range can be used to approximate the amount of produced or consumed hydrogen

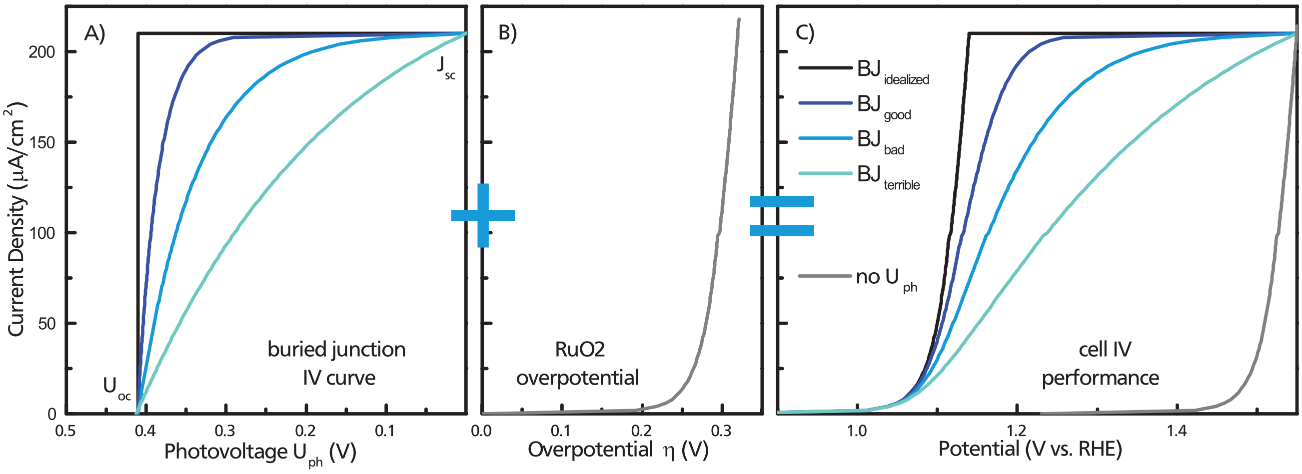

Figure 9.23.: *Schematic on the interaction between (A) the buried junctions (BJ) IV curve, and (B) the catalysts IV behaviour, in order to produce (C) the overall EC cell performance of the sample. For this simple approach the correlation between the 3 graphs is $U(J) = 1.23\,\mathrm{V}$ vs RHE $+ \eta(J) - U_{ph}(J)$. The open circuit potential (U_{oc}) and the short circuit current density (J_{sc}) values are similar to those observed for $3C_{RuO2}$, and the η is an averaging of (001) and (110) RuO_2 behaviour from [234].*

molecules. This approach yields a total production of

$$\#H_2^{HER} = \frac{1}{2q}\int_{-0.200\,\mathrm{V\ vs\ RHE}}^{0.004V\,vs.RHE} J(V)\frac{dt}{dV}dV \approx -5.4\times10^{16} \tag{9.3}$$

H_2 molecules from the cathodic current at potentials below 0.004 V vs RHE. In above equation $J(V)$ is the current density, and dt/dV the scan rate. The same approach can be used to determine the amount of

$$\#H_2^{HOR} = \frac{1}{2q}\int_{0.004\,\mathrm{V\ vs\ RHE}}^{0.436V\,vs.RHE} J(V)\frac{dt}{dV}dV \approx 2.1\times10^{16} \tag{9.4}$$

oxidised hydrogen molecules from the anodic current density. Assuming 2.37×10^{15} atoms per square centimetre on a perfectly flat (001) 3C SiC surface (lattice constant 4.36 Å [246]), this would correspond to roughly 9 monolayers of H_2. It is to be expected that the amount of oxidised hydrogen molecules is smaller than the initially production, as part of the hydrogen will diffuse away from the surface. Because the 'activation passivation behaviour' explanation could be ruled out, it stands to reason that the HOR of those 9 monolayers is responsible for the initial current density slope.

The second current density rise in figure 9.21 has been identified as the OER. As mentioned above, its position is in excellent agreement with the potential approximated from the XPS interface experimental data. For current densities $\leq 10\,\mu\mathrm{A/cm^2}$ the observed Tafel slope of 37 mV/decade is in excellent agreement with previous reports of 33 to 56 mV/decade for RuO_2 [234, 242]. Above $10\,\mu\mathrm{A/cm^2}$, the Tafel slope changes and is not longer really linear. A rough approximation yields a significantly higher slope of 359 mV/decade for the $J^{s.state*}$ between 20 and $100\,\mu\mathrm{Acm^2}$.

As discussed in chapter 2, four electron reactions like the OER can only be described accurately by the Butler-Volmer equation 2.29 if there is a single one electron reaction as rate determining step. Because the Tafel slope mechanis are based on the Butler-Volmer equation, a situation without such a rate determining step in the OER could result in a deviation from linear Tafel slopes. However, Stoerzinger et al. reported an almost perfectly linear

Tafel behaviour for (100) and (110) RuO_2 up to 300 μA/cm^2 in 0.1 M KOH [234].

An alternative explanation would be a competing surface reaction, which could block reaction sites. The most likely candidate would be the anodic dissolution of the RuO_2 layer. RuO_2 in alkaline pH 13 solutions is only stable up to a potential of approximately 1 V vs RHE, see figure 9.22. Dissolution of RuO_2 would also explain the decrease of photocurrent density at potentials exceeding 1.7 V vs RHE.

Should the RuO_2 covered area diminish over the course of the experiment, this should (simplified) result in a superposition of two current voltage behaviours, one for the RuO_2 catalysed areas and another one for 3C SiC catalysed areas. The later one should exhibit a behaviour similar to $3C_{pir,NH4F}$. Once the RuO_2 coverage is too small as that all reactions can take place at catalyst sites, the performance is bound to decrease.

Another explanation for the lower slope is the photo-current/voltage behaviour of the buried junction. So far, the photovoltage has always been discussed as a more or less constant term, while it can be highly dependent on the current density. Should the available photovoltage decrease strongly with the increased current density, this would also result in a decrease of the observed Tafel slope.

For solar cells this relation is frequently displayed in form of current potential (IV) curves. In this case, the IV behaviour of the buried 3C SiC/RuO_2 junction has to be combined with the Tafel plots of the catalyst layer. For a simple approximation, the potential

$$U(J) = 1.23\,\text{V vs RHE} + \eta(J) - U_{ph}(J) \qquad (9.5)$$

at a given current density J would be correlated to the overpotential η and the photovoltage U_{ph}. Figure 9.23 displays a schematic of the two separate behaviours and the resulting EC cell behaviour, where the voltages for a certain current density are added up.

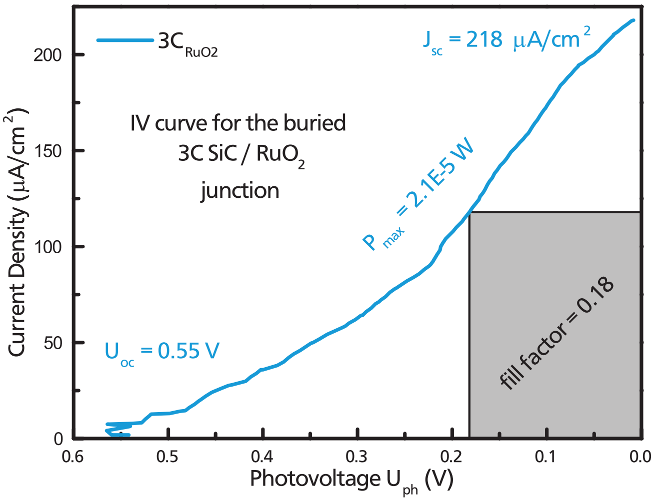

Figure 9.24.: *Extrapolated IV curve of the buried 3C SiC / RuO_2 junction. The characteristic values are displayed in the graph.*

Neglecting effects like the blocked reaction sites by possible RuO_2 dissolution and so on, the reverse process can be used to approximate the actual IV behaviour of the buried 3C SiC / RuO_2 junction. Figure 9.24 displays the IV curve of the 3C SiC / RuO_2 interface, which was extrapolated from the OER in figure 9.21. While the buried junction is able to provide an open circuit potential (U_{oc}) of 0.55 V and a short circuit current density (J_{sc}) of 218 μA/cm^2, the almost linear IV behaviour results in a small maximum power point (P_{max}), and thus an equally small fill factor of 0.18. For comparison, good commercial silicon solar cells exhibit fill factors of around 0.8 [247, 248]. An IV behaviour like this makes it very obvious that the 3C SiC / RuO_2 interface would have to be optimized in order to get a competitive level of performance from this kind of device setup.

9.4 Conclusion

Possible improvements of the n-type 3C SiC water splitting performance via catalyst over layers were investigated in the context of this chapter. It was shown that the OER onset of the 3C SiC samples

$3C_{NiO}$ and $3C_{NiO}$ with catalysts, can be approximated rather well from the buried junction's diffusion potential V_d, as determined from XPS interface experiments, and the catalysts IV properties. Knowledge of the catalytic performance actually allows an approximation of the buried junctions characteristic IV behaviour. A separation that was not possible as long as both factors (catalyst and junction) remained unknown in at least a semi quantitative manner.

The addition of a catalyst layer results in a significantly decreased Tafel slope (steeper increase of photocurrent with potential) for both catalysts. However, the buried junctions do not supply the anticipated high photovoltages, thus still requiring an additional bias potential to power the OER. For $3C_{NiO}$, this can be traced back to an unfavourable alignment of the respective valence bands.

Additionally both samples seem to suffer from Fermi level pinning in the 3C SiC absorber layer as result of surface states 0.54 eV below the conduction band edge. As $3C_{NiO}$ and $3C_{RuO2}$ both display the same V_d in the interface experiments, the obvious assumption would be that in both interfaces Fermi level pinning occurs as result of the same kind of surface states. From the energy position a (+/++) C vacancy could be responsible, as this should be located 0.58 eV below the conduction band edge [249].

These surface states are apparently not present for 3C SiC samples without the catalyst layers, as SD_{CVD} displays an onset ($0.5\,\mu A/cm^2$) potential of 0.24 V vs RHE. The U_{oc} for the 3C SiC / 0.1 M KOH interface junction will therefore be 0.99 V plus the necessary OER overpotential for the 3C SiC surface, and thus likely above 1.23 V.

In theory, buried junctions between 3C SiC and high work function catalysts, like RuO_2, have a lot of potential. An obvious next step would be the optimization of the junctions, as those are the limiting factor at the moment, especially with regard to the surface states. The obvious solution would be a 3C SiC homojunction between the n-type bulk 3C SiC and a thin highly p-type layer on top. This would offer the best chance of producing an un-pinned buried junction with a possibly high diffusion potential V_d.

Alternatively, the 3C SiC / metal oxide interfaces could be optimized by different preparation methods, like a high temperature annealing under hydrogen atmosphere in order to get a hydrogen terminated surface instead of the C-H / Si-OH used so far [250, 251]. Further possible procedures would be annealing of the deposited catalyst layer, or initial deposition of a thin (approx. 5 nm) pure metal film which is then subsequently oxidised in order to prevent re-oxidation of the 3C SiC surface.

10 Final Considerations

This final chapter will give a short summary of the obtained results, discuss the consequences in a broader context and give an outlook on possible future developments.

10.1 Summary and Outlook

The goal of this work was to generally evaluate the potential performance of 3C SiC for water splitting applications. For this a number of single domain and epitaxial n-type 3C SiC samples were investigated with various methods. It was also shown that the employed sample preparation methods resulted in a Si-OH / C-H surface termination and an ohmic back contact for the annealed Ni back contacts.

An EC cell for direct photoelectrochemical water splitting is a complex system. This is especially true for interface junctions, were the total performance will depend on the 3C SiC/electrolyte junctions IV behaviour, which in turn depends on the sample surface and defect state density, recombination and the catalytic performance of the uppermost electrode layer. Without knowledge of catalyst overpotential $\eta(U)$, for example, it is impossible to determine the junctions IV behaviour. Therefore information must be obtained from situations where some of the those factors are negligible.

It was shown, that the photocurrent density at high bias potentials is mostly determined from the flux of photo-generated holes to the electrode surface, which could be approximated very well via the Gärtner equation 7.13. The low current densities observed for $SD_{\#1}$ and $SD_{\#2}$ could thus be traced to 3C SiC's low absorption coefficient α ($\approx 210\,\mathrm{cm}^{-1}$ for $\lambda = 455\,\mathrm{nm}$), in combination with small hole diffusion length L_p ($\approx 197\,\mathrm{nm}$) and a small depletion layer width, as result of the high doping concentration n_D.

Using CVD in order to grow a $5\,\mu\mathrm{m}$ epitaxial 3C SiC layer on top of a SD sample resulted in a significant improvement of the photocurrent at 1.6 V vs RHE,

author **for the OER**	shape [μm]	n_D [cm^{-3}]	electrolyte []	illumination [W/cm^2]	current density [μA/cm^2]	approximation for AM1.5 **[μA/cm^2]**
Lauermann [27]	6 to 12 *on Si*	10^{16-18}	0.1M NaOH	0.4 *'white'*	450 (2 V vs RHE)	113
Yasuda [29]	303 *bulk*	2×10^{19}	1M H_2SO_4	1 *AM1.5*	< 1 *no bias*	< 0.1
Sun [252]	1000 *on 4H SiC*	10^{16-18}	0.1M NaOH	0.1 *AM1.5*	150 (1.5 V vs RHE)	150
this work ($SD_{\#2}$)	152 *bulk*	5×10^{17}	0.1M KOH	0.02 455 nm	29 (1.6 V vs RHE)	100
this work ($3C_{RuO2}$)	1.5 *on Si*	1×10^{17}	0.1M KOH	0.02 455 nm	229 (1.6 V vs RHE)	790
this work (SD_{CVD})	5 *on 3C SiC*	4×10^{16}	0.1M KOH	0.02 455 nm	545 (1.6 V vs RHE)	1880

author **for the HER**	shape [μm]	n_A [cm^{-3}]	electrolyte []	illumination [W/cm^2]	current density [μA/cm^2]	approximation for AM1.5 **[μA/cm^2]**
Kato [31]	20 *on 6H SiC*	3×10^{16}	1M H_2SO_4	1 *AM1.5*	2900 (0.2 V vs RHE)	290
Ichikawa [253]	30 *on 4H SiC*	1×10^{15}	1M H_2SO_4	1 *AM1.5*	2300 (−0.3 V vs RHE)	230

Table 10.1.: *Summary of reported investigations of 3C SiC for direct photoelectrochemical water splitting. The n-doped samples used for the oxygen evolution reaction (OER) are displayed on top, and the p-doped samples used for the hydrogen evolution reaction (HER) are displayed on the bottom. In many cases the employed illumination was not the standard* 1000 W/m^2 *AM1.5* (0.1 W/cm^2)*, thus - for comparabilities sake - the rightmost column displays an approximation of the current density under standard AM1.5 conditions.*

from 29 μA/cm^2 ($SD_{\#2}$) to 545 μA/ cm^2 (SD_{CVD}). While the doping concentration of the epitaxial layer was one order of magnitude below the two SD samples, this should only result in an improvement by a factor of 2 at most. The obvious conclusion is, that the epitaxial layer displays a significantly higher hole diffusion length L_p of 4400 nm.

As all other measurements in this work, the measurements mentioned above were performed with monochromatic light, as this made the evaluation easier. In everyday use, the light source would be a continuous AM 1.5 spectrum [20]. The behaviour under such conditions can be approximated easily via integration of the Gärtner equation 7.13 over the wavelength λ. Which yields

$$J = q\int I_0(\lambda)[1-\frac{\exp[-\alpha(\lambda)W_D]}{1+\alpha(\lambda)L_p}]\,d\lambda \qquad (10.1)$$

the total current density in dependence of depletion layer width W_D and hole diffusion length L_p. I_0 is the number of incident photons of a given wavelengths per square centimetre. Neglecting reflection losses, the measured photocurrent of 545 μA/ cm^2 for SD_{CVD} would thus correspond to a 1.88 mA/cm^2 under AM 1.5 illumination. The validity of this approach has been confirmed by measurements of the photocurrent for monochromatic light of different wavelengths.

While there are not many works on 3C SiC for water splitting applications some can be found and compared to the work at hand, they are summarized in table 10.1. The reports on n-type 3C SiC for the OER are displayed on top. As can be seen all three previous investigations report (approximated) current densities of 150 μA/cm^2 or below for AM1.5 illumination in the potential range from

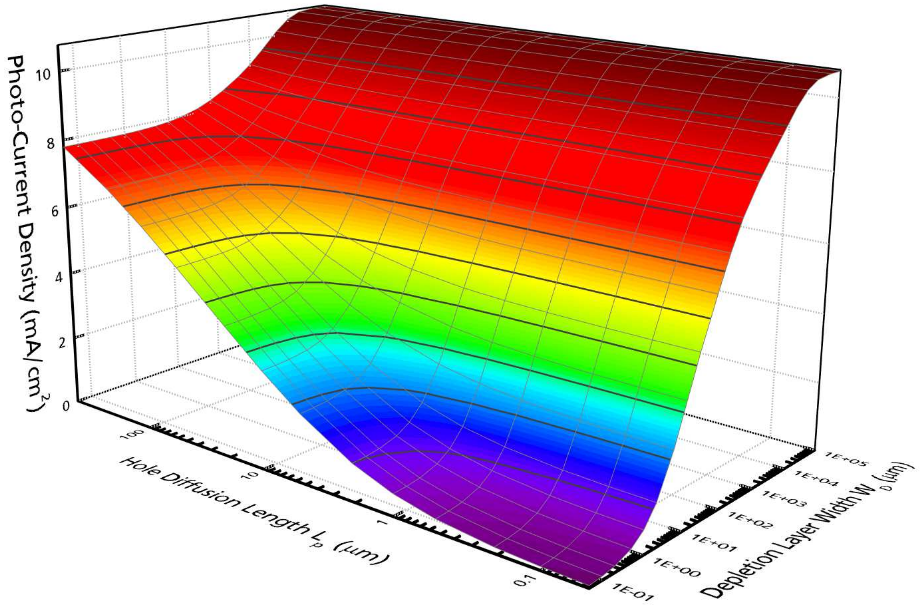

Figure 10.1.: *Approximated photocurrent density as function of depletion layer width W_D and hole diffusion length L_p. The graph is based on equation 10.1. Values for the absorption coefficient α are mostly from the measurements presented in the previous chapters, but were supplemented by data from [254] for small wavelengths.*

1.5 to 2.0 V vs RHE. This is roughly similar to the value of $100\,\mu\text{A/cm}^2$ for the bulk 3C SiC sample $SD_{\#2}$ found within the context of this work, see chapter 7. However, the RuO_2 covered epitaxial 3C SiC layer on silicon $3C_{RuO2}$ and the lowly doped high quality epitaxial 3C SiC layer on bulk 3C SiC SD_{CVD}, presented in chapters 9 and 8 of this work, significantly outperform those values with 790 and $1880\,\mu\text{A/cm}^2$. The later being an improvement by one order of magnitude.

In order to be commercially viable, a direct photoelectrochemical water splitting cell would have to produce a current density of approximately $10\,\text{mA/cm}^2$. Assuming a band gap of 2.3 eV, the maximum obtainable photocurrent for 3C SiC would be

$$J_{max}^{3CSiC} = q \int_{280\,\text{nm}}^{545\,\text{nm}} I_0(\lambda)\text{d}\lambda = 10.72\,\text{mA/cm}^2 \quad , \tag{10.2}$$

which means that the necessary current density could be reached, but only if more than 93.3 % of the incoming photons could be harvested for the water splitting reaction.

Figure 10.1 displays the obtainable photocurrent for a 3C SiC electrode as function of W_D and L_p. Even for $L_p = 50\,\mu\text{m}$, the depletion layer width W_D would still have to be approximately 4.35 mm thick in order to achieve the desired $10\,\text{mA/cm}^2$. Which in turn would require intrinsic 3C SiC with a doping concentration in the range of $1 \times 10^7\,\text{cm}^{-3}$ (eq. 2.8). A 3C SiC layer of approximately 5 mm would neither be feasible from a production nor a handling point of view. While appropriate preparation of the electrode, like a reflecting back contact or a structured surface in order to disperse the incident light, might reduce the necessary sample thickness 3C SiC alone does not seem like the first choice for thin film applications.

However, Heidarzadeh simulated the performance of a 3C SiC / Si tandem cell [255]. Their calculations yielded a possible short circuit current of $13.46\,\text{mA/cm}^2$ and an open circuit potential of 2.13 V. It should be noted though, that they also report a $13.56\,\text{mA/cm}^2$ current density for a pure

3C SiC pn-junction cell of 5 μm thickness, which completely contradicts above considerations (even exceeding the calculated maximum possible photocurrent).

Another future approach could be to increase the absorption properties of the 3C SiC electrode [256]. While the absorption coefficient as a direct result of the materials dispersion curve, and thus the density of states, can not be changed, it might be possible to add additional photo excitation pathways. A high concentration of deep acceptor or donator states could function as an intermediate band, which would then allow transitions from the valence band to the intermediate band, and from there to the conduction band [257, 258]. This is called the 'impurity photovoltaic effect' (IPV) [259]. While Beaucarne and Richards [260, 261] proposed 3C SiC as a material for IPV cells, there are no reports on the performance of such devices yet.

For all measured samples in this work, a significant bias potential had to be applied in order for a reasonable percentage of the incoming holes to participate in the OER at the 3C SiC surface, which is a result of an insufficient photovoltage and recombination. It was shown, that recombination at the 3C SiC surface is high for low potentials but its impact decreases with increasing potential. As recombination is a result of slow charge transfer across the 3C/electrolyte interface, the obvious solution to prevent it is the addition of a catalyst layer in order to improve the kinetics. NiO and RuO_2 catalytic layers were investigated, and neither of the two exhibited the high recombination rates observed for pure 3C SiC.

It was found that the onset potential, and thus the photovoltage, is strongly dependant on the surface preparation. A roughly polished, defect rich surface will perform considerably worse than a finer polished or unpolished sample, as part of the potential drop will occur over the defect states. The defect rich samples also showed significantly higher degradation rates. SD_{CVD} offered the lowest onset potential, 0.24 V vs RHE for a current density of 0.5 μA, and 0.53 V vs RHE for a current density of 10 μA.

Therefore, the supplied photovoltage of SD_{CVD} at 0.5 μA has to be 0.99 V plus the necessary overpotential η needed for the OER at this current density at the 3C SiC surface. Depending on the 3C SiC η these values could be sufficient for self driven water splitting with a good catalyst. With a catalyst layer on top, the 3C SiC electrode will change from an interface to a buried junction. Meaning that the available photovoltage and current voltage behaviour will no longer be determined by the 3C SiC / electrolyte, and instead be the 3C SiC / catalyst junction.

Thus, NiO and RuO_2 were chosen as catalyst systems. Both exhibit high work functions, 5.36 eV for NiO and 6.65 eV for RuO_2, which should induce a large band bending in the 3C SiC. The 6 to 7 nm thick catalyst layers were deposited in the context of 2 XPS interface experiments ($3C_{RuO2}$ and $3C_{NiO}$), where it was found that the interface was strongly pinned by defect states 0.54 eV below the conduction band edge. As a result, the observed onset potentials for $3C_{RuO2}$ and $3C_{NiO}$ were higher, and the photovoltage lower than for pure 3C SiC surfaces.

It can be concluded, that those defect states are a result of the metal oxide catalyst deposition, because the pure 3C SiC is not pinned there, as evident from the observed onset potentials. For the future, it would therefore be interesting to identify the defect states responsible for the Fermi level pinning at the 3C SiC metal oxide interface, and find preparation methods to reduce or prevent their creation. This might be achieved by simply annealing the 3C SiC / metal oxide catalyst system [262], or via a different in situ cleaning procedures, like annealing under hydrogen in order to get a clean H terminated 3C SiC surface [250, 263–265].

Another approach would be to first deposit a few monolayers of pure metal on the 3C SiC, thus preventing further oxidation of the 3C SiC surface. The metal could then be oxidised by annealing under oxygen, and additional metal oxide could be deposited as needed. This kind of preparation approach has proven quite efficient for the deposition of passivation layers on silicon for water splitting applications [266–269].

Finally, the buried junction could also be realized as a homojunction, which should exhibit less defects. This could be achieved by depositing a thin epitaxial p^+ 3C SiC layer via CVD on the n-type 3C SiC bulk sample. Additional passivation and catalyst layers could then added as needed without influencing the buried junction. A sufficient high doping of the p^+ layer would ensure that charge carriers could traverse any barriers from the p^+ 3C SiC / catalyst interface via tunneling.

10.2 Conclusion

3C SiC is one of the few materials suitable for direct photoelectrochemical water splitting with a single junction. Its band gap of 2.3 eV would allow to reach the desired photocurrent density of 10 mA/cm^2. However, this would require 93.3 % of the incoming photons of suitable wavelength to be used, and thus require a lot of thought in cell design (structured surface, reflective back contact, pin design and so on). Because the catalytic performance of 3C SiC itself is poor, an additional catalyst layer would very likely be needed in order to operate the cell near the maximum photocurrent without the need for a bias potential.

Designing and optimizing the setup outlined above would require a lot of research activity, as there is little experience with 3C SiC for solar cell device building. Also 3C SiC is difficult to stabilize upon growth, and thus expensive, despite the abundance supply of its raw materials. While further investigation of the material system, and especially a possible improvement of the absorption properties via the impurity photovoltaic effect are exciting, it must also be asked whether the same efficiency can not be reached by simpler means.

With the transition from a a 3C SiC / electrolyte interface junction to a buried 3C SiC / catalyst junction, the outstanding chemical durability of 3C SiC may no longer be as relevant. An optimized, buried 3C SiC junction might produce 10 mA and a sufficient photovoltage to drive the water splitting reaction, but other systems, like thin film a-Si/μ-Si multi-junction cells, are already close to this level of performance [270–272]. This kind of multi-junction approach allows more control over the cells current voltage characteristics, thus allowing an optimization of the achievable photocurrent at the required photovoltage. Additionally, the production cost are comparatively low, and the required thin films ca be deposited easily on suitable surfaces of various shapes.

It is therefore the opinion of the author, that 3C SiC on its own will not be a competitive absorber material for direct photoelectrochemical water splitting in the foreseeable future, unless there is a breakthrough regarding the impurity photovoltaic effect in SiC. In the meantime, 3C SiC and other SiC polytypes might still be very useful as contact and passivation layers in combination with silicon based absorber systems.

Acknowledgements

First of all, many thanks to professor Wolfram Jaegermann and professor Didier Chaussende, who made it possible for me to work on this fascinating project. Despite leaving me essentially a free hand in my research, there was no lack in helpful discussions. It was a great pleasure to be part of both groups.

Second, many thanks to my parents, Christiane and Jörn, who have always encouraged me to find my own way and never take anything for granted. They instilled in me the fundamental curiosity that drove me to do science. And, of course, my sister and other relatives for their encouragement and support.

Many thanks as well to Joachim Klett and Jürgen Ziegeler, the two old hands taught me a lot and found the time to read and discuss my thesis despite their successful transition to industry.

It was a great pleasure to get to know and work with all the great people in Grenoble, especially Nikolaos Tsavdaris, Kanaparin Ariyawond, and Yun Ji Shi. You were the ideal company for exploring France.

The same is true for the members of the AG Jaegermann in Darmstadt, especially the other water splitters: Jona, Andi, Thorsten, Natascha, and Paula. It was a great time doing science with you. Special thanks are due to Hans Wardenga, who performed the Hall measurements on 3C SiC for me, and Thomas Späth, who performed the HREELS meaurements.

Many thanks as well to Kassem Alassad, for finding the time to grow epitaxial 3C SiC layers for me the day after his own PhD. defence! Also many thanks to his boss, Gabriel Ferro, who supplied the 3C SiC on Si wafer.

Thanks to all the great people of the IDS Funmat graduate school, I seldom had the opportunity to learn so much (about science and culture) in such a short time.

I am grateful for the financial support by the DFG in the framework of the Excellence Initiative, Darmstadt Graduate School of Excellence Energy Science and Engineering (GSC 1070). And I really enjoyed the close collaboration within my second graduate school, a great way to learn everything about the various aspects of the energy transformation.

Lots of thanks are due to Loki, Sigyn, Lancelot, Frau Flausch, Sheepthulu, Supersheep, Mr. R. and the whole flock for their fluffy support no matter how dark the hour.

Thanks to Margit Maly, who was my rock in turbulent waters until she herself could stand firm no longer.

And finally, many many thanks to my friends Anna-Lena, Alex, Andreas, Anke, Benjamin, Carolin, Janek, David, Hanna, JePe, JOle, Kaja, Karo, Kathrin, multiple Kevins, Laura, Lisa, Maike, Marco, multiple Martins, Matthias, Nele, Paddy, Sang, many Sebastians, some Silvias and Stefan who where a never ending source of support and encouragement no mater what. Also, you guys are just great company!

A Appendix

A.1 Abbreviations

3C SiC	cubic silicon carbide
CB	conduction band
CE	counter electrode
CL	chopped light (measurements)
CPE	constant phase element
CPS	counts per second
EC	electrochemical
EIS	electrochemical impedance spectroscopy
FK	Fuchs Kliewer surface phonon
HER	hydrogen evolution reaction
HOR	hydrogen oxidation reaction
HREELS	high resolution electron energy loss spectroscopy
IMFP	inelastic mean free path
IPV	impurity photovoltaic effect
IV	current potential (curves)
LEED	low energy electron diffraction
LOPC	LO phonon-plasmon coupled mode
OCP	open circuit potential
OER	oxygen evolution reaction
ORR	oxygen reduction reaction
PES	photoelectron spectroscopy
RDS	rat determining step
RHE	reducible hydrogen electrode
RE	reference electrode
RSF	relative sensitivity factor
SHE	standard hydrogen electrode
TLM	transfer length method
UPS	Ultraviolet photoelectron spectroscopy
VB	valence band
WE	working electrode
XPS	X-Ray photoelectron spectroscopy

A.2 List of Symbols

a	atomic lattice distance
C_{SC}	semiconductor capacity
E_{BG}	band gap
E_{bin}	binding energy
E_F	Fermi energy
E_{kin}	kinetic energy
E_R	rest potential
E_{Redox}	redox potential
E_λ	photon energy
f	frequency
F	Faraday constant
h	Plancks constant
I_E	ionisation energy
j	current density
J	current density
J^{dark}	dark current density
J^{onset}	onset current density
J^{onset*}	corrected onset current density
$J^{s.state}$	steady state current density
$J^{s.state*}$	corrected steady state current density
k	wave vector / Boltzmann constant
k_r	rate constant
L_p	hole diffusion length
m_0	electron mass
n_A	acceptor doping concentration
N_A	average atomic density
N_{CB}	effective density of states in the conduction band
n_D	donator doping concentration
N_{VB}	effective density of states in the valence band
R	gas constant, resistance
T	temperature
U	potential, voltage
U_{FB}	flat band potential
v	speed
V_d	diffusion potential
W_d	depletion layer width

α	absorption coefficient, CPE degree of dispersion
β	asymmetry parameter
ε_0	vacuum permittivity
ε_S	static dielectric constant
η	overpotential
θ	angle of emission
λ	wavelength
λ_A	inelastic mean free path
λ_{DB}	de-Broglie wavelength
ν	reaction rate, wave number
τ	lifetime
φ	phase shift
ω	XPS electron take off angle
ΔG	activation energy
$\Delta \nu$	Raman shift
Φ	work function
Φ_B	Schottky barrier height
X	electron affinity

A.3 Additional Informations for Chapter 9

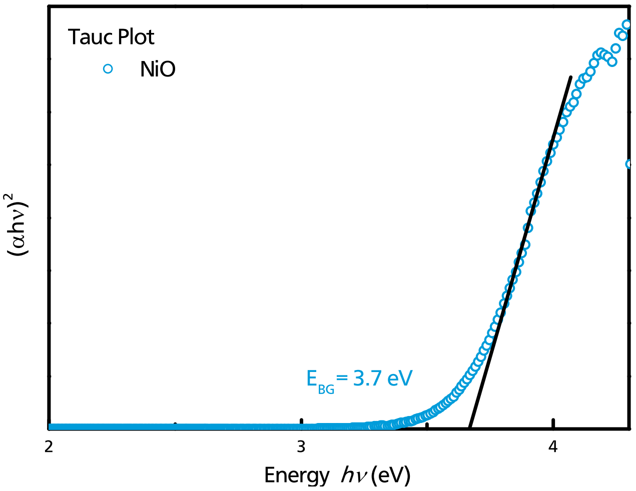

Figure A.1.: *Tauc plot for NiO. The only reference on the nature of the transition states it to be a direct transiton [273]. The measurement was performed on a thin NiO layer on a SiO_2 substrate.*

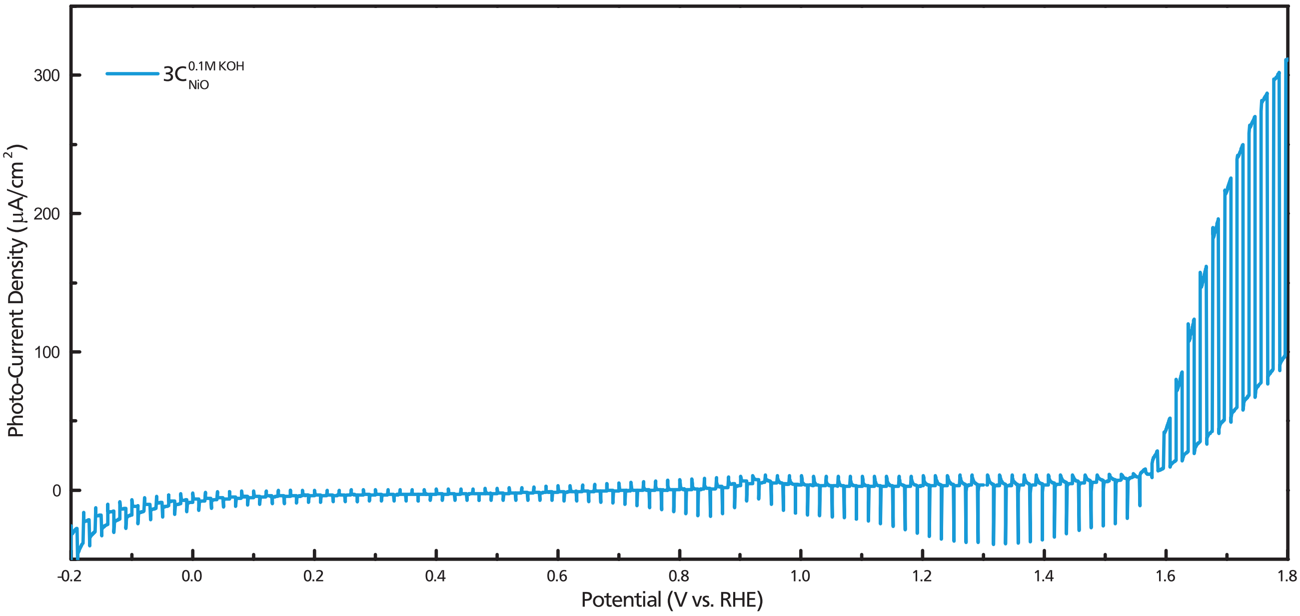

Figure A.2.: *Photocurrent behaviour of* $3C_{NiO}$ *in 0.1 M KOH under* 200 W/m^2 *illumination from a* 455 nm *LED. While* $J^{s.state*}$ *displays the expected value of zero until the OER onset at approximately* 1.5 V vs RHE, J^{onset} *shows a complex behaviour of cathodic current densities.*

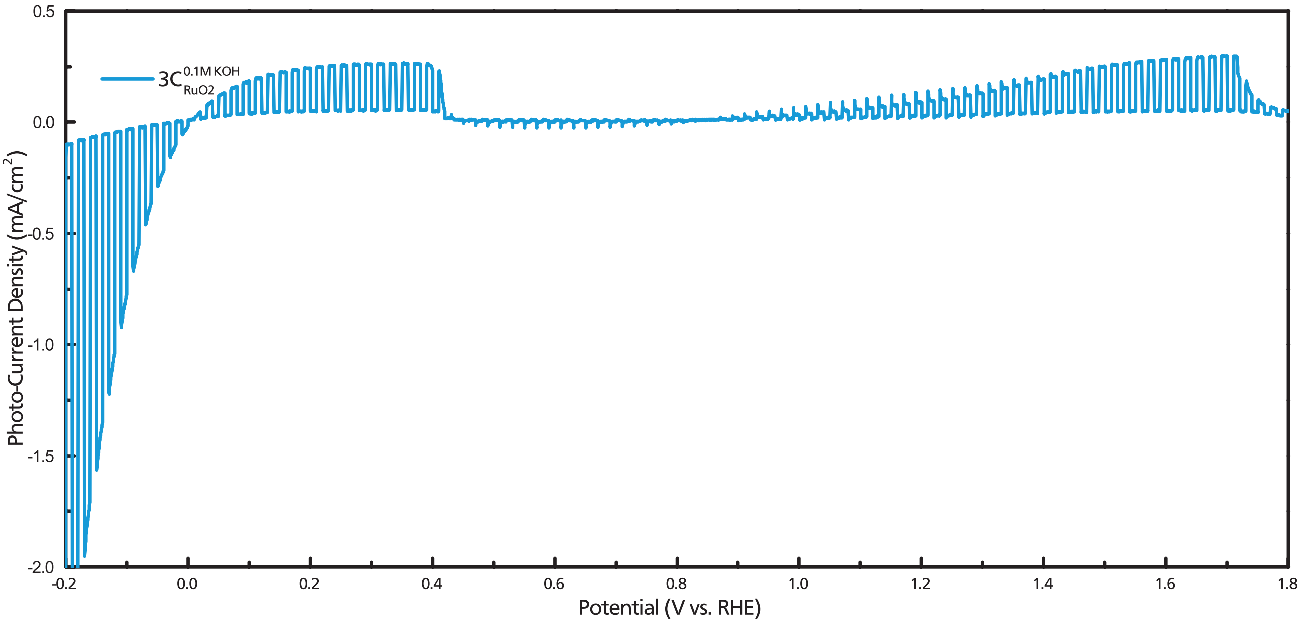

Figure A.3.: *Photocurrent behaviour of* $3C_{RuO2}$ *in 0.1 M KOH under* 200 W/m^2 *illumination from a* 455 nm *LED. The high cathodic current at potentials below* 0.004 V vs RHE *is a result of the HER, and the produced hydrogen is subsequently oxidised in the potential region from 0.004 to* 0.436 V vs RHE.

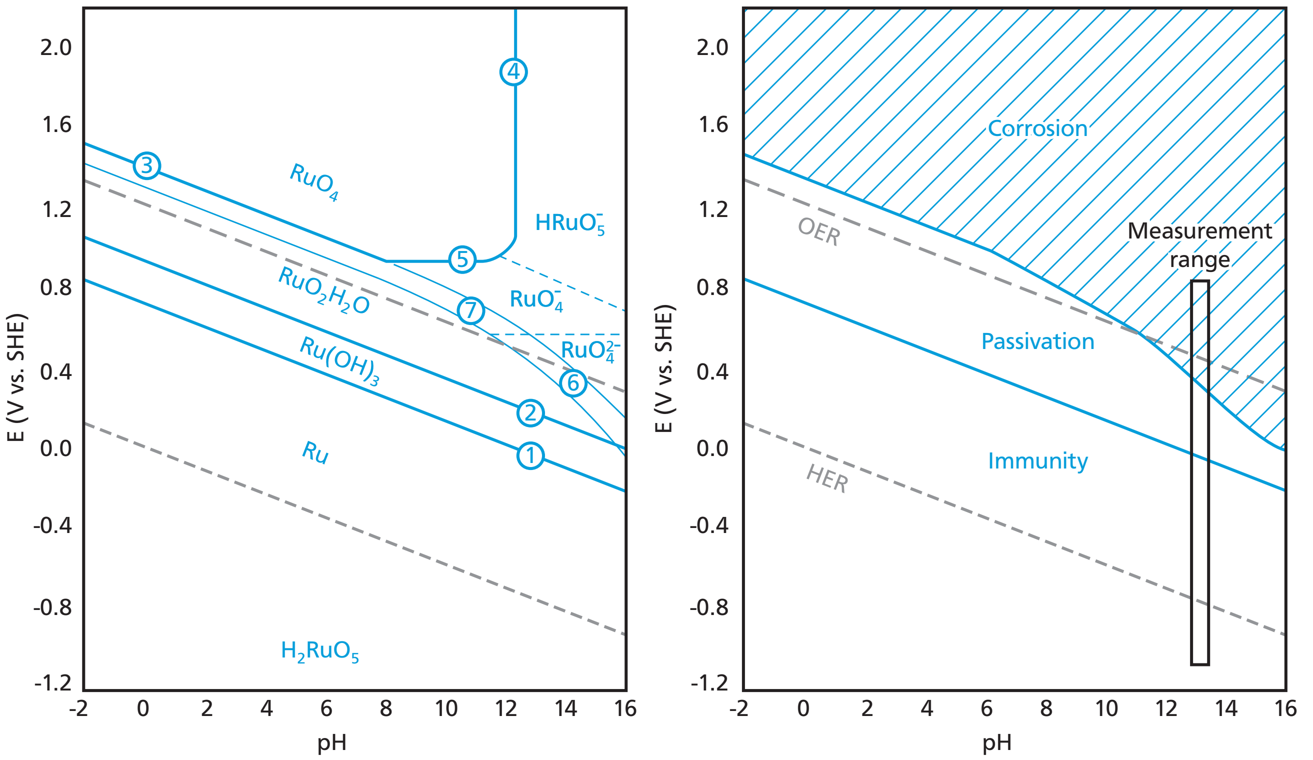

Figure A.4.: *Potential-pH diagram of ruthenium, after [243, 244].*

The most important reactions for the ruthenium-water system, after [243, 244].

Heterogeneoils reactions involving two solid components-electrochemical reactions

$$Ru + 3\,H_2O{=}Ru(OH)_3 + 3\,H^+ + e^- \qquad (A.1)$$

$$(E_{SHE} = 0.738 - 0.059 \cdot pH)$$

$$Ru(OH)_3{=}RuO_2 + H_2O + H^+ + e^- \qquad (A.2)$$

$$(E_{SHE} = 0.937 - 0.059 \cdot pH)$$

$$RuO_2 + 2H_2O{=}RuO_4 + 4\,H^+ + 4\,e^- \qquad (A.3)$$

$$(E_{SHE} = 0.937 - 0.059 \cdot pH)$$

Heterogeneous reactions involving one solid component-chemical reaction

$$RuO_4 + H_2O{=}HRuO_5^- + H^+ \qquad (A.4)$$

$$(\log(HRuO_5^-) = -12.10 + pH)$$

Electrochemical reactions

$$RuO_4^-{=}RuO_4 + e^- \qquad (A.5)$$

$$(E_{SHE} = 0.950 - 0.059 \cdot \log(RuO_4^-))$$

$$RuO_2 + 2\,H_2O{=}RuO_4^{2-} + 4\,H^+ + 2\,e^- \qquad (A.6)$$

$$(E_{SHE} = 2.005 - 0.118 \cdot pH + 0.030 \cdot \log(RuO_4^{2-}))$$

$$RuO_2 + 2H_2O + RuO_4^- + 4\,H^+ + 3\,e^- \qquad (A.7)$$

$$(E_{SHE} = 1.533 - 0.079 \cdot pH + 0.020 \cdot \log(RuO_4^-))$$

Bibliography

[1] Kristina Grifantini. What It Takes to Power Google, 2011.

[2] European Commission. Energy Statistics of the European Union : Concepts and Definitions on All Flows (" Aggregates ") and Products. Technical Report February, 2015.

[3] Eurostat. Supply, transformation and consumption of solid fuels - annual data (nrg_101a), 2015.

[4] Eurostat. Supply, transformation and consumption of oil - annual data (nrg_102a), 2015.

[5] Eurostat. Supply, transformation and consumption of gas - annual data (nrg_103a), 2015.

[6] Eurostat. Supply and transformation of nuclear energy - annual data (nrg_104a), 2015.

[7] Eurostat. Supply, transformation and consumption of renewable energies - annual data (nrg_107a), 2015.

[8] Shahriar Shafiee and Erkan Topal. When will fossil fuel reserves be diminished? *Energy Policy*, 37(1):181–189, 2009.

[9] Mikael Höök and Xu Tang. Depletion of fossil fuels and anthropogenic climate change-A review. *Energy Policy*, 52:797–809, 2013.

[10] Christophe McGlade and Paul Ekins. The geographical distribution of fossil fuels unused when limiting global warming to 2 ÂřC. *Nature*, 517(7533):187–190, 2015.

[11] M.R. Allen, D.J. Frame, C. Huntingford, C.D. Jones, J.A. Lowe, M. Meinshausen, and N. Meinshausen. Warming caused by cumulative carbon emissions towards the trillionth tonne. *Nature*, 458(7242):1163–1166, 2009.

[12] Bundesgesetzblatt. Gesetz für den Vorrang Erneuerbarer Energien (Erneuerbare-Energien-Gesetz - EEG) sowie zur Änderung des Energiewirtschaftsgesetzes und des Mineralölsteuergesetzes. Teil I(13):305–309, 2000.

[13] D Böhme, W Dürrschmidt, and M Van Mark. Erneuerbare Energien in Zahlen. *Bundesministerium für Umwelt, Naturschutz und Reaktorsicherheit*, page 136, 2013.

[14] Hans-Joachim Ziesing. Energieverbrauch in Deutschland 2013. Technical report, 2014.

[15] Carl H. Hamann, A. Hamnett, and Wolf Vielstich. *Electrochemistry*. WILEY-VCH, 2 edition, 2007.

[16] Andrei Y Khodakov, Wei Chu, and Pascal Fongarland. Advances in the Development of Novel Cobalt Fischer-Tropsch Catalysts for Synthesis of Long-Chain Hydrocarbons and Clean Fuels. *American Chemical Society*, 107(5):1692–1744, 2007.

[17] Charles C. L. McCrory, Suho Jung, Ivonne M. Ferrer, Shawn M. Chatman, Jonas C. Peters, and Thomas F. Jaramillo. Benchmarking Hydrogen Evolving Reaction and Oxygen Evolving Reaction Electrocatalysts for Solar Water Splitting Devices. *Journal of the American Chemical Society*, 137(13):4347–4357, 2015.

[18] Michael G Walter, Emily L Warren, James R McKone, Shannon W Boettcher, Qixi Mi, Elizabeth a Santori, and Nathan S Lewis.

Solar water splitting cells. *Chemical Reviews*, 110(11):6446–73, nov 2010.

[19] Bernhard Kaiser, Wolfram Jaegermann, S. Fiechter, and H. J. Lewerenz. DIRECT PHOTOELECTROCHEMICAL CONVERSION OF SUN LIGHT INTO HYDROGEN FOR CHEMICAL ENERGY STORAGE. *Bunsen-Magazin*, 4:104–111, 2011.

[20] ASTM. Standard Tables for Reference Solar Spectral Irradiances : Direct Normal and. *Astm*, 03(Reapproved):1–21, 2013.

[21] Zhe Chuan Feng. *SiC Power Materials*. Springer, 2004.

[22] Lisa M. Porter and R. F. Davis. A critical review of ohmic and rectifying contacts for silicon carbide. *Materials Science and Engineering*, 34:83–105, 1995.

[23] Jerry L. Hudgins, Grigory S. Simin, Enrico Santi, and M. Asif Khan. An assessment of wide bandgap semiconductors for power devices. *IEEE Transactions on Power Electronics*, 18(3):907–914, 2003.

[24] W. J. Choyke, D. R. Hamilton, and Lyle Patrick. Optical properties of 15R SiC: Luminescence of nitrogen-exciton complexes, and interband absorption. *Physical Review*, 132(1962):2023–2031, 1963.

[25] M. Gleria and R. Memming. Charge Transfer Processes at large band Gap semiconductor Electrodes: Reactions at SiC-Electrodes. *Journal of Electroanalytical Chemistry*, 65:163–175, 1975.

[26] H Morisaki, H Ono, and K Yazawa. Photoelectrochemical Properties of Single-Crystalline n-SiC in Aqueous Electrolytes. *Journal of The Electrochemical Society*, 131(9):2081–2086, 1984.

[27] I. Lauermann, R. Memming, and D. Meissner. Electrochemical Properties of Silicon Carbide. *Journal of The Electrochemical Society*, 26(1):73–80, 1997.

[28] J. van de Lagemaat, D. Vanmaekelbergh, and J. J. Kelly. Photoelectrochemical characterization of 6H-SiC. *Journal of Applied Physics*, 83(11):6089, 1998.

[29] Tomonari Yasuda, Masashi Kato, Masaya Ichimura, and Tomoaki Hatayama. SiC photoelectrodes for a self-driven water-splitting cell. *Applied Physics Letters*, 101(5):053902, 2012.

[30] Quan-Bao Ma, Bernhard Kaiser, Jürgen Ziegler, Dominic Fertig, and Wolfram Jaegermann. XPS characterization and photoelectrochemical behaviour of p-type 3C-SiC films on p-Si substrates for solar water splitting. *Journal of Physics D: Applied Physics*, 45(32):325101, aug 2012.

[31] Masashi Kato, Tomonari Yasuda, Keiko Miyake, Masaya Ichimura, and Tomoaki Hatayama. Epitaxial p-type SiC as a self-driven photocathode for water splitting. *International Journal of Hydrogen Energy*, 39(10):4845–4849, mar 2014.

[32] Yu.M. Tairov and V.F. Tsvetkov. Investigation of growth processes of ingots of silicon carbide single crystals. *Journal of Crystal Growth*, 43(2):209–212, 1978.

[33] D. Chaussende, F. Mercier, A. Boulle, F. Conchon, M. Soueidan, G. Ferro, A. Mantzari, A. Andreadou, E. K. Polychroniadis, C. Balloud, S. Juillaguet, J. Camassel, and M. Pons. Prospects for 3C-SiC bulk crystal growth. *Journal of Crystal Growth*, 310:976–981, 2008.

[34] Gabriel Ferro. 3C-SiC Heteroepitaxial Growth on Silicon: The Quest for Holy

Grail. *Critical Reviews in Solid State and Materials Sciences*, 40(1):56–76, 2015.

[35] Siegfried Hunklinger. *Festkörperphysik*. Oldenbourg, 1 edition, 2007.

[36] Wolfgang Demtröder. *Experimentalphysik 3 - Atome, Moleküle und Festkörper*. Springer, 3 edition, 2005.

[37] S. M. Sze and Kwok K Ng. *Physics Of Semiconductor Devices*. WILEY-INTERSCIENCE, 3rd edition, 2007.

[38] R. Kaplan and R. J. Wagner. Electron Cyclotron Resonance In Cubic SiC. *Solid State Communications*, 55(1):67–69, 1985.

[39] J. Kono, S. Takeyama, H. Yokoi, N. Miura, M. Yamanaka, M. Shinohara, and K. Ikoma. High-field cyclotron resonance and impurity transition in n-type and p-type 3C-SiC at magnetic fields up to 175 T. *Physical Review B*, 48(15):10909–10916, 1993.

[40] Lyle Patrick and W. J. Choyke. Static Dielectric Constant of SiC. *Physical Review B*, 2(6):3–4, 1970.

[41] L. A. Hemstreet and C. Y. Fong. ENERGY BAND STRUCTURE OF 3C SiC. *Solid State Communications*, 9:643–647, 1971.

[42] L. A. Hemstreet and C. Y. Fong. Electric Band Structure and Optical Properties of 3C-SiC, BP and BN. *Physical Review B*, 6(4):1464–1480, 1972.

[43] A. R. Lubinsky, D. E. Ellis, and G. S. Painter. Electronic structure and optical properties of 3C-SiC. *Physical Review B*, 11(4):1537–1546, 1975.

[44] V. I. Gavrilenko, S. I. Frolov, and N. I. Klyui. Electronic band structure and optical properties of cubic silicon carbide crystals. *Physica B*, 185:394–399, 1993.

[45] C. H. Park, Byoung Ho Cheong, Keun Ho Lee, and K. J. Chang. Structural and electronic properties of cubic, 2H, 4H, and 6H SiC. *Physical Review B*, 49(7):4485–4493, 1994.

[46] C. Persson and U. Lindefelt. Relativistic band structure calculation of cubic and hexagonal SiC polytypes. *Journal of Applied Physics*, 82(11):5496–5508, 1997.

[47] Darrell D. Ebbing. *General Chemistry*. 3rd edition, 1990.

[48] Julio de Paula Peter Atkins. *Physical Chemistry*. W. H. Freemann and Company, 9 edition, 2010.

[49] R. Memming. *Semiconductor Electrochemistry*. WILEY-VCH, 2 edition, 2015.

[50] B. E. Conway and B. V. Tilak. Interfacial processes involving electrocatalytic evolution and oxidation of H2, and the role of chemisorbed H. *Electrochimica Acta*, 47(22-23):3571–3594, 2002.

[51] Qing Tang and De-en Jiang. Mechanism of Hydrogen Evolution Reaction on 1T-MoS2 from First Principles. *ACS Catalysis*, 6:4953–4961, 2016.

[52] A. G C. Kobussen and G. H. J. Broers. The oxygen evolution on La0.5Ba0.5CoO3. Theoretical impedance behaviour for a multi-step mechanism involving two adsorbates. *Journal of Electroanalytical Chemistry*, 126(1-3):221–240, 1981.

[53] John O'M. Bockris and Takaaki Otagawa. Mechanism of Oxygen Evolution on Perovskites. *J. Phys. Chem*, 87(32):2960–2971, 1983.

[54] H. Willems, A.G.C. Kobussen, J.H.W. De Wit, and G.H.J. Broers. The oxygen evolution

reaction on cobalt. *Journal of Electroanalytical Chemistry and Interfacial Electrochemistry*, 170(1-2):227–242, 1984.

[55] Sixto Giménez and Juan Bisquert. *Photoelectrochemical solar fuel production: From basic principles to advanced devices*. 2016.

[56] Stephen Fletcher. Tafel slopes from first principles. *Journal of Solid State Electrochemistry*, 13(4):537–549, 2009.

[57] Joachim Klett. *Interface and catalyst investigation for solar water splitting*. PhD thesis, TU Darmstadt, 2016.

[58] R. A. Batchelor and A. Hamnett. Surface States on Semiconductors. *Modern Aspects of Electrochemistry*, (22):265–415, 1992.

[59] Laurence M. Peter. Energetics and kinetics of light-driven oxygen evolution at semiconductor electrodes: The example of hematite. *Journal of Solid State Electrochemistry*, 17(2):315–326, 2013.

[60] R. A. Marcus. On the Theory of Oxidation-Reduction Reactions Involving Electron Transfer. I. *The Journal of Chemical Physics*, 24(5):966, 1956.

[61] R. A. Marcus. Generalization of the Activated Complex Theory of Reaction Rates. II. Classical Mechanical Treatment. *The Journal of Chemical Physics*, 41(9):2624, 1964.

[62] Dieter K. Schroder. *SEMICONDUCTOR MATERIAL AND DEVICE Third Edition*. John Wiley & Sons, 3rd edition, 2006.

[63] S. Hüfner. *Very High Resolution Photoelectron Spectroscopy*. Springer, 2007.

[64] H. Bubert and H. Jenett. *Surface and Thin Film Analysis: Purinciples, Instrumentation, Applications*. WILEY-VCH, 2002.

[65] M.P. Seah and W.A. Dench. Quantitative electron spectroscopy of surfaces. *Surface and Interface Analysis*, 1(4):46–55, 1979.

[66] C. J. Powell and A. Jablonski. NIST Electron-Mean-Free-Path Database 71, 2010.

[67] M. P. Seah and S. J. Spencer. Ultrathin SiO2 on Si II. Issues in quantification of the oxide thickness. *Surface and Interface Analysis*, 33(8):640–652, 2002.

[68] John F. Moulder, William F. Stickle, Peter E. Sobol, and Kenneth D. Bomben. *Handbook of X-ray photoelectron spectroscopy*. Physical Electronics, Inc., 1995.

[69] Siegfried Hofmann. *Auger- and X-Ray Photoelectron Spectroscopy in Materials Science*. Springer, 1st edition, 2003.

[70] Paul van der Heide. *X-Ray Photoelectron Spectroscopy - An Introduction to Principles and Practices*. WILEY, 2012.

[71] Richard Gehrenbeck. Electron diffraction: fifty years ago. *Physics Today*, (January), 1978.

[72] C. Davisson and L. H. Germer. Diffraction Of Electrons By A Crystal Of Nickel. *The Physical Review*, 30(6):632–635, 1927.

[73] M. A. Van Hove, W. H. Weinberg, and C. M. Chan. *Low-Energy Electron Diffraction*. Springer Verlag, 1st edition, 1986.

[74] M. A. Van Hove and J. B. Pendry. Dynamical low energy electron diffraction methods. *Journal of Physics C: Solid State Physics*, 8:1362, 1975.

[75] Olaf Stenzel. *Das Dünnschichtspektrum*. Akademie Verlag, 1st edition, 1996.

[76] W. Demtröder. *Experimentalphysik 2 - Elektrizität und Optik*. Springer, 5 edition, 2008.

[77] J. Tauc. Optical properties and electronic structure of amorphous Ge and Si. *Materials Research Bulletin*, 3(1), 1968.

[78] Brian D. Viezbicke, Shane Patel, Benjamin E. Davis, and Dunbar P. Birnie. Evaluation of the Tauc method for optical absorption edge determination: ZnO thin films as a model system. *Physica Status Solidi (B)*, 11(8):n/a–n/a, 2015.

[79] W Hayes. Scattering of light by solids. *Contemporary Physics*, 16(1):69–91, 1975.

[80] H. Yugami, S. Nakashima, A. Mitsuishi, A. Uemoto, M. Shigeta, K. Furukawa, A. Suzuki, and S. Nakajima. Characterization of the free-carrier concentrations in doped β-SiC crystals by Raman scattering. *Journal of Applied Physics*, 61(1):354, 1987.

[81] Arnoud Zoubir, editor. *Raman Imaging - Techniques and Applications*. Springer, 2012.

[82] S. Nakashima and H. Harima. Raman Investigation of SiC Polytypes. *physica status solidi (a)*, 162(1):39–64, 1997.

[83] Andrezej Lasia. *Electrochemical Impedance Spectroscopy and its Applications*. 1 edition, 2014.

[84] Bryan Hirschorn, Mark E. Orazem, Bernard Tribollet, Vincent Vivier, Isabelle Frateur, and Marco Musiani. Determination of effective capacitance and film thickness from constant-phase-element parameters. *Electrochimica Acta*, 55(21):6218–6227, 2010.

[85] G. J. Brug, A. L. G. van den Eeden, M. Sluyters-Rehbach, and J. H. Sluyters. The Analysis Of Electrode Impedances Complicated By The Presence Of A Constant Phase Element. *Journal of Electroanalytical Chemistry*, 176:275–295, 1984.

[86] M. E. Orazem and B Tribollet. *Electrochemical Impedance Spectroscopy*. 2008.

[87] Nobelprize.org.

[88] Neal Fairley. CasaXPS, 2017.

[89] S. Hüfner. *Photoelectron spectroscopy: principles and applications*. Springer Science & Business Media, 3rd edition, 2003.

[90] G. K. Wertheim. Shape of core-electron photoemission spectra from metals. *Physical Review B*, 25(3):1987–1989, 1982.

[91] D. Briggs and J. T. Grant. *Surface Analysis by Auger and Photoelectron Spectroscopy*. IM Publications,, 2003.

[92] Neal Fairley. *CasaXPS Manual*. CasaXPS, 2.3.15 edition, 2009.

[93] Donald R. Wheeler and Stephen V. Pepper. Angle-resolved X-ray photoelectron spectroscopy of epitaxially grown (100) β-SiC to 1300 C. *Surface and Interface Analysis*, 10(2-3):153–162, 1987.

[94] I. Kusunoki and Y. Igari. XPS study of a SiC film produced on Si(100) by reaction with a C2H2 beam. *Applied Surface Science*, 59:95–104, 1992.

[95] M. Diani, J. L. Bischoff, L. Kubler, and D. Bolmont. X-ray photoelectron diffraction observation of β-SiC(001) obtained by electron cyclotron resonance plasma assisted growth on Si(001). *Applied Surface Science*, 68(4):575–582, 1993.

[96] Pu Sen Wang. Oxidation kinetics of silicon carbide whiskers studied by X-ray photoelectron spectroscopy. *Journal of Materials Science*, 26:1655–1658, 1991.

[97] R.J Iwanowski, K Fronc, W Paszkowicz, and M Heinonen. XPS and XRD study

of crystalline 3C-SiC grown by sublimation method. *Journal of Alloys and Compounds*, 286(1-2):143–147, may 1999.

[98] Jean Charles Arnault, Samuel Saada, Sophie Delclos, Licinio Rocha, Luciana Intiso, Riccardo Polini, Alon Hoffman, Shaul Michaelson, and Philippe Bergonzo. Surface science contribution to the BEN control on Si(100) and 3C-SiC(100): Towards ultrathin nanocrystalline diamond films. *Chemical Vapor Deposition*, 14(7-8 SPEC. ISS.):187–195, 2008.

[99] S Wee, C Feng, H Hng, L Tan, C Tin, R Hu, and R Coston. Surface chemical states on 3C-SiC/Si epilayers. *Applied Surface Science*, 81(100), 1994.

[100] G. Dufour, F. Rochet, F. C. Stedile, Ch. Poncey, M. De Crescenzi, R. Gunnella, and M. Froment. SiC formation by reaction of Si(001) with acetylene: Electronic structure and growth mode. *Physical Review B - Condensed Matter and Materials Physics*, 56(7):4266–4282, 1997.

[101] Thomas Seyller. Passivation of hexagonal SiC surfaces by hydrogen termination. *Journal of Physics: Condensed Matter*, 16(17):S1755–S1782, 2004.

[102] Sarit Dhar, Oliver Seitz, Mathew D Halls, Sungho Choi, Yves J Chabal, and Leonard C Feldman. Chemical properties of oxidized silicon carbide surfaces upon etching in hydrofluoric acid. *Journal of the American Chemical Society*, 131(46):16808–13, nov 2009.

[103] S. Nakanishi, H. Tokutaka, K. Nishimori, S. Kishida, and N. Ishihara. The difference between 6H-SiC (0001) and (0001) faces observed by AES, LEED and ESCA. *Applied Surface Science*, 41-42(C):44–48, 1989.

[104] V. Van Elsbergen, T. U. Kampen, and W. Mönch. Surface analysis of 6H-SiC. *Surface Science*, 365(2):443–452, 1996.

[105] Fredrik Owman and Per Martensson. STM study of the SIC (0001) R3xR3 surface. *Surface Science*, 330:L639–L645, 1995.

[106] L. I. Johansson, Fredrik Owman, and Per Mårtensson. High-resolution core-level study of 6 H -SiC(0001). *Physical Review B*, 53(20):13793–13802, 1996.

[107] J. Schardt, Ch. Bram, S. Müller, U. Starke, K. Heinz, and K. Müller. LEED structure determination of hexagonal alpha-SiC surfaces. *Surface Science*, 337(95):232–242, 1995.

[108] U. Starke, Ch. Bram, P. Steiner, W. Hartner, L. Hammer, K. Heinz, and K. Miiller. The (0001) surface of 6H-SiC : morphology , composition and structure. *Applied Surface Science*, 89:175–185, 1995.

[109] R. Kaplan. Surface Structure And Composition Of beta- And 6H-SiC. *Surface Science*, 215:111–134, 1989.

[110] S. Hara, W.F.J. Slikerman, J.F. van der Veen, I Ohdomari, S. Misawa, E. Sakuma, and S. Yoshida. Elemental Composition of beta-SiC(001) Surface Phases Studied by Medium Energy Scattering. *Surface Science Letters*, 231, 1990.

[111] R. Kaplan. Surface studies of epitaxial beta SiC on Si (100). *Journal of Applied Physics*, 56(6):1636–1641, 1984.

[112] T. M. Parrill and Y. W. Chung. Surface analysis of cubic silicon carbide (001). *Surface Science*, 243(1-3):96–112, 1991.

[113] T Balster, V M Polyakov, H Ibach, and J A Schaefer. A study of surface band bendings

and charge densities of SiC(001) 2x1 and c(2x2) by high-resolution electron-energy-loss spectroscopy. *Surface Science*, 416(1-2):177–183, 1998.

[114] C. Coletti, K. V. Emtsev, a. a. Zakharov, T. Ouisse, D. Chaussende, and U. Starke. Large area quasi-free standing monolayer graphene on 3C-SiC(111). *Applied Physics Letters*, 99(May 2013):2011–2014, 2011.

[115] Ronald Fuchs and K. L. Kliewer. Optical Modes of Vibration in an Ionic Crystal Slab Including Retardation. II. Radiative Region. *Physical Review*, 150(2):573–588, 1966.

[116] H. Nienhaus, T. U. Kampen, and W. Mönch. Phonons in 3C-, 4H-, and 6H-SiC. *Surface Science Letters*, 324(1), 1995.

[117] H. Nienhaus, V. van Elsberg, and W. Mönch. Vibrations at 3C-SiC (001)-(3 x 2) surfaces. *The European Physical Journal B*, 182:179–182, 1999.

[118] V. M. Polyakov, T. Balster, S. Sloboshanin, F. S. Tautz, H. Ibach, and J. A. Schaefer. Surface state-derived electronic transitions of SiC (001). *Surface Science*, 420:87–94, 1999.

[119] S. Tong Lee and G. Apai. Surface phonons and CH vibrational modes of diamond (100) and (111) surfaces. *Physical Review B*, 48(4):2684–2693, 1993.

[120] Takashi Aizawa, Toshihiro Ando, and Yoichiro Sato. High-resolution electron-energy-loss spectroscopic study of epotaxially grown diamond (111) and (100) surfaces. *Physical Review B*, 48(24), 1993.

[121] H. Ibach, H. Hopster, and Brett A Sexton. Analysis of surface reactions by spectroscopy of surface vibrations. *Applications of Surface Science*, 1(1):1–24, 1977.

[122] H. Ibach, H. Wagner, and D. Bruchmann. Dissociative chemisorption of H2O on Si(100) and Si(111) - a vibrational study. *Solid State Communications*, 42(6):457–459, 1982.

[123] J. A. Schaefer, F. Stucki, D. J. Frankel, W. Göpel, and G. J. Lapeyre. Adsorption of H, O, and H2O at Si(100) and Si(111) surfaces in the monolayer range: A combined EELS, LEED, and XPS study. *Journal of Vacuum Science & Technology B*, 2(3):359–365, 1984.

[124] Ch. Stuhlmann, G. Bogdanyi, and H. Ibach. Surface phonons of the hydrogen-terminated Si(111)(1x1) surface. *Physical Review B*, 45(12):6786–6792, 1992.

[125] P. Gupta, V. L. Colvin, and S. M. George. Hydrogen desorption kinetics from monohydride and dihydride species on silicon surfaces. *Physical Review B*, 37(14):8234–8243, 1988.

[126] Q Tong, E Schmidt, and U Ggselea. Hydrophobic silicon wafer bonding. *Applied Physics Letters*, 64(5):625–627, 1994.

[127] H. R. Philipp. Intrinsic Optical Absorption in Single-Crystal Silicon Carbide. *Physical Review*, 111(2):3–4, 1958.

[128] J. Pelletier, D. Gervais, and C. Pomot. Application of wide-gap semiconductors to surface ionization: Work functions of AlN and SiC single crystals. *Journal of Applied Physics*, 55(4):994–1002, 1984.

[129] Werner Kern. The Evolution of Silicon Wafer Cleaning Technology. *Journal of the Electrochemical Society*, 137(6):1887–1892, 1990.

[130] Martin Beerbom, Oliver Henrion, Andreas Klein, Thomas Mayer, and Wolfram

Jaegermann. XPS analysis of wet chemical etching of GaAs (110) by Br2-H2O: comparison of emersion and model experiments. *Electrochimica Acta*, 45:4663–4672, 2000.

[131] M. Beerbom, Th Mayer, W. Jaegermann, D. R. Batchelor, and D. Schmeißer. Synchrotron-induced photoemission of GaAs electrodes after electrochemical treatment in aqueous electrolytes. *Analytical and Bioanalytical Chemistry*, 374(4):650–653, 2002.

[132] H. Landolt and R. Börnstein. *Group III Condensed Matter*. Springer, 2005.

[133] A. A. Lebedev. Heterojunctions and superlattices based on silicon carbide. *Semiconductor Science and Technology*, 21(6):R17–R34, 2006.

[134] J. Crofton, L.M. Porter, and J.R. Williams. The Physics of Ohmic Contacts to SiC. *physica status solidi (b)*, 202(1):581–603, 1997.

[135] Sang Youn Han and Jong-Lam Lee. Characteristics of Schottky contacts on n-type 4HâĂŞSiC using IrO2 and RuO2. *Journal of Applied Physics*, 94(9):6159, 2003.

[136] Yu Cao, Lars Nyborg, Urban Jelvestam, and Danqing Yi. Effect of pre-treatment and nickel layer thickness on nickel silicide/silicon carbide contact. *Applied Surface Science*, 241(3-4):392–402, 2005.

[137] G. Ferro, T. Chassagne, A. Leycuras, F. Cauwet, and Y. Monteil. Strain Tailoring in 3C-SiC Heteroepitaxial Layers Grown on Si(100). *Chemical Vapor Deposition*, 12(8-9):483–488, 2006.

[138] T. Gutt, H. M. Przewlocki, K. Piskorski, A. Mikhaylov, and M. Bakowski. PECVD and Thermal Gate Oxides on 3C vs. 4H SiC: Impact on Leakage, Traps and Energy Offsets. *ECS Journal of Solid State Science and Technology*, 4(9):M60–M63, 2015.

[139] J. A. Edmond, J. Ryu, J. T. Glass, and R. F. Davis. Electrical Contacts to Beta Silicon Carbide Thin Films. *Journal of The Electrochemical Society*, 135(2):359–362, 1988.

[140] J. Wan, M. A. Capano, and M. R. Melloch. Formation of low resistivity ohmic contacts to n-type 3C-SiC. *Solid-State Electronics*, 1(January):2–5, 2002.

[141] Jae Il Noh, Kee Suk Nahm, Kwang Chul Kim, and Michael a. Capano. Effect of surface preparation on Ni ohmic contact to 3C-SiC. *Solid-State Electronics*, 46:2273–2279, 2002.

[142] Jens Eriksson, Fabrizio Roccaforte, Filippo Giannazzo, Raffaella Lo Nigro, Vito Raineri, Jean Lorenzzi, and Gabriel Ferro. Improved Ni/3C-SiC contacts by effective contact area and conductivity increases at the nanoscale. *Applied Physics Letters*, 94(11):112104, 2009.

[143] Hiroyuki Nagasawa, Kuniaki Yagi, Takamitsu Kawahara, and Naoki Hatta. Reducing planar defects in 3C-SiC. *Chemical Vapor Deposition*, 12(8-9):502–508, 2006.

[144] H. Heidarzadeh, H. Baghban, H. Rasooli, M. Dolatyari, and A. Rostami. A new proposal for Si tandem solar cell: Significant efficiency enhancement in 3C SiC/Si. *Optik - International Journal for Light and Electron Optics*, nov 2013.

[145] U. Lindefelt. Doping-induced band edge displacements and band gap narrowing in 3C-, 4H-, 6H-SiC, and Si. *Journal of Applied Physics*, 84(5):2628, 1998.

[146] J. Kuriplach, M. Šob, G. Brauer, W. Anwand, E.-M. Nicht, P. Coleman, and N. Wagner. Positron affinity in semiconductors: Theoretical and experimental studies. *Physical Review B*, 59(3):1948–1955, 1999.

[147] D E Eastman. Photoelectric Work Functions of Transition, Rare-Earth, and Noble Metals. *Physical Review B*, 2(1):1–&, 1970.

[148] B. G. Baker, B. B. Johnson, and G. L C Maire. Photoelectric work function measurements on nickel crystals and films. *Surface Science*, 24(2):572–586, 1971.

[149] Herbert B. Michaelson. The work function of the elements and its periodicity. *Journal of Applied Physics*, 48(11):4729, 1977.

[150] Paul A. Tipler and Ralph A. Llewellyn. *Modern Physics*. W. H. Freemann and Company, 5th edition, 2008.

[151] H. W. Nesbitt, D. Legrand, and G. M. Bancroft. Interpretation of Ni2p XPS spectra of Ni conductors and Ni insulators. *Physics and Chemistry of Minerals*, 27(5):357–366, 2000.

[152] Andrew P. Grosvenor, Mark C. Biesinger, R. St C Smart, and N. Stewart McIntyre. New interpretations of XPS spectra of nickel metal and oxides. *Surface Science*, 600(9):1771–1779, 2006.

[153] A. M. Cowley and S. M. Sze. Surface states and barrier height of metal-semiconductor systems. *Journal of Applied Physics*, 36(10):3212–3220, 1965.

[154] G K Wertheim, S B DiCenzo, and S E Youngquist. Unit Charge on Supported Gold Clusters in Photoemission Final State. *Physical Review Letters*, 51(25), 1983.

[155] Joachim Klett, Stefan Krähling, Benjamin Elger, Rolf Schäfer, Bernhard Kaiser, and Wolfram Jaegermann. The Electronic Interaction of Pt-Clusters with ITO and HOPG Surfaces upon Water Adsorption. *Z. Phys. Chem.*, 228(4-5):503–520, 2014.

[156] Jafar Safarian and Thorvald a. Engh. Vacuum Evaporation of Pure Metals. *Metallurgical and Materials Transactions A*, 44(February):747–753, 2012.

[157] H. Y. Wong. Oxidized nickel as a heating element in vacuum. *Brit. J. Appl. Phys.*, 17, 1966.

[158] N. W. Cheung, P. J. Grunthaner, F. J. Grunthaner, J. W. Mayer, and B. M. Ullrich. Metal-semiconductor interfacial reactions: Ni/Si system. *Journal of Vacuum Science & Technology*, 18(3):917–923, 1981.

[159] Yu Cao, Lars Nyborg, and Urban Jelvestam. XPS calibration study of thin-film nickel silicides. *Surface and Interface Analysis*, 41(6):471–483, jun 2009.

[160] P. L. Tam and L. Nyborg. Sputter deposition and XPS analysis of nickel silicide thin films. *Surface and Coatings Technology*, 203(19):2886–2890, 2009.

[161] A Bächli, M.-A Nicolet, L Baud, C Jaussaud, and R Madar. Nickel film on (001) SiC: Thermally induced reactions. *Materials Science and Engineering: B*, 56(1):11–23, 1998.

[162] Lucia Calcagno, E. Zanetti, Francesco La Via, Fabrizio Roccaforte, Vito Raineri, Sebania Libertino, Filippo Giannazzo, Marco Mauceri, and Paolo Musumeci. Schottky-Ohmic Transition in Nickel Silicide/SiC System: Is it Really a Solved Problem? *Materials Science Forum*, 433-436:721–724, 2003.

[163] J.P. Gambino and E.G. Colgan. Silicides and ohmic contacts. *Materials Chemistry and Physics*, 52(2):99–146, 1998.

[164] L. J. Chen. Metal Silicides: An Integral Part of Microelectronics. *Journal of the Minerals, Metals & Materials Society*, 57(9):24–33, 2005.

[165] A. Ouerghi, A. Kahouli, D. Lucot, M. Portail, L. Travers, J. Gierak, J. Penuelas, P. Jegou, A. Shukla, T. Chassagne, and M. Zielinski. Epitaxial graphene on cubic SiC(111)/Si(111) substrate. *Applied Physics Letters*, 96(19):191910, 2010.

[166] G. Johansson, J. Hedman, A. Berndtssson, M. Klasson, and R. Nilsson. Calibration Of Electron Spectra. *Journal of Electron Spectroscopy and Related Phenomenon*, 2:303–326, 1974.

[167] G Witek, M Noeske, G Mestl, S Shaikhutdinov, and R J Behm. Interaction of platinum colloids with single crystalline oxide and graphite substrates: A combined AFM, STM and XPS study. *Catalysis Letters*, 37(1-2):35–39, 1996.

[168] Toma Susi, Thomas Pichler, and Paola Ayala. X-ray photoelectron spectroscopy of graphitic carbon nanomaterials doped with heteroatoms. *Beilstein Journal of Nanotechnology*, 6:177–192, 2015.

[169] Konstantin V Emtsev, Aaron Bostwick, Karsten Horn, Johannes Jobst, Gary L Kellogg, Lothar Ley, Jessica L McChesney, Taisuke Ohta, Sergey a Reshanov, Jonas Röhrl, Eli Rotenberg, Andreas K Schmid, Daniel Waldmann, Heiko B Weber, and Thomas Seyller. Towards wafer-size graphene layers by atmospheric pressure graphitization of silicon carbide. *Nature materials*, 8(3):203–207, 2009.

[170] Ayato Nagashima, Kenji Nuka, Hiroshi Itoh, Takeo Ichinokawa, Chuhei Oshima, and Shigeki Otani. Electronic states of monolayer graphite formed on TiC(111) surface. *Surface Science*, 291(1-2):93–98, 1993.

[171] Nivedita Biswas, Jason Gurganus, and Veena Misra. Work function tuning of nickel silicide by co-sputtering nickel and silicon. *Applied Physics Letters*, 87(17):171908, 2005.

[172] Robert Doering and Yoshio Nishi. *Handbook of Semiconductor Manufacturing Technology*. 2nd edition, 2008.

[173] C Jacob, P Pirouz, H.-I Kuo, and M Mehregany. High temperature ohmic contacts to 3C silicon carbide films. *Solid-State Electronics*, 42(12):2329–2334, 1998.

[174] F Mansfeld, S Lin, Y C Chen, and H Shih. Minimization of High-Frequency Phase Shifts in Impedance Measurements. *Journal of The Electrochemical Society*, 135:906–907, 1988.

[175] R. Memming. The Role of Energy Levels in Semiconductor-Electrolyte Solar Cells. *Journal of The Electrochemical Society*, 125(1):117, 1978.

[176] Christopher M. A. Brett and Ana Maria Oliveira Brett. *Electrochemistry*. Oxford University Press, 1 edition, 1994.

[177] L. M. Peter and R. Peat. SURFACE REOMBINATION AT SEMICONDUCTOR ELECTRODES - PART I. TRANSIENT AND STEADY-STATE PHOTOCURRENTS. *Journal of Electroanalytical Chemistry*, 165:29–40, 1984.

[178] Laurence Peter. Dynamic aspects of semiconductor photoelectrochemistry. *Chemical Reviews*, 90(5):753–769, 1990.

[179] L. M. Peter, J. Li, R. Peat, H. J. Lewerenz, and J. Stumper. FREQUENCY RESPONSE ANALYSIS OF INTENSITY MODULATED PHOTOCURRENTS AT SEMICONDUCTOR ELECTRODES. *Electrochimica Acta*, 35:1657–1664, 1990.

[180] E. A. Ponomarev and L. M. Peter. A generalized theory intensity modulated photocurrent spectroscopy (IMPS). *Journal of Electroanalytical Chemistry*, 396:219–226, 1995.

[181] I. H. Malitson. Interspecimen Comparison of the Refractive Index of Fused Silica. *Journal of the Optical Society of America*, 55(10):1205, 1965.

[182] Peter T. B. Shaffer and Robert G. Naum. Refractive Index and Dispersion of Beta Silicon Carbide. *Journal of the Optical Society of America*, 59(11):1498, nov 1969.

[183] Wolfgang W. Gärtner. Depletion-Layer Photoeffects in Semiconductors. *Physical Review*, 116:84–87, 1959.

[184] Lyle Patrick and W. J. Choyke. Optical Absorption in n-Type Cubic SiC. *Physical Review*, 161(1963):1964–1966, 1969.

[185] Gary Lynn Harris. *Properties of Silicon Carbide*. inspec, 1995.

[186] M.J. Madou, B.H. Loo, K.W. Frese, and S.Roy Morrison. Bulk and surface characterization of the silicon electrode. *Surface Science*, 108(1):135–152, 1981.

[187] Matthias Sachsenhauser, Ian D. Sharp, Martin Stutzmann, and Jose A. Garrido. Surface State Mediated Electron Transfer Across the N-Type SiC/Electrolyte Interface. *Journal of Physical Chemistry C*, 120(12):6524–6533, 2016.

[188] K. Darowicki, S. Krakowiak, and P. Ślepski. Selection of measurement frequency in Mott-Schottky analysis of passive layer on nickel. *Electrochimica Acta*, 51(11):2204–2208, 2006.

[189] F. La Mantia, H. Habazaki, M. Santamaria, and F. Di Quarto. A critical assessment of the Mott-Schottky analysis for the characterisation of passive film-electrolyte junctions. *Russian Journal of Electrochemistry*, 46(11):1306–1322, 2010.

[190] Zuzana Vlčková Živcová, Václav Petrák, Otakar Frank, and Ladislav Kavan. Electrochemical impedance spectroscopy of polycrystalline boron doped diamond layers with hydrogen and oxygen terminated surface. *Diamond and Related Materials*, 55:70–76, 2015.

[191] M. Ichimura, H. Tajiri, Y. Morita, N. Yamada, and A. Usami. Excess carrier lifetime of 3C-SiC measured by the microwave photoconductivity decay method. *Applied Physics Letters*, 70(13):1745, 1997.

[192] Vytautas Grivickas, Georgios Manolis, Karolis Gulbinas, Kstutis Jarašinas, and Masashi Kato. Excess carrier recombination lifetime of bulk n -type 3C-SiC. *Applied Physics Letters*, 95(24):10–13, 2009.

[193] Patrik Ščajev, Jawad Hassan, KÈľstutis Jarašiunas, Masashi Kato, Anne Henry, and J. Peder Bergman. Comparative studies of carrier dynamics in 3C-SiC layers grown on Si and 4H-SiC substrates. *Journal of Electronic Materials*, 40(4):394–399, 2011.

[194] J. W. Sun, I. G. Ivanov, R. Liljedahl, R. Yakimova, and M. Syväjärvi. Considerably long carrier lifetimes in high-quality 3C-SiC(111). *Applied Physics Letters*, 100(25), 2012.

[195] A. A. Lebedev, A. M. Strel'chuk, D. V. Davydov, N. S. Savkina, A. S. Tregubova, A. N. Kuznetsov, V. A. Solov'ev, and N. K. Poletaev. Electrical characteristics of p-3C-SiC/n-6H-SiC heterojunctions grown by sublimation epitaxy on 6H-SiC substrates. *Applied Surface Science*, 184(1-4):419–424, 2001.

[196] R. Peat and L. M. Peter. Determination of the electron diffusion length in p-GaP by intensity modulated photocurrent measurements with an electrolyte contact. *Applied Physics Letters*, 51(5):328, 1987.

[197] J. S. Shor and A. D. Kurtz. Photoelectrochemical Etching of 6H-SiC. *Journal of The Electrochemical Society*, 141(3):2–5, 1994.

[198] J. S. Shor and R. M. Osgood. Broad-Area Photoelectrochemical Etching of n-Type Beta-SiC. *Electrochemical Society Letters*, 140(8):123–125, 1993.

[199] D. H. van Dorp and J. J. Kelly. Photoelectrochemistry of 4H-SiC in KOH solutions. *Journal of Electroanalytical Chemistry*, 599(2):260–266, 2007.

[200] D. H. Van Dorp, J L Weyher, and J J Kelly. Anodic etching of SiC in alkaline solutions. *Journal of Micromechanics and Microengineering*, 17(4):S50–S55, 2007.

[201] Xiaoge Gregory Zhang. *Electrochemistry of Silicon and its Oxide*. Kluwer Academic Publishers, 2001.

[202] J. Ashley Taylor, Gerald M. Lancaster, and J. Wayne Rabalais. Chemical reactions of N2+ ion beams with group IV elements and their oxides. *Journal of Electron Spectroscopy and Related Phenomena*, 13(3):435–444, 1978.

[203] D F Mitchell, K B Clark, J A Bardwell, W. N. Lennard, G.R. Massoumi, and I.V. Mitchell. Film Thickness Measurements of SiO2 by XPS. *Surface and Interface Analysis*, 21:44–50, 1994.

[204] Martyn H. Kibel and Patrick W. Leech. X-ray Photoelectron Spectroscopy Study of Optical Waveguide Glasses. *Surface and Interface Analysis*, 24(9):605–610, 1996.

[205] J. W. Keister, J. E. Rowe, J. J. Kolodziej, H. Niimi, H.-S. Tao, T. E. Madey, and G. Lucovsky. Structure of ultrathin SiO2/Si(111) interfaces studied by photoelectron spectroscopy. *Journal of Vacuum Science & Technology A: Vacuum, Surfaces, and Films*, 17(4):1250, 1999.

[206] F. J. Himpsel, F. R. McFeely, A. Taleb-Ibrahim, J. A. Yarmoff, and G. Hollinger. Microscopic structure of the SiO2/Si interface. *Physical Review B*, 38(9), 1988.

[207] M. P. Seah and S. J. Spencer. Ultrathin SiO2 on Si IV. Intensity measurement in XPS and deduced thickness linearity. *Surface and Interface Analysis*, 35(6):515–524, jun 2003.

[208] Martin A. Green and Mark J. Keevers. Optical properties of intrinsic silicon at 300K. *Progress in Photovoltaics: Research and Applications*, 3.3:189–192, 1995.

[209] Kassem Alassaad. *Addition of Ge to the H-Si-C chemical system during SiC epitaxy*. Phd. thesis, Universite de Lyon, 2014.

[210] Maher Soueidan, Gabriel Ferro, Olivier Kim-Hak, François Cauwet, and Bilal Nsouli. Vapor-liquid-solid growth of 3C-SiC on α-SiC substrates. 1. Growth mechanism. *Crystal Growth and Design*, 8(3):1044–1050, 2008.

[211] Nikoletta Jegenyes, Jean Lorenzzi, Veronique Soulière, Jacques Dazord,

François Cauwet, and Gabriel Ferro. Investigation of 3C-SiC(111) Homoepitaxial Growth by CVD at High Temperature. *Materials Science Forum*, 645-648:127–130, 2010.

[212] Michael W. Davidson Douglas B. Murphy. *Fundamentals of Light Microscopy and Electronic Imaging*. WILEY, 2 edition, 2012.

[213] Hiroshi Harima. Raman scattering characterization on SiC. *Microelectronic Engineering*, 83(1):126–129, jan 2006.

[214] Rolando Guidelli, Richard G. Compton, Juan M. Feliu, Eliezer Gileadi, Jacek Lipkowski, Wolfgang Schmickler, and Sergio Trasatti. Defining the transfer coefficient in electrochemistry: An assessment (IUPAC Technical Report). *Pure and Applied Chemistry*, 86(2):245–258, 2014.

[215] Robert Schafranek, Judith Schaffner, and Andreas Klein. In situ photoelectron study of the (Ba,Sr)TiO3/RuO2 contact formation. *Journal of the European Ceramic Society*, 30(2):187–192, 2010.

[216] Quan-Bao Ma, Bernhard Kaiser, and Wolfram Jaegermann. Novel photoelectrochemical behaviors of p-SiC films on Si for solar water splitting. *Journal of Power Sources*, 253:41–47, may 2014.

[217] B. Beverskog and I. Puigdomenech. Revised Pourbaix diagrams for nickel at 25-300 C. *Corrosion Science*, 38(12):2121–2135, 1996.

[218] Lena Trotochaud, James K. Ranney, Kerisha N. Williams, and Shannon W. Boettcher. Solution-cast metal oxide thin film electrocatalysts for oxygen evolution. *Journal of the American Chemical Society*, 134(41):17253–17261, 2012.

[219] R. D. L. Smith, M. S. Prevot, R. D. Fagan, Z. Zhang, P. a. Sedach, M. K. J. Siu, S. Trudel, and C. P. Berlinguette. Photochemical Route for Accessing Amorphous Metal Oxide Materials for Water Oxidation Catalysis. *Science*, 60:60–63, mar 2013.

[220] R. J. Powell and W. E. Spicer. Optical Properties of NiO and CoO. *Physical Review B*, pages 2182–2193, 1970.

[221] G A Sawatzky and J W Allen. Magnitude and Origin of the Band-Gap in Nio. *Physical Review Letters*, 53(24):2339–2342, 1984.

[222] A.J. Varkey and A.F. Fort. Solution growth technique for deposition of nickel oxide thin films. *Thin Solid Films*, 235(1-2):47–50, 1993.

[223] S. Hüfner. Electronic structure of NiO and related 3d-transition-metal compounds. *Advances in Physics*, 43(2):183–356, 1994.

[224] Zhengjun Zhang, Ye Zhao, and Minmin Zhu. NiO films consisting of vertically aligned cone-shaped NiO rods. *Applied Physics Letters*, 88(3):1–3, 2006.

[225] J. Olivier, B. Servet, M. Vergnolle, M. Mosca, and G. Garry. Stability/instability of conductivity and work function changes of ITO thin films, UV-irradiated in air or vacuum. Measurements by the four-probe method and by Kelvin force microscopy. *Synthetic Metals*, 122(1):87–89, 2001.

[226] Mark T. Greiner, Michael G. Helander, Zhi Bin Wang, Wing Man Tang, and Zheng Hong Lu. Effects of processing conditions on the work function and energy-level alignment of NiO thin films. *Journal of Physical Chemistry C*, 114(46):19777–19781, 2010.

[227] K. Xerxes Steirer, Paul F. Ndione, N. Edwin Widjonarko, Matthew T. Lloyd, Jens Meyer, Erin L. Ratcliff, Antoine Kahn, Neal R. Armstrong, Calvin J. Curtis, David S. Ginley, Joseph J. Berry, and Dana C. Olson. Enhanced efficiency in plastic solar cells via energy matched solution processed NiO x interlayers. *Advanced Energy Materials*, 1(5):813–820, 2011.

[228] K. S. Kim and Nicholas Winograd. X-RAY PHOTOELECTRON SPECTROSCOPC STUDIES OF NICKEL-OXYGEN SURFACES USING OXYGEN AND ARGON ION-BOMBARDMENT. *Surface Science*, 43:625–643, 1974.

[229] Kung T. Ng and David M. Hercules. Studies of nickel-tungsten-alumina catalysts by x-ray photoelectron spectroscopy. *The Journal of Physical Chemistry*, 80(19):2094–2102, 1976.

[230] D. A. Wruck and M. Rubin. Structure and Electronic Properties of Electrochromic NiO Films. *Journal of The Electrochemical Society*, 140(4):1097–1104, 1993.

[231] S. R. Jiang, P. X. Yan, B. X. Feng, X. M. Cai, and J. Wang. The response of a NiOx thin film to a step potential and its electrochromic mechanism. *Materials Chemistry and Physics*, 77(2):384–389, 2003.

[232] Mark C. Biesinger, Brad P. Payne, Leo W M Lau, Andrea Gerson, and Roger St C Smart. X-ray photoelectron spectroscopic chemical state Quantification of mixed nickel metal, oxide and hydroxide systems. *Surface and Interface Analysis*, 41(4):324–332, 2009.

[233] Youngmin Lee, Jin Suntivich, Kevin J May, Erin E Perry, and Yang Shao-horn. Synthesis and Activities of Rutile IrO 2 and RuO 2 Nanoparticles for Oxygen Evolution in Acid and Alkaline Solutions. *The Journal of Physical Chemistry Letters*, 3:399–404, 2012.

[234] Kelsey A. Stoerzinger, Liang Qiao, Michael D. Biegalski, and Yang Shao-Horn. Orientation-dependent oxygen evolution activities of rutile IrO2 and RuO2. *Journal of Physical Chemistry Letters*, 5(10):1636–1641, 2014.

[235] David J. Morgan. Resolving ruthenium: XPS studies of common ruthenium materials. *Surface and Interface Analysis*, 47(11):1072–1079, 2015.

[236] A. J. Hartmann, M. Neilson, R. N. Lamb, K. Watanabe, and J. F. Scott. Ruthenium oxide and strontium ruthenate electrodes for ferroelectric thin-films capacitors. *Applied Physics A: Materials Science and Processing*, 70(2):239–242, 2000.

[237] K. Frohlich, K. Husekova, D. Machajdik, J. C. Hooker, N. Perez, M. Fanciulli, S. Ferrari, C. Wiemer, A. Dimoulas, G. Vellianitis, and F. Roozeboom. Ru and RuO2 gate electrodes for advanced CMOS technology. *Materials Science and Engineering B: Solid-State Materials for Advanced Technology*, 109(1-3):117–121, 2004.

[238] Md Tamez Uddin, Yohann Nicolas, Celine Olivier, Thierry Toupance, Mathis M. Müller, Hans Joachim Kleebe, Karsten Rachut, Jürgen Ziegler, Andreas Klein, and Wolfram Jaegermann. Preparation of RuO2/TiO2 mesoporous heterostructures and rationalization of their enhanced photocatalytic properties by band alignment investigations. *Journal of Physical Chemistry C*, 117(42):22098–22110, 2013.

[239] S. Bhaskar, P. S. Dobal, S. B. Majumder, and R. S. Katiyar. X-ray photoelectron spectroscopy and micro-Raman analysis of con-

ductive RuO2 thin films. *Journal of Applied Physics*, 89(5):2987, 2001.

[240] K. S. Kim and N. Winograd. X-Ray Photoelectron Spectroscopic Studies of Ruthenium-Oxygen Surfaces. *Journal of Catalysis*, 35:66–72, 1974.

[241] H. J. Lewerenz, S. Stucki, and R. Kötz. Oxygen Evolution and Corrosion: XPS Investigation on Ru and RuO2 Electrodes. *Surface Science*, 126:463–468, 1983.

[242] Etsushi Tsuji, Akihito Imanishi, Ken Ichi Fukui, and Yoshihiro Nakato. Electrocatalytic activity of amorphous RuO2 electrode for oxygen evolution in an aqueous solution. *Electrochimica Acta*, 56(5):2009–2016, 2011.

[243] M J N Pourbaix, J Van Muylder, N de Zoubov, and C PROTECTION. Electrochemical properties of the platinum metals. *Platinum Metals Review*, 3(2):47–53, 1959.

[244] M J N Pourbaix, J Van Muylder, N de Zoubov, and C PROTECTION. Electrochemical properties of the platinum metals. *Platinum Metals Review*, 3(2):47–53, 1959.

[245] T. E. Lister, Y. V. Tolmachev, Y. Chu, W. G. Cullen, H. You, R. Yonco, and Z. Nagy. Cathodic activation of RuO2 single crystal surfaces for hydrogen-evolution reaction. *Journal of Electroanalytical Chemistry*, 554-555(1):71–76, 2003.

[246] J. Schardt, J. Bernhardt, U. Starke, and K. Heinz. Atomic Structure of Hexagonal 6H- and 3C-SiC Surfaces. *Surface Review and Letters*, 05(01):181–186, 1998.

[247] BSolar. Silicon solar cell datasheet (TG18.5 BR), 2011.

[248] SolarSilicon. Silicon solar cell datasheet (Eff. Code 196).

[249] W. J. Choyke, H. Matsunami, and G. Pensl. *Silicon Carbide - Recent Major Advances*. Springer, 1 edition, 2004.

[250] Hidekazu Tsuchida, Isaho Kamata, and Kunikazu Izumi. Si-H Bonds on the 6H-SiC(0001) Surface after H2 Annealing. *Japanese Journal of Applied Physics*, 36, 1997.

[251] N Sieber, Th. Seyller, R Graupner, L Ley, R Mikalo, P Hoffmann, D.R. Batchelor, and D. Schmeißer. PES and LEED study of hydrogen- and oxygen-terminated 6H-SiC (0001) and (000-1) surfaces. *Applied Surface Science*, 184(1-4):278–283, 2001.

[252] Jianwu Sun, Valdas Jokubavicius, Lu Gao, Ian Booker, Mattias Jansson, Xinyu Liu, Jan P. Hofmann, Emiel J. M. Hensen, Margareta Linnarsson, Peter Wellmann, Iñigo Ramiro, Antonio Marti, Rositsa Yakimova, and Mikael Syväjärvi. Solar driven energy conversion applications based on 3C-SiC. *Mater. Sci. Forum*, 858:1028–1031, 2016.

[253] Naoto Ichikawa, Masashi Kato, and Masaya Ichimura. The enhanced performance of 3C-SiC photocathodes for the generation of hydrogen through the use of cocatalysts. *Applied Physics Letters*, 109(15), 2016.

[254] S.G Sridhara, T.J Eperjesi, R.P Devaty, and W. J. Choyke. Penetration depths in the ultraviolet for 4H, 6H and 3C silicon carbide at seven common laser pumping wavelengths. *Materials Science and Engineering: B*, 61-62:229–233, jul 1999.

[255] H. Heidarzadeh, H. Baghban, H. Rasooli, M. Dolatyari, and A. Rostami. A new proposal for Si tandem solar cell : Significant

efficiency enhancement in 3C SiC / Si. *Optics*, 125(3):1292–1296, 2014.

[256] Martin A Green. Multiple Band and Impurity Photovoltaic Solar Cells: General Theory and Comparison to Tandem Cells. *Progress in Photovoltaics: Research and Applications*, 9:137–144, 2001.

[257] G. Güttler and H. J. Queisser. Impurity Photovoltaic Effect in Silicon. *Energy Conversion*, 10:51–55, 1970.

[258] L Cuadra, A Mani, N Lopez, and A Luque. Intermediate Band Photovoltaics Overview. *3rd World Conference on Photovoltaic Energy Conversion*, pages 3–8, 2003.

[259] Gottfried H. Bauer. *Photovoltaic Solar Energy Conversion*. Springer, 1 edition, 2015.

[260] G. Beaucarne, A. S. Brown, M. J. Keevers, R. Corkish, and M. A. Green. The Impurity Photovoltaic (IPV) Effect in Wide-Bandgap Semiconductors: an Opportunity for Very-High-Efficiency Solar Cells? *Progress in Photovoltaics: Research and Applications*, 10:345–353, 2002.

[261] B. S. Richards, A. Lambertz, R. P. Corkish, C. A. Zorman, M. Mehregany, M. Ionescu, and M. A. Green. 3C-SiC as a future photovoltaic material. *3rd World Conference on Photovoltaic Energy Conversion*, pages 2738–2741, 2003.

[262] Matthew T. McDowell, Michael F. Lichtermann, Azhar I. Carim, Rui Liu, Shu Hu, Bruce S Brunschwig, and Nathan S Lewis. The Influence of Structure and Processing on the Behavior of TiO 2 Protective Layers for Stabilization of n-Si/TiO 2 /Ni Photoanodes for Water Oxidation. *ACS Applied Materials / Interfaces*, 7, 2015.

[263] N. Sieber, T. Stark, Th Seyller, L. Ley, C. A. Zorman, and M. Mehregany. Origin of the split Si-H stretch mode on hydrogen terminated 6H-SiC(0001): Titration of crystal truncation. *Applied Physics Letters*, 80(25):4726–4728, 2002.

[264] Z Y Xie, C H Wei, L Y Li, Q M Yu, and J H Edgar. Gaseous etching of 6H-SiC at relatively low temperatures. *Journal of Crystal Growth*, 217(July 1999):115–124, 2000.

[265] M. Soueidan, G. Ferro, J. Dazord, Y. Monteil, and G. Younes. Surface preparation of Alpha-SiC for the epitaxial growth of 3C-SiC. *Journal of Crystal Growth*, 275(1-2):1011–1016, 2005.

[266] Brian Seger, Thomas Pedersen, Anders B Laursen, Peter C K Vesborg, Ole Hansen, and Ib Chorkendor. Using TiO 2 as a Conductive Protective Layer for Photocathodic H 2 Evolution. *Journal of the American Chemical Society*, 135:1057–1064, 2013.

[267] Brian Seger, David S Tilley, Thomas Pedersen, Peter C K Vesborg, Ole Hansen, Michael Grätzel, and Ib Chorkendorff. Silicon protected with atomic layer deposited TiO 2 : durability studies of photocathodic H 2 evolution. *RCS Advances*, 3:25902–25907, 2013.

[268] Brian Seger, S David Tilley, Thomas Pedersen, Peter C K Vesborg, Ole Hansen, Michael Grätzel, and Ib Chorkendorff. Silicon protected with atomic layer deposited TiO2: conducting versus tunnelling through TiO 2. *Journal of Materials Chemistry A*, 1:15089–15094, 2013.

[269] Bastian Mei, Brian Seger, Thomas Pedersen, Mauro Malizia, Ole Hansen, Ib Chorkendor, and Peter C K Vesborg. Protection of p + - n-Si Photoanodes by Sputter-Deposited

Ir/IrO. *The Journal of Physical Chemistry Letters*, 5:1948–1952, 2014.

[270] Jürgen Ziegler, Bernhard Kaiser, Wolfram Jaegermann, Félix Urbain, Jan Philipp Becker, Vladimir Smirnov, and Friedhelm Finger. Photoelectrochemical and photovoltaic characteristics of amorphous-silicon-based tandem cells as photocathodes for water splitting. *ChemPhysChem*, 15(18):4026–4031, 2014.

[271] Félix Urbain, Vladimir Smirnov, Jan Philipp Becker, Uwe Rau, Jürgen Ziegler, Bernhard Kaiser, Wolfram Jaegermann, and Friedhelm Finger. Application and modeling of an integrated amorphous silicon tandem based device for solar water splitting. *Solar Energy Materials and Solar Cells*, 140:275–280, 2015.

[272] Félix Urbain. *Light induced water splitting using multijunction thin film silicon solar cells*. PhD thesis, Forschungszentrum Jülich, 2016.

[273] S Chakrabarty and K Chatterjee. Synthesis and Characterization of Nano-Dimensional Nickelous Oxide (NiO) Semiconductor. *Journal of Physical Sciences*, 13:245–250, 2009.

List of Figures

List of Tables

Index

CV

1985 Born in Hamburg

1996-2005 A-Levels, Julius-Leber-School (Hamburg)

2003 Student Exchange, Canton (New York State)

2005-2006 Voluntary Ecological Year, Hamburg Wasser

2006-2012 Diploma in Physics, Ruprecht-Karls-University Heidelberg

Diploma Thesis: *'Analysis Of Doping Induced Changes In The System Alpha-NPD:MoO$_3$ Via FTIR'*

Prof. A. Pucci

2013-2017 PhD in Materials Science,
Technische Universität Darmstadt
Université Grenoble Alpes

Title: *'Cubic Silicon Carbide For Direct Photoelectrochemical Water Splitting'*

Prof. W. Jaegermann & Prof. D. Chaussende

Abstract

The goal of this work was to investigate cubic silicon carbide as anode material for direct photoelectrochemical water splitting. From the performed measurements (mostly photoelectron spectroscopy, electrochemical measurements, Raman and UV-Vis spectroscopy) n-type cubic silicon carbide's low oxygen evolution efficiency could be related to some fundamental problems.

Primarily, the attainable photocurrent is limited by the flux of photo generated holes to the semiconductor surface. As cubic silicon carbide is a indirect semiconductor, the low absorption coefficient in combination with a high doping concentration and low hole diffusion length were determined as limiting factors. An additional epitaxial n^- cubic silicon carbide film resulted in a significant improvement of the photocurrent.

The obtainable photovoltage and recombination losses are mostly dependent on the surface properties. While a buried junction between the silicon carbide and a thin catalyst layer has proven to be promising for improving both properties, it still needs optimization, as Fermi level pinning from interface defect states drastically reduces the photovoltage.

Résumé

Le but de ce travail était d'évaluer la capacité du carbure de silicium cubique comme matériau d'anode pour le fractionnement photo-électrochimique direct de l'eau. Les données obtenues (principalement par spectroscopie de photoélectrons, électrochimie, spectrométrie Raman et spectrométrie UV-Vis) ont permis d'identifier les problèmes fondamentaux à l'origine de la faible efficacité du carbure de silicium cubique dopé n pour la production d'oxygène. Le courant photoélectrique atteignable est principalement limité par le flux de trous vers la surface du semi-conducteur, et générés par l'absorption de photon. Comme le carbure de silicium cubique possède une bande interdite de nature indirecte, le faible coefficient d'absorption combiné à un dopage élevé et à une faible longueur de diffusion des trous ont été déterminés comme des facteurs limitant. La mise en œuvre d'un film épitaxial additionnel de carbure de silicium cubique ayant un faible dopage n, a conduit à une augmentation significative du courant photoélectrique.

La tension photoélectrique obtenue et les pertes dues aux recombinaisons dépendent principalement des propriétés de surface. Même si l'utilisation de jonctions enterrées entre le carbure de silicium et des films minces de catalyseurs s'est révélée prometteuse pour l'amélioration des deux propriétés, une optimisation soigneuse est nécessaire car la forte densité d'états d'interface liés à des défauts limitent considérablement la tension photoélectrique.